

PH.D. IN ASTRONOMY, ASTROPHYSICS
AND SPACE SCIENCE
CYCLE XXXII

Observation and Characterization of the Solar Turbulent Convection

Giorgio Viavattene
A.Y. 2018/2019

Supervisor: Dario Del Moro

Co-supervisor: Giuseppe Consolini
Co-supervisor: Luca Giovannelli

Coordinator: Paolo De Bernardis

Deputy Coordinator: Nicola Vittorio

Abstract

The turbulent solar magneto-convection is one of the most intriguing phenomena observed in our star. The convection zone regulates the energy transport from the radiative zone to the photosphere (where the photons are free to escape) by means of the bulk displacement of the solar plasma. The motions of convective cells is established by the gravitational field and the vertical temperature gradient and it basically consists in the upflow of the hotter and brighter plasma elements (the so-called granules) and the downflow of the colder and darker plasma elements (the intergranular lanes). The latter are turbulent due to the high stratification in density of the solar convective plasma and they are considered the drivers of the solar convection. This mere scenario is considerably complicated by the presence of the photospheric magnetic fields, which interact with the convection pattern and alter it, originating a large variety of phenomena, such as the appearance of magnetic bright points in the intergranular lanes or the onset of micropores.
These phenomena are rather well explained by radiative magnetohydrodynamical (MHD) numerical simulations, which combine the properties of the solar plasma with the presence of the interacting magnetic fields and with the radiative transfer of the light. Despite the good agreement between radiative MHD simulations and high resolution observations, there are still several scientific open questions to be addressed and several processes that are not completely clear.
High resolution spectro-polarimetry is the more suitable methodological tool that can be used to infer the physical conditions of the solar convective plasma. In fact, the polarization states at different wavelengths of the incoming solar light own the imprinting of the physical parameters of the solar atmosphere, which can be extracted using inversion techniques. To do this, we need high spatial (< 100 km on the solar surface), spectral ($R > 200.000$) and temporal (few tenth of seconds) resolution spectro-polarimetric data acquired with top level technology instruments and telescopes.
In this PhD thesis, of the PhD program in "Astronomy, Astrophysics and Space Science" of the jointly collaboration between University of Rome La Sapienza, University of Rome Tor Vergata and Istituto Nazionale di Astrofisica, I am interested in the study of the physical properties of the solar turbulent magneto-convection using two complementary approaches: data analysis of high-resolution spectro-polarimetric dataset, and design, development and realization of instrumentation for Solar Physics applications.
In the Introduction, I present the current knowledge on turbulent solar magneto-convection, the parameters used to describe the convective plasma and the observation evidences compared to the theoretical approach of radiative MHD simulations. Then, I discuss on the open scientific questions on solar convection the instruments and methods needed and the organization of the manuscript.
The Second Chapter is devoted to the theory of solar spectro-polarimetry, the radiative transfer and the analysis methods used in this thesis, the Center of Gravity Method (CoG) and the Inversion Techniques. After describing the dataset, I introduce my contribution to the data

analysis part of this manuscript. I present a comparison analysis between the CoG method and the inversion techniques, showing evidences that the inversion techniques tend to overestimate weak magnetic fields in Quiet Sun regions. After that, I use the same dataset to evaluate the vertical heat flux maps, a proxy of the entropy production rate, which can be used as a clue to study the solar convection. With this analysis, I obtain strong evidenced that the solar turbulent convection satisfies the simmetry conjecture predicted by the Gallavotti-Cohen Fluctuation Theorem, analyzing the solar convection as a non-equilibrium stationary-state system.
The Third Chapter is dedicated to the spectro-polarimetric instrumentation required for the observation of the solar convection. After describing the theory behind the operation of a Fabry-Perot Interferometer (FPI), I present three instrumental activities. I partecipated in the design, assembly and test phases of a FPI prototype controlled with one of the first digital controller, featuring its electronical noise and resulting spectral stability. This kind of digital control could substitute the old analog ones and they will be of fundamental importance for the next generation spectro-polarimetric imaging instruments based on FPIs. After that, I realized a feasibility study of a narrow band imager based on large diameter FPIs and off-axis parabolic mirrors, starting from the conceptual design of Greco and Cavallini, using Zemax software. I implemented a new 3D version of the optical scheme, pointing out the improvements and the tolerance problem, and suggesting possible solutions to overcome these instrumental issues. At the end of this Chapter, I present the optical scheme of a full-disk solar synoptic telescope based on the Magneto-Optical Filters (MOF) technology that I entirely designed with Zemax. The new Tor vergata Solar Synoptic Telescope (TSST) will consist in this MOF-based telescope coupled with an Hα solar telescope, and it will be used for large scale patterns studies, Space Weather applications and flare forecasting.
The last Chapter summarizes the results that I obtained during my PhD, discussing the achieved scientific impact and instrumental improvements. The thesis is concluded by discussions on future developments of the work done.

Contents

Chapter 1

Introduction: the Solar Convection

1.1 The solar magneto-convection

Convection due to a vertical temperature gradient is one of the most frequent type of fluid motion in the Universe and yet one of the most complex since it is a non-linear and a non-local process (Stein, 2012). Solar convection is of fundamental importance for the internal structure and appearance of our star, and it originates a large variety of phenomena that can be observed in the solar atmosphere.
The solar convection has been described by the *Rayleigh-Bénard* theory (Getling, 2001; Ching, 2014), which describes the convection as a system consisting in a layer of fluid where a vertical temperature gradient is applied and placed inside a gravitational field (Getling, 2001; Ching, 2014). This description predicts the onset of stable convective cells of approximately hexagonal shape, with the hotter material moving upwards in the central part of the cells and the cooler material moving downwards at the edges of the cells. Nevertheless, the Rayleigh-Bénard theory is not accurate enough to describe the high dynamics of the solar convection, because it is a very peculiar case of convection due to several reasons. Firstly, the downflow plasma of the solar convection is turbulent due to the high density stratification in the upper convection layer. This determines a particular type of convection with unstable and evolving convective cells. Secondly, the whole solar surface is permeated by magnetic fields, originated by the dynamo processes in the internal layers of the Sun, that causes a perturbation of the typical Rayleigh-Bénard convection pattern, since the Lorentz force inhibits the motion perpendicular to the field. For this reason, the processes presented in this introduction are referred to the *solar magneto-convection*. Furthermore, the solar surface is a radiative systems where there is a transition of the energy transport: in the lower layers the energy transport is regulated by the convection, maintained by the moving fluid; instead, in the upper layers the radiation is carried out by the free-streaming photons. In addition, there are several concomitant processes, such as the ionization and molecules dissociation, that greatly complicate the description and make the analytical solution impossible to reach. This complexity requires a more detailed description and modeling of the solar magneto-convection, using high resolution observations and a theoretical support from radiative magnetohydrodynamics simulation.
From the point of view of the statistical thermodynamics, the solar magneto-convection is a non-equilibrium process which represents a prototype phonomenon for the emergence of complexity in out-of-equilibrium systems, which manifests in the emergence of spatial ordering.

1.1.1 The parameters of the convection

In this section, we introduce some parameters used to describe the convective fluids and that can be used also to describe the solar convection.
Considering the characteristic length scale H (means the characteristic dimension of the convective phenomenon) and the characteristic temperature scale Δ (means the temperature difference between the upper and the lower part of the convective cell), we can define the characteristic velocity scale $\sqrt{\alpha g H \Delta}$ and the characteristic time scale $\sqrt{H/(\alpha g \Delta)}$.
With these definitions, we can introduce the Rayleigh and Nusselt numbers:

$$Ra = \frac{\alpha g \Delta H^3}{\nu \kappa} \tag{1.1}$$

$$Nu = \frac{Q}{k\Delta/H} \tag{1.2}$$

where α is the volume expansion coefficient, g is the acceleration of gravity, $\nu = \eta/\rho$ is the kinematic viscosity (with η the viscosity and ρ the density), κ is the thermal diffusivity, Q is the transferred heat flux by the fluid convection across any horizontal plane, $k = \kappa \rho_0 c$ (with ρ_0 the internal density of the convective cell when its movement starts to occur), c is the specific heat capacity of the fluid and $k\Delta/H$ is the transferred heat flux due to the conduction.
The Rayleigh number Ra quantifies how much the driving buoyancy force is greater than the kinematic viscosity and the thermal diffusivity. If the Ra number is greater than a critical value Ra_c, the steady-state convection starts and the temperature at a fixed position is independent of time. When Ra increases of few orders of magnitude, firstly the temperature fluctuations become chaotic and the nearby points remain correlated. If Ra increases of several orders of magnitude, the turbulence starts and the spatial coherence is lost. According to numerical simulations, the Ra number for the solar photospheric convection varies between 10^{14} and 10^{28} Nordlund et al. (2009).
The Nusselt number Nu quantifies the heat flux transferred by the convection with respect to the one transferred by conduction. For the upper surface of the convective zone the Nu number is greater than 1; recent simulations gives value greater than $5 \div 10$ Nordlund et al. (2009).
These two numbers describes the physical properties of the convective fluid, in our case the solar photospheric plasma. Currently, there is a strong interest for an experimental determination of the Rayleigh number of the solar photospheric plasma, more so there are no experimental methods to its direct measurement. This information will be really valuable to increase the reliability of the numerical simulations in order to obtain a more realistic theoretical approach. Present laboratory experiments in strong turbulent convection (Niemela et al., 2000) are able to reach values of the Ra number of about 10^{16} and they show a strong dependence with the Nu number: $Nu \propto Ra^{1/2}$. According to the theory of Kraichnan (Kraichnan, 1962), there should be a logarithmic correction in the relation between Ra and Nu: $Nu \propto Ra^{1/2}/[\ln Ra]^{3/2}$. The experiments with high Ra numbers do not confirm this prediction, but they show a large spectrum of bifurcations for $Ra >> 10^{16}$ (Urban et al., 2014), that indicate the onset of unstable situations. In (Berrilli, 2003) there is a good review in which the Ra and the Nu numbers, estimated from laboratory experiments and numerical simulations of convection in different spatial scales, are largely discussed and compared with velocity and intensity pattern of spectral (Berrilli et al., 1999) and spectro-polarimetric observations (Berrilli et al., 2002).

1.1.2 Connections with Mixing Length Theory

Since we are talking about convection, we can not skip the description of the first convection theory that has been introduced to describe the stellar convection: the Mixing Length Theory (MLT) (Böhm-Vitense, 1958) and its extension to include turbulence effects (Canuto and Mazzitelli, 1991, 1992). MLT has been used for decades to describe the stellar convection and the stellar evolution in 1D geometry. The MLT is based on a plasma element which is in pressure equilibrium with the surrounding. The plasma element moves upward because it has higher temperature, higher entropy and lower density with respect to surrounding, and viceversa for the plasma element that moves downward driven by the gravity. After moving for a *mixing length* distance l, the plasma element dissolves in the surrounding. Usually the mixing length distance is equal to some multiple of the pressure scale height.
Despite the success of this theory, the description of the convection that it provides is far from realistic. The MLT is an non adequate description for the Sun because the solar turbulent convection occurs to many pressure and density scale heights. Since the Sun in a spatially-resolved celestial body, there are several observed physical processes which are not contemplated by the MLT. In addition, the local approach of the MLT is not adequate to describe the temperature and velocity fluctuations on the solar photosphere, which are mainly determined by the radiative cooling on the boundary layer of the photosphere, and not by local conditions.
This is to underline that we need more realistic 3D models to describe the dynamics of the solar convection, and that we can use the solar convection as a prototype of the stellar convection for star with masses approximately in the range from 0.5 to 6 solar masses.

1.1.3 The observation of the solar convection

W. Herschel was the first to observe the solar convection, describing it as hot clouds floating over a colder solar surface (Herschel, 1801). The terms *granules* was coined by W. R. Dawes (Dawes, 1864) to describe the shape of the convection pattern observed on the solar surface.
There are several spectro-polarimetric observations of the solar magneto-convection, which report a lot of information about the morphology, the evolution and the interaction with the magnetic fields; some examples are (Berrilli et al., 2001, 2002; Del Moro, 2004; Roudier et al., 2003; Wilken et al., 1997; Krieg et al., 2000; Hirzberger, 2002; Puschmann et al., 2005). The shapes, widths and shifts of the spectral lines are the fingerprints of the convective motion, because they are connected to the convective velocity field and to the correlations between velocity and temperature, which cause spectral line asymmetries (Asplund et al., 2000). The most used spectral lines to investigate the solar convection are the Fe lines, because they are mainly formed in the stable overshooting layer of the solar convection. The overshooting layer is a convectively stable and stratified layer which is formed immediately above the convectively unstable convection zone. In this overshooting region the Schwarzschild criterion is not validy anymore (Landi Degl'Innocenti, 2004). The overshooting region is generated by the momentum of the moving convective plasma, which drags the plasma beyond the unstable region. In few words, when we observe the solar convection, we are observing the stable overshooting region.
As an example, Fig. 1.1 shows the typical solar granulation pattern, as seen on the high resolution spectro-polarimetric dataset used in this thesis near the continuum of the Fe I 630.15 nm spectral line. The granules are hotter and brighter than the surrounding plasma, they move upwards due to the buoyancy force and they have higher entropy. Instead, the *intergranular lanes*, which surround the granules, are cooler and darker, they move downwards and they have lower entropy. The solar convection is constituted by a sort of fountain-like cell structure

with vertical hot plasma jets surrounded by lanes of falling cool plasma. The dimension of the convective cells is approximately 1 Mm, which correspond to the horizontal scale where the convective motions are driven by the radiative cooling. The dimension of the granules is dictated by the equation of conservation of mass. The upper layers of the convection zone are highly stratified in density and mass, and the density scale height is smaller than the typical dimension of the granules. This high gradient of density creates a marked asymmetry in the solar convective flows: the rising plasma from higher to lower density can not carry all its plasma mass, so it diverges and turns over within a scale height; the descending plasma moves from lower to higher density and it is compressed during its downward movement, therefore it becomes turbulent. The convective downflow turbulent plumes are the best candidates for maintaining/driving the solar convection due to their high efficienty in exchanging heat. For this reason, the solar convection must be described including turbulent processes in the intergranular lanes: this is why we talk about *turbulent solar convection*.
The density of the solar convective plasma goes from 10^{-5} kg/m^3 in the granules to 10^{-3} kg/m^3 in the intergranular lanes. The typical vertical velocities of the upflow and downflow movement of the solar photospheric convective cells is between -2 km/s and +2 km/s approximately. In addition, upflow plasma occupies 2/3 of the solar photospheric area and downflow plasma occupies 1/3 of the area. This area asymmetry causes the observed convective blue-shift of photospheric spectral lines (Löhner-Böttcher et al., 2018).
By imposing the conservation of mass, we obtain that the upflowing plasma through a convective cell with a vertical velocity v_z, approximated as a cylinder of radius r, must flow out sideways over a distance equal to the scale height H and with a velocity v_H:

$$\pi r^2 \rho v_z \approx 2\pi r H \rho v_H \tag{1.3}$$

and therefore the horizontal dimension of a convective granular cell is of the order of:

$$r \approx 2H \frac{v_H}{v_z} \tag{1.4}$$

Both observations and numerical simulations agree indicating an horizontal dimension of approximately 1 Mm, which correspond to a little more of an arcsecond (Berrilli et al., 2001, 2002; Del Moro, 2004; Nordlund and Stein, 1991). The average vertical velocity of the upflow must be over 1.5 km/s to support the radiative losses on the surface and the horizontal velocity must be lower than the speed of the sound. Obviously, the movement of the solar convective cells is limited by the velocity of the sound in photosphere, which is approximately 7 km/s: in fact, both the vertical pure convective movement and the horizontal advected one can not exceed the velocity of the sound. Therefore, the movement of the convective cells cannot be supersonic. The vertical dimensions of convective granular cells is of the order of 20÷30 Mm, and consequently the time scale of the convective cells evolution is 5÷10 minutes. In (Del Moro, 2004), indeed, a pattern recognition algorithm is presented and used to derive the horizontal velocity maps of the granules motion measuring their displacement and their lifetime, confirming what was said before.
The granules that carry too much energy to be dissipated by radiative cooling and by the horizontal sideway tend to develop a dark center with a downflow motion, due to a negative buoyancy triggered by the rise of pressure at the center of the granule; this process enhances the horizontal movement of the plasma from the center to the edge of the granules. These so-called *exploding granules* have been reported in several observations and theoretical works (Roudier et al., 2001; Rast, 1995; Hirzberger et al., 1999; Simon et al., 1991).
Regarding the solar surface convection entropy, it drives the convective motions that we observe

on the Sun, because the high density fluid pulled down by the gravity has low entropy, with respect to the upper part of the granules which have high entropy. The entropy can be therefore used as a tool to study the physical properties and behaviour of the solar convection.
Apparently, the high density stratification influences also the temperature and velocity patterns and their evolution. The vertical heat flux on the solar photospheric convection can be computed from the product of the temperature and the vertical velocity. The statistical properties of this physical parameter, used as a proxy of the entropy production rate, has been analyzed in this thesis (see Chapter 2) in order to verify the Fluctuation Relation of Gallavotti-Cohen (Gallavotti and Cohen, 1995; Gallavotti, 1999) for steady-state non-equilibrium systems on the solar turbulent convection.
The solar surface is the place where the photons can escape from one mean free path. The opacity χ of this layer is governed by the electrons, and it is very sensitive to temperature variation of the order of $\chi \approx T^{10}$. Since this great sensitivity with the temperature, the photons can escape from larger depths in the cooler intergranular lanes than from smaller depths in the hotter central part of the granules. This is why the solar surface appears as a corrugated surfaces (Carlsson et al., 2004; Nordlund et al., 2009), as reported in Fig. 1.2.
So far, we described the convection pattern in absence of magnetic fields. But the solar quiet photosphere is permeated by the presence of magnetic fields from few tenths of Gauss to 1 kGauss which alter the solar convection pattern (Nordlund et al., 2009; Stein, 2012; Bellot Rubio and Orozco Suárez, 2019). The sum of the magnetic pressure with the gas pressure inside a magnetic element of the solar surface is equal to the gas pressure in its surrounding because the pressure balance is valid. In addition, the term $\mathbf{J} \times \mathbf{B}$ (where $\mathbf{B}$ is the magnetic field and $\mathbf{J}$ is the current) must be added in the equation of motion. This approach is used to describe the high magnetic energy density in the magnetized elements of the solar photosphere. These magnetic flux tubes elements are emptied and therefore they appear brighter because in the magnetic flux tubes the radiation comes from deeper layers of the solar atmosphere, which are hotter: in fact they are called *magnetic bright points* (MBPs). The MBPs are moved by the convection flow because descending into the solar convection zone the gas pressure $p_g = nK_BT$ becomes larger than the magnetic pressure $p_{mag} = B^2/(2\mu)$, and therefore the diverging upflows transport the magnetic field elements in the quiet Sun (see Fig. 1.3), since the plasma beta $\beta = p_g/p_{mag}$ becomes greater than 1 (Domínguez Cerdeña et al., 2003; Vögler et al., 2005; Stein and Nordlund, 2006; Van Kooten and Cranmer, 2017). They are usually observed in high-contrast images in the G-band at 430 nm of the solar spectrum due to the CH molecules dissociation caused by the slightly high temperature in this magnetized regions. The magnetic fields elements with a sub-arcsecond dimension emerge continuously in the solar photosphere with both magnetic polarity. There are several observations reporting phenomena of coalescence, fragmentation and cancellation between them, which are driven by buoyancy and advection (the elements with strong magnetic fields) (Viticchié, 2012; Viticchiè et al., 2011; Viticchié et al., 2010; Sánchez Almeida et al., 2010; Criscuoli et al., 2012; Stangalini et al., 2009; Romano et al., 2012; Martínez González and Bellot Rubio, 2009; Guglielmino et al., 2012).
There are various effect induced by the presence of the magnetic fields in the solar convection. The magneto-convection causes an erosion of the magnetic structure due to the diffusivity. In addition, the radiative cooling leads to the formation of upflow plumes with strong magnetic fields, which are associated to the MBPs. All these results obtained in magneto-convection simulations are supported by several observations (Viticchié et al., 2010; Viticchiè et al., 2011; Viticchié, 2012).
In several papers (Giannattasio et al., 2013, 2014a,b, 2018, 2019), the displacement spectrum

$< (\Delta r)^2 > \propto \tau^{\gamma}$ of the solar magnetic elements has been evaluated, where Δr is the distance between two magnetic elements, τ is the time since the first detection and γ is the diffusive exponent. The found values between $\gamma \approx 1.20$ and $\gamma \approx 1.55$ from the granular to the super-granular scale confirm that the magnetic elements follow a super-diffusive dynamics regime. These works provide strong evidence of how the magnetic elements of the solar photospheric convection are transported by the convection motions.
Another interesting phenomenon of the solar magneto-convection is the limb behaviour of the solar granulation. Also in absence of magnetic fields, near to the solar limb, the granulation shows an hilly-corrugated pattern with the granules higher than the intergranular lanes with a vertical drop of about 80 km. Adding the presence of the magnetic fields, the sides of the granules appear brighter due to the low density of the magnetic flux tubes with respect to the surrounding, because they are observed at high optical depths and these layer have higher temperature. The net effect is that the presence of the magnetic fields enhances the corrugated appearance of the granules, as reported in Fig. 1.4 (Carlsson et al., 2004). If the magnetic fields in the intergranular lanes is large enough, these bright sides of the granulation cells form the solar *faculae*, a sort of magnetic bright network around the solar active regions.
In the Solar Physics community it is widely accepted that, since the photospheric convection is the last source of mechanical energy, it can be the driver of the chromospheric and coronal heating through magnetohydrodynamic (MHD) turbulence, energy dissipation in Alfvén waves and torsional waves and resistive electrical currents (Srivastava et al., 2017; Stangalini et al., 2017).
All these physical phenomena regarding the solar magneto-convection are nowadays studied with top level spectro-polarimetric instrumentation based on imaging interferometry or slit spectroscopy. Today's instruments, especially those based on Fabry-Perot Interferometers, installed on large diameter solar telescopes up to 1-meter of aperture and equipped with adaptive optics sytems, are at their limit regarding the spatial resolution and the polarimetric sensitivity. In fact, the structures like the MBPs have dimensions less than 1 arcsecond and they possess low polarimetric signals (generated by Zeeman effect) especially in the linear polarization (see Chapter 3 for a quantitative evaluation). Currently there is a great need to build large diameter solar telescope, such as the Daniel K. Inouye Solar Telescope (DKIST) (Keil et al., 2009; Woeger, 2016; Rast, 2015; Tritschler et al., 2015) and the European Solar Telescope (EST) (Collados, 2008; Collados et al., 2010a,b, 2013; Zuccarello and EST Team, 2012), with a 4-meter class primary mirror, which will allow a major ability to capture photons and to reach an angular resolution of 0.04 arcseconds (corresponding to approximately 20 km on the solar photosphere) with the assistance of adaptive optics and multi-conjugated adaptive optics.
In the framework of the construction of this new large diameter solar telescopes, new instrumentation with top level technology and innovative systems is needed to address the open scientific questions on solar convection, such as the center-to-limb variation of the magnetic field in the intergranular lanes, the *internetwork*, the height variation and the origin of the magnetic field vector of the internetwork (see after).

1.2 The solar convection as a laboratory for far-from-equilibrium systems

In the previous section, we described the observative features of the solar convection. In this section, we present the peculiarity of the solar convection from a physical point of view,

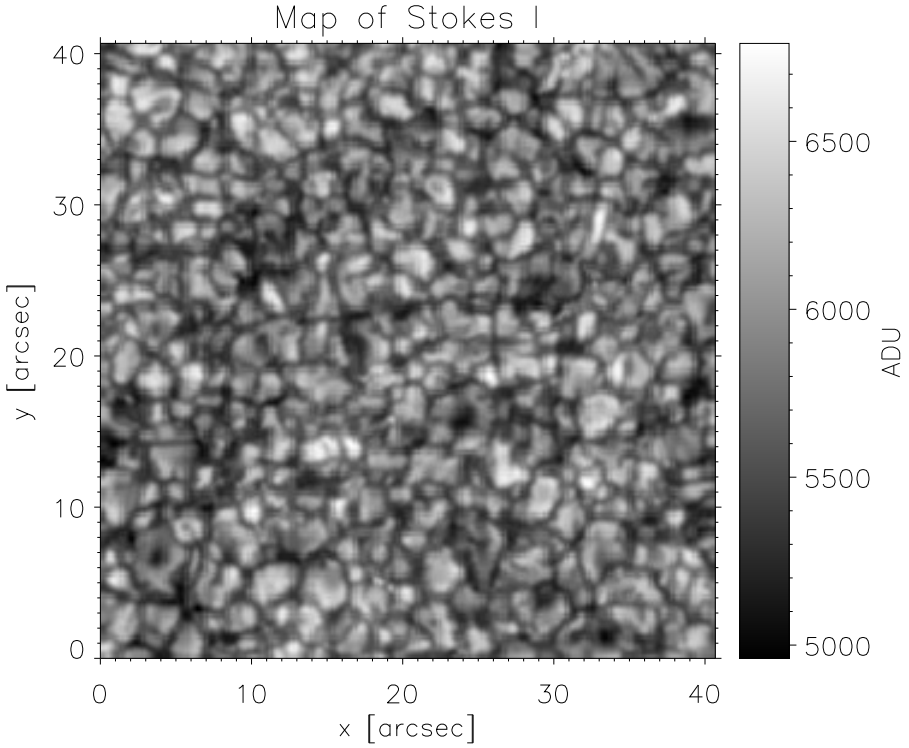

Figure 1.1: Image of the solar granulation pattern from the dataset used in this thesis near the continuum of the Fe I 630.15 nm spectral line. The hot and bright rising granules are surrounded by cooler and darker intergranular lanes.

especially regarding the statistical thermodynamics.

The physical system of the solar convection presents phenomena related to strong turbulence in the intergranular lanes caused by the high density stratification and by the high *Ra* number of the solar upper convection layer. In addition, the entire solar surface is permeated by the presence of diffuse magnetic fields which interact and alter the convection pattern. For these reasons, the solar convection is a very particular type of convection: it is a *turbulent magneto-convection*. The Sun is the only observable system in which we can study these extreme and concomitant processes.

First of all, the high Rayleigh number ($\geq 10^{12}$) of the solar convection is not reproducible in laboratory experiments. Niemela and coauthors were able to reach Rayleigh numbers of the order of 10^7 (Niemela et al., 2000), and Shang and coauthors were able to reach 10^9 on a cylindrical cell filled with water (Shang et al., 2005). Furtheremore, the high density stratification of the solar convection is far from being established in controlled experiments.

Secondly, linear and non-linear statistical thermodynamics predicts that in systems far-from-equilibrium there is a spontaneous production of entropy, which is at the origin of the irreversibility, according to the second law of Thermodynamics. Since, the solar turbulent magneto-convection is driven by the entropy fluctuation in the granules and in the intergranular lanes, we can think to use the measured entropy and its fluctuations to characterize the dynamical and the thermodynamical state of the solar convection. In fact, it is well known that there is a positive net flux of entropy on the solar surface due to the photon and energy radiation in an irreversible way.

Therefore, we can use the turbulent solar magneto-convection as a laboratory to characterize

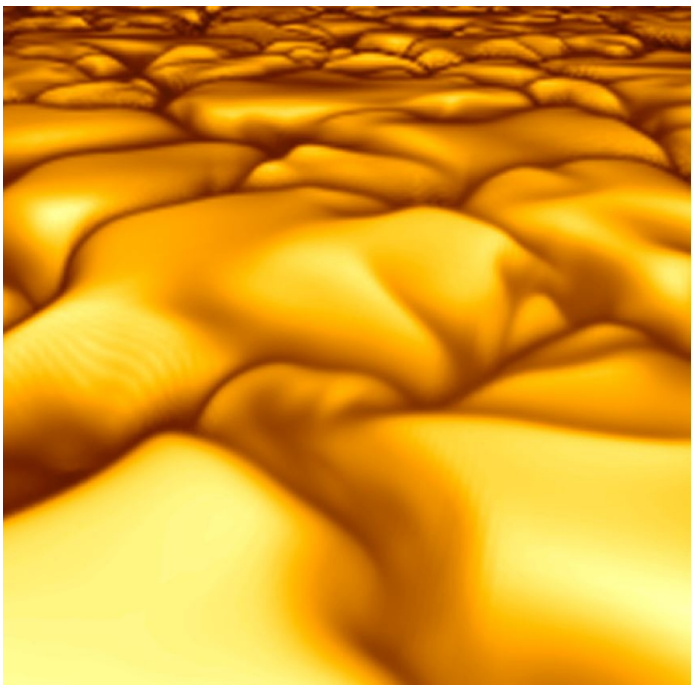

Figure 1.2: Corrugated surface of the solar photosphere due to turbulent convection. Image from a magneto-convection simulation from (Nordlund et al., 2009; Carlsson et al., 2004).

the systems in far-from-equilibrium regime. Solar spectro-polarimetry is the tool that comes to us to perform remote measurements of the physical properties of the solar atmosphere. Using the remote sensing of the polarization states of the incoming light at different wavelenghts with large diameter solar telescopes and their suite of spectro-polarimetric instruments, we are able to extract the physical properties of the solar atmospheric plasma by inverting the radiative transfer equation of the light.
The acoustic oscillations on the photosphere have a mean period of 5 minutes and they are caused by pressure waves that generate a bulk plasma upwards/downwards movement, which is superimposed with the convection cells movement. In order to make more precise our analysis, we have to use a $k_h - \omega$ filter (Title et al., 1989) with a cuf-off velocity of 7 km/s (which correspond to the sound speed on the solar photosphere) in order to separate the oscillations generated by the photospheric convection with respect to the signal generated by the acoustic oscillations (Landi Degl'Innocenti, 2004).

1.2.1 State of the art of the solar convection

We present here a brief overview of the state of the art of solar convection from a theoretical point of view and simulations.
In the following paragraphs, we will make use of the term "pressure scale height", we will therefore introduce the concept in the framework of a quasi-static approximation. Considering that the acceleration of gravity is approximately constant close to the solar photosphere and that it must be balanced by the pressure gradient, the other terms of Eq. 1.8 can be neglected, and we obtain the equation of the *hydrostatic equilibrium*:

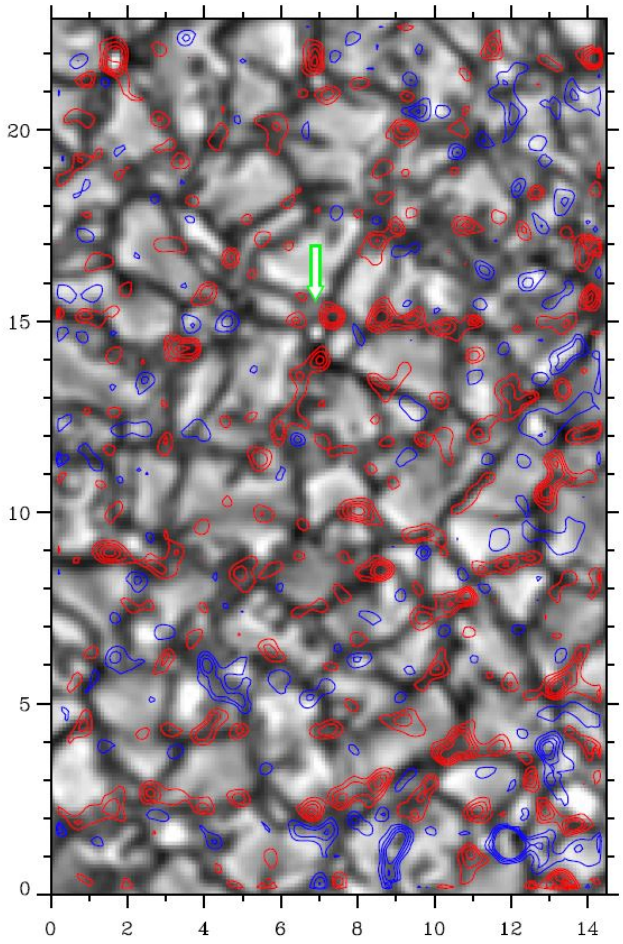

Figure 1.3: Granulation pattern image with magnetogram contours superimposed at 30, 50, 70 and 90 G from observations in Fe I 630.25 nm spectral line. The axes are in arcsecons. The green arrow indicates a magnetic bright point. Figure from (Domínguez Cerdeña et al., 2003).

$$-\frac{p}{\rho}\frac{\partial \ln p}{\partial z} = \frac{\partial \Phi}{\partial z} = g \tag{1.5}$$

Assuming the temperature to be constant, the pression p decrease exponentially with the height z:

$$p = p_0 e^{-z/H_p} \tag{1.6}$$

where $H_p = p/(\rho g)$ is the pressure scale height.
We present the hydrodynamics description of the solar convection treating the solar convective plasma as a compressible fluid. The following equations are at the basics for numerical modeling and we present them in the Eulerian form.
The *conservation of the mass* is expressed by the continuity equation:

$$\frac{\partial \rho}{\partial t} = -\nabla \cdot (\rho \mathbf{v}) \tag{1.7}$$

which means that a local density variation is balanced by a rapid expansion in the lateral direction caused by a variation of the mean density with high in an ascending flow.
The *equation of motion* assumes the following form:

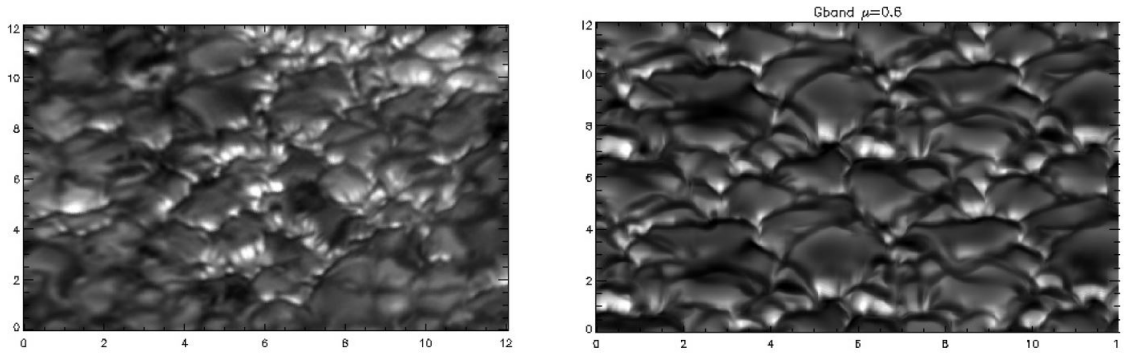

Figure 1.4: Enhanced corrugated appearance of the solar granulation near the solar limb due to the presence of magnetic fields in the intergranular lanes. Comparison between observations (left panel) and simulations (right panel). Figure from (Carlsson et al., 2004).

$$\frac{\partial(\rho\mathbf{v})}{\partial t} = -\nabla\cdot(\rho\mathbf{v}\mathbf{v}) - \nabla p - \rho\nabla\Phi - \nabla\cdot\hat{\tau}_{visc} \tag{1.8}$$

where Φ is the gravitational potential and $\hat{\tau}_{visc}$ is the viscous stress tensor.
Then, relaxing the quasi-static approximation, the *kinetic energy equation* can be obtained by multiplying Eq. 1.8 by $\mathbf{v}$:

$$\frac{\partial E_{kin}}{\partial t} = -\nabla\cdot(E_{kin}\mathbf{v}) - \mathbf{v}\cdot\nabla p - \rho\mathbf{v}\cdot\nabla\Phi + viscous\ terms \tag{1.9}$$

which means that the local variation of the kinetic energy are enforced by the transport of the kinetic energy, the work performed by the gradient of the pressure force, the work performed by the gravity force and the work performed by the viscosity force.
In the conservative form, the *conservation of the energy* is ensured by the following equation:

$$\frac{\partial U}{\partial t} = -\nabla\cdot(E\mathbf{v}\mathbf{v}) - p(\nabla\cdot\mathbf{v}) + Q_{rad} + Q_{visc} \tag{1.10}$$

where U is the internal energy per unit of volume, Q_{rad} is the radiative heating and Q_{visc} is the heating caused by the viscosity.
The radiative heating can be written in terms of the radiative flux $Q_{rad} = -\nabla\cdot\mathbf{F}_{rad}$, with:

$$\mathbf{F}_{rad} = \int_\nu\int_\Omega I_\nu(\Omega,\mathbf{r},t)\Omega\, d\Omega\, d\nu \tag{1.11}$$

where ν is the frequency of the radiation, Ω is the solid angle and I_ν is the radiation intensity that can be obtained by the *radiative transfer equation* (see Chapter 2):

$$\frac{\partial I_\nu}{\partial\tau_\nu} = S_\nu - I_\nu \tag{1.12}$$

where S_ν is the source function and τ_{nu} is the optical depth, defined using the geometrical depth ds as $d\tau_\nu = \rho\chi_\nu ds$, where χ_ν is the absorption coefficient.
The system of the hydrodynamics equation of the solar convection is closed by the *equations of state*: $p = p(\rho, E)$ and $\chi_\nu = \chi_\nu(\rho, E)$.
Eq. 1.10, 1.11 and 1.12 show clearly the connection between the hydrodynamics and the radiative transfer theory, explaining why solar physicists use to unify MHD simulations with radiative transfer codes for polarized light in order to study and interpret the solar convection

observations. Solar spectro-polarimetry is the most powerful tool to investigate the solar turbulent magneto-convection because the physical properties of the convection pattern and the interacting magnetic fields leave several imprints on the Zeeman-induced polarization signals of the spectral lines, which can be recovered by inverting the radiative transfer equation for polarized light applied to spectro-polarimetric observations.
The interaction with the magnetic fields complicates considerably the problem, because the term $\mathbf{J} \times \mathbf{B}$ must to be included in the equation of motion. The effect of the magnetic fields on the convection pattern are reproduced pretty good with simulations in (Vögler et al., 2005). Starting from solar convection simulations and adding a uniform vertical magnetic field of various increasing strengths, the principal visible effect is the reduction of the granules dimension, and secondly the appearance of magnetic field elements in the intergranular lanes. These two combined effects would cause the onset of *micropores* in the downflow plasma located in the intersection of various intergranular lanes (Vögler et al., 2005; Cattaneo et al., 2003). The micropores are the embryos of the pores, small darker magnetic regions, which, in turn, if the magnetic field is strong enough, can evolve in the sunspots. In this sense, the intergranular magneto-convection can influence the formation and the evolution of the solar active regions characterized by the presence of sunspots. The onset, the evolution and the coalescence of the micropores is only predicted by numerical simulations; currently there are no observations of these phenomena.
Nowadays, there is a good agreement between spectro-polarimetric observations and numerical simulations, but some observed phenomena are not well reproduced by simulations. O. Steiner proposed to use the distribution of the magnetic flux density to compare the observations and the simulations (Steiner, 2003). The results show a good agreement except for high magnetic field strengths. The asymmetry between upflows and downflows, which may be responsible of overall flux balance in the convection zone through the storage of magnetic flux energy, is well reproduced with simulations in (Nordlund et al., 2009; Stein and Nordlund, 2006). Their simulations confirm that the granular flow disperses the magnetic flux tubes in the intergranular lanes, promoting the cancellation and the cohalescence processes of the magnetic elements, described before. Other simulations (Vögler et al., 2005) show that the magnetic field lines are very concentrated near the solar surface and that they tend to spread out in several directions below the surface.
To integrate our discussion on radiative MHD simulations, we report in Fig. 1.5 a result obtained with Bifrost simulation code (Gudiksen et al., 2011; Carlsson and Hansteen, 2005). It is mainly based on MHD equations coupled with energy, momentum and radiative transfer equations, resolved numerically imposing boundary conditions. The image shows the temperature and velocity behaviour from the convection zone up to the solar corona. The transition region is between the reddish and the white part. The red color scale indicate the temperature of the zones above the photosphere. The white line stands for $\tau_c = 1$. The color scale in the bottom part of the image indicates the vertical velocity of the layer below the photpshere, with downflow in red and upflow in blue. The strong downflow motions in the intergranular lanes are turbulent, as stated in the observational description of the solar convection. In addition, the magnetic field lines emerge in the strong downflow intergranular lanes.
So far, we described how the numerical simulations have been also used to explain the physical processes or to validate the observational hypotheses. Numerical simulations can be also used to formulate predictions about observations. Recent simulations (Calvo et al., 2016), in fact, show how the MBPs may not all be of magnetic origin, but some of them could be of convective origin. According to the authors, in absence of the magnetic field, the swirling motion in low density small regions could produce a depression due to the centrifugal force. In this case, the

enhancement of the radiation is caused by the fact that the radiation in the depression comes from an hotter deeper layer, and not from an emptied magnetic flux tubes. This phenomenon has not yet been observed due to spatial resolution limitation, but it is labeled as a scientific case candidate for the European Solar Telescope.

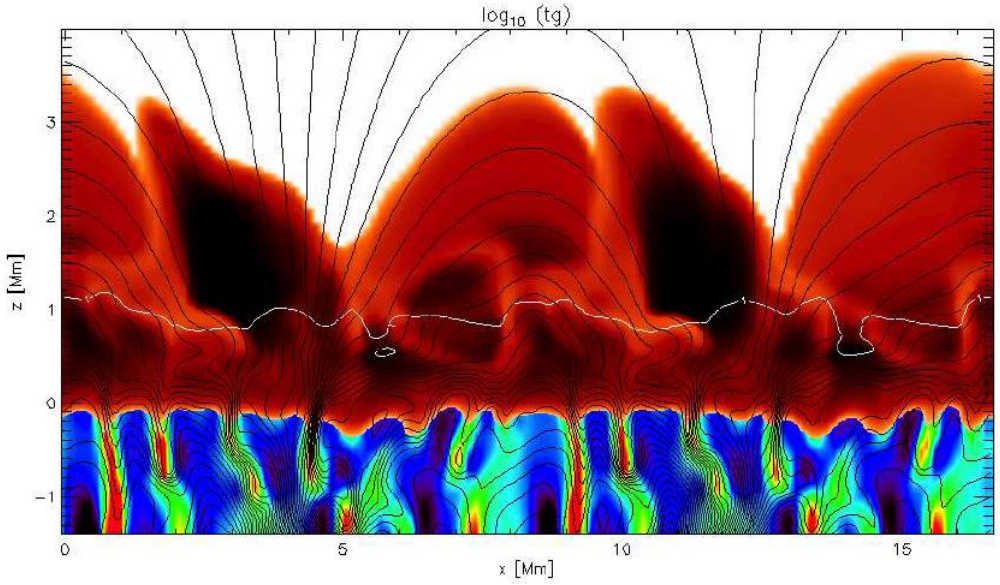

Figure 1.5: Simulation with Bifrost from the top of the convection zone up to the solar corona. The transition region is between the reddish and the white part. The color scale indicate the temperature. The white line stands for $\tau_c = 1$. The color scale in the bottom part of the image indicates the vertical velocity, with downflow in red and upflow in blue. Figure from (Carlsson and Hansteen, 2005)

1.2.2 Open scientific questions on the solar magneto-convection

Although there is a large number of high resolution spectro-polarimetric observations provided by current large diameter solar telescopes, there are still several open scientific questions about the solar turbulent magneto-convection (Bellot Rubio and Orozco Suárez, 2019). We present here a short list of these, which have been selected as scientific cases for the new generation 4-meter class solar telescopes:

- *Downflow turbulent plumes*: there is a strong agreement in the Solar Physics community that the drivers of the solar magneto-convection are the turbulent downflow plumes in the intergranular lanes, but it is not clear if they are supersonic or not (Lagg et al., 2006);

- *Overshooting region*: there are no direct evidences of the real extension of the stable overshooting region over the unstable convective region (Nordlund et al., 2009);

- *Overshooting region between the radiative and the convective zones*: there should be also an inferior overshooting region between the radiative zone and the convective zone (at 0.7 solar radius approximately), which should transport the processed material in the convective region (Landi Degl'Innocenti, 2004). More knowledge on this internal overshooting region can be very helpful for improving models of stellar structure and evolution;

- *Small-scale interaction between magnetic fields and convection*: there is a strong interaction between the solar convection and the photospheric magnetic fields (Viticchié et al., 2010; Giannattasio et al., 2013), but their joint behaviour in small scale structure (< 80 km on the solar surface) is not appreciable with present resolution limit of large diameter solar telescopes;

- *Viscosity and diffusivity parameters*: the characteristic parameters of the solar plasma, such as the kinematic viscosity ν and the thermal diffusivity κ are not measurable with spectro-polarimetric methods and they are provided only by numerical simulations (Nordlund et al., 2009);

- *Parameters of the convection*: Rayleigh and Nusselt numbers are also extimated with radiative MHD numerical simulations and they have a huge range of variability over several order of magnitude (Nordlund et al., 2009): $10^{14} < Ra < 10^{28}$, $5 < Nu < 100$;

- *Internal structure of small-scale magnetic flux concentration*: the observed asymmetries in Stokes V profiles suggests the existence of magnetic canopies and flows (Viticchié, 2012); the observational characterization of their internal structure may help to improve the current magneto-convection simulations (Steiner et al., 1998; Vögler et al., 2005; Stein and Nordlund, 2006; Rempel, 2014). With high resolution observations, we will help to map the height variation and jumps of the magnetic field vector and velocity (Rezaei et al., 2007; Martínez González et al., 2012; Buehler et al., 2015);

- *Magnetic bright points (MBPs)*: as said before, MBPs are observed in the solar G-band as small-scale magnetic features with a kG magnetic field strength at the spatial resolution limit with current solar telescopes (Zwaan, 1987; Abramenko et al., 2010; Viticchié et al., 2010); they could play an important role on the solar total irradiance since it is suspected that they are the small bricks of the solar magnetism. They could be also connected to the diffusion of the magnetic fields (Giannattasio et al., 2013, 2014a,b, 2018, 2019; Utz et al., 2010; Abramenko et al., 2011) and they could excite solar magnetohydrodynamics (MHD) waves (Muller et al., 1994);

- *Emergence and evolution of magnetic fields in granular convection*: the magnetic fields can emerge on the solar photosphere in different ways, i.e. with low-lying magnetic loops located in the intergranular lanes (Centeno et al., 2007; Viticchié, 2012) or with vertical fields in quiet Sun granules (Orozco Suárez et al., 2008), and in both cases the time scale is few minutes. Other process involved in the integranular lanes is the magnetic flux cancellation (two magnetic features of opposite polarities come into contact and disappear) (Viticchié et al., 2009), which is at the polarization limit of detectability.

1.2.3 Instruments and methods

To answer the scientific questions of this thesis, we need robust and reliable methods and instruments. High resolution spectro-polarimetry is the best tool to investigate the physical properties of the solar turbulent magneto-convection. As said before, the shape, the wavelength shift and the width of the spectral lines are the fingerprint of the convective motions. In addition, the magnetic counterpart of the solar convection lives a footprint on the polarization state of the incoming light due to the Zeeman effect (Landi Degl'Innocenti, 2004). These two reasons are the strong points of the use of high resolution spectro-polarimetry for solar convection studies.

The core of this approach lies in the radiative transfer equation for polarized light, which describes how the solar radiation propagates and interact with the solar atmospheric medium and how the polarization state at different wavelengths is influenced by the solar atmospheric conditions. In particular, starting from high resolution spectro-polarimetric data, spectro-polarimetric inversions are able to retrieve a stratification of the physical parameters that originate the observed polarimetric signals at different wavelengths (del Toro Iniesta and Ruiz Cobo, 2016). The theory of the radiative transfer for polarized light and of the spectro-polarimetric inversions is presented in Chapter 2.
The high resolution spectro-polarimetric data must be acquired with telescope with an aperture large enough to guarantee to reach an angular resolution of approximately 0.20 arcsec, which correspond to ∼120 km on the solar surface. The only way to increase the spatial resolution and the number of collecting photons (and so to increase to polarimetric accuracy) is to increase the aperture of the telescope, and this is the main purpose for which telescopes like EST or DKIST are being built.
The telescope must be equipped with high performance instruments able to select the various polarization states at different wavelengths of the solar incoming light. The most suitable instruments to perform this kind of analysis are the Fabry-Perot Interferometers (FPIs), which are able to retrieve 2D images at different wavelengths positions in various spectral regions. A polarimeter used in conbination with FPIs is able to select the various polarization states of the light. The FPIs are to be preferred with respect to slit spectrograph because they have higher transparency and efficienty with a quite good spectral resolution. For more details on FPIs, see Chapter 3.
As an example, in this thesis, I make use of an high resolution spectro-polarimetric dataset acquired with the Interferometric BIdimensional Spectro-polarimeter (IBIS) (Cavallini, 2006) installed on the 70cm diameter (spatial resolution 120 km) Dunn Solar Telescope (DST) (Dunn, 1964b,a). The dataset has been analyzed using different methods and with different purposes, as shown in Chapter 2.

1.3 Goals of this thesis

The aim of this thesis is to provide a better characterization of the solar turbulent magneto-convection using two complementary approach: data analysis and instrumentation design and development.
Regarding the data analysis part, I decided to use IBIS/DST high-resolution spectro-polarimetric data to study the properties of the solar convection observed in the solar photosphere. I investigated which analysis method is the more suitable to study high resolution spectro-polarimetric data of solar convection comparing two of the most used ones: the Center of Gravity Method (Rees et al., 1989; Rees and Semel, 1979) and the Inversion Techniques (Ruiz Cobo and del Toro Iniesta, 1992; Socas-Navarro, 2015; Socas-Navarro et al., 2015). After discussing pros and cons of each method and their best applicability based on scientific context, I used the same spectro-polarimetric dataset to provide a first indication of the validity of the Gallavotti-Cohen Fluctuation Relation (Gallavotti and Cohen, 1995) in the framework of the real astrophysical system of the solar convection. This validity test allows us to assert that the solar turbulent convection satisfies the simmetry properties predicted by the Gallavotti-Cohen Fluctuation Relation for non-equilibrium stationary-state systems. Afterwards, I decided to use the results of this validity test to provide a first raw estimation of the Rayleigh number of the solar photospheric plasma.

Regarding the instrumental part, instead, I want to propose some technological and optical solutions needed to perform high resolution spectro-polarimetric observations of the solar convection. I partecipated in the design, assembly and test phases of a Fabry-Perot interferometer prototype controlled with one of the first digital controller. This kind of digital controller will be of fundamental importance for new generation imaging instruments for large diameter upcoming solar telescopes, for a better spectral stability and a finer spectral resolution. I proposed a new optical scheme based on off-axis parabolic mirrors and large diameter Fabry-Perot interferometers for spectro-polarimetric imaging instruments, as a variant of an optical configuration proposed by Greco and Cavallini (Greco and Cavallini, 2013). At the end, I entirely realized the optical scheme of a full-disk solar telescope based on magneto-optical filters: it will acquire complementary data for studying large scale convection patterns, Space Wheather applications and flare forecast.

1.3.1 Organization of the manuscript

The organization of the manuscript is led by the two complementary approach, data analysis and instrumentation, that I decided to follow during my PhD. Therefore the entire thesis, after the Introduction, is arranged in two macro-blocks, in which I present my best contributions in both the scientific data analysis of solar convection and the interconnected instruments design and development which are needed to provide high-resolution spectro-polarimetric dataset for the solar convection studies. This thesis is organized in four chapters as follows:

- In this first Chapter, I reported on the physical properties of the solar magneto-convection, on the parameters and the observation of the solar photospheric convection, the state of the art in this research field and the open scientific questions, and finally the instruments and the methods that can be used for answer;
- The second Chapter is entirely devoted to the analysis of a spectro-polarimetric dataset of the solar convection. After presenting the radiative transfer for the polarized light and two of the most used analysis method for spectro-polarimetric dataset, I described two analysis performed during my PhD program. I compared the Center-of-Gravity Method and the Inversion Techniques on an high resolution spectro-polarimetric dataset showing that spectro-polarimetric inversions tend to overestimate the magnetic field intensity in weak magnetic fields regions. After that, I used the same dataset to verify if the solar turbulent convection satisfies the simmetry properties predicted by the Gallavotti-Cohen Fluctuation Relation;
- The third Chapter starts with a general overview on instrumentation for Solar Physics, with particular attention on FPIs and MOF-based instruments, showing their application fields and their limitations. I described all the design, development, assembly and test phases of an FPI prototype controlled with a digital controller in the framework of the GREST project. After, I presented a feasibility study of a narrow band imager based on two FPIs with off-axis parabolic mirrors. I concluded this Chapter showing the optical scheme of the TSST telescope based on MOF technology;
- The fourth Chapter concludes the manuscript and summarizes the obtained results on the solar convection research field and portrays the future perspectives of this work.

Chapter 2

Spectro-polarimetric analysis of a solar convection dataset

This Chapter is entirely devoted to analysis of solar spectro-polarimetric data acquired with the Dunn Solar Telescope and the Interferometric BI-dimensional Spectro-polarimeter. After introducing the theory of the radiative transfer for polarized light and two of the most used methods to analyze this kind of data, I present the results obtained in this thesis: a comparison analysis between the Center of Gravity Method and the inversion techniques, and a validity analysis of the Gallavotti-Cohen Fluctuation Theorem on the solar turbulent convection, viewing the solar convection as a Non-Equilibrium Steady-State system.

2.1 Solar Spectro-polarimetry

Solar spectro-polarimetry is a powerful tool to investigate physical processes occurring in the solar atmosphere. The different states of polarization at different wavelengths have in fact encoded the information about the dynamics and the thermodynamic state of the solar plasma and the interacting magnetic field. Therefore the radiative transfer equation for polarized light is at the core of this approach (Viavattene, 2016).

2.1.1 The polarization of light

A beam of light that propagates in an isotropic medium can be interpreted as a superposition of electromagnetic waves, each described by the electric field vector, which is contained in the plane perpendicular to the propagation direction.
If the beam is propagated along the z axis, the electromagnetic wave components along the x and y axes can be written as follows:

$$E_x(t) = A_x(t)e^{-i[\omega t - \delta_x(t)]} \tag{2.1}$$

$$E_y(t) = A_y(t)e^{-i[\omega t - \delta_y(t)]} \tag{2.2}$$

where $\delta_x(t)$ and $\delta_y(t)$ represent the phase shift of the x and y components, $A_x(t)$ and $A_y(t)$ their amplitudes and ω the frequency.
With these five parameters it is possible to represent any electromagnetic wave.

The most convenient way to decribe the polarization of an electromagnetic wave is introducing a set of four parameters, called the *Stokes parameters*, defined as:

$$I = k(< |E_x(t)|^2 > + < |E_y(t)|^2 >) = k(A_x^2 + A_y^2) \tag{2.3}$$

$$Q = k(< |E_x(t)|^2 > - < |E_y(t)|^2 >) = k(A_x^2 - A_y^2) \tag{2.4}$$

$$U = k(< E_x(t)^* E_y(t) > + < E_y(t)^* E_x(t) >) = 2k(A_x A_y cos\delta(t)) \tag{2.5}$$

$$V = ik(< E_x(t)^* E_y(t) > - < E_y(t)^* E_x(t) >) = 2k(A_x A_y sin\delta(t)) \tag{2.6}$$

where * means the complex coniugated, k is a proportionality constant equal for all Stokes parameters, $\delta(t) = \delta_x(t) - \delta_y(t)$ is the total phase difference between the x and y components and <> stands for time average.
We can introduce then the *Stokes vector*:

$$\boldsymbol{I} = \begin{pmatrix} I \\ Q \\ U \\ V \end{pmatrix} = (I, Q, U, V)^\dagger \tag{2.7}$$

where I stands for the total intensity, Q and U give information about linear polarization and V about circular polarization.
The defined quantities are real and measurable, and follow the relationship $I^2 \geq Q^2 + U^2 + V^2$, where the equality is valid only if the radiation is completely polarized. When, instead, $Q = U = V = 0$, the radiation does not present polarization. In the other cases, the radiation is partially polarized.
In the real case, the total intensity is given by the sum of polarized component and unpolarized component:

$$I = I_p + I_{np} \tag{2.8}$$

The degree of linear polarization is given by:

$$\Pi_l = \frac{\sqrt{Q^2 + U^2}}{I} \tag{2.9}$$

the degree of circular polarization by:

$$\Pi_c = \frac{V}{I} \tag{2.10}$$

and the total degree of polarization by the sum of these two contributes.

2.1.2 The Zeeman effect

In 1896, by laboratory experiments, P. Zeeman discovered that the spectral lines are influenced by the magnetic field. He noticed that the effect of the magnetic field is to produce the splitting of the spectral lines and that the various components have different polarization states. These phenomena were explained by the electron theory of Lorentz.

The Zeeman effect was initially used to understand the fine structure of atoms, but after the discovery of magnetic fields on the Sun, when Hale (Hale, 1908a,b,c) observed splitting of the lines in a sunspot, the Zeeman effect has become an invaluable tool for the diagnostics of solar magnetic fields.
In the classical Lorentz theory that describes the phenomena of absorption, emission and scattering in a spectral line, the atom is represented as an electron oscillating around the nucleus under the action of a harmonic force with frequency ν_0.
The presence of a magnetic field **B** perturbes the electron oscillations, and consequently the emerging spectrum. This is called the *normal Zeeman effect*. Then, in accordance with the theory of Larmor, the new oscillation can be decomposed into three components with frequencies ν_0, $\nu_0 - \nu_L$ and $\nu_0 + \nu_L$, where $\nu_L = \frac{eB}{4\pi mc}$ is the Larmor frequency.

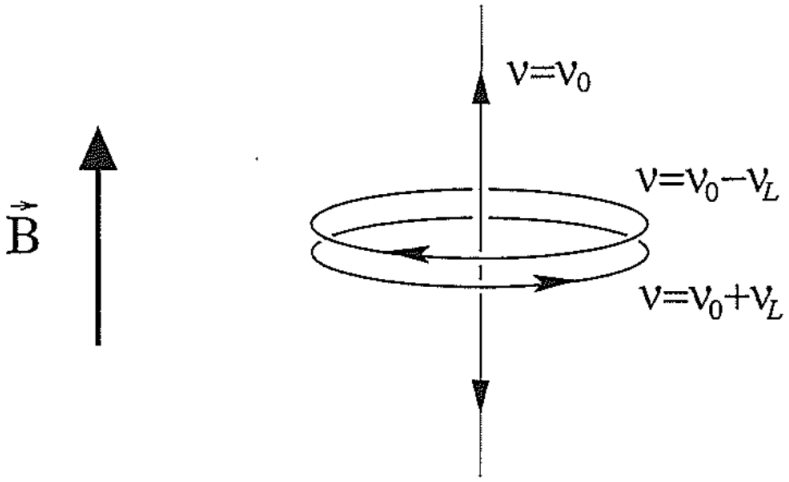

Figure 2.1: Representation of the atom in the Lorentz classical theory in the presence of a magnetic field (Bellot Rubio 1998).

The component of the oscillation in the direction of **B** (the π-component) mantains its natural frequency ν_0, while the circular components in the plane perpendicular to **B** (the σ-components) have their frequencies shifted by $\pm\nu_L$. Then, looking perpendicularly to the magnetic field, we observe linear polarization parallel to the magnetic field at frequency ν_0 and linear polarization perpendicular to the magnetic field at frequencies $\nu_0 - \nu_L$ and $\nu_0 + \nu_L$; while, looking along the magnetic field, we observe only the two components at frequencies $\nu_0 - \nu_L$ and $\nu_0 + \nu_L$ circularly polarized, one clockwise and the other counterclockwise (Fig. 2.1).
If the spectral lines are split into four or more components, we have the so-called *anomalous Zeeman effect*, which is not interpreted within the classical theory, but within quantum theory. From a quantum point of view, we know that, for most atomic energy levels, in case of not too strong magnetic fields as those usually found in the solar photosphere (lower than a few kilogauss), the orbital angular momentum **L** and the spin **S** are coupled (Russell-Saunders or LS coupling) and the total angular momentum is given by $\mathbf{J} = \mathbf{L} + \mathbf{S}$. The magnetic field splits the level (L,S,J) in $2J + 1$ Zeeman sublevels, which are characterized by a magnetic quantum number $M = -J, ..., +J$. Obviously in the transitions are valid the selection rules: $\Delta J = 0, \pm 1$ and $\Delta M = 0, \pm 1$. The transition which has $\Delta M = 0$ produces the π-components, $\Delta M = +1$ produces the σ_b-components and $\Delta M = -1$ the σ_r-components. The components can also be indicated by the indices $j = -1, 0, +1$ which correspond respectively to b, p and r.

Following Wittmann (Wittmann, 1974), the shift in the wavelengths of the individual Zeeman components i_j with respect to the original position is given by:

$$\Delta\lambda_{B,i_j} = \frac{e\lambda_0^2 B}{4\pi mc^2}(g_l M_l - g_u M_u)_{i_j} \tag{2.11}$$

where l and u stand for the lower and upper level of the line transition, g is the Landé factor of the level, e and m the charge and the mass of the electron, c the velocity of light and λ_0 the central wavelenght of the line under exam.
In c.g.s. system of measurement, the previous formula can be written as follows:

$$\Delta\lambda_{B,i_j} = 4.66864 * 10^{-5}(g_l M_l - g_u M_u)_{i_j} B\lambda_0^2 \tag{2.12}$$

The Landé factor is given by:

$$g = \begin{cases} \frac{3}{2} + \frac{S(S+1)-L(L+1)}{2J(J+1)} & \text{if } J \neq 0 \\ 0 & \text{otherwise} \end{cases} \tag{2.13}$$

The strength of the various Zeeman components can be expressed as:

$$S_{i_j} = \frac{s_{i_j}}{\sum_{i_j=1}^{N_j} s_{i_j}} \tag{2.14}$$

where the summation is extended to the number of levels and the unnormalized strenghts s_{i_j} of the various Zeeman components are reported in the table:

	$\Delta M = +1 \quad (\sigma_b)$	$\Delta M = 0 \quad (\pi)$	$\Delta M = -1 \quad (\sigma_r)$
$\Delta J = +1$	$(J_u + M_u)(J_l + M_u)$	$2(J_u^2 - M_u^2)$	$(J_u - M_u)(J_l - M_u)$
$\Delta J = 0$	$(J_u + M_u)(J_u - M_u + 1)$	$2M_u^2$	$(J_u - M_u)(J_u + M_u + 1)$
$\Delta J = -1$	$(J_l - M_u)(J_u - M_u + 2)$	$2(J_l^2 - M_u^2)$	$(J_l + M_u)(J_u + M_u + 2)$

Table 2.1: Unnormalized strenghts s_{i_j} of the various Zeeman components

In general, the Zeeman pattern can be rather complicated. However, if the fine structure of the pattern can not be resolved, the case can be treated in terms of *equivalent Zeeman triplets* (Landi Degl'Innocenti, 1982), having shifted frequencies of:

$$\Delta\lambda = \frac{e\lambda_0^2}{4\pi mc^2} g_{eff} B \tag{2.15}$$

where the Landè effective factor is:

$$g_{eff} = \frac{1}{2}(g_l + g_u) + \frac{1}{4}(g_l - g_u)[J_l(J_l+1) - J_u(J_u+1)] \tag{2.16}$$

2.1.3 The radiative transfer for polarized light

Now, I discuss the concepts of radiative transfer through a magnetized atmosphere, such as the solar atmosphere. Later, I present the Milne-Eddington approximation.
The propagation of the electromagnetic radiation through a stellar atmosphere is a complex, non-linear, three dimensional and time dependent problem, that involves the properties of the whole atmosphere (Landi Degl'Innocenti and Landolfi, 2004a; Landi Degl'Innocenti, 2004;

Viavattene et al., 2019c). Following the notation of Landi Degl'Innocenti (Landi Degl'Innocenti and Landi Degl'Innocenti, 1985) the equation of radiative transfer (hereafter referred to as RTE) for the polarized light in a plane parallel atmosphere, which describes how the radiation propagates through the solar atmosphere, is:

$$\frac{d\mathbf{I}}{d\tau} = \mathbf{K}(\mathbf{I} - \mathbf{S}) \tag{2.17}$$

where $\mathbf{I}$ is the Stokes vector defined in Eq. 7.7, which gives a complete description of the state of polarization of light, τ is the optical depth at the wavelenght of the transitions, $\mathbf{K}$ is the 4×4 propagation matrix and $\mathbf{S}$ is the suorce function vector. These last two quantities contain all the properties of the medium that are relevant to the formation of the line.
In local thermodynamic equilibrium (LTE) conditions the source function vector is:

$$\boldsymbol{S} = \begin{pmatrix} B_\lambda(T) \\ 0 \\ 0 \\ 0 \end{pmatrix} = (B_\lambda(T), 0, 0, 0)^\dagger \tag{2.18}$$

where $B_\lambda(T) = \frac{2\pi hc^2}{\lambda^5} \frac{1}{e^{\frac{hc}{\lambda kT}} - 1}$ is the Planck function at the local temperature T.
The propagation matrix of the RTE takes the form:

$$\boldsymbol{K} = \begin{pmatrix} \eta_I & \eta_Q & \eta_U & \eta_V \\ \eta_Q & \eta_I & \rho_V & -\rho_U \\ \eta_U & -\rho_V & \eta_I & \rho_Q \\ \eta_V & \rho_U & -\rho_Q & \eta_I \end{pmatrix} \tag{2.19}$$

The diagonal elements of this matrix describe the phenomena of *absorption* (with the same amount of energy in all the polarization states), the symmetrical elements stand for the *dichroism* (differential absorption in the various polarization states), and those antisymmetric for the phenomena of *dispersion* (transfer among the various polarization states). In this way, the RTE can be consider a conservation equation because the energy and the polarization state of the light at a given point in the atmosphere can vary only due to emission, absorption, dichroism and dispersion processes.
The elements of the propagation matrix are given by:

$$\eta_I = 1 + \frac{\eta_0}{2}\left[\phi_p sin^2\gamma + \frac{\phi_b + \phi_r}{2}(1 + cos^2\gamma)\right] \tag{2.20}$$

$$\eta_Q = \frac{\eta_0}{2}\left[\phi_p - \frac{\phi_b + \phi_r}{2}\right] sin^2\gamma\, cos2\chi \tag{2.21}$$

$$\eta_U = \frac{\eta_0}{2}\left[\phi_p - \frac{\phi_b + \phi_r}{2}\right] sin^2\gamma\, sin2\chi \tag{2.22}$$

$$\eta_V = \frac{\eta_0}{2}[\phi_r - \phi_b] cos\gamma \tag{2.23}$$

$$\rho_Q = \frac{\eta_0}{2}\left[\psi_p - \frac{\psi_b + \psi_r}{2}\right] sin^2\gamma\, cos2\chi \tag{2.24}$$

$$\rho_U = \frac{\eta_0}{2}\left[\psi_p - \frac{\psi_b + \psi_r}{2}\right] sin^2\gamma\, sin2\chi \tag{2.25}$$

$$\rho_V = \frac{\eta_0}{2}[\psi_r - \psi_b]cos\gamma \tag{2.26}$$

where $\phi_{p,b,r}$ and $\psi_{p,b,r}$ are the absorption and the dispersion profiles, the indeces p, b, r stand for the π and $\sigma_{b,r}$ (blue and red) components of the Zeeman multiplet, η_0 is the line-to-continuum absorption coefficients ratio, and γ and χ are respectively the inclination and the azimuth of the magnetic field vector with respect to the line-of-sight (LoS)(Fig. 2.2).

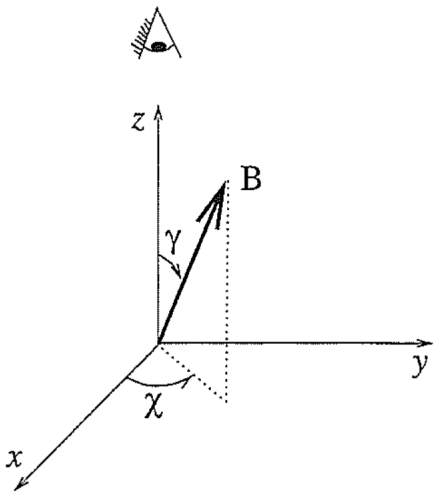

Figure 2.2: Coordinates system for the angles of the magnetic field vector (Bellot Rubio 1998).

$\phi_{p,b,r}$ and $\psi_{p,b,r}$ can be written as the sum of some absorption and dispersion profiles of the components p, b, r as follows:

$$\phi_j = \frac{1}{\sqrt{\pi}} \sum_{M_l - M_u = j} S_{M_l M_u, j}\, H(a, v) \tag{2.27}$$

$$\psi_j = \frac{2}{\sqrt{\pi}} \sum_{M_l - M_u = j} S_{M_l M_u, j}\, F(a, v) \tag{2.28}$$

where $S_{M_l M_u, j}$ are the strenghts of the components, the index $j = -1, 0, +1$ corresponds to b, p, r.
The total shift of the wavelenght due to the magnetic field and the Doppler effect of the plasma motion, in Doppler units, is given by:

$$v = \frac{\lambda - \lambda_0}{\Delta\lambda_D} + \frac{\Delta\lambda_B}{\Delta\lambda_D} - \frac{\lambda_0 v_{LOS}}{c\Delta\lambda_D} \tag{2.29}$$

where v_{LOS} is the plasma velocity along the line of sight (LOS) and the Doppler width is:

$$\Delta\lambda_D = \frac{\lambda_0}{c}\left(\frac{2kT}{M} + v_{mic}^2\right)^{\frac{1}{2}} \tag{2.30}$$

with k the Boltzman constant, T the temperature, M the mass of the atom involved in the transition and v_{mic} the microturbolence velocity (Mihalas, 1977).
$H(a, v)$ and $F(a, v)$ are the Voigt and the Faraday-Voigt functions:

$$H(a,v) = \frac{a}{\pi}\int_{-\infty}^{\infty} e^{-y^2}\frac{1}{(v-y)^2+a^2}\,dy \tag{2.31}$$

$$F(a,v) = \frac{1}{\pi}\int_{-\infty}^{\infty} e^{-y^2}\frac{(v-y)}{(v-y)^2+a^2}\,dy \tag{2.32}$$

a is the so-called damping parameter, which measures the effective frequency of collisions in Doppler units:

$$a = \frac{\Gamma\lambda_0^2}{4\pi c\Delta\lambda_D} \tag{2.33}$$

where Γ is the line damping parameter used in order to describe the effects of the pressure in the line's broadening.

The Milne-Eddington approximation

The Milne-Eddington approximation provides an analytical solution to the radiative transfer problem. The first heuristic derivation of the RTE solution for Stokes parameters of a Zeeman triplet was made by Unno (Unno, 1956). It has been extended by Rachkovsky (Rachkovsky, 1963, 1967) to include the magneto-optical effect and by Beckers (Beckers, 1969a,b) to treat the Zeeman multiplets. The general theory of the formation of a line for polarized light was made by Landi degl'Innocenti (Landi Degl'Innocenti, 1983b,a). In the Milne-Eddington atmosphere, all atmospheric quantities are constant with depth and the source function is linear with the optical depth:

$$\mathbf{S} = \mathbf{S}_0 + \mathbf{S}_1\tau = (S_0 + S_1\tau)(1,0,0,0)^\dagger \tag{2.34}$$

Furthermore also the propagation matrix is constant with depth, and this implies that all the parameters that define the spectral line formation (i.e. the line-to-continuum absorption coefficient, the Doppler width and the damping parameter) are constant with depth and also the magnetic field vector and the velocity along the line-of-sight are constant through the atmosphere, and the RTE has a very simple analytical solution. The fact that the atmospheric quantities are constant limits the cases in which this analytical solution can be applied; we will see later that, when there are gradients in atmospheric quantities, the resolution of the RTE requires a numerical approach.
The analytical solutions are given by:

$$I = S_0 + \Delta^{-1}[\eta_I(\eta_I^2 + \rho_Q^2 + \rho_U^2 + \rho_V^2)]S_1 \tag{2.35}$$

$$Q = -\Delta^{-1}[\eta_I^2\eta_Q + \eta_I(\eta_V\rho_U - \eta_U\rho_V) + \rho_Q\Pi]S_1 \tag{2.36}$$

$$U = -\Delta^{-1}[\eta_I^2\eta_U + \eta_I(\eta_Q\rho_V - \eta_V\rho_Q) + \rho_U\Pi]S_1 \tag{2.37}$$

$$V = -\Delta^{-1}[\eta_I^2\eta_V + \eta_I(\eta_U\rho_Q - \eta_Q\rho_U) + \rho_V\Pi]S_1 \tag{2.38}$$

where:

$$\Delta = \eta_I^2(\eta_I^2 - \eta_Q^2 - \eta_U^2 - \eta_V^2 + \rho_Q^2 + \rho_U^2 + \rho_V^2) - \Pi^2 \tag{2.39}$$

$$\Pi = \eta_Q \rho_Q + \eta_U \rho_U + \eta_V \rho_V \tag{2.40}$$

As is easily seen, the parameters $\eta_I, \eta_Q, \eta_U, \eta_V, \rho_Q, \rho_U, \rho_V$ and also the analitical expressions depend only by nine paramters: (B, γ, χ) describing the properties of magnetic field vector, (S_0, S_1) describing the source function, $(\eta_0, \Delta\lambda_D, a)$ describing the shape of the line and v_{LoS}, the shift of the line due to the Doppler effect of the plasma motion.

2.1.4 Formal solution of the RTE

The main problem in astrophysics is to be able to measure the physical properties of an object starting from the observed spectrum. Unfortunately we can not make in situ measurements of temperature, velocity, magnetic field, density; but they must be extracted from the physical properties of polarized light. The only possible way to do this is to solve the RTE, which contains the relationships between the observable Stokes spectrum and the unknown physical quantities in the medium (Ruiz Cobo and del Toro Iniesta, 1992).
Consider the homogeneous equation (Landi Degl'Innocenti and Landi Degl'Innocenti, 1985):

$$\frac{d\mathbf{I}_h}{d\tau_c} = \mathbf{K}\,\mathbf{I}_h \tag{2.41}$$

where $\mathbf{I}_h$ represents a solution of this equation and τ_c is the continuum optical depth. We indicate with $\mathbf{O}(\tau_c, \tau_c^{'})$ a linear operator which gives the transformation of the homogeneous solution between two points at optical depth τ_c and $\tau_c^{'}$:

$$\mathbf{I}_h(\tau_c) \equiv \mathbf{O}(\tau_c, \tau_c^{'})\mathbf{I}_h(\tau_c^{'}) \tag{2.42}$$

$\mathbf{O}(\tau_c, \tau_c^{'})$ is known as the evolution operator and it must satisfy the following two relations:

$$\mathbf{O}(\tau_c, \tau_c) = \mathbf{1} \tag{2.43}$$

$$\mathbf{O}(\tau_c, \tau_c^{''}) = \mathbf{O}(\tau_c, \tau_c^{'})\mathbf{O}(\tau_c^{'}, \tau_c^{''}) \tag{2.44}$$

The variation of $\mathbf{I}_h$ with respect to τ_c will be given by:

$$\frac{d\mathbf{I}_h(\tau_c)}{d\tau_c} = \frac{d\mathbf{O}(\tau_c, \tau_c^{'})}{d\tau_c}\mathbf{I}_h(\tau_c) \tag{2.45}$$

On the other hand, substituting the definition of the evolution operator in the homogeneous equation, we get:

$$\frac{d\mathbf{I}_h(\tau_c)}{d\tau_c} = \mathbf{K}(\tau_c)\mathbf{O}(\tau_c, \tau_c^{'})\mathbf{I}_h(\tau_c^{'}) \tag{2.46}$$

Equating these last two equations we will obtain:

$$\frac{d\mathbf{O}(\tau_c, \tau_c^{'})}{d\tau_c} = \mathbf{K}(\tau_c)\mathbf{O}(\tau_c, \tau_c^{'}) \tag{2.47}$$

Now we can use the evolution operator as a factor of integration. Multiplying the RTE by $\mathbf{O}(\tau_c^{'}, \tau_c)$:

$$\mathbf{O}(\tau_c^{'},\tau_c)\frac{d\mathbf{I}}{d\tau_c} = \mathbf{O}(\tau_c^{'},\tau_c)\mathbf{K}(\mathbf{I}-\mathbf{S}) \tag{2.48}$$

The left-hand side is equal to:

$$\mathbf{O}(\tau_c^{'},\tau_c)\frac{d\mathbf{I}}{d\tau_c} = \frac{d}{d\tau_c}[\mathbf{O}(\tau_c^{'},\tau_c)\mathbf{I}(\tau_c)] - \frac{d\mathbf{O}(\tau_c^{'},\tau_c)}{d\tau_c}\mathbf{I}(\tau_c) \tag{2.49}$$

The first term on the right-hand of the precedent equation, using the previous relations, can be rewritten as:

$$\frac{d}{d\tau_c}[\mathbf{O}(\tau_c^{'},\tau_c)\mathbf{I}(\tau_c)] = -\mathbf{O}(\tau_c^{'},\tau_c)\mathbf{K}(\tau_c)\mathbf{S}(\tau_c) \tag{2.50}$$

Integrating with respect to the optical depth between τ_0 and τ_1, we obtain:

$$\mathbf{I}(\tau_1) = \mathbf{O}(\tau_1,\tau_0)\mathbf{I}(\tau_0) - \int_{\tau_0}^{\tau_1}\mathbf{O}(\tau_1,\tau_c)\mathbf{K}(\tau_c)\mathbf{S}(\tau_c)\,d\tau_c \tag{2.51}$$

The first term of the solution takes into account the contribution of the boundary condition $\mathbf{I}(\tau_0)$ after travelling throughout the atmosphere between τ_0 and τ_1, and the second one adds the contribution of the light emitted $\mathbf{K}(\tau_c)\mathbf{S}(\tau_c)$ in each layer of optical thickness $d\tau_c$ after crossing the atmosphere between τ_c and τ_1.
In the case of stellar atmospheres the observer is placed at $\tau_1 = 0$ and, at the limit, there are no photons that arrive directly outside from inside:

$$\lim_{\tau_0\to\infty}\mathbf{O}(0,\tau_0)\mathbf{I}(\tau_0) = 0 \tag{2.52}$$

And then finally, we can write the formal solution in the following way:

$$\mathbf{I}(0) = \int_0^{\infty}\mathbf{O}(0,\tau_c)\mathbf{K}(\tau_c)\mathbf{S}(\tau_c)\,d\tau_c \tag{2.53}$$

2.1.5 Response functions

Because of the algebraic properties of matrices in the RTE, we understand that the problem is non-linear, and this increases the difficulty of solving the problem. Usually such problems are faced with perturbation theory: in our case we perform a perturbation analysis of the problem in which small perturbations in the model atmosphere parameters that propagate linearly cause small variations in the Stokes spectrum (Ruiz Cobo and del Toro Iniesta, 1992).
Let us denote the parameters of the model $(T, p_e, B, \theta, etc, ..)$ using the generic notation:

$$\mathbf{x}(\tau_c) = [x_1(\tau_c), x_2(\tau_c), ..., x_{m-1}(\tau_c), x_m(\tau_c)] \tag{2.54}$$

Considering small perturbations $\delta x_i(\tau_c)$, in a first order approximation, the induced variations in the propagation matrix and in the source function can be written as:

$$\delta\mathbf{K}(\tau_c) = \sum_{i=1}^{m}\frac{\partial\mathbf{K}}{\partial x_i}\delta x_i(\tau_c) \tag{2.55}$$

$$\delta\mathbf{S}(\tau_c) = \sum_{i=1}^{m}\frac{\partial\mathbf{S}}{\partial x_i}\delta x_i(\tau_c) \tag{2.56}$$

These small variations in $\mathbf{K}$ and $\mathbf{S}$ will produce small changes in the Stokes vector $\delta\mathbf{I}$, and all this has repercussions in the RTE:

$$\frac{d(\mathbf{I}+\delta\mathbf{I})}{d\tau_c} = (\mathbf{K}+\delta\mathbf{K})(\mathbf{I}+\delta\mathbf{I}-\mathbf{S}-\delta\mathbf{S}) \tag{2.57}$$

If the perturbations are small, at the first order will be:

$$\frac{d(\delta\mathbf{I})}{d\tau_c} = \mathbf{K}(\delta\mathbf{I}-\delta\mathbf{S}) + \delta\mathbf{K}(\mathbf{I}-\mathbf{S}) \tag{2.58}$$

If we introduce an effective source function:

$$\tilde{\mathbf{S}} \equiv \delta\mathbf{S} - \mathbf{K}^{-1}\delta\mathbf{K}(\mathbf{I}-\mathbf{S}) \tag{2.59}$$

we can write:

$$\frac{d(\delta\mathbf{I})}{d\tau_c} = \mathbf{K}(\delta\mathbf{I}-\tilde{\mathbf{S}}) \tag{2.60}$$

This last relation is formally identical to the RTE itself, and then, by analogy, the solution will be given by:

$$\delta\mathbf{I}(0) = \int_0^\infty \mathbf{O}(0,\tau_c)\mathbf{K}(\tau_c)\tilde{\mathbf{S}}(\tau_c)\,d\tau_c \tag{2.61}$$

Let us introduce now the response function vector $\mathbf{R}_i(\tau_c)$, which tells us how the Stokes profiles are changed due to the perturbations of atmospheric parameters:

$$\mathbf{R}_i(\tau_c) \equiv \mathbf{O}(0,\tau_c)\left[\mathbf{K}(\tau_c)\frac{\partial\mathbf{S}}{\partial x_i} - \frac{\partial\mathbf{K}}{\partial x_i}(\mathbf{I}-\mathbf{S})\right] \tag{2.62}$$

In terms of the response functions (RFs), the solution of the RTE can be written as follows:

$$\delta\mathbf{I}(0) = \sum_{i=1}^{m}\int_0^\infty \mathbf{R}_i(\tau_c)\;\delta x_i(\tau_c)\,d\tau_c \tag{2.63}$$

So, the final modification of the observed Stokes profiles at a given wavelength is given by a sum of terms, each relating to a physical quantity of the medium. Each term is the integral along the whole atmosphere of the perturbation of the physical parameter multiplied by the corresponding response function (Ruiz Cobo and del Toro Iniesta, 1994).
The response functions directly provide the sensitivity of the Stokes spectrum to perturbations of the physical conditions of the medium. Especially for this reason the RFs are the key point of the whole discussion.
In theory the RFs can be evaluated numerically with a series of steps:

- synthesis of the Stokes spectrum in a model atmosphere;
- perturbe an atmospheric parameter and synthesize the "perturbed" Stokes spectrum;
- calculate the ratio between the difference of the two spectra and the perturbation;
- repeat all the steps above for each optical depth, each wavelength and each atmospheric parameter.

This work would be very long and laborious. But if we realize that we know (although approximatively) the evolution operator, the propagation matrix, the source function, and the Stokes profiles, we can understand that we have all the elements to calculate RFs except for the derivatives of **K** and **S**. In LTE, **S** is equal to the Planck function and so its derivative depends only on the temperature. The evaluation of the derivative of **K** is reduced, passing by the derivatives of the absorption and dispersion profiles, to the calculation of the derivatives of the Voigt and the Faraday-Voigt function, given by (Ruiz Cobo, 1992):

$$\frac{\partial H(a,v)}{\partial v} = 4aF(a,v) - 2vH(a,v) \tag{2.64}$$

$$\frac{\partial F(a,v)}{\partial v} = \frac{1}{\sqrt{\pi}} - aH(a,v) - 2vF(a,v) \tag{2.65}$$

$$\frac{\partial H(a,v)}{\partial a} = -2\frac{\partial F(a,v)}{\partial v} \tag{2.66}$$

$$\frac{\partial F(a,v)}{\partial a} = \frac{1}{2}\frac{\partial H(a,v)}{\partial v} \tag{2.67}$$

2.2 Analysis Methods of spectro-polarimetric data

In this section, I present two methods used for analyzing solar spectro-polarimetric data. The simple Center of Gravity Method, which works in weak field approximation, and the more complex spectro-polarimetric inversion techniques. I describe also the operation of two of the most used spectro-polarimetric inversion codes: SIR and NICOLE.

2.2.1 Center of Gravity Method

The Center of Gravity (CoG) Method (Semel, 1967; Rees and Semel, 1979; Landi Degl'Innocenti and Landolfi, 2004b) is one of the easiest spectro-polarimetric analysis method used to solve the RTE in the weak field approximation and to obtain the value of the LoS magnetic field and LoS velocity of the solar plasma element which emits the radiation. Under this approximation the magnetic field intensity is assumed to be below few hundreds of Gauss (depending on the observed spectral line), constant with respect to the optical depth and proportional to the amplitude of the Stokes V lobes. The weak field approximation is valid provided that $\bar{g}\frac{\Delta\lambda_B}{\Delta\lambda_D} << 1$, where $\bar{g}$ is the effective Landé factor of the observed spectral line, $\Delta\lambda_B$ is the Zeeman splitting and $\Delta\lambda_D$ is the Doppler width of the line.
The initial step of this technique is the measurement of the right and left (positive and negative, respectively) circular polarization of the observed spectral line:

$$I_{\pm}(\lambda) = \frac{1}{2}\left[I(\lambda) \pm V(\lambda)\right] \tag{2.68}$$

The LoS (longitudinal) component of the magnetic field is obtained from the following equation:

$$B_{||} = B\cos\gamma = \frac{1.071 \times 10^9}{\bar{g}\lambda_0^2}(\lambda_+ - \lambda_-) \tag{2.69}$$

where λ_0 is the center of the observed wavelength (from laboratory measurements) in $\mathring{A}$ and λ_+ and λ_- are respectively the positions of the positive and the negative lobes of the Stokes V profile:

$$\lambda_\pm = \frac{\int [I_c - I_\pm(\lambda)]\, \lambda\, d\lambda}{\int [I_c - I_\pm(\lambda)]\, d\lambda} \tag{2.70}$$

where I_c is the intensity of the unpolarized continuum and the integral are extended over the entire line profile.
Similarly, the LoS velocity can be determined using the following equation:

$$v_{LoS} = \frac{\int I(\lambda)\lambda\, d\lambda}{\int I(\lambda) d\lambda} \tag{2.71}$$

This method, which requires short computational time, is usually used to have a rapid estimation of the longitudinal components of the magnetic field intensity and the velocity on the solar atmosphere.

2.2.2 Spectro-polarimetric inversion techniques

The previous approximations can only reproduce simple atmospheres. Nature is always more complex than this. In solar spectro-polarimetric data, asymmetric Stokes profiles are commonly observed and it is necessary to increase the complexity of the atmospheric model in order to match the observations. In fact, the physical parameters of the solar atmosphere vary with the optical depth, and therefore with the geometrical depth. The approach to analyze this kind of solar spectro-polarimetric data is using the strategy of the inversions. If we know the physical quantities of the atmosphere, applying the RTE, we can make *synthesis* of the emergent Stokes spectrum. But one of the fundamental goals of solar physics is to solve the opposite problem, called the *inversion* problem, that is to extract the physical conditions of the atmosphere from the observed Stokes spectrum.
It is important to underline that an inversion code applied to spectro-polarimetric data will return a *stratification* of the physical parameters of the atmosphere along the optical depth, and so (depending on the observed spectral line) along the atmospheric height. Inversion codes find a numerical solution of the RTE using iterative processes, until a best fit between the observed Stokes profiles $\mathbf{I}^{obs}(\lambda)$ and the synthetic ones $\mathbf{I}^{syn}(\lambda)$ is achieved by minimizing a merit function.
In the inversion codes, each solar atmosphere element is often represented with a magnetic component $\mathbf{I}_m$ and a non-magnetic component $\mathbf{I}_{nm}$ shuffled with the respective filling factor f_m and f_{nm} ($\mathbf{I} = f_m\mathbf{I}_m + f_{nm}\mathbf{I}_{nm}$,with $f_m + f_{nm} = 1$) in order to simulate the unresolved magnetic atmospheric elements.

The merit function

The values of parameters that define the model are the basic ingredients used to solve the radiative transfer equation in order to obtain $\mathbf{I}^{syn}(\lambda)$. The resulting Stokes spectrum is a function of these parameters, here denoted by $\mathbf{x}$. In the case of Milne-Eddington atmosphere the vector $\mathbf{x}$ has nine components, but in the general case it has $N \times p + r$ components, where p are the physical quantities varying with depth in a grid of N points in which the atmosphere is

discretized and r are the single-value parameters of the model. Therefore changes in the shapes of the Stokes profiles are very difficult to predict when modification in the physical parameters occur. A way to solve this problem is to invoke the perturbations theory. During the inversion, the differences between the observed Stokes profiles and the synthetic ones are used to modify $\mathbf{x}$ in order to reach the best agreement.
The inversion itself proceeds to minimize the merit function defined as follows:

$$\chi^2 \equiv \frac{1}{\nu} \sum_{k=1}^{4} \sum_{i=1}^{M} [I_k^{obs}(\lambda_i) - I_k^{syn}(\lambda_i)]^2 \frac{w_{ki}^2}{\sigma_i^2} \tag{2.72}$$

where the index $k = 1, ..., 4$ stands for the four Stokes profiles, $i = 1, ..., M$ for the wavelenght sample at which the spectrum is known, ν is the number of degrees of freedom, the factors w_{ki}^2 are the weights at the various Stokes profiles and σ_i are the uncertanties in the observations.
The minimization of the merit function is very complex because $\mathbf{I}^{syn}(\mathbf{x})$ depends non-linearly from $\mathbf{x}$. To overcome this problem we adopt the Levenberg-Marquardt algorithm (Levenberg, 1944; Marquardt, 1963), which combines the advantages of two methods: the steepest descent method and the Hessian method using the derivatives of χ^2 with respect to model parameters.
Before going into the details of the numerical procedure, we must show that the derivatives of χ^2 can be expressed in terms of the RFs.
Let us indicate with $\delta\mathbf{I}^{syn}$ the variations of Stokes spectrum induced by the changes δx_q in the model parameters x_q. At the first-order, $\delta\mathbf{I}^{syn}$ is given by:

$$\delta\mathbf{I}^{syn}(\lambda) = \sum_q \mathbf{R}_{x_q}(\lambda)\, \delta x_q\, \Delta z \tag{2.73}$$

where $\mathbf{R}_{x_q}(\lambda)$ represents the RFs of $\mathbf{I}$ to changes in x_q and Δz the spacing adopted to discretize the atmosphere.
Starting from the definition of the merit function, the variation of χ^2 after a perturbation $\delta\mathbf{I}^{syn}$ can be written as:

$$\delta\chi^2 = -\frac{2}{\nu} \sum_{k=1}^{4} \sum_{i=1}^{M} \frac{I_k^{obs}(\lambda_i) - I_k^{syn}(\mathbf{x}, \lambda_i)}{\sigma_i^2}\, w_{ki}^2\, \delta I_k^{syn}(\lambda_i) \tag{2.74}$$

Combining the precedent relations, the partial derivatives of χ^2 with respect to x_j are given by:

$$\frac{\partial\chi^2}{\partial x_j} = -\frac{2\Delta z}{\nu} \sum_{k=1}^{4} \sum_{i=1}^{M} \frac{I_k^{obs}(\lambda_i) - I_k^{syn}(\mathbf{x}, \lambda_i)}{\sigma_i^2}\, w_{ki}^2\, R_{x_j,k}(\lambda_i) \tag{2.75}$$

and, approximatively, the second-order derivative of χ^2 is given by:

$$\frac{\partial^2\chi^2}{\partial x_j \partial x_m} \simeq \frac{2\Delta z}{\nu} \sum_{k=1}^{4} \sum_{i=1}^{M} \frac{w_{ki}^2}{\sigma_i^2}\, R_{x_j,k}(\lambda_i)\, R_{x_m,k}(\lambda_i) \tag{2.76}$$

The power of this method lies in the fact that the first and the second derivative of the merit function are directly connected with the RFs.

The Levenberg-Marquardt algorithm

In this section, I show the two methods used in the Levenberg-Marquardt algorithm (Press and Flannery, 1992; Levenberg, 1944; Marquardt, 1963) and the structure of the algorithm itself.

The steepest descent method

The problem we have to solve can be summarized as follows: given a model $\mathbf{x}$, we have to find the perturbation $\delta\mathbf{x}$ such that the synthetic Stokes profiles emerging from the new model $\mathbf{x}^{'} = \mathbf{x} + \delta\mathbf{x}$ minimize the χ^2.
Assuming that the model parameter x_j is perturbed by a small quantity δx_j, at the first order, the synthetic Stokes spectrum will be given by:

$$\mathbf{I}^{syn}(\lambda, \mathbf{x} + \delta\mathbf{x}) \simeq \mathbf{I}^{syn}(\lambda, \mathbf{X}) + \mathbf{R}_{x_j}(\lambda)\, \delta x_j\, \Delta z \tag{2.77}$$

Then the value of the χ^2 will be:

$$\chi^2(\mathbf{x} + \delta\mathbf{x}) = \frac{1}{\nu} \sum_{k=1}^{4} \sum_{i=1}^{M} [I_k^{obs}(\lambda_i) - I_k^{syn}(\mathbf{x}, \lambda_i) - R_{x_j,k}(\lambda_i)\, \delta x_j\, \Delta z]^2\, \frac{w_{ki}^2}{\sigma_i^2} \tag{2.78}$$

In order that the χ^2 is minimum, the first derivative with respect to δx_j must be zero. This condition allows us to determine the value δx_j that minimize the χ^2. Deriving the previous equation and setting it equal to zero we obtain:

$$\delta x_j = -\frac{\nu}{2\Delta z} \frac{\partial \chi^2}{\partial x_j} \left[\sum_{k=1}^{4} \sum_{i=1}^{M} \frac{w_{ki}^2}{\sigma_i^2} R_{x_j,k}^2(\lambda_i) \right]^{-1} \tag{2.79}$$

Consequently the new atmosphere $\mathbf{x}^{'} = \mathbf{x} + \delta\mathbf{x}$ is expected to improve the fit, and in its turn this atmosphere can be used to obtain new perturbations.
This process must be repeated until the convergence. But close to the minimum, the gradient of χ^2 tends to zero and the perturbations are too small, and then this method loses its efficiency. Hence, a more efficient method is to be preferred when we approach the solution.

The Hessian method

When we are closer to the minimum, the χ^2 can be developed in series up to second order:

$$\chi^2(\mathbf{x} + \delta\mathbf{x}) \simeq \chi^2(\mathbf{x}) + \nabla\chi^2(\mathbf{x}) \cdot \delta\mathbf{x} + \frac{1}{2}\, \delta\mathbf{x} \cdot H^{'} \cdot \delta\mathbf{x} \tag{2.80}$$

where $H^{'}$ is the Hessian matrix containing the second derivatives with respect to the model parameters:

$$H_{jk}^{'} = \frac{\partial^2 \chi^2}{\partial x_j \partial x_k} \tag{2.81}$$

$\delta\mathbf{x}$ minimize the χ^2 when the partial derivatives of $\chi^2(\mathbf{x} + \delta\mathbf{x})$ with respect to the components of $\delta\mathbf{x}$ are zero. This leads to the condition:

$$\nabla\chi^2(\mathbf{x}) + H^{'} \cdot \delta\mathbf{x} = 0 \tag{2.82}$$

from which it follows that:

$$\delta \mathbf{x} = -H^{'-1} \nabla \chi^2(\mathbf{x}) \tag{2.83}$$

Obviously the Hessian method is valid only near the minimum, where the series expansion has meaning.

The algorithm

The Levenberg-Marquardt algorithm was developed in order to varying smoothly between the steepest descent method and the Hessian method. In fact, far from the minimum the steepest descent method is to be preferred, but it becomes inefficient as the solution is approached; in the latter case turning to the Hessian method is thus necessary.
For this purpose, the information contained in the Hessian matrix are used to replace the factors that accompany $\frac{\partial \chi^2}{\partial x_j}$ in the steepest descent method, in order to produce small perturbations:

$$\delta x_j = -\frac{1}{(\lambda + 1) H'_{jj}} (\nabla \chi^2)_j \tag{2.84}$$

where λ is an arbitrary factor used to control the jump between the two methods and H'_{jj} is the jth diagonal element of the Hessian matrix.
The elements of the Hessian matrix will be given by:

$$H_{jk} = \begin{cases} H'_{jk}(1+\lambda) & \text{if } j \neq k \\ H'_{jk} & \text{otherwise} \end{cases} \tag{2.85}$$

which yields:

$$\nabla \chi^2 + H \cdot \delta \mathbf{x} = 0 \tag{2.86}$$

So, when $\lambda \gg 1$, the Hessian matrix is forced to be diagonally dominant and the gradient method is used.
When we approach the minimum, λ becomes $\lambda \ll 1$ and we turn to the Hessian method.
Therefore according to the Levenberg-Marquardt algorithm, the minimization of the χ^2 proceeds as follows:

1. Specify the initial atmosphere $\mathbf{x}$ and set λ to a small value;

2. Resolve $\nabla \chi^2 + H \cdot \delta \mathbf{x} = 0$ for the perturbation $\delta \mathbf{x}$;

3. Check if the new atmosphere $\mathbf{x}' = \mathbf{x} + \delta \mathbf{x}$ minimize the χ^2. If this is not the case, take the initial atmosphere and increase λ by a factor of 10 and repeat step 2;

4. If the χ^2 is minimized, take the new atmosphere $\mathbf{x}'$ as the initial atmosphere and decrease λ by a factor of 10 and repeat step 2;

5. Stop the procedure when χ^2 is small enough.

2.2.3 SIR code

The SIR (Stokes Inversion based on Response function) code (Ruiz Cobo, 1992; Ruiz Cobo and del Toro Iniesta, 1992, 1994) is a package for the synthesis and the inversion of spectral lines formed in presence of a magnetic field. The code takes into account the polarization induced by the Zeeman effect and it deals with all four Stokes parameters. It was introduced by Ruiz Cobo and del Toro Iniesta in 1992 and it is developed for an automatic analysis of solar spectrum in LTE conditions.
In *synthesis* mode (see block diagram in Fig. 2.3), the program calculates the four Stokes parameters emerging from a model atmosphere. This is obtained by solving numerically the RTE for polarized light. After evaluating $\mathbf{K}$ and $\mathbf{S}$ in LTE and the atomic populations using Saha and Boltzmann equations (Landi Degl'Innocenti and Landolfi, 2004a; Landi Degl'Innocenti, 2004), the program calculates the emerging Stokes spectrum. The initial model parameters $(T, p_e, v_{mic}, \mathbf{B}, \theta, \phi, v_{LOS})$ are specified in a grid of points (called *nodes*) in logarithmic scale of the continuum optical depth at 5000 Å. In Fig. 2.5 there is an explanation of the concept of the nodes introduced by SIR. In addition, in the initial model, the user is allowed to specify the macroturbulence velocity, the contamination of stray-light, the filling factor (in the case of two components atmosphere) and the instrumental PSF (point spread function).
SIR assumes hydrostatic equilibrium. After each step of the iteration, the electronic pressure of the already perturbed model is put in hydrostatic equilibrium using the equation of state of an ideal gas.
After evaluating $\mathbf{K}$ and $\mathbf{S}$, SIR solves the RTE with a hermitian method (Bellot Rubio et al., 1998), which is based on a Taylor expansion of the Stokes vector until the fourth order in the optical depth. This method is more general than a Milne-Eddington code, because it allows to deal with arbitrary complex stratifications of each physical parameter (in Milne-Eddington case all should be constant).
Therefore, in synthesis mode the code proceeds in this order:

1. The files with atomic parameters and the abundances are read;

2. The RTE is integrated numerically for the wavelength specified in the grid file. If the atmosphere consists of two different components, the emerging Stokes spectra for each components, denoted with $\mathbf{I}_1(\lambda)$ and $\mathbf{I}_2(\lambda)$, are computed individually and next they are mixed according with the respective filling factor f_1 and f_2 (with $f_1 + f_2 = 1$): $\mathbf{I} = f_1\mathbf{I}_1 + f_2\mathbf{I}_2$;

3. If the macroturbulence velocity is specified, the effect of macroturbulence is described by a gaussian:

$$M(\lambda - \lambda_0, v_{mac}) = \frac{1}{\sqrt{2\pi}\sigma} e^{-\frac{(\lambda-\lambda_0)^2}{2\sigma^2}} \tag{2.87}$$

   and they are convolved with the Stokes vector: $\mathbf{I}^* = \mathbf{I} * M$.
   Likewise if the instrumental point spread function (PSF) is available.

4. Add the contribution of stray-light according to the α parameter:

$$\mathbf{I}_{obs} = (1 - \alpha)\mathbf{I}^* + \alpha\mathbf{I}_{str} \tag{2.88}$$

The synthesis module is also able to calculate the response functions corresponding to all the atmospheric parameters.
Considering that the models are calculated along the line of sight, if the solar region to be studied is not at the center of the solar disk, it is possible to specify the cosine of the heliocentric angle.

Figure 2.3: Block diagram of the synthesis of Stokes profiles in LTE conditions, like in the SIR code. Figure from (del Toro Iniesta and Ruiz Cobo, 2016)

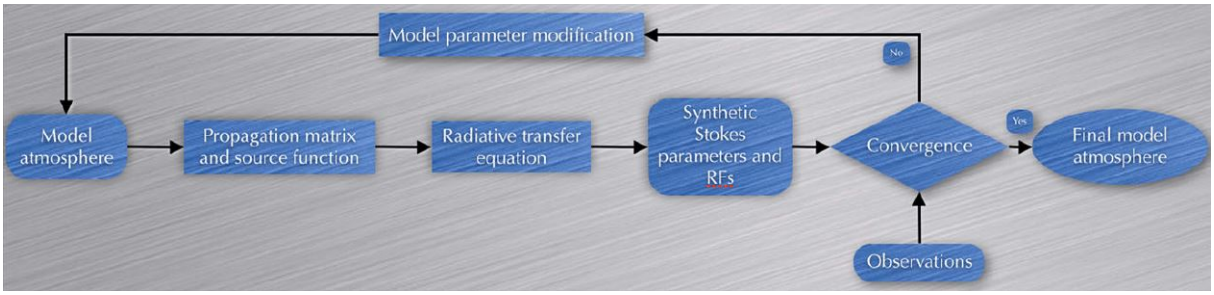

Figure 2.4: Block diagram of the inversion of Stokes profiles in LTE conditions, like in the SIR code. Figure from (del Toro Iniesta and Ruiz Cobo, 2016)

In *inversion* mode (see block diagram in Fig. 2.4), SIR fits a combination of observed Stokes parameters and modifies iteratively an initial model atmosphere until the correspondent Stokes profiles match perfectly with the observed ones. This allows us to know the magnetic, thermal and dynamical structure of the atmosphere where the Stokes profiles are formed. To do the inversion, SIR implementes a Levenberg-Marquardt algorithm in order to minimize the difference between the observed Stokes profiles and the initial synthetic ones. As we had seen, this algorithm transforms the non-linear problem in a linear one; the final solution is found with the *Singular Value Decomposition* (SVD) algorithm (Ruiz Cobo and del Toro Iniesta, 1992; Press and Flannery, 1992), in order to take into account the different sensitivity of the Stokes profiles to a specific atmospheric parameter in the various optical depth according to the sensitivity of the RFs.
The inversion of Stokes profiles is done with the minimization of the merit function between the observed Stokes profiles and the synthetic ones. In SIR it is possible to set the weights for the Stokes profiles, for example when a magnetic region is analyzed, it could be appropriate to increase the weight of the Stokes V parameter.
The minimization of the merit function is done by changing iteratively the initial model atmosphere set by the user. This process modifies the initial model with some perturbations until the observed Stokes spectrum matches with the synthetic one.
To reduce the number of free parameters, the perturbations of the physical quantities, that depend on the optical depth and that characterize the initial model atmosphere, are calculated in the grid of *nodes*. In this way, for each physical quantity, the whole stratification is written as a

function of a set of nodes. Once the number of nodes for each physical quantity is specified, the code positions the optical depths at which the perturbations will be searched. If there is only one node, the perturbations suggested by the Levenberg-Marquardt algorithm are simply add to the values of the physical quantities under exam at all heights. If two nodes are allowed, the perturbations are linearly interpolated in the whole atmosphere. With three nodes a parabolic interpolation is applied. With four or more nodes a cubic-spline interpolation is applied.

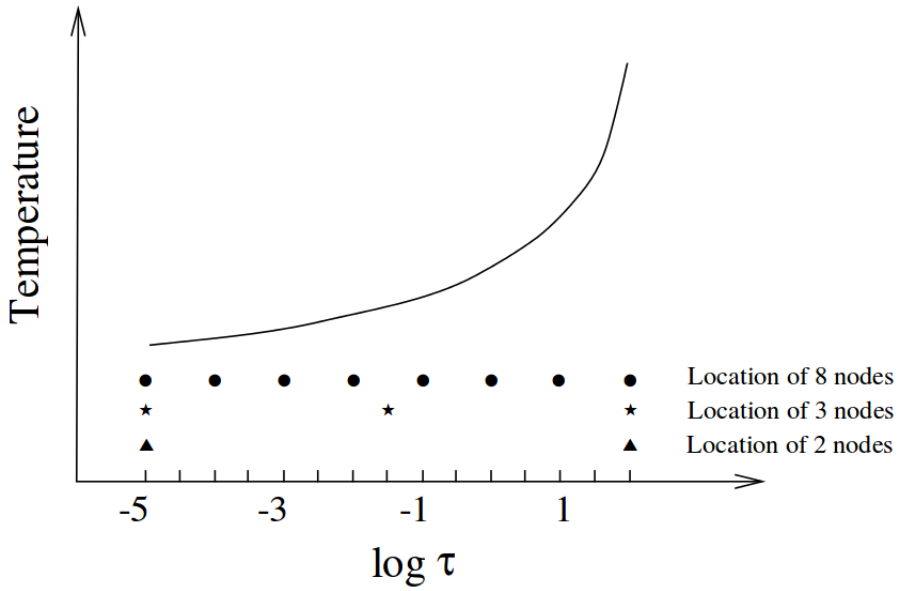

Figure 2.5: Schematic explanation of the nodes in the particular case of the temperature profile along the optical depth.

SIR allows the user to specify the number of the nodes for each physical quantity. The set of iterations that is done without modifying the number of the nodes is called *cycle*. Usually for the inversion, SIR needs two or three cycles to reach the final solution. During each cycle, the number of free parameters is normally increased in order to have more flexibility to reach the solution.
Regarding the evaluation of errors, defining $\delta I_{ki} \equiv I_k^{obs}(\lambda_i) - I_k^{syn}(\lambda_i)$, it is possible to write the weighted squared difference between the synthetic spectra and the observed ones:

$$\sum_{i,k} \delta I_{ki}^2 \frac{\omega_{ki}^2}{\sigma_{ki}^2} = \nu\chi^2 \tag{2.89}$$

The perturbation to one atmospheric parameter does not affect the other ones because we are assuming that the atmosphere model are independent to each other. If m parameters are inverted, it is possible to find a set of perturbations $\delta x(\tau)$ to the model parameters that minimize the χ^2, assuming that each one being responsible of a fractional part $\frac{1}{m}$ of the observed differences δI_{ki}^2. Using the definition of the RFs, it is possible to write:

$$\frac{\delta I_{ki}}{\sqrt{m}} = R_{x,k}(\lambda_i, \tau)\delta x(\tau)\Delta\tau \tag{2.90}$$

and therefore:

$$\sigma_x^2(\tau) = [\delta x(\tau)]^2 = \frac{\nu\chi^2}{m(\Delta\tau)^2 \sum_{i,k} R_{x,k}^2(\lambda_i,\tau)\frac{w_{k,i}^2}{\sigma_i^2}} \tag{2.91}$$

It is evident that the uncertainties are proportional to the inverse of the RFs to changes in $x(\tau)$. Obviously, the physical parameters that have less influence on the emergent Stokes spectrum are computed with larger errors: this happens outside the atmospheric regions where the observed spectral lines are mainly formed, according to the sensitivity of the RFs.

2.2.4 NICOLE code

The NICOLE (Non-LTE Inversion COde using the Lorien Engine) code (Socas-Navarro et al., 1998, 2000; Socas-Navarro, 2015; Socas-Navarro et al., 2015) works in NLTE Zeeman induced polarization regime. It is able to perform synthesis and inversions of various photospheric and chromospheric spectral lines. The structure of NICOLE is similar to the one of SIR (i.e. for the plane-parallel geometry), but, with respect to SIR, NICOLE can be used in a larger range of atmospheric heights (from the photosphere to the chromosphere) and it follows this assumptions:

- The NLTE populations of the atomic levels are computed using the statistical equilibrium;
- The hydrostatic equilibrium is an option; the electron pressure at the top of the atmosphere can be used as boundary condition;
- The direction and the emitted freqency of a photon are independent of those of a previously absorbed one (Complete angle and frequency redistribution, CRD);
- The code is also able to take into account the hyperfine structure of the spectral lines.

As in SIR, also NICOLE use the Levenberg-Marquardt algorithm to minimize the χ^2 merit function. The NLTE condition implemented by NICOLE are very useful for the analysis of the chromospheric lines. The fact that the opacity and the source function are non-linearly and non-locally connected to the atmospheric parameters implies that a perturbation applied to an atmospheric parameter at a given atmospheric point s_i produces variations in the source function and in the propagation matrix even in other points s_j of the atmosphere. This leads to a slightly different definition of the RFs (Socas-Navarro et al., 2000):

$$\mathbf{R}(x_j, s_i) = \mathbf{O}(s, s_i)\left[\frac{\delta\mathbf{S}(s_i)}{\delta x(s_i)} - \frac{\delta\mathbf{K}(s_i)}{\delta x(s_i)}\mathbf{I}(s_i)\right] \tag{2.92}$$

In addition, NICOLE uses the so-called *Fixed Departure Coefficient* (FDC) approximation (Socas-Navarro et al., 1998) to evaluate the analytical expression of the RFs in the NLTE conditions. NICOLE allows to a non-equispaced location of the nodes; in this way it is possible to place the nodes more densely in the atmospheric heights where the RFs are more sensible.

In *synthesis* mode (see block diagram in Fig. 2.6), NICOLE is able to retrieve the Stokes profiles starting from one or more atmospheric model, which inclused all the atmospheric parameters at different atmospheric heights. It starts evaluating the NLTE atomic populations (neglecting the presence of a magnetic field) and imposing the statistical equilibrium; then it calculates the Zeeman splitting, it solves the equation of state of an ideal gas and finally it solves the RTE for polarized light.

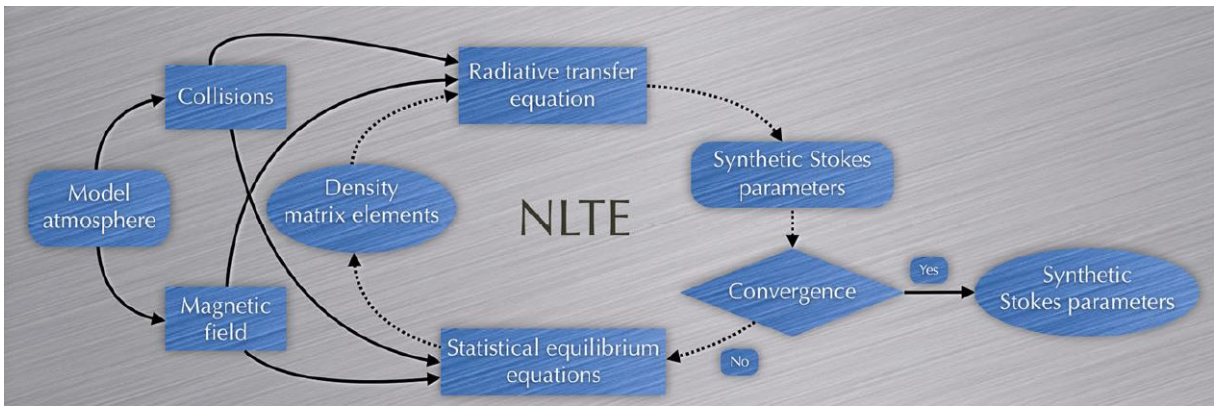

Figure 2.6: Block diagram of the synthesis of Stokes profiles in NLTE conditions, like in the NICOLE code. Figure from (del Toro Iniesta and Ruiz Cobo, 2016)

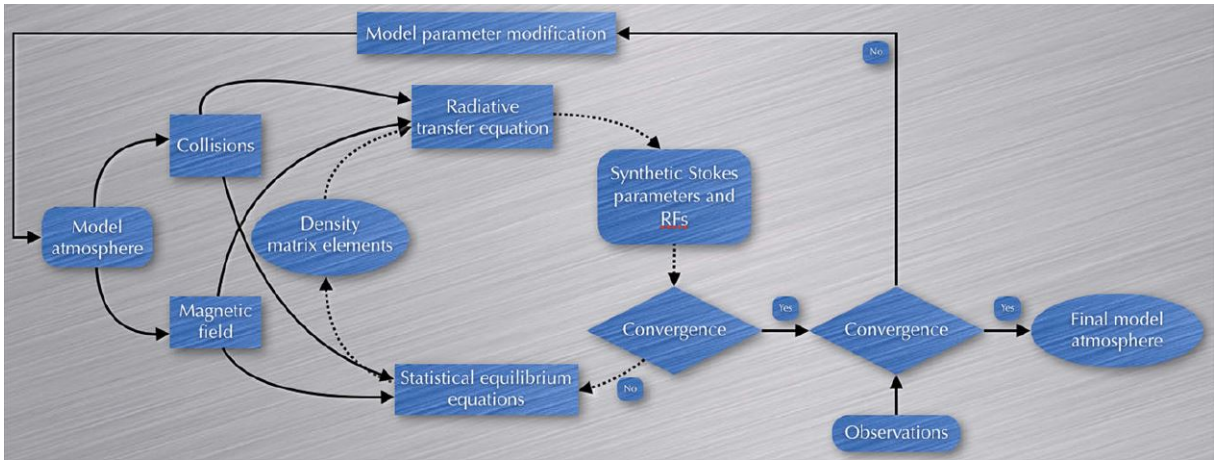

Figure 2.7: Block diagram of the inversion of Stokes profiles in NLTE conditions, like in the NICOLE code. Figure from (del Toro Iniesta and Ruiz Cobo, 2016)

If necessary, the user is allowed to choose the solving method of the RTE: Hermitian integration (Bellot Rubio et al., 1998), Quadratic and cubic DELO-Bezier (de la Cruz Rodríguez and Piskunov, 2013), the DELO-linear (Rees et al., 1989), the DELO-parabolic (Trujillo Bueno, 2003), and the Weakly Polarizing Media (WPM) (Sánchez Almeida and Trujillo Bueno, 1999). As in SIR, it is possible to take into account the stray light profile, the macroturbulence velocity and the instrumental PSF profile.

In *inversion* mode (see block diagram in Fig. 2.7), NICOLE modifies the initial atmospheric model, and so it modifies the initial synthetic Stokes profiles, until they matches with the observed Stokes profiles by minimizing the merit function χ^2_j and making use of the new definition of the RFs (Eq. 2.92):

$$\chi^2_j = \frac{1}{4N_\lambda} \sum_{k=1}^{4} \frac{\sum_{i=1}^{N_\lambda} R^2_{kj}(\lambda_i)[I^{obs}_k(\lambda_i) - I^{syn}_k(\lambda_i)]^2}{\sum_{i=1}^{N_\lambda} R^2_{kj}(\lambda_i)\sigma^2_k(\lambda_i)} \tag{2.93}$$

where N_λ is the number of spectral points. It can be noticed that this new merit function takes into account the fact that there are wavelengths in which an atmospheric parameter has a larger RF (and so more sensitivity).

The error δx_j that affects each model parameter x_j is expressed by:

$$\delta x_j^2 = \frac{4N_\lambda}{N_{par}} \chi^2 (\alpha^{-1})_{jj} \tag{2.94}$$

where N_λ is the number of spectral points, N_{par} is the number of free parameters and α the Hessian matrix.

2.3 Comparison between Center of Gravity Method and Spectro-polarimetric Inversions on a quiet-Sun convection dataset

In this section, I present a comparison analysis on a solar convection dataset of the results obtained from spectro-polarimetric analysis of IBIS/DST data using the Center of Gravity Method and spectro-polarimetric inversions performed with NICOLE code. This results has been presented at the 8th Young Researcher Meeting in Cagliari (2017, from 29th May to 1st June) and has been published in (Viavattene et al., 2018).

2.3.1 DST, IBIS and IBIS dataset

DST: Richard B. Dunn Solar Telescope

The Richard B. Dunn Solar Telescope (DST, Fig. 2.8 (Dunn, 1964a,b)) is one of the largest solar telescope in the world. It is located in Sacramento Peak (2804 m above the sea level), National Solar Observatory (NSO), New Mexico. The DST is basically a vertical-axis solar telescope with a turret heliostat on the summit of the tower (41 m above the ground) which directs the solar light inside the 1.2 m diameter vertical evacuated optical tube. The turret is made by a 0.76 m flat optical window and two 1.1 m diameter flat mirrors that reflect the light to a 1.6 m diameter spherical mirror located in the bottom of the tower (59 m underground), which, in its turn, creates a 0.51 m diameter image of the Sun in the observing room, located at the ground level, where the science instruments are installed. For a complete view of the DST, see Fig. 2.9. The DST is equipped with an Adaptive Optics (AO) System (Rimmele, 2004), which uses a Shack-Hartmann wave front sensor, a tip-tilt mirror and a deformable mirror to compensate the image motion and distortion induced by the turbulence of the Earth atmosphere.
The DST is used for high resolution imaging and spectro-polarimetry of the solar atmosphere (photosphere and chromosphere). It is equipped with the following instruments, placed after the AO:

- Facility InfraRed Spectropolarimeter (FIRS)
- Spectro-POlarimeter for INfrared and Optical Regions (SPINOR)
- Interferometric BI-dimensional Spectro-polarimeter (IBIS)
- Rapid Oscillations in the Solar Atmosphere (ROSA)

Among all, IBIS is the instrument more suitable for our analysis due to the high spatial ($\simeq$0.2"), spectral ($R > 200.000$) and temporal (few seconds) resolution reached by the instrument.

Figure 2.8: Richard B. Dunn Solar Telescope (DST), Sacramento Peak, National Solar Observatory (NSO), New Mexico.

IBIS: Interferometric BIdimensional Spectropolarimeter

IBIS (Cavallini, 2006; Cavallini et al., 2001; Reardon and Cavallini, 2008; Righini et al., 2010) is a double Fabry-Perot interferometer working in axial mode and in a classical mount, see Fig. 2.10. IBIS can operate in a large spectral region, from 580 to 860 nm, with high spectral resolution $R = 205.000 \div 320.000$, depending on the observed spectral line. The optical scheme of IBIS is reported in Fig. 2.11. The light coming from the telescope is focused by L0 in the field stop (FS), then the beam is collimated by L1, converged by L2 and then collimated again by L3. The collimated beam passes through the two FPIs, among which the filter wheel (FWH) is located: this optical configuration is used to minimize the ghost images and the spurious reflection between the two FPIs. The outgoing collimated beam is focused by L4 in the science camera (CCD1), preceded by the polarimeter. The secondary optical paths are used for the optical collimation and spectral calibration of the instrument. CCD2 acquires broad band images in the continuum near the observed spectral line. TV5 acquires images of the FS. TV4 is used to control the correct illumination of D. TV2 is used to control the correct centering of FPI1 and FPI2, by inserting BS2. The Cadmium halogen lamp (HL) is used for the spectral calibration of IBIS (by inserting M8 and BS3), having first centered its beam using TV3. The photomultiplier (PMT) is used for the spectral scan of the HL (pointing M9 to PMT), useful for the initial calibration of the initial spectral position of the FPIs. The LASER is used for the parallelism of the optical plates of the FPIs (by inserting M7 and pointing M9 to TV1 and using the lenses inside LW). Between m1 and L0 (not shown in the scheme), there is the polarimetric modulator, made of two Liquid Crystal Variable Retarders (LCVR). Between M3 and CCD1 (not shown in the scheme), there are a Polarizing Beam Splitter (PBS) and a corrective lens used to reduce the astigmatism introduced by the PBS.

The spectral scan is performed via a spacing scan of the two optical cavities of the FPIs. At each spectral position sampled by IBIS, CCD1 acquires two images (thanks to the PBS) corresponding to two different modulation states, usually [I+V and I-V, I+Q and I-Q, I+U and

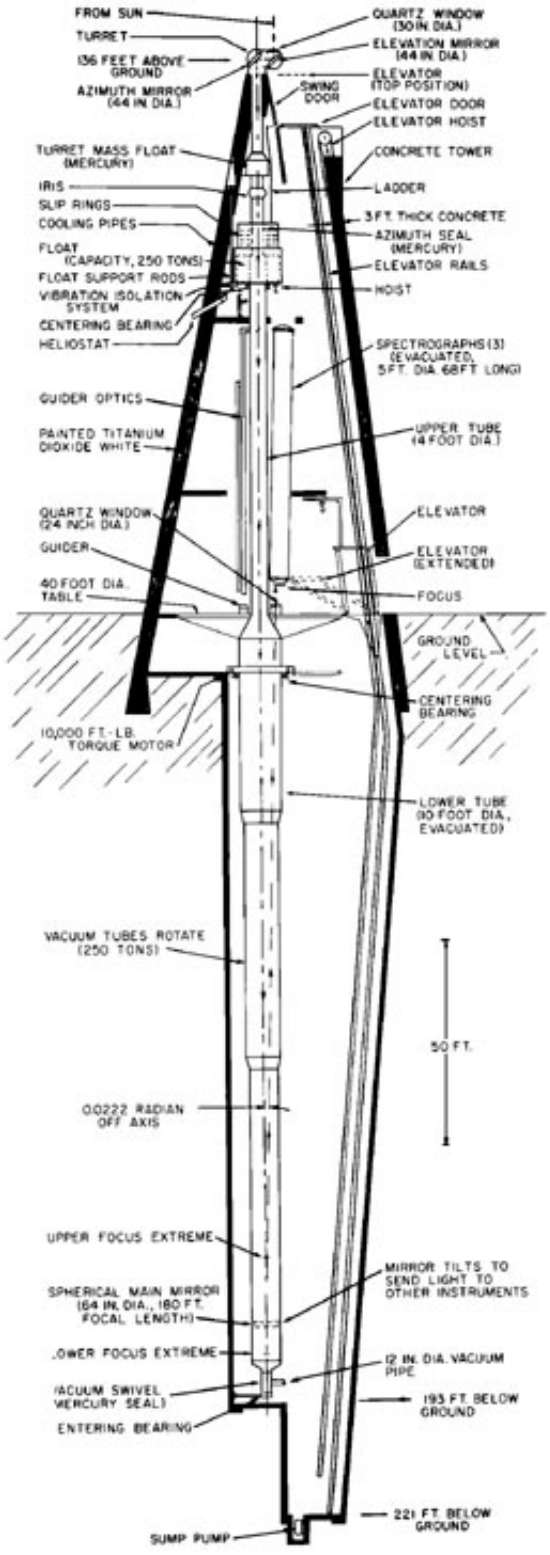

Figure 2.9: Scheme of the DST.

I-U]. The integration time per modulation state and wavelength is typically 80 ms. A complete spectral scan requires approximately 80-90 sec. The pixel scale is 0.08 arcsec and the spatial

resolution is 0.2 arcsec at 617.3 nm.

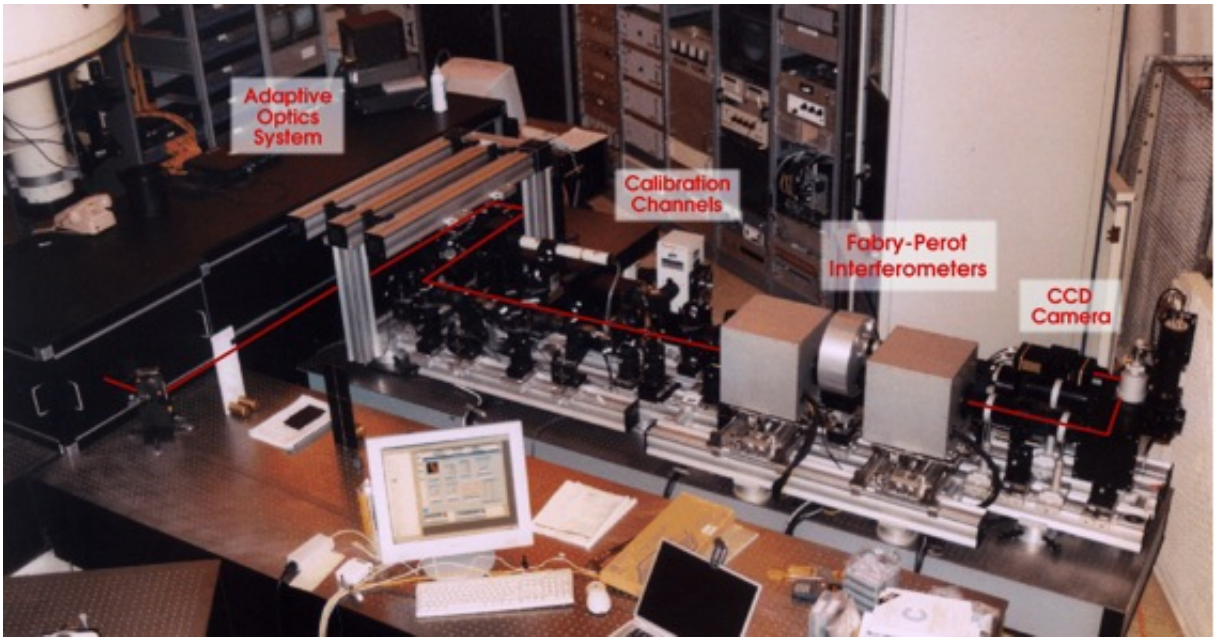

Figure 2.10: IBIS optical setup at DST. The fundamental optical component are labelled and the principal optical path is represented by a red line.

IBIS dataset

The IBIS dataset used for our analysis, and also used in this PhD thesis, was acquired on 2006 November 21st with IBIS/DST. IBIS measured the four Stokes profiles (I, Q, U, V) in the spectral region containing the two Fe I 630.15 nm and 630.25 nm lines and simulntaneous and co-spatial broadband images in the adjacent spectral region. The Field-of-View (FoV) imaged by IBIS is 40×40 arcsec^2, which correspond approximately to 30×30 Mm^2 on the solar photosphere, and it is located near to the solar disk center. The spatial resolution is 0.17 arcsec, which corresponds approximately to $\simeq$120 km on the solar photosphere. The time resolution is 89 seconds (corresponding to the time to perform a complete specral scan) and the total duration of the dataset is about one hour (41 time steps in total). This dataset is also described and used in this works (Viavattene et al., 2018; Viticchié et al., 2009; Del Moro et al., 2015, 2017). The dataset has been calibrated with the IBIS standard pipeline (Viticchié et al., 2010). In Fig. 2.12 an example of the spectral scanning performed by IBIS of Stokes I profile (left panel) and Stokes V profile (right panel) are shown. Both the Fe I 630.15 nm and 630.25 nm spectral line are clearly visible. At 630.28 nm is visible a telluric line due to absorption of water in the Earth atmosphere in Stokes I. As expected, the telluric line shows no circular polarization signal (Stokes V). In Fig. 2.13 an example of Stokes I map (left panel) and Stokes V map (right panel) are shown. The spectral position of the Stokes I map is centered in the continuum near the 630.15 nm spectral line, while the spectral position of the Stokes V map is centered in the negative lobe of the same spectral line. In the Stokes I map, the photospheric granulation is visible, which is associated to the temperature of the solar photosphere: the central part of the granules is hotter, while the intergranular lanes are cooler. In the Stokes V map, several coherent magnetic structure are visible. It can be noted that these magnetic structures do not

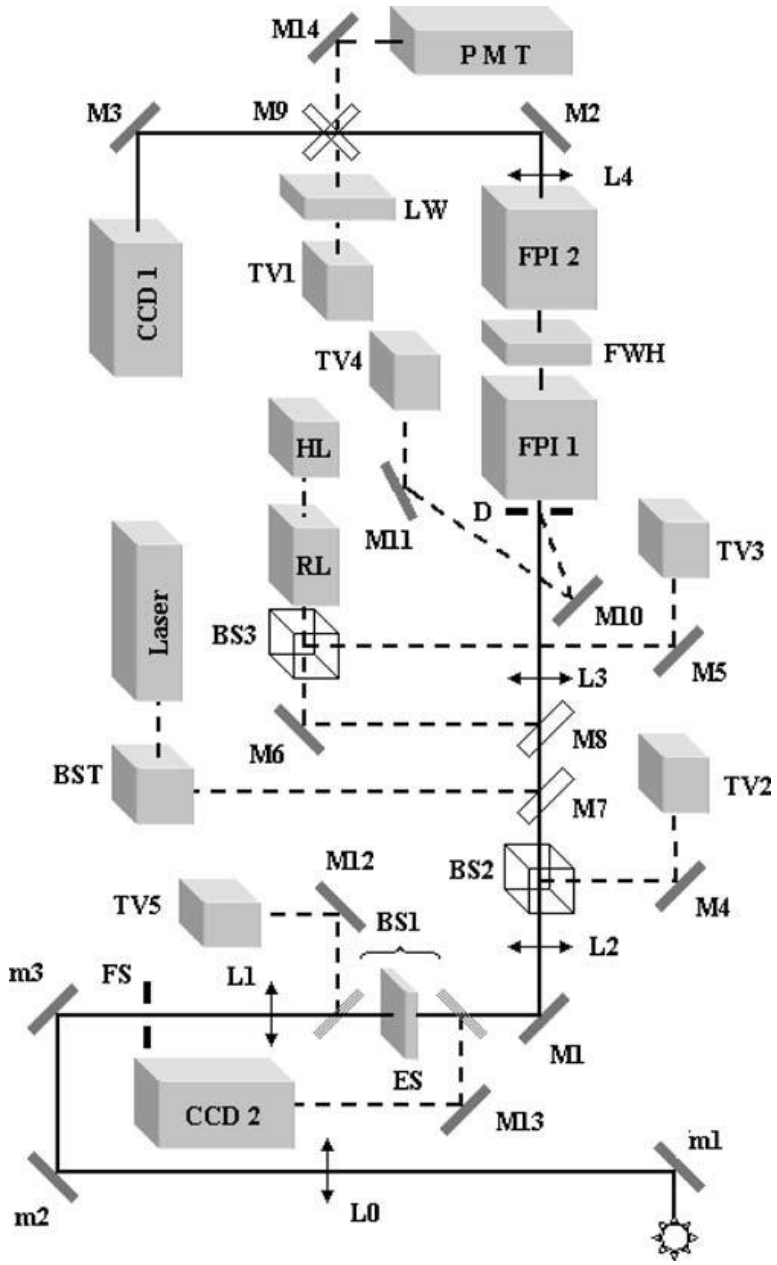

Figure 2.11: Optical scheme of IBIS. The principal optical path is represented with solid black line, while the secondary optical path are represented with dashed black line. The transparent objects represent the movable optical component, which can be inserted/extracted in/from the principal optical path. The labels are: M, m: mirror, L: lens, FS: field stop, ES: electronic shutter, BS: beam splitter, CCD: CCD camera, TV: TV camera, BST: beam steering, FPI: Fary-Perot Interferometer, FWH: filter wheel, HL: halogen lamp, LW: lens wheel, PMT: photomultiplier, RL: relay lens, W: window. Figure from (Cavallini, 2006).

exhibit an evident counterpart in the Stokes I map: therefore the magnetic field intensity is not enough to inhibit noticeably the solar granulation pattern.
In addition to spectro-polarimetric data, IBIS acquires also G-band (430.5 $\pm$ 0.5 nm) images with a pixel scale of 0.037 arcsec and an exposure time of 15 ms.

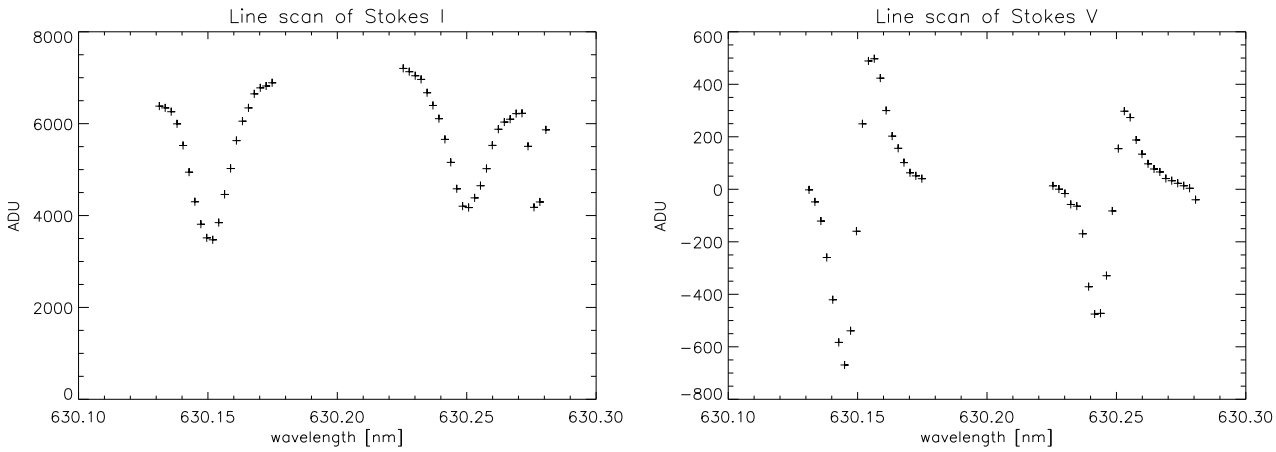

Figure 2.12: Left panel: IBIS scan of Stokes I profile of Fe I 630.15 nm and 630.25 nm spectral lines. At 630.28 nm is visible a telluric line due to absorption of water in the Earth atmosphere. Right panel: IBIS scan of Stokes V profile of Fe I 630.15 nm and 630.25 nm spectral lines. As expected, the telluric line shows no circular polarization signal. All counts are reported in Analog-Digital Units (ADU).

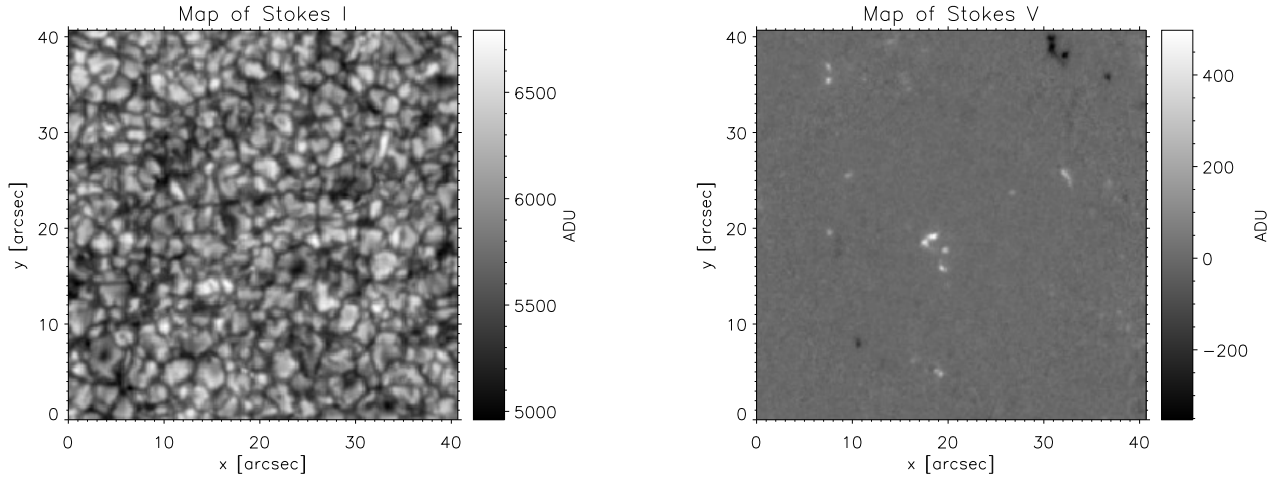

Figure 2.13: Left panel: Map of Stokes I in the continuum. Right panel: Map of Stokes V in the negative lobe of the 630.15 nm line. Counts are reported in Analog-Digital Units (ADU).

2.3.2 Comparison between CoG and Inversions

After describing the DST, the IBIS instrument and the IBIS dataset, now I present a comparison study of this dataset analyzed with both the CoG Method and spectro-polarimetric inversions. This study is focused on the characterization of the solar convection using two physical parameter of the solar photosphere recovered from the analysis.
Regarding the CoG analysis, we used Eq. 2.69 and Eq. 2.71 to compute the LoS magnetic field intensity and the LoS velocity pixel by pixel and for each temporal frame, so obtaining maps of the temporal evolution of $B_{||}$ and v_{LoS}, hereafter called B_{CoG} and v_{CoG}, respectively.
The dataset has been also analyzed with NICOLE inversion code. During the inversion, the following atmospheric parameters has been set: temperature with three nodes, LoS velocity with two nodes, magnetic field constant with height, no macro-turbulence and no micro-turbulence considered and instrumental profiles taken into account. The initializing atmosphere model was Harvard-Smithsonian Reference Atmosphere (Gingerich et al., 1971). The choice guarantees

that NICOLE inversions return an adequate atmosphere stratification without data over-fitting: in fact, the decision of these number of nodes for the various atmospheric parameter is a compromise between the quality of the data (spectral sampling, signal-to-noise ratio and number of spectral lines) and the complexity (number of degrees of freedom) of the output model atmosphere which can be retrieved by the inversions. In this analysis, the temporal frames with poor seeing are rejected.
I focus my attention in the comparison analysis of the LoS components of the magnetic field intensity and velocity of the dataset treated with CoG Method (B_{CoG} and v_{CoG}) and NICOLE inversions (B_{inv} and v_{inv}) using a code developed in Interactive Data Language (IDL). The resulting magnetic field map of one temporal frame are reported in Fig. 2.14. It is interesting to note that, although the analysis has been performed pixel by pixel, the two methods retrieve coherent magnetic structures.
I also compare the Probability Density Functions (PDFs) of the longitudinal component of the magnetic field assessed with both methods. In this analysis, pixels with magnetic field intensity lower than three times the noise value have been excluded. The two PDFs are reported in Fig. 2.15. We can notice that in the PDF of B_{CoG} (left panel) the wings break down at approximately $\pm$500 G: this behaviour is caused by the saturation effect of the CoG Method for magnetic fields greater than 400 G, because the weak field approximation is not valid anymore. The PDF of B_{inv} (right panel), instead, is very peculiar: apart from some pixels which have $B < 1000$ G (since we are observing a Quiet Sun region), its central part is not symmetric and two asymmetric bumps are clearly visible. A probable explanation of these two features is related to the fact that inversions techniques tend to overestimate weak magnetic fields (Viavattene et al., 2018; del Toro Iniesta and Ruiz Cobo, 2016): in fact, the pixel that should have lower values are shifted to higher values by the inversions, and therefore they concur to the formation of the two bumps. In Fig. 2.16 we report a scatter plot of the correlation between B_{inv} and B_{CoG}: it can be noticed that the linear fit of the scatter plot (dashed blue line) has a slope greater that the first bisector (continuous red line), and this confirm what assessed before. At the end of this analysis, we can assert that, considering the saturation effect of the CoG for $B > 400$ G, the weak magnetic fields retrieved by NICOLE inversion code are systematically larger than the ones retrieved by the CoG Method. This effect happens also for the magnetic field inclination angle, as discussed in (del Toro Iniesta and Ruiz Cobo, 2016).
Similarly, I present now the same analysis for the LoS velocity evaluated with both methods. In Fig. 2.17 I report the velocity maps at one time step evaluated with the CoG Method (left panel) and with the NICOLE inversions (right panel). In these two maps the granulation pattern is clearly visible, with upflow in the central part of the granules and downflow in the intergranular lanes. In Fig. 2.18 we show the PDFs of v_{Cog} (left panel) and v_{inv} (right panel). Both have the maximum at 0 km/s, but different shapes: the PDF of v_{CoG} is more symmetric due to the CoG and weak field approximation assumption and because the CoG Method retrieve the physical information "averaged" in the atmospheric layer where the spectral line is mainly formed (approximately at $log\tau = -1$ for the 630.15 nm spectral line) and so where the RF has its maximum; the PDF of v_{inv} is more asymmetric because, considering that NICOLE inversions retrieve a velocity profile with respect to the optical depth, in the chosen atmospheric layer ($log\tau = -1$, the same of the CoG Method for comparison) the value of the velocity is affected by the value in the neighboring atmospheric layers. In addition, in the ascending part of the PDF of v_{inv}, a spike and two bumps are present: the spike is due to the initialization value of the velocity in the NICOLE non-converged inversions, which stands for the pixel with unchanges initial value of the velocity; the two bumps are due to "errors" in the NICOLE inversions, meaning that in some pixels the inversions retrieve high value of downflow

velocity associated with high photospheric temperature profiles, they have no physical meaning and they are few statistically. This statement has been confirmed creating masks on the pixels corresponding to the velocity values of the bumps in the PDF of v_{inv} and analyzing the PDF of the photospheric temperature in the pixels selected by the masks.
We also have to say that there could be some cross-talks between the atmospheric parameters determined by the inversion techniques, in our case the magnetic field intensity and the LoS velocity. This cross-talks could be due to the fact that estimated atmospheric parameters could be not independent variables in the Hessian method of the minimization of the merit function implemented in the inversion algorithm. With the present spectro-polarimetric remote sensing techniques we cannot assert if there are a cross-talks between two or more atmospheric parameters because we do not have in-situ measurements of the physical parameters in the solar photosphere. Probably a comparison with radiative MHD simulations could be clarifying in this regard Gudiksen et al. (2011); Carlsson and Hansteen (2005).
Concluding, in one hand, the inversion techniques requires more computation time, they are able to retrieve the stratification of the atmospheric parameters along the solar atmosphere, but they tend to overestimate weak magnetic field intensity and inclination angle. On the other hand, the CoG Method requires less computation time, but it requires more assumptions and it retrieves the "averaged" values of B_{LoS} and v_{LoS} in the atmospheric layers which contribute more to the formation of the observed spectral line shape, and also an "averaged" value in the pixel (no filling factor) and therefore in the volume.
Regarding the assumptions, inversion techniques are more general and requires only LTE or NLTE approximation; on the contrary, the CoG Method is applicable when the magnetic field intensity is below few hundred of Gauss (so the Zeeman splitting is less than the Doppler width), constant with the optical depth and proportional to the amplitude of Stokes V.

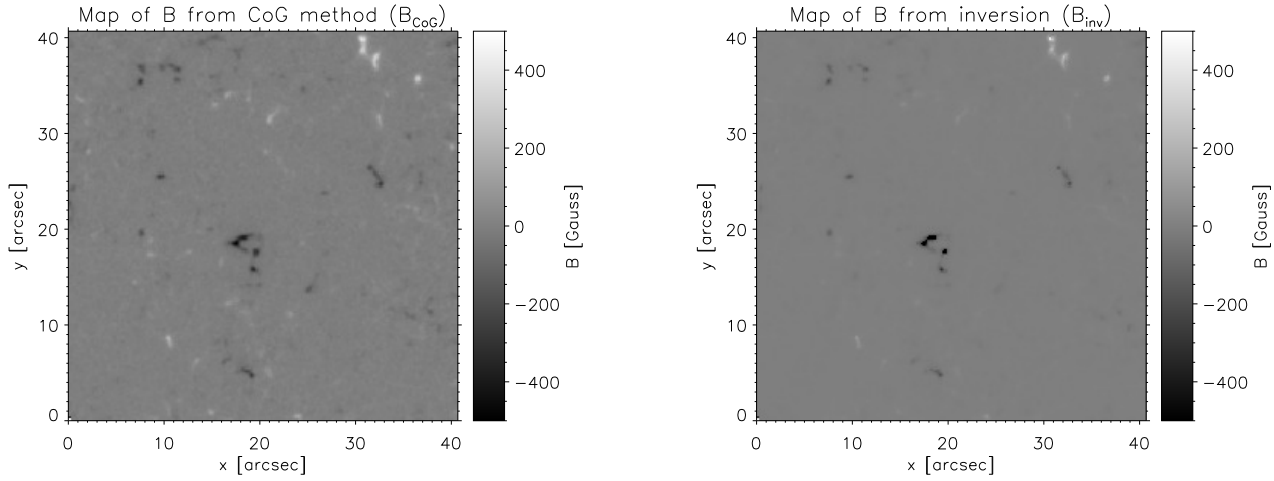

Figure 2.14: Left panel: Map of the longitudinal component of the magnetic field evaluated with the CoG Method. The map is saturated between ±500 G (black/white), according to the weak field approximation regime for the observed spectral line. Right panel: Map of the magnetic field evaluated with NICOLE inversions. The map is saturated between ±500 G (black/white) for comparison with the other map.

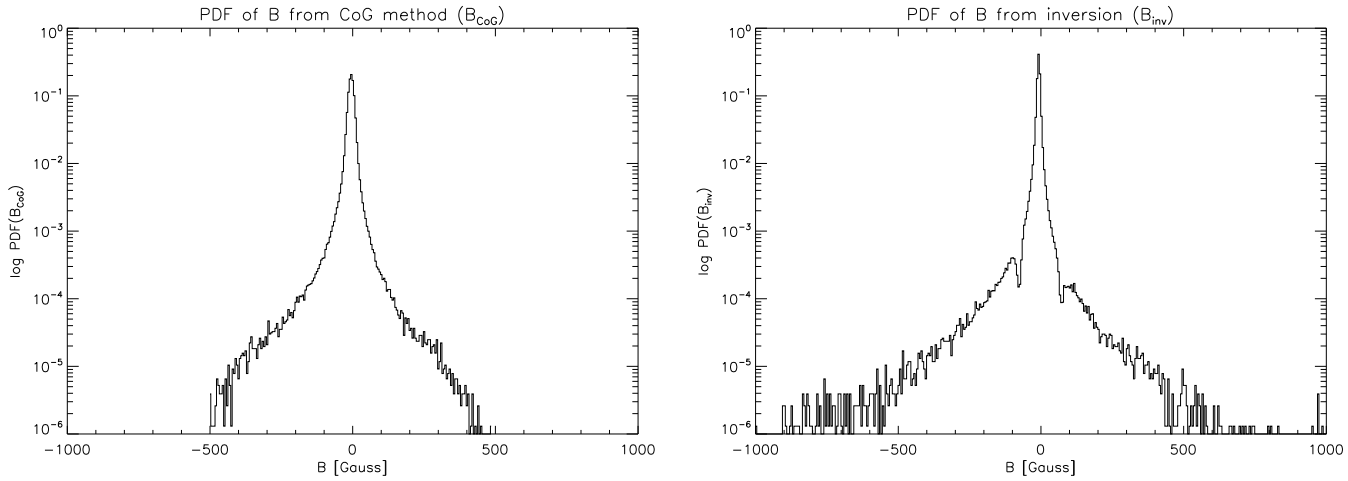

Figure 2.15: Left panel: PDF of the longitudinal component of the magnetic field evaluated with CoG Method. Right panel: PDF of the longitudinal component of the magnetic field evaluated with NICOLE inversions.

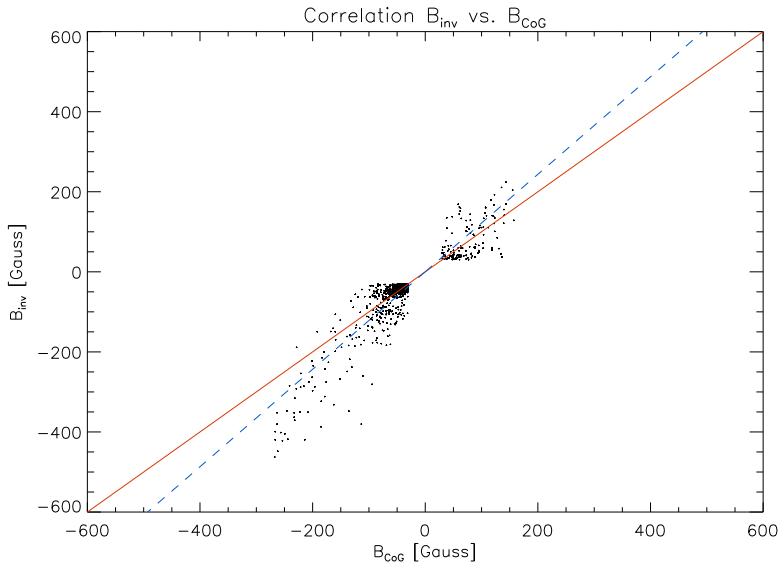

Figure 2.16: Scatter plot of the correlation between B_{inv} and B_{CoG}. Pixel below three times the noise level are masked. Dashed blue line: linear fit of the scatter plot. Continuous red line: first bisector.

2.4 The Solar Convection as a Non-Equilibrium and Steady State System

In this section, I present a validity analysis of the Gallavotti-Cohen Fluctuation Theorem on the solar photosphere, treating the turbulent solar convection as a system out of equilibrium and in a steady state. These results has been presented at the 9th Young Researcher Meeting in Salerno (2018, from 10th to 13th July) and at the 3rd SoHe (Italian Solar and Heliospheric Community) Meeting in Turin (2018, from 28th to 31th October) and published in (Viavattene et al., 2019a,b).

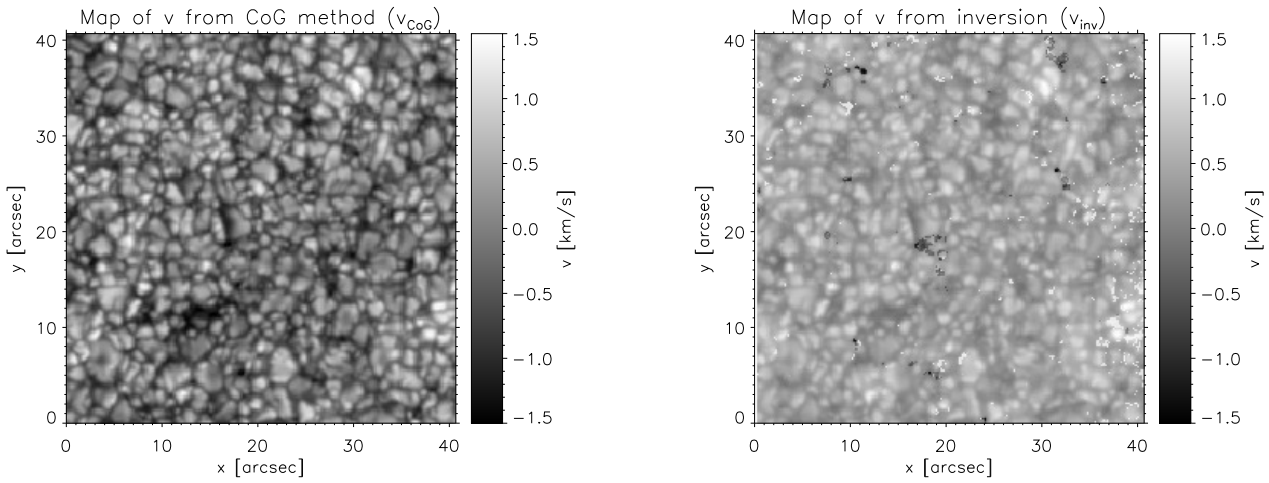

Figure 2.17: Left panel: Map of the longitudinal component of the velocity evaluated with the CoG Method. Right panel: Map of the longitudinal component velocity evaluated with NICOLE inversions.

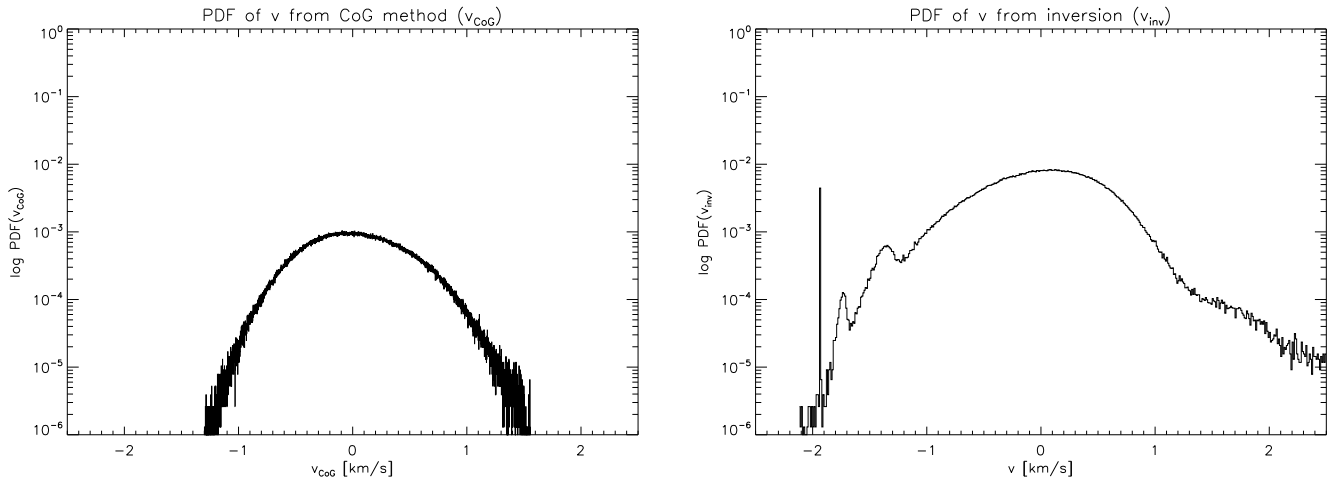

Figure 2.18: Left panel: PDF of the longitudinal component of the velocity evaluated with CoG Method. Right panel: PDF of the longitudinal component of the velocity evaluated with NICOLE inversions.

2.4.1 Non-equilibrium systems

A large variety of natural systems are in a non-equilibrium state, manifesting a very complex dynamics. In statistical thermodynamics, the properties of these systems are described in terms of the entropy production rate, which is the physical parameter that estimates the departure from equilibrium (De Groot and Mazur, 2013). The dynamics of this systems is linked with the contraction (non-conservation) of the phase-space of the system. Since there is no general theory on the connections between the fluctuating macroscopic behaviour and the microscopic parameters of far-from-equilibrium systems, the study of the statistics of these fluctuations could be of relevant importance to formulate this general theory (Hurtado et al., 2011).

Among the innumerable non-equilibrium systems, the turbulent solar convection is one of the most interesting, being the Sun a natural laboratory where the physics of turbulent convection with high Rayleigh number can be investigated. Therefore, I study the turbulent solar convection as a dissipative Non-Equilibrium Steady-State (NESS) system. Nowadays, the high

resolution spectro-polarimetric observations allow us to investigate with great detail the dynamics and the thermodynamics of the solar convection on the solar photosphere.
The measure of the entropy production rate is one of the key issues of non-equilibrium statistical thermodynamics. According to the second law of thermodynamics, the manifestation of the irreversible nature of these systems is proved by the fact that there is a non-zero spontaneous entropy production rate:

$$\sigma(\mathbf{r},t) = \sum_i J_i(\mathbf{r},t) X_i(\mathbf{r},t) > 0 \tag{2.95}$$

where $\mathbf{r}$ is the position, t is the time, $J_i(\mathbf{r},t)$ is a generic thermodynamic flux quantity, $X_i(\mathbf{r},t)$ is the associated generalized thermodynamic force or affinity and the i index takes into account the various contributions to the entropy production rate. In the case of the solar convection, we will gather our attention on the local vertical heat flux $\mathbf{J}_q(\mathbf{r},t)$, which will be evaluated from the LoS velocity and the solar photospheric temperature.

2.4.2 The Gallavotti-Cohen Fluctuation Theorem

In the last decades, several overtures have been presented to describe these large fluctuations of the entropy production rate averaged in time in non-equilibrium systems. Among those, the Gallavotti-Cohen Fluctuation Theorem (GCFT) (Gallavotti and Cohen, 1995) is one of the most important. The Gallavotti-Cohen Fluctuation Relation (GCFR) describes some symmetry features of entropy production rate and deviations in the non-linear and far from equilibrium regime: under the assumption of a time-reversal and chaotic dynamics, it states that the probability distribution of phase-space contraction over large time scale ($\tau \to \infty$) satisfies a non-trivial symmetry property (Lebowitz and Spohn, 1999), which can be expressed as follows:

$$\lim_{\tau\to\infty} \frac{1}{\tau\sigma_+} ln \frac{\pi_\tau(+p)}{\pi_\tau(-p)} = p \tag{2.96}$$

where $\pi_\tau(\pm p)$ is the probability of finding positive or negative values (fluctuations) of the dimensionless characterization of the contraction of the phase space p and σ_+ is the average phase space contraction rate over an infinite time. In a nutshell, the GCFR describes the breaking of the entropy production rate symmetry in large time interval in NESS systems. In general, the GCFR is also valid for a flux quantity J (i.e. heat, energy, momentum flux, entropy production rate, etc.) because it treats the statistics of a variable related to the phase-space contraction rate (Ciliberto et al., 2004). Thus, in this case the GCFR can be written as follows:

$$\lim_{\tau\to\infty} \frac{1}{\tau} ln \frac{\pi(+J_\tau)}{\pi(-J_\tau)} \propto \alpha_+ J_\tau \tag{2.97}$$

where α_+ is a constant with a dimension of $[\mathrm{s}^{-1}\mathrm{J}^{-1}]$ and $J_\tau(\mathbf{r}) = \frac{1}{\tau}\int_t^{t+\tau} J(\mathbf{r},t')dt'$ is the time average of J. Although the GCFR was initially inferred for global variables, it was demonstrated that it is also valid in time averaged quantity (Gallavotti, 1999; Evans and Searles, 2002).
The GCFR has been tested with both numerical simulations and experimental works. Ciliberto et al. (Ciliberto et al., 2004) tested the validity of the GCFR with a von Karman experimental setup (two counter-rotating plane-parallel disks) and in a wind tunnel experiment. Shang et al. (Shang et al., 2005) proved the validity of the GCFR in a controlled experiment with a cylindrical cell filled with water with high Rayleigh number (up to 10^9) inserted in a vertical temperature gradient. The latter case is the most interesting for our purpose because it is really

similar to the solar convection phenomenon.

2.4.3 The vertical heat flux as a proxy of the entropy production rate

We already saw that the convection process occurs in the convection zone, an internal layer of the Sun (see Introduction). In this region, the plasma flow transports a large fraction of energy, according to the Schwarzschild criterion (Landi Degl'Innocenti, 2004), with the upflow of the hotter plasma (granules) and the downflow of the cooler one (intergranular lanes), driven by the surface entropy sink. The solar convection is also characterized by the process of turbulence, especially in the downflow plasma. Therefore, the dissipative process of the turbulent solar convection, viewed as a NESS system, are an equaled laboratory to test the GCFT.
The analysis has been performed by using spectro-polarimetric Quiet Sun observations: the dataset has been chosen because in the Quiet Sun there are only small magnetic field (of the order of few tens of Gauss) which are low enough not to alter the granulation pattern of the solar granulation. In this approximation, the back-reaction of the magnetic field on the plasma motion can be negletted $\mathbf{J} \times \mathbf{B} \simeq 0$, and so we can use the standard fluid equations for the heat transport to describe the solar convection:

$$\partial_t \mathbf{v} + (\mathbf{v} \cdot \nabla)\, \mathbf{v} = -\frac{1}{\rho}\nabla p + \nu \nabla^2 \mathbf{v} - \nabla\Omega \tag{2.98}$$

$$\partial_t T + \mathbf{v} \cdot \nabla T = \kappa \nabla^2 T \tag{2.99}$$

where Ω is the gravitational potential, ν is the plasma viscosity, κ is the temperature diffusivity coefficient, $\vec{v}$ the velocity, T the temperature and p the pressure.
In this regime, the entropy production rate can be written in terms of the heat flux, $\mathbf{J}_q$, and the temperature gradient, ∇T, as follows (De Groot and Mazur, 2013),

$$\sigma = -\frac{1}{T^2}\mathbf{J}_q \cdot \nabla T \tag{2.100}$$

so that assuming the temperature gradient to be constant, $\nabla T = const$, the heat flux provides a proxy of the entropy production rate.
Here, I present a validity analysis of the GCFR on the solar turbulent convection, seen as a NESS system.

2.4.4 Data analysis: validity of the GCFR on the solar turbulent convection

Basing on the previous discussion and following Shang et al. (Shang et al., 2005), we can evaluate the local entropy production rate $\sigma(\mathbf{r}, t)$ from the local vertical heat flux $j(\mathbf{r}, t)$, assuming that the heat transport occurs mainly in the vertical (radial) direction:

$$\sigma(\mathbf{r}, t) \approx V_0 j_z(\mathbf{r}, t) \nabla_z \left(\frac{1}{T}\right) \tag{2.101}$$

where V_0 is the volume over which the local properties are evaluated and $\nabla_z \left(\frac{1}{T}\right)$ is the vertical gradient of the temperature T, which is responsible for maintaining the convection.
The local vertical heat flux can be computed as follows:

$$j_z(\mathbf{r},t) \approx v_{LoS}(\mathbf{r},t)\delta T(\mathbf{r},t) \tag{2.102}$$

where $v_{LoS}(\mathbf{r},t)$ is the plasma LoS velocity and $\delta T(\mathbf{r},t) = T(\mathbf{r},t) - T_0$, with T_0 being the average bulk temperature.
The dataset used for these analysis is the same of that used in the previous Section for the comparison analysis between inversions with NICOLE and the CoG Method. The dataset is very suitable and appropriate for this analysis because the FoV of IBIS points at the disk center and in this way the vertical (radial) direction coincides with the LoS, and, in addition, because in the FoV there are no significant magnetic structures, so that the convection pattern is not altered by the presence of magnetic field.
The local vertical heat flux can be evaluated using temperature and velocity maps, using Eq. 2.102, as discussed in (Viavattene et al., 2019a). The temperature maps have been evaluated using the black body radiation law (Rodriguez Hidalgo et al., 1992; Caccin and Penza, 2000) applied to the broadband images. In particular, we evaluated the temperature maps from the Stefan-Boltzmann law, assuming LTE conditions:

$$T(\mathbf{r},t) = T_{eff}\sqrt[4]{C(\mathbf{r},t)} \tag{2.103}$$

where $T_{eff} = 5780$ K is the average temperature of the solar photosphere (Landi Degl'Innocenti, 2004) and the contrast has been defined as:

$$C(\mathbf{r},t) = I(\mathbf{r},t)/\bar{I}(t) \tag{2.104}$$

with $\bar{I}(t)$ being the average of the intensity I for each temporal frame.
Since we are evaluating the temperature maps using the Stefan-Boltzmann law applied to broad band images, we consider that the evaluated temperature is associated to the base layer of the solar photosphere within the photon mean free path, which is approximately 100 km (Judge et al., 2015).
I evaluated the LoS velocity maps using the CoG Method (Rees and Semel, 1979; Rees et al., 1989; Semel, 1967) applied to the Fe I 630.15 nm spectral line, also discussed and compared with inversion techniques in (Viavattene et al., 2018), using Eq. 2.71. The identification of the atmospheric layer where the LoS velocity has been measured is more intricate. To estimate the height of the LoS velocity signal, I exploited the RFs (Ruiz Cobo and del Toro Iniesta, 1992, 1994; Caccin et al., 1977; Penza et al., 2004a,b; Cristaldi and Ermolli, 2017). To remind, RFs quantify which is the atmospheric layer in which the Stokes profiles are more sensible to perturbations in the atmospheric parameters; in few words, RFs tells us the heigh of the atmospheric layer where the information encoded in the spectral line in mainly formed. I evaluated the RFs for the LoS velocity for the Fe I 630.15 nm spectral line using solar standard parameters (Caccin et al., 1977). By averaging those RFs, I obtain the RF for the LoS velocity reported in Fig. 2.19. From the full-width half-maximum (FWHM) and the shape of the RF of the LoS velocity, I can assert that the atmospheric layer associated with the LoS velocity has a height of $\approx 70^{+80}_{-50}$ km above the base of the photosphere.

Thus, the temperature maps and the LoS velocity maps that we have measured are associated to the same atmospheric layer within the measured errors, so we can quietly combine them to evaluate the local vertical heat flux, which therefore can be associated with the same layer on the solar atmosphere.
The velocity maps $v_z(\mathbf{r},t)$ and the temperature maps $T(\mathbf{r},t)$ can be combined to compute the

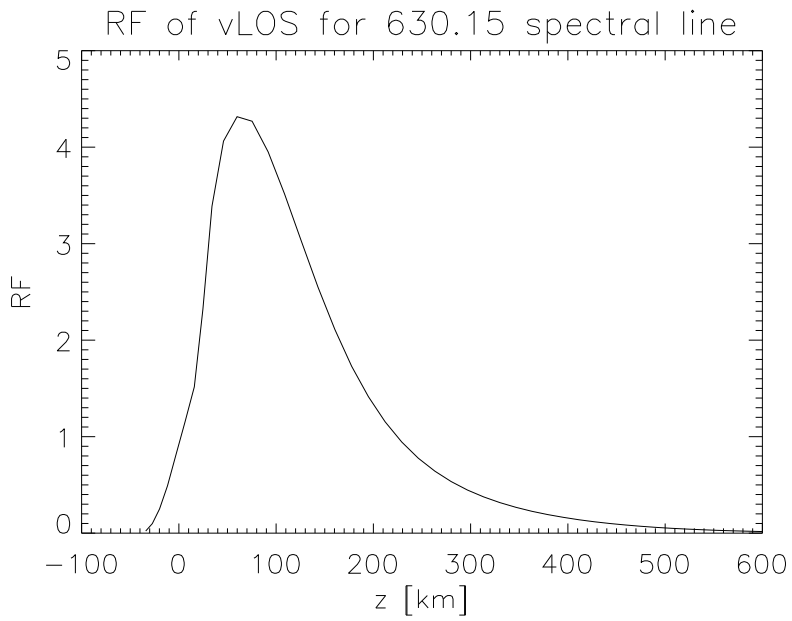

Figure 2.19: Average RF of v_{LoS} for Fe I 630.15 nm spectral line.

local vertical heat flux $j_z(\mathbf{r}, t)$ (namely the vertical heat-flux per unit surface):

$$j_z(\mathbf{r}, t) = \rho C_p v_z(\mathbf{r}, t) \delta T(\mathbf{r}, t) \tag{2.105}$$

where ρ is the solar photospheric density, C_p the heat capacity at constant pressure, $v_z(\mathbf{r}, t)$ is the plasma velocity along the vertical direction and $\delta T(\mathbf{r}, t) = T(\mathbf{r}, t) - T_0$, with T_0 the average bulk temperature. For further discussion, see (Viavattene et al., 2019a). Assuming ρC_p as a constant quantity, the heat flux in Eq. (2.107) can be written as

$$j_z(\mathbf{r}, t) = \rho C_p j'_z(\mathbf{r}, t) \tag{2.106}$$

where $j'_z(\mathbf{r}, t) = v_z(\mathbf{r}, t) \delta T(\mathbf{r}, t)$. Thus, the study of heat flux fluctuations can be limited to study the fluctuations of $j'_z(\mathbf{r}, t)$ (unit measure km $\cdot$ K /s). Since the FoV of IBIS was at the disk center, we can assume $v_z \simeq v_{LoS}$.
As usually done in solar convection studies, the temperature and the LoS velocity maps have been filtered using a subsonic $k_h - \omega$ filter, in order to remove the signal of the acoustic oscillations that are present in the solar photosphere (Title et al., 1989). Using Eq. 2.69, we compute the magnetic field intensity with the CoG Method from the polarimetric signal of Stokes V and we exclude from our analysis the pixel with a magnetic field greater than 50 Gauss (black pixels in Fig. 2.20 and Fig. 2.21 left panel), in order to analyze only Quiet Sun (non-magnetic) regions.
In Fig. 2.20 I report a sample of a temperature map (left panel) and the co-temporal LoS velocity map. In Fig. 2.21 left panel, I report one of the map of the local vertical heat flux evaluated using Eq. 2.102.

Comparing the temperature map, the LoS velocity map and the local vertical heat flux map, we can notice that they resemble to the granulation and the convection pattern. In Fig. 2.21 right panel, I show the distribution of the local vertical heat flux for all the time steps of the dataset. We can notice that the distribution is clearly asymmetric and non-Gaussian, and this confirms the non-equilibrium nature of the solar convection.

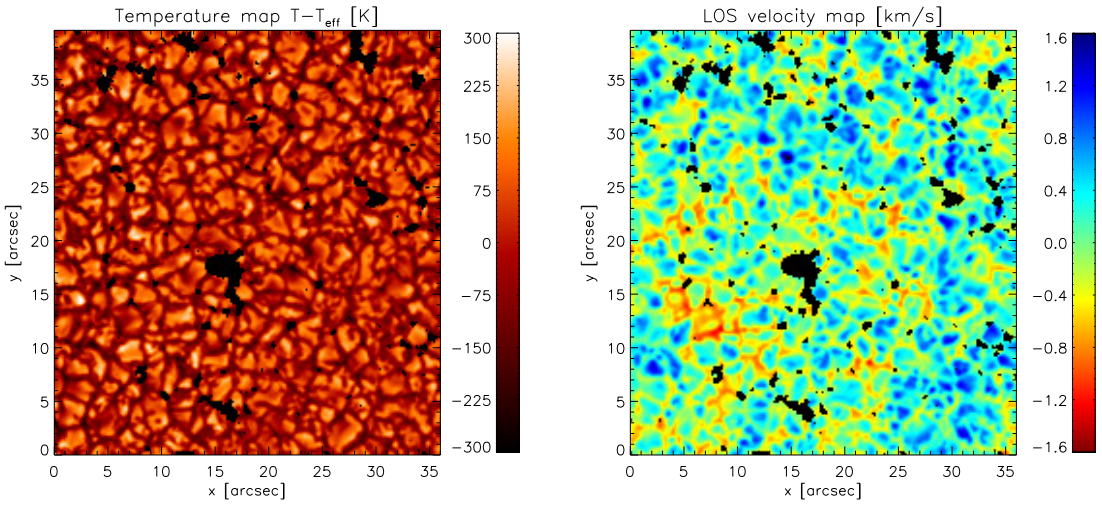

Figure 2.20: Left panel: a sample of a temperature map evaluated using the black body radiation law. The map shows the temperature fluctuations from the average temperature of the solar photosphere (T_{eff}). Right panel: the co-temporal LoS velocity map evaluated using the CoG method. Black pixels mask those regions excluded from our analysis because they have magnetic field intensity greater than 50 Gauss.

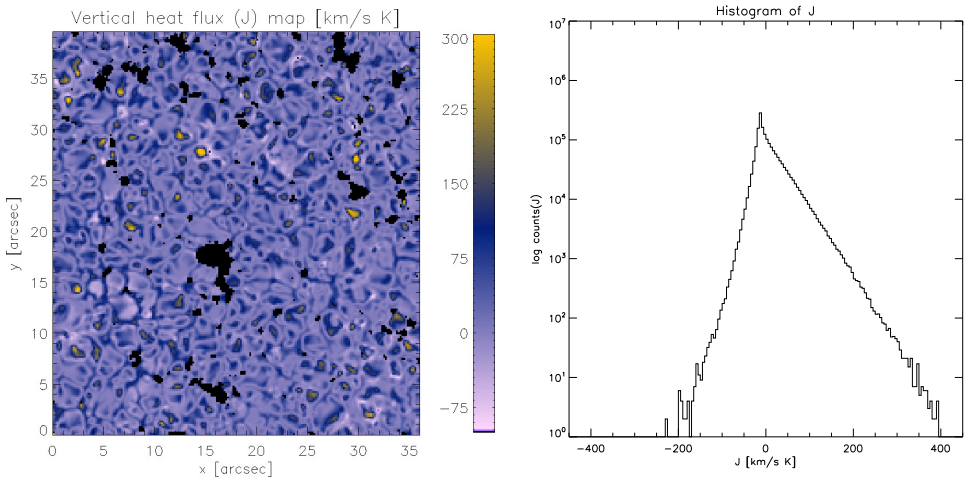

Figure 2.21: Left panel: sample vertical heat flux map. As above, black pixels mask those regions excluded from analysis. Right panel: histogram of the vertical heat flux for the whole dataset.

To improve the statistics of the dataset and to test the steady-state of the GCFR, we compute a running average of the vertical heat flux j_z over a time step interval τ:

$$J_\tau(\mathbf{r},t) = \frac{1}{\tau}\int_t^{t+\tau} j_z'(\mathbf{r},t')dt' \tag{2.107}$$

Hereafter, $J_1(\mathbf{r},t)$ is the local vertical heat flux for each temporal frame, $J_2(\mathbf{r},t)$ is the average of the local vertical heat flux between two consequent temporal frames, $J_3(\mathbf{r},t)$ between three consequent temporal frames, and so forth. The Probability Density Functions (PDFs) for the different values of $J_\tau(\mathbf{r},t)$ has been evaluated using the Kernel Method (Kaiser and Schreiber, 2002) in order to have the values of the various $J_\tau(\mathbf{r},t)$ normalized to unit variance. In Fig.

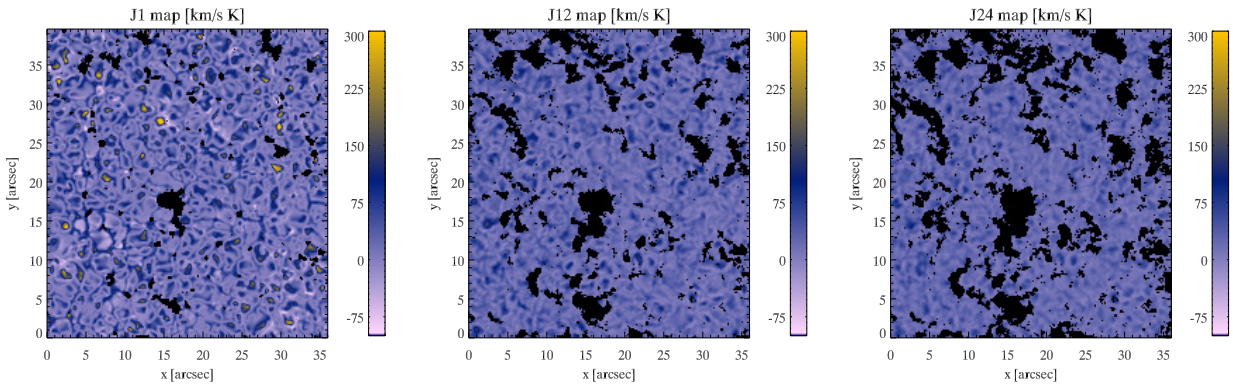

Figure 2.22: Left panel: $J_1(\mathbf{r},t)$ map. Central panel: $J_{12}(\mathbf{r},t)$ map. Right panel: $J_{24}(\mathbf{r},t)$ map.

2.22, I report a mosaic of the maps of $J_1(\mathbf{r},t)$, $J_{12}(\mathbf{r},t)$ and $J_{24}(\mathbf{r},t)$, to show the evolution of $J_\tau(\mathbf{r},t)$ when τ increases. We can see that the convection pattern smears when τ increases. In addition, there are more black (excluded) pixels when we increase the time average due to the evolution and the motion of the magnetic features. The PDFs of $J_2(\mathbf{r},t)$, $J_4(\mathbf{r},t)$, $J_8(\mathbf{r},t)$ and $J_{16}(\mathbf{r},t)$, are reported in Fig. 2.23. We can notice that the PDFs shrink when τ increases, and the most probable value tends to a non-zero value for high values of τ (Viavattene et al., 2019b). The PDFs of J_τ at each τ show a non-Gaussian and asymmetric shape. The observed distribution of the vertical heat flux proxy resembles the non-Gaussian distributions observed in various non-equilibrium phenomena (De Groot and Mazur, 2013; Ciliberto et al., 2004), such as turbulent media.
In Fig. 2.24 I report the logarithmic ratio of PDF($\pm J_\tau$) from Eq. 2.97 for the same values of J_τ for which the PDFs have been plotted. I overplot the linear fits with dashed lines performed in the linear parts of the plots. The showed error bars have been evaluated using the theory of error propagation assuming that the error associated with each bin of the PDFs is of the order of $\sqrt{N_{bin}}$, where N_{bin} is the number of counts in the bin. We can mark that the slopes of the linear fits increase when τ increases.
From Eq. 2.97, the quantity $\alpha(\tau)$ acquires a linear dependence on τ,

$$\ln \frac{\pi(+J_\tau)}{\pi(-J_\tau)} \sim \alpha_+ \tau J_\tau \tag{2.108}$$

which is expected to be valid in an asymptotic regime ($\tau \to \infty$), and, thus, $\alpha(\tau) \sim \alpha_+ \tau$.

In Fig. 2.25 we show the plot of the α parameter evaluated using Eq. 2.108. Following Eq. 2.108 and according to Shang et al. (Shang et al., 2005), the α parameter can be written in this way (asymptotic limit):

$$\alpha(\tau) = \alpha_+ \tau + \beta \tag{2.109}$$

I performed a linear fit of α for large values of τ ($\gtrsim$ 900 s) and we obtained: $\alpha_+ = (560 \pm 10) \cdot 10^{-6}$ km^{-1} K^{-1} and $\beta = (-15 \pm 1) \cdot 10^{-2}$ km^{-1} K^{-1} s. It can be clearly seen that there is a good linear behaviour for $\tau_0 \sim 600 \div 800$ s, which is the typical lifetime of the convection cells (Berrilli et al., 2002). In addition, using the asymptotic value $J_\infty \sim 20$ km $\cdot$ K/s, and introducing $\alpha'_+ = J_\infty \alpha_+$, we can evaluate the typical dissipation time scale $\tau_{diss} \sim 1/(\alpha'_+)^{-1} \sim 100 \div 120$ s, which is in the same range of the typical velocity decorrelation

time on the solar surface (Berrilli et al., 2002). These two evidences reinforce considerably our validity test.
A final raw analysis can be done to try a first experimental extrapolation of the Ra number of the solar photospheric plasma. Starting from the values of Ra and α_+ of Shang et al. (Shang et al., 2005), and assuming a similarity between the convective water of their experiment and the convective solar photospheric plasma, one can attempt an extrapolation of the Ra number for the solar photospheric plasma, which return to be of the order of 10^{18}. This value is approximately in the large range of values suggested by radiative MHD simulations ($10^{14} < Ra < 10^{28}$). This is a very rude extrapolation because in (Shang et al., 2005) there are no values of Ra from 10^9 to 10^{17}, so that this extrapolation is so daring. If there were more experimental values, the extrapolation would have been more accurate.

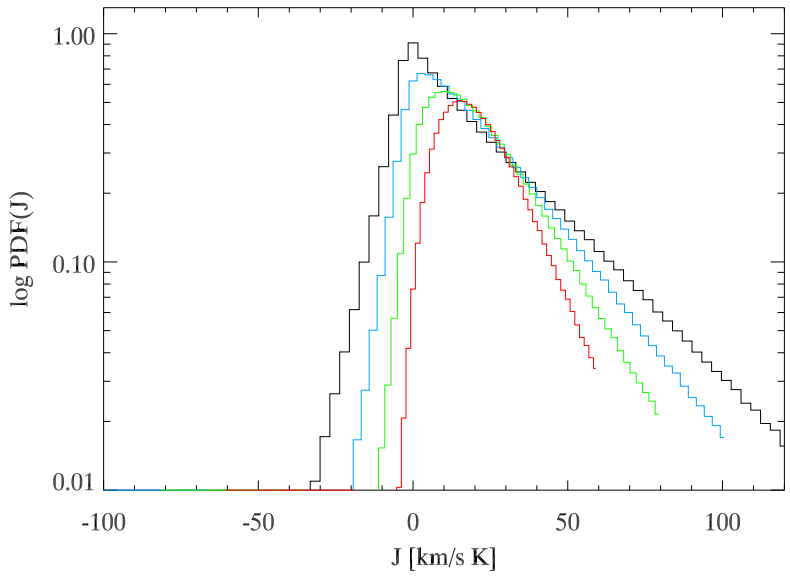

Figure 2.23: PDFs of the various $J_\tau(\mathbf{r}, t)$ evaluated with the Kernel Method: black is for $J_2(\mathbf{r}, t)$, light blue for $J_4(\mathbf{r}, t)$, green for $J_8(\mathbf{r}, t)$ and red for $J_{16}(\mathbf{r}, t)$.

2.4.5 Conclusions and future developments

In this last section, I reported my study on the statistics properties of the local vertical heat flux, which is a proxy of the local entropy production rate, evaluated on the solar photosphere, where the turbulent solar convection is present. I obtained strong evidences that the solar turbulent convection, in non-magnetic regions, satisfies the symmetry properties of the GCFR for NESS systems, similarly to the systems studied by (Ciliberto et al., 2004) and by (Shang et al., 2005), with the difference that the solar convection is a natural system and not a laboratory experiment. Therefore, my work could be considered as the first verification of the GCFR on an real natural astrophysical system, such as the solar convection, which can be study with high resolution spectro-polarimetric observations.
Future developments of this work could be some validity test of the GCFT also in solar magnetic regions, for example in the sunspot. In this case, the LoS velocity v_{LoS} and the magnetic field intensity B may be evaluated using inversion techniques if the CoG method saturates. I could expect two possible situations:

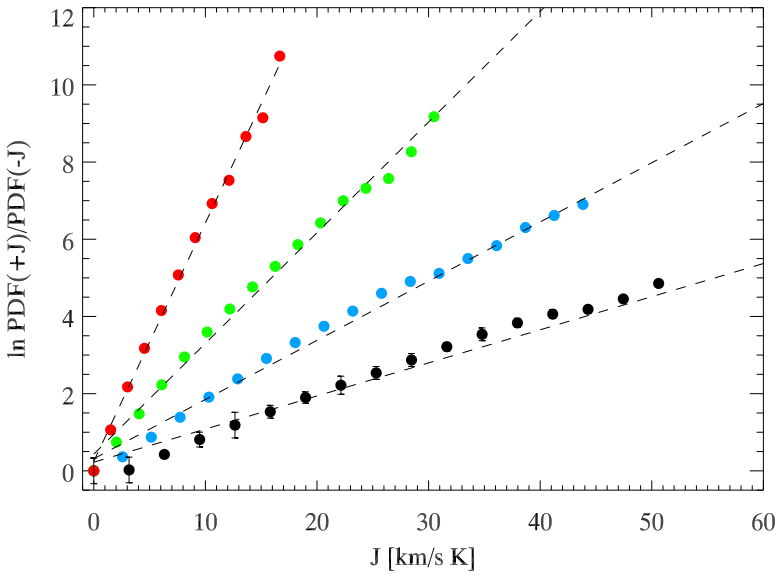

Figure 2.24: Logarithmic ratios averaged with τ evaluated using Eq. 2.97. Same colours of Fig. 2.23. The dashed lines are the linear fits performed in the linear parts of the plots. The showed errors have been evaluated using the theory error propagation as described in the text.

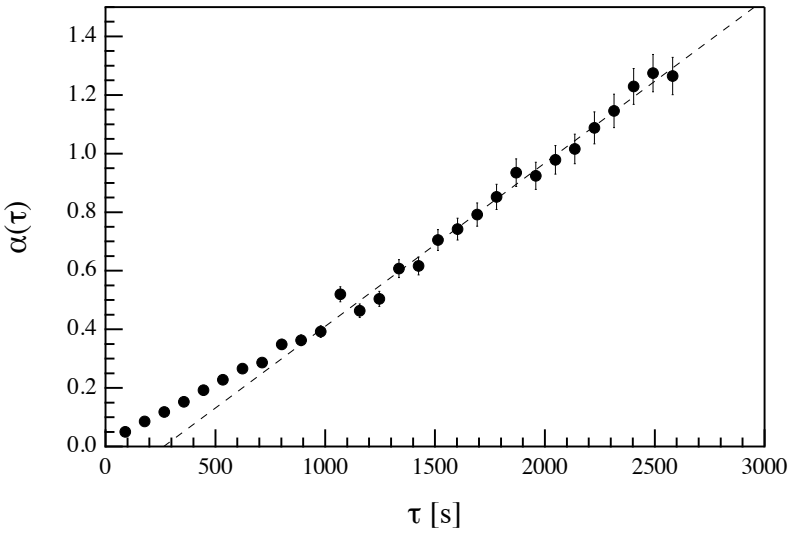

Figure 2.25: α parameter from Eq. 2.109 with respect to τ. The dashed line is the linear best fit for $\tau \gtrsim 900$ s.

1. The GCFR may not be valid because high magnetic fields strongly inhibit the solar convection in solar magnetic regions;

2. The GCFR may be valid but in another regime, with a different value of the α parameter (turbulent magneto-convection).

I am thinking on using both the possible situations to discern where is the transition between the Quiet non-magnetic Sun and the magnetic Sun where magnetic fields start to inhibit

the convection.
Another future development of this work could be to investigate the validity of the GCFR also in longer dataset ($\geq$ 15-20 hours), i.e. Hinode datasets (Giannattasio et al., 2013, 2014a,b, 2018), in order to inquire the validity in more longer temporal averages with respect to the typical granulation times, exploring also the mesogranulation and the supergranulation convection times.

Chapter 3

Solar Physics instrumentation development

3.1 Instrumentation for Solar Physics

3.1.1 General Overview

Modern Solar Physics requires top level technologies for its telescopes and their suite of instruments to acquire spectro-polarimetric data with high spatial, temporal and spectral resolution in order to study the magnetic, dynamic and thermodynamic properties of the solar atmosphere.
An obvious feature is that solar telescopes are operational during the day, and this raises the problem that the solar radiation concurs to warm the surrounding soil and create seeing (air turbulence) problems. This problem is addressed in several ways. The most common is to place the solar telescope on top of a tower (25-30 m) so as to be above the turbulent layer of air generated by the heating of the ground, in addition to covering the ground with white gravel to decrease turbulence around the telescope (see THEMIS solar telescope (Mein and Rayrole, 1985; Arnaud et al., 1996, 1998; Gelly et al., 2016)). One of the most classic solutions for solar telescopes is to use a system of two moving mirrors, called coelostates, which reflects the sunlight downwards inside the tower, where often the optical path is completely evacuated to limit the effects of seeing inside the optical tube caused by the concentration of sunlight (see Vacuum Tower Telescope (VTT (Artus, 1976; Schmidt and Soltau, 1987; Soltau, 1985, 1987)); Sweedish Solar Telescope (SST (Scharmer et al., 1999, 2003)); or Dunn Solar Telescope (DST (Dunn, 1964a,b))). Other solutions are to build the telescope on a platform located in the middle of a lake (see Big Bear Solar Observatory (BBSO (Goode et al., 2003; Denker et al., 2004, 2005, 2006; Cao et al., 2010))), or to build the telescope (usually with a Gregorian optical scheme and with a heat rejecter in the primary focus) with a fully open truss tube, exploiting the natural wind to flush the hot air from the optical path (see GREGOR solar telescope (Schmidt et al., 2012a,b; Soltau et al., 2012) or the upcoming European Solar Telescope (EST (Collados, 2008; Collados et al., 2010a,b, 2013; Zuccarello and EST Team, 2012))).
The first limiting parameter for the spatial resolution is the aperture D of the telescope, which sets the angular resolution (Rayleigh criterion) at $\alpha_{min} = 1.22\frac{\lambda}{D}$, where λ is the observed wavelength. Obviously the optical quality of the instruments must not limit the resolution provided by the aperture diameter. An Adaptive Optics (AO) system, which minimize the daytime seeing (blurring, image motion and image distortion), is mandatory to improve the effective angular resolution to be close to the diffraction limit resolution of the telescope. Alternatively,

a Multi Conjugate Adaptive Optics (MCAO) can be better since it provides a larger corrected field-of-view. Sensors must have the correct pixel scale to sample the images on the focal plane: two pixels must correspond to one spatially resolved element according to the Nyquist theorem. New generation 4-meters class solar telescope, such as the Daniel K. Inouye Solar Telescope (DKIST, (Keil et al., 2009; Woeger, 2016; Rast, 2015; Tritschler et al., 2015)) and the European Solar Telescope (EST, (Collados, 2008; Collados et al., 2010a,b, 2013; Zuccarello and EST Team, 2012)) promise an angular resolution of 0.04 arcsec, which corresponds approximately to 20 km on the solar surface.
To study the physics of the solar surface and atmosphere, a solar telescope is usually equipped with several spectrometer based on different technologies, which are instruments able to select a certain wavelength and to record its intensity. To express the ability of an instrument to distinguish a spectral feature, we introduce the resolving power:

$$\mathcal{RP} = \frac{\lambda}{\Delta\lambda} \tag{3.1}$$

where λ is the observed wavelength and $\Delta\lambda$ is the smallest spectral interval that can be resolved. Nowadays, we have 2D sensors and we want to recover 3D information. There are two different approach to do this: to select a slice of the image and to disperse different components of the spectrum locating them in different parts of the sensor and then moving the slice across the image (slit-spectroscopy), or to filter the incoming light of the whole image so to let pass only a small part of the spectrum and then changing the spectral position of the filter (spectro-imaging). Both these techniques require an instrumental time that must be less that the evolution time of the phenomenon that we want to observe. This is a real instrumental challenge if we are interested in studying solar atmosphere dynamics, because the Sun is an extended source. Recently, there are proposals to use Integral Field Units (IFUs) also on solar telescopes, allowing to obtain spectra of various portion of the image in different position of the sensor, avoiding the instrumental time of the spatial or spectral scan (Calcines et al., 2013). Curiously, in solar spectro-polarimetry there are not enough photons: for example, if we use a 60 cm telescope, an high resolution spectrograph with 1pm of bandwidth at $\lambda = 500$ nm, a field-of-view of 0.3"$\times$0.33", an exposure time of 1 ms and a total optical efficiency of the 1%, only 400 photons will reach the sensor (Stix, 2004). If we consider that we have also to select the polarization states of the photons and that the umbra regions emit less photons, it is clear that we do not collect enough light from the Sun. Therefore, contrary to what one might think, solar high resolution observation are photon starved; from here arises the need to build large diameter solar telescope, i.e. DKIST and EST, with simple optical schemes with the fewest possible mirrors, and equipped with instruments characterized by high efficiency and high transparency.

3.1.2 High resolution solar telescope vs. full disk solar telescope

The Sun is the best known star due to its proximity to the Earth compared to other stars. The proximity of the Sun therefore makes it possible to observe many physical phenomena with a great level of detail and resolution, so that Solar Physics is considered as the Rosetta Stone of Astrophysics. Seen from the Earth, the Sun is a disk of approximately 32 arcmin of diameter and it varies slightly due to the ellipticity of the Earth's orbit.
Once this consideration is made, it is clear that can not exist an "universal solar telescope" able to perform both high resolution observations and full disk observations. Therefore the solar telescopes can be divided in two large and complementary categories, depending on the scientific purpose of the observations:

- *High resolution solar telescope*: usually they are large diameter solar telescopes (> 50 cm) in order to have an high spatial resolution of about $0.05 \div 1$ arcsec (corresponding to $40 \div 700$km on the solar surface/atmosphere) and to enlarge the amount of the collected photon, needed for high spectral resolution. The spatial resolution is improved by an AO or MCAO system up to the theoretical diffraction limited resolution given by the telescope diameter. They have an evacuated or totally open optical path to reduce the internal seeing. The field of view covers a small area of the Sun, i.e. 50×50 arcsec^2 or less. They are equipped with grating spectrographs (Littrow, Czerny-Turner or other optical configurations) or with Fabry-Perot Interferometers to perform the spectral analysis of the solar radiation. They can carry out simultaneous observations in different spectral lines using various instruments at the same time;

- *Full disk solar telescope*: usually they are smaller diameter solar telescope (< 50 cm) because they do not need high spatial resolution to observe the whole disk of the Sun (typical resolution $\simeq$ 1-2 arcsec). Their field of view is large enough to include the whole solar disk and a small portion of the sky. They are equipped with low spectral resolution Fabry-Perot Interferometers (usually used in a convergent beam) or high spectral resolution Magneto-Optical Filters or narrow band Interference Filter. They perform monochromatic observations in a single spectral line.

Both of this solution have been explored in this thesis. I participated in the design, development, realization and test phases of a Fabry-Perot Interferometer prototype digitally controlled, I optimized an optical design of an instrument based on two large-diameter Fabry-Perot Interferometer proposed by Greco and Cavallini, and I realized the whole optical scheme of the new full disk solar telescope of the University of Rome Tor Vergata based on Magneto-Optical Filters, the *Tor vergata Solar Synoptic Telescope*. Considering that Fabry-Perot Interferometers are promising for up-coming large diameter solar telescope, they are treated more in detail in this manuscript.

3.1.3 Fabry-Perot Interferometers vs. Long Slit Spectrograph

We need both spatial and spectral information of the solar region of interest in order to reconstruct it in a 3D datacube, in which two dimensions correspond to the two spatial dimensions and the third dimension corresponds to the wavelengths. The main problem is that our sensors are 2D detectors, and therefore we have to reconstruct the datacube one plane after another. To do this, there are two different techniques:

- Spectro-imaging (like a Fabry-Perot Interferometer): we acquire monochromatic images using a filter and then change the spectral position of the filter during the scan;

- Long-slit grating spectroscopy: the spectrometer disperses the light of a monodimensional strip of the solar region that goes inside the slit, and then we move the slit along the solar surface.

As said before, modern Solar Physics requires fast instruments capable of freezing the physical conditions of the datacube before the system can evolve: therefore, the acquisition time is a key point. In fact, if the instrument spends more time to acquire the data than the typical evolution time of the phenomena under examination, the datacube will not be "simultaneous": in spectro-imaging, the phenomena evolve during the spectral scan, and therefore some spectral

information is lost; instead, in long-slit spectroscopy, the phenomena evolve during the spatial scanning, and thus some spatial information is lost.
In (Hernandez, 1988; Judge et al., 2010) there is a comparison between the Fabry-Perot Interferometer and the grating spectrometer transparency, having both the same resolving power $\mathcal{RP}$. For the Fabry-Perot Interferometer the transmitted flux is:

$$\Phi_{FP} = \tau I A \pi^2 [2.8 \mathcal{RP}]^{-1} \tag{3.2}$$

where τ counts the transmission losses in the instruments, I is the source intensity and A is the Fabry-Perot area. For the grating spectrometer, instead, the flux is:

$$\Phi_G = \tau I A \mathcal{RP}^{-1} \beta \, 2 sin\psi \tag{3.3}$$

where β is the angular height, ψ is the blaze angle of the grating and A is the grating area. The ration of the fluxes of the Fabry-Perot Interferometer and the grating spectrometer (with a typical $\psi = 30°$ is:

$$\frac{\Phi_{FP}}{\Phi_G} = 3.4 \, \beta^{-1} \tag{3.4}$$

Considering that for a very luminous spectrometer β is at maximum equal at 0.1 (Hernandez, 1988), we understand that the Fabry-Perot Interferometer is the most efficient between the two spectrometer, at least for a factor of 30. This large factor is the reason why the Fabry-Perot Interferometer are so attractive for Solar Physics studies and for high resolution observations. Afterwards I will describe the Fabry-Perot theory and its applications in Solar Physics, which will be matter of study of my PhD program.

3.2 Fabry-Perot Theory and Application in Solar Physics

3.2.1 FPI theory: multiple beam interference

In this section I present the theory behind the Fabry-Perot Interferometer (FPI), following (Hernandez, 1988; Born and Wolf, 1959; Fowles, 1989; Vaughan, 1989; Cavallini, 2006). An FPI is an optical cavity made by two parallel highly reflecting mirrors, as shown in Figure 3.1.

Considering firstly an *ideal* FPI, with perfectly parallel plates and without defects, it is possible to calculate the optical path difference (OPD) between two consecutive emerging beams:

$$l = \mu(AB + BC) = \mu \left(\frac{t}{cos\theta_i} + \frac{t cos\, 2\theta_i}{cos\, \theta_i} \right) = 2\mu t cos\theta_i \tag{3.5}$$

where μ is the refraction index between the two plates, t is their geometrical distance and θ_i is the internal incident angle, which is connected with the external one through the Snell's law. Other parameters are defined in Figure 3.1. The phase difference between the two beams is:

$$\psi = 2\pi \frac{l}{\lambda} = \frac{4\pi\mu t \, cos\theta_i}{\lambda} \tag{3.6}$$

Given the transmission t and the reflection r coefficients of the coating, the transmitted electric fields of ray m are:

$$E_t(1) = t^2; \; E_t(2) = t^2 r^2 e^{i\psi}; \; E_t(3) = t^2 r^4 e^{i2\psi}; \; \ldots; \; E_t(m) = t^2 r^{2(m-1)} e^{i(m-1)\psi} \tag{3.7}$$

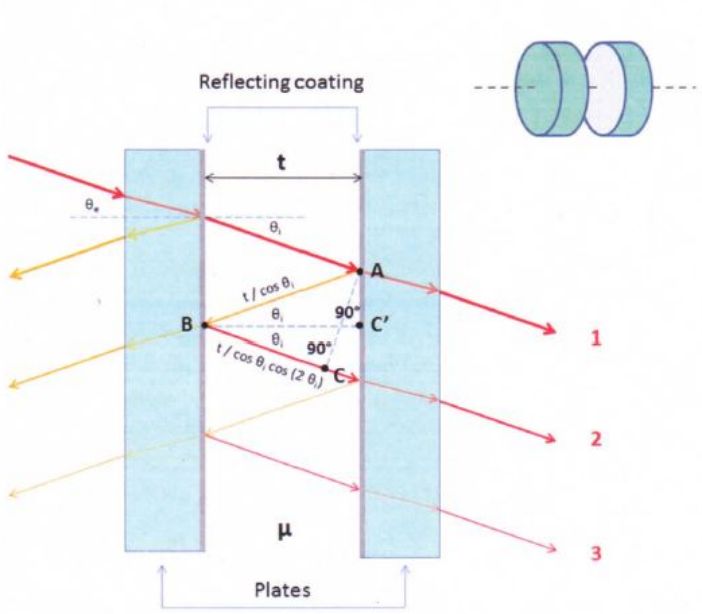

Figure 3.1: Scheme of a Fabry-Perot Interferometer and the optical path of light rays.

This is a geometrical progression with ratio $r^2e^{i\psi}$ and, for an infinite number of beams, the transmitted electric field will be:

$$E_t = \sum_{m=1}^{\infty} t^2 r^{2(m-1)} e^{i(m-1)\psi} = \frac{t^2}{1 - r^2 e^{i\psi}} = \frac{T}{1 - Re^{i\psi}} \tag{3.8}$$

having defined $t^2 = T$ and $r^2 = R$, respectively the transmission and reflection coefficients. It could be also taken into account the absorbing coefficient A with $T + R + A = 1$. The transmitted intensity is given by:

$$I_T = E_t \cdot E_t^* = \frac{T^2}{|1 - Re^{i\psi}|^2} = \frac{T^2}{(1-R)^2} \frac{1}{1 + \frac{4R}{(1-R)^2} sin^2(\frac{\psi}{2})} = \tag{3.9}$$

$$= \left(1 - \frac{A}{1-R}\right)^2 \left[1 + \frac{4R}{(1-R)^2} sin^2\left(\frac{2\pi\mu t\, cos\theta_i}{\lambda}\right)\right]^{-1} = \left(1 - \frac{A}{1-R}\right)^2 \mathcal{A}(\lambda) \tag{3.10}$$

where $\mathcal{A}(\lambda) = \left[1 + \frac{4R}{(1-R)^2} sin^2\left(\frac{2\pi\mu t\, cos\theta_i}{\lambda}\right)\right]^{-1}$ is the so-called *Airy function.*
Similarly, the reflected electric fields of the beam m are:

$$E_r(1) = \sqrt{R};\ E_r(2) = T\sqrt{R}e^{i\psi};\ \ldots;\ E_r(m) = T\sqrt{R}e^{i\psi}R^{(m-2)}e^{i(m-2)\psi} \tag{3.11}$$

Again, this is a geometrical progression with ratio $Re^{i\psi}$ and, for an infinite number of beams, the reflected electric field will be:

$$E_r = \sqrt{R} + T\sqrt{R}e^{-i\psi} \sum_{m=2}^{\infty} R^{m-2} e^{i(m-2)\psi} = \sqrt{R} + \frac{T\sqrt{R}e^{i\psi}}{1 - Re^{i\psi}} \tag{3.12}$$

The intensity of the reflected radiation is given by:

$$I_R = (1-A) - (1-A)\mathcal{A}(\lambda) + \frac{A^2 R \mathcal{A}(\lambda)}{(1-R)^2} \tag{3.13}$$

3.2.2 Resolving power, FWHM, Free Spectral Range

Now, I analyze the FPI as an interference filter. In Fig. 3.2 the spectral transparency of an FPI with respect to wavelength is shown, and it has several peaks, like a comb. Referring to Fig. 3.2, we examine the principal instrumental characteristics of a FPI:

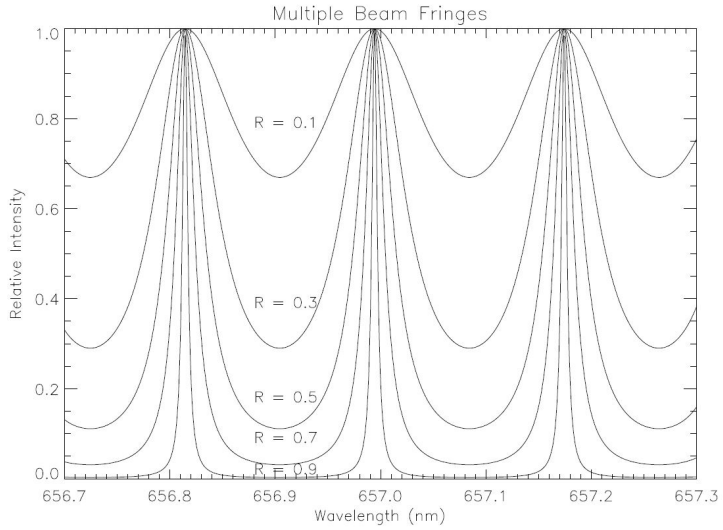

Figure 3.2: Transparency profile of a FPI at different values of R.

- **Free Spectral Range (FSR)**: is the wavelength distance $(\lambda - \lambda')$ between two consecutive maxima (found by imposing $2\mu t\, cos\theta_i = n\lambda$, with n interference order):

$$FSR = \frac{\lambda'}{n} = \frac{\lambda\lambda'}{2\mu t\, cos\theta_i} \cong \frac{\lambda^2}{2\mu t\, cos\theta_i} \tag{3.14}$$

- **Full Width at Half Maximum (FWHM)**: found by imposing $\mathcal{A}(\lambda) = \frac{1}{2}$:

$$FWHM \cong \frac{\lambda(1-R)}{n\pi\sqrt{R}} = \frac{1-R}{\pi\sqrt{R}}\, FSR = \frac{1-R}{\pi\sqrt{R}} \frac{\lambda^2}{2\mu t\, cos\theta_i} \tag{3.15}$$

- **Reflective Finesse**: which defines the quality of the ideal FPI:

$$F_R = \frac{FSR}{FWHM} \cong \frac{\pi\sqrt{R}}{1-R} \tag{3.16}$$

- **Spectral Resolving Power**:

$$SRP = \frac{\lambda}{FWHM} \cong \frac{\pi\sqrt{R}}{1-R} \frac{2\mu t\, cos\theta_i}{\lambda} = nF_R \tag{3.17}$$

- **Contrast**: defined as the ratio between the maximum T_M and the minimum T_m transparency:

$$C = \frac{T_M}{T_m} = \left(\frac{1+R}{1-R}\right)^2 \tag{3.18}$$

There are three different methods to perform the *wavelength scanning* with the FPI: the spacing scanning (the wavelength shift $\delta\lambda = \lambda\frac{\delta t}{t}$ is produced by a varyation δt of the spacing between the two plates), the refraction scanning (the wavelength shift $\delta\lambda = \lambda\frac{\delta\mu}{\mu}$ is produced by a variation of the refraction index $\delta\mu$ obtained by varying the gas pressure between the two plates), and the tilt scanning (the wavelength shift $\delta\lambda \cong \left(\frac{\mu_e}{\mu}\right)^2 \frac{\theta_e^2}{2}$ is produced varying the inclination of the two plates with respect to the incident beam).

3.2.3 The real FPI and the optical mount

The *real* FPI is affected by other issues that have to be taken into account, such as the two plates could be not perfectly parallel and flat, they could have polishing impurities or the non-perfectly collimated beam. These defects cause a broadening of the spectral profile and a performance decline of the FPI, which can be taken into account by introducing other terms and defining the effective finesse. The effect of a non planar plates can be modelled using the spherical defects finesse $F_{SD} = \frac{\lambda}{2\delta_{SD}}$, where δ_{SD} is the peak-to-valley value of the deviation from a flat surface. The polishing defects can be described using a Gaussian defect finesse $F_{GD} = \frac{\lambda}{4.7\,\delta_{GD}}$, where δ_{GD} is the root mean square (RMS) of the difference between the real and the ideal surface, assuming that polishing errors are gaussian-like. The parallelism defect can be described with $F_{PD} = \frac{\lambda}{\sqrt{3}\delta_{PD}}$, where δ_{PD} is the difference between the maximum and the minimum value of the plates distance. The divergence defects can be described with $F_{DIV} = \frac{\lambda}{t\theta_{DIV}^2}$, where θ_{DIV} is the divergence angle of the incident beam. The total effective finesse of the FPI will be:

$$F_E = \left(\frac{1}{F_R^2} + \frac{1}{F_{SD}^2} + \frac{1}{F_{GD}^2} + \frac{1}{F_{PD}^2} + \frac{1}{F_{DIV}^2}\right)^{-\frac{1}{2}} \tag{3.19}$$

The spectral response of an FPI is a spectral comb and in this shape it is not usefull for spectral imaging application. To select only a peak of the spectral response comb of an FPI, we need another filter, the so-called *prefilter*. The passband of the prefilter must be chosen very carefully to match the FPI FSR and according to the purpose of the instrument. The combination of the FPI and the prefilter will allow to select the spectral region under investigation; in this way a single peak can scan this region without having a second peak entering in the region meanwhile. Obviously, the optical quality of the prefilter must not diminish the performance of the whole instrument. If the FPI is used to analyze different regions of the spectrum, various prefilters are necessary (usually mounted in a filter wheel).
To install an FPI-based instrument on a solar telescope an optical relay system is used, which is made of various lenses. There are two main optical configurations or layouts to place a FPI in an optical instrument (Righini et al., 2010; Kentischer et al., 1998; Scharmer, 2006; Reardon and Cavallini, 2008), shown in Figure 3.3:

- Classic mount (CM): the FPI (or the FPIs in multi-etalon instruments) is placed in the image of the pupil (where the collimated beam of the rays coming from the center of the FoV intersect the collimated inclined beam of the rays coming from the edge of the FoV) and then it is equivalent to place an enlarged interferometer in front of the entrance pupil of the telescope. The rays coming from one image point in the FoV fill the whole FPI plates, so they pass through the FPI with different angles with respect to the optical axis and they will form the image in the image plane. The effective plates separation

(seeing by the light due to the various angle) generates a wavelength gradient across the FoV due to the angles of the rays. Since the rays with equal inclination in the pupil image form one image point, the parallelism errors and the plate surfaces errors will cause a broadening of the spectral profile. The spectral resolution is given not only by the reflective finesse, but also by the parallelism and the flatness of the plates, which are taken into account in the effective finesse. In this case the telescope f-number is limited by the maximum wavelength shift that can be tolerated on the focal plane, but the large scale plates distance errors limit the FPI useful area; in other words, all the pixel of the FoV will have the same bandpass but not the same exactly wavelength, in fact there is a blue-shift going from the center to the edge of the FoV, which is usually calibrated in the pipelines routines;

- Telecentric mount (TM): The FPI (or the FPIs in multi-etalon instruments) is placed in an image plane. Each point of the image inside the two plates has the same cone angle, which is given by the incoming f-number. This cone angle should be as less as possible in order to minimize the spectral broadening. Since each point of the image inside the plates of the FPI corresponds to a specific point of the solar image, there is not wavelength blue-shift in the image on the image plane. The spectral resolution is imposed by the reflectivity of the plate coating and by the incoming f-number. The FPI should be slightly shifted from the focal plane in order to avoid the re-imaging of the dust situated on the plates of the FPI. In this case the telescope f-number is imposed by the minimum allowed optical quality, but the useful area of the FPI is dictated by the maximum local detuning that can be tolerated on the focal plate; in other words, all the pixel of the FoV will have the same wavelength but not the same bandpass.

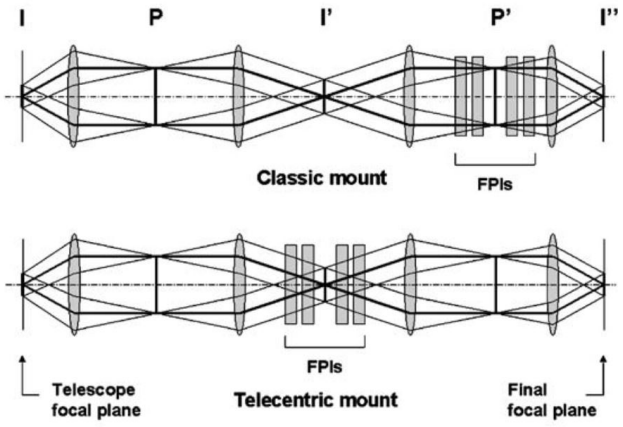

Figure 3.3: Classic and telecentric mount of a FPI. Figure from (Cavallini, 2006)

There are advantages and disadvantages in both optical configuration, which are summarized in Table 3.1 (Kentischer et al., 1998). A good comparison between the two optical mounts could be given by IBIS (Cavallini, 2006) and the Italian Panoramic Monochromator (IPM) (Cavallini, 1998): IBIS is made by two FPIs working in classical mount, whereas IPM is made by an FPI working in telecentric mount and a Universal Birifrangent Filter (UBF).

	Collimated Mount	Telecentric Mount
Broadening mechanism	reflectivity and plate shape	reflectivity and f-number
Wavelength shift across the FoV	yes	no
Wavefront distortion	large	low
Influence of dust on the image	low	large
Alignment sensitivity	large	low
Blocking ghosts reflections	difficult	easy
Influence of plate shape	broadening	wavelength shift

Table 3.1: Advantages and disadvantages of the classical and telecentric mounts for FPI-based instruments. Table from (Kentischer et al., 1998).

3.2.4 Application in Solar Physics

An approach largely used in Solar Physics is combining two or more FPIs in series in order to obtain high spectral resolution ($\mathcal{RP} \geq 100\,000$) and large FSR by selecting a single transmission peak choosing appropriately the FSRs of the FPIs. In this case a proper optical design is mandatory to minimize the spurious spectral effects due to multiple reflection and ghost images. In recent FPI, the prefilter is placed between the two FPIs to reduce the unwanted reflections and ghosts images. This approach is used in the Interferometric BI-dimensional Spectro-polarimeter (IBIS) (Cavallini et al., 2001; Cavallini, 2006; Reardon and Cavallini, 2008; Righini et al., 2010), the instrument that provides the dataset for this thesis (see after).
In Solar Physics, the Capacitance Stabilized Etalon (CSE), based on multiple beam interferometry of a FPI, has several applications and it performs a spacing spectral scanning. The two plates are kept parallel to each other and they are moved one with respect to the other using piezo-electric actuators and the relative position between the two plates is monitored by capacitance sensors. For new 4-meters class solar telescopes (i.e. DKIST, EST) the high quality control of the parallelism is crucial to guarantee the high spectral resolution, which highly depends on the OPD and the bandwidth spectral position. The maximum tolerated drift in wavelength is about 0.02 pm.
The measurement of the polarization state of the light is carried out with a polarimetric unit placed after the FPI, which contains various retarders and polarizers automatically rotated at different combinations of angles in order to select the polarization states of the incoming light I, Q, U and V.
There are several top-level scientific cases about the physical processes involved in the solar convection that can be addressed and investigated using FPI-based instruments, which have been listed in the Introduction of this thesis.
In addition to these scientific cases related to solar convection, FPIs are also used for study the fast dynamics of the chromosphere and for high resolution observations of the sunspots; these two kind of observations require high cadence instruments and high efficienty and transparency instruments (less luminosity flux in the sunspots), respectively.
All these scientific cases imply some instrumental requirements of the up-coming 4-meter class solar telescopes (i.e. EST and DKIST). We have already seen that if we want to observe in polarimetric mode, at high spatial, temporal and spectral resolution, the measurements are photon starved. Therefore the first limiting parameter of high resolution solar observations is the number of photon per pixel:

$$Z = (S/N)^2 = \Phi \Delta\lambda \Delta x^2 \Delta t \tag{3.20}$$

where S/N is the signal-to-noise ratio, Φ is the flux of photons per unit wavelength, time and resolution element (so it takes into account the transparency of the telescope optics, instrument optics, and the quantum efficiency of the camera), $\Delta\lambda$ is the spectral sampling, Δx is the spatial sampling and Δt is the temporal sampling. Considering that the spatial and the temporal samplings are connected together by the characteristic evolution speed v of the observed phenomenon ($\Delta x = v\Delta t$), we can evaluate the correct temporal sampling to monitor the evolution of the phenomenon, which must be less than the proper evolution time of the phenomenon itself:

$$\Delta t = \left(\frac{(S/N)^2}{\Phi \Delta\lambda v^2} \right)^{1/3} \tag{3.21}$$

To be able to study in great detail the scientific cases listed above, the temporal sampling should be of the order of few tenth of seconds or few minutes. If there are not enough photons, the spatial and temporal sampling must be rescaled and, if they are not proper with the observed phenomenon, it will produce a smearing of the observed solar scene.
The only way to increase the collecting number of photons is to enlarge the entrance pupil diameter, and therefore to built large diameter solar telescope. Considering that the photon flux is proportional to the collecting area of the primary mirror $\Phi = \Psi D^2$, where D is the diameter of the primary mirror, the Eq. 3.20 becomes:

$$(S/N)^2 = \Psi D^2 \Delta\lambda \Delta x^2 \Delta t \tag{3.22}$$

If we want to achieve the scientific cases for the solar convection, we must perform observation at the diffraction limit of the telescope $\Delta x_{diffr} = \lambda/D$ and with the correct temporal sampling $\Delta t_{diffr} = \Delta x_{diffr}/v = \lambda/(Dv)$, then the signal-to-noise ratio will be given by:

$$(S/N)^2_{diffr} = \Psi D^2 \Delta\lambda \Delta x^2_{diffr} \Delta t_{diffr} = \Psi \frac{\lambda^3 \Delta\lambda}{v} \frac{1}{D} \tag{3.23}$$

This latter equation demonstrates that observations at the diffraction limit of the telescope and with the correct temporal sampling are limited by the photon flux. In addition, counter-intuitively, the signal-to-noise ratio decreases with the diameter of the primary mirror. This is a further confirmation that solar telescopes and their instrumentation must be optimized to have as much photon flux as possible and that the use of FPI-based instruments is convenient with respect to long-slit spectrograph.
The spectral sampling, instead, is given by a reasonable compromise between the FPI instrumental time to perform a complete spectral scan, the number of spectral sampled points and the integration time for each spectral step to reach the desired signal-to-noise ratio. Usually few tenth of spectral point are needed by the inversion codes. Obviously a great number of spectral point increases the precision of the inversion retrievals and therefore also the precision of the atmospheric parameters. Going from high resolution spectral scan to low resolution spectral scan, the spectral step spans from 3 pm to 100 pm, and this requires an high precision control of the parallelism and the spacing scan of the plates of an FPI.
To achieve the scientific cases for the solar convection listed in the Introduction, modern solar telescopes and FPI-based instruments should reach the following instrument requirements:

1. Large diameter solar telescope (4-meter class) to reach a diffraction limited angular resolution of 0.026 arcsec, corresponding to 20 km on the solar surfaces;

2. AO or MCAO to have a seeing-corrected FoV of 40×40 arcsec^2 and efficient Heat Rejection (HR) system to avoid the internal seeing;

3. Large wavelength coverage from 390 nm to 1600 nm and multi-line spectral observations;

4. Polarimetric sensitivity and accuracy of the order of 10^{-5};

5. Observations in the following spectral lines: Fe I 525.02 nm, Fe I 617.3 nm, Fe I 557.6 nm, Mg I 517.3 nm, Fe I 630.15 nm, Fe I 630.25 nm, Fe I 1565 nm, Si I 1082.7 nm, Fe I 520.5 nm and G-band;

6. 15÷30 spectral sampling with an integration time of 1÷3 seconds and a time sampling (cadence) of 15÷90 seconds

7. High signal-to-noise ratio from 100 to 2000;

8. Spectral sampling from 2 pm to 100 pm, depending on the spectral line and on the scientific purpose.

All these instrumental requirements are quite challenging and ambitious, but they could be attained with modern optical designs, modern optical reflection coatings, polarization-free optical relays and FPI-based instruments.

3.3 FPI Prototype for the GREST Project

We have seen that the science cases and the resulting instrumental requirements lead to the use of FPI-based instruments. The fine control of the positioning and the parallelism of the two plates of an FPI is of fundamental importance to obtain the correct spectral sampling. In this section of this work we report our contribution to the design of a FPI CSE controlled with one of the first digital controllers for this kind of instruments, which will replace the old analogical ones. The development of digital controllers is one of the most important technological challenging for large-diameter FPIs, which will be largely used in the instrument suite of the up-coming large-diameter 4-meter class solar telescopes (i.e. EST or DKIST).

3.3.1 Design of a digital controlled FPI

The GREST FPI 50 and the ADS100 are two prototypes developed by the Solar Physics Group of the University of Rome Tor Vergata and the ADS International company (http://www.ads-int.com/) of Lecco (Milan, Italy) inside the GREST WP3 project (http://www.est-east.eu/est/index.php/grest). The GREST FPI 50 is a CSE with an optical cavity of 50 mm in diameter driven by three piezoelectric actuators (PZT) placed in a 120° geometry and monitored by six capacitive sensors coupled in capacitive bridge circuits. The ADS100 is a new digital controller for FPI, a pathfinder for the future digital controllers of the next generation large diameter FPI for EST, which will substitute the old analogical controllers, such as the I.C. Optical Systems (ICOS) CS100.

Scientific requirements

The scientific requirements of new generation CSE can be inferred taking four spectro-polarimetric lines observed with IBIS/DST as case study:

- Considering the 617.3 nm Fe I spectral line sampled between 617.311 nm and 617.359 nm in 22 spectral point, we have a single step spectral distance of 2.3 pm;
- Considering the 854.2 nm Ca II spectral line sampled between 854.125 nm and 854.300 nm in 21 spectral point, we have a single step spectral distance of 8.8 pm;
- Considering the 854.2 nm Ca II spectral line sampled between 854.125 nm and 854.300 m, and adding 5 spectral points between 854.000 nm and 854.125 nm on the left of the line core and adding 5 spectral points between 854.300 nm and 854.425 nm on the right of the line core, we obtain a single step spectral distance of 17.5 pm in the line wings and of 31.3 pm in the line core;
- Considering a symmetric sample of the wings of the 854.2 nm Ca II spectral line with a step going from 854.000 nm to 854.425 nm, we have a spectral step of 425 pm.

and therefore the typical scan steps of the CSE will be:

- 8.6 nm fine spectral scan;
- 24 nm medium resolution spectral scan;
- 190 nm low resolution spectral scan.

Other scientific requirements are:

- Typical scanning range between 100 nm and 400 nm;
- Typical PZT stroke between 5 nm and 30 nm;
- Spectral scanning frequency between 10 Hz and 30 Hz.

Mechanical scheme

The GREST FPI 50 prototype, as mentioned before, is an FPI with an optical cavity of 50 mm in diameter driven by 3 PZT in a 120° geometry and its parallelism is monitored by 5 capacitors. The GREST FPI 50 has been designed in order to have similar geometry to the one of the ICOS FPIs. This FPI have been used to test the new ADS100 developed by the ADS International company.
The general mechanical scheme is shown in Fig. 3.4 (GREST project ref. 653982, 2017). The GREST FPI 50 is composed by two cylindrical parts that host the two mirros of the optical cavity and which can be tilted one respect to the other using three DM10 micrometers produced by Thorlabs (https://www.thorlabs.com/), which, in their turn, press on the pins of the PZTs. Moving this three DM10, it is possible to set the initial coarse parallelism of the optical cavity. Six other DM10 micrometers are used to control the distance between the two gold surface of the capacitors, in order to set the correct working distance at 50 μm. The DM10 micrometer (see Fig. 3.5) has a coarse adjustment of 12.7mm range and a fine adjustment of 250 μm range with 25 μm per revolution. The resolution of the fine control knob is 0.5 μm.
The mechanical parts host also five capacitive sensors. Referring to Fig. 3.4, two capacitive sensors are coupled in a capacitive bridge to control the tilt along the x axis (blue circles), other two capacitive sensors are coupled in a capacitive bridge to control the tilt along the y axis (light blue circles), and the last capacitive sensor (green circles; coupled with an external capacitive sensor, see later) is used to monitor the distance between the two parts of the mechanical

assembly. Therefore this five capacitor are used to monitor the tilt and the distance of the two optical mirrors which made the optical cavity, placed at the center of the mechanical assembly. The fine movement of the mirrors is driven by the three PZTs (red circles).
Other schemes of the mechanical assembly are reported in the Appendix (from Fig. 5.1 to Fig. 5.7).

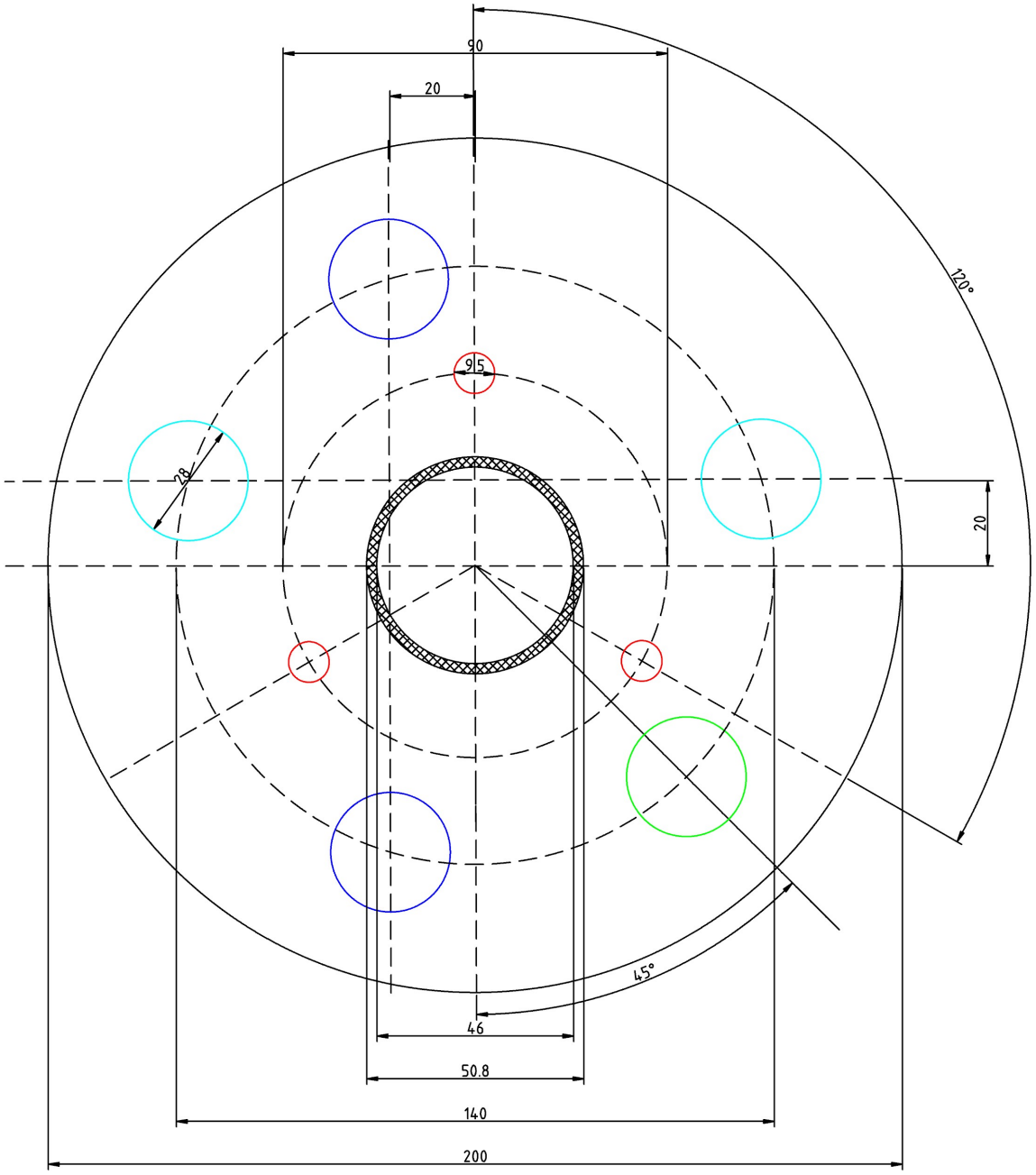

Figure 3.4: General scheme of the GREST FPI 50. The optical cavity is placed at the center. The blue circles are the position of the capacitive sensors monitoring the tilt along the x axis. The light blue circle are the position of the capacitive sensors monitoring the tilt along the y axis. The green circle is the position of the z axis capacitive sensor which monitor the distance between the two parts of the prototype. The red circles are the positions of the 3 PZTs.

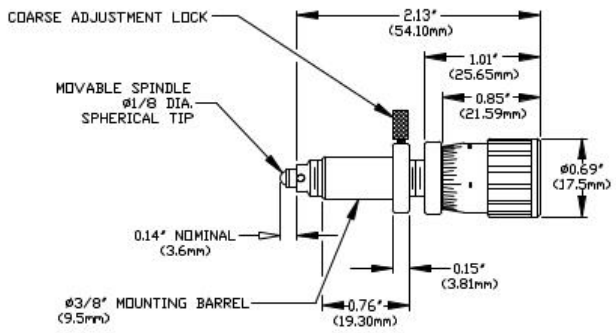

Figure 3.5: Thorlabs DM10 micrometer.

Optical cavity

The mirror of the optical cavity are two optical flat produced by Edmund Optics Ltd. (https://www.edmundoptics.com/). They are two optical flats of 50.8 mm in diameter, the main surface is uncoated (so the reflectivity as a mirror is of the order of 4%) and the optical quality is $\lambda/20$. They are kept in place at the center of the mechanical assembly using two teflon screws in order to avoid deformations due to tension forces. The technical drawing of the 50.8 mm optical flat is reported in Appendix in Fig. 5.8.

Capacitive sensors

Each capacitive sensor is made by a couple of custom made flat mirrors produced by the italian company Gestione SILO S.R.L. (https://www.gestionesilo.it/). The mirrors have a cylindrical shape and one face of the cylinder has a beveled edge. The top smaller faces of the mirrors are coated in gold without quartz protection, with a diameter of 12.6 mm. The inclined beveled surface is also coated with unprotected gold, giving the possibility to connect the electric wires to realize the capacitance circuit. Two mirrors, one in front of the other, constitute a capacitor. At the working distance of 50 μm, the capacity is 22 pF. The lower part of the capacitive sensor is mounted in a fixed position in the lower part of the GREST FPI 50, as shown in Fig. 5.6 in the Appendix. The upper part of the capacitive sensor is mounted on a movable PTFE (teflon) cylinder piston (in order to reduce the friction), actuated by a DM10 micrometer in order to set the correct working distance, as shown in Fig. 5.7 in the Appendix. The technical drawing of the gold mirrors is reported in Fig. 5.9 in the Appendix.

Piezoelectric actuators

The GREST FPI 50 prototype fine movement is actuated by three PZTs SMPAK15553D4 (see Fig. 3.6) produced by STEMiNC (https://www.steminc.com/), with the following characteristics: dimensions (L×W×H) 3×3×5 mm, capacitance 0.15 μF $\pm$ 20%, displacement 4 μm at 150 V $\pm$ 10%, max input voltage 150 V DC, blocking force 330 N at 150 V, stiffness 55 N/μm, total stroke 4 μm, single step 4 nm. They have been chosen according to the requirements of the FPI prototype and for its low hysteresis and good linearity, especially in the stroke between 3 μm and 4 μm. The PZTs move a small metal piston, which push on the DM10 micrometers, as shown in Fig. 5.5 in Appendix.

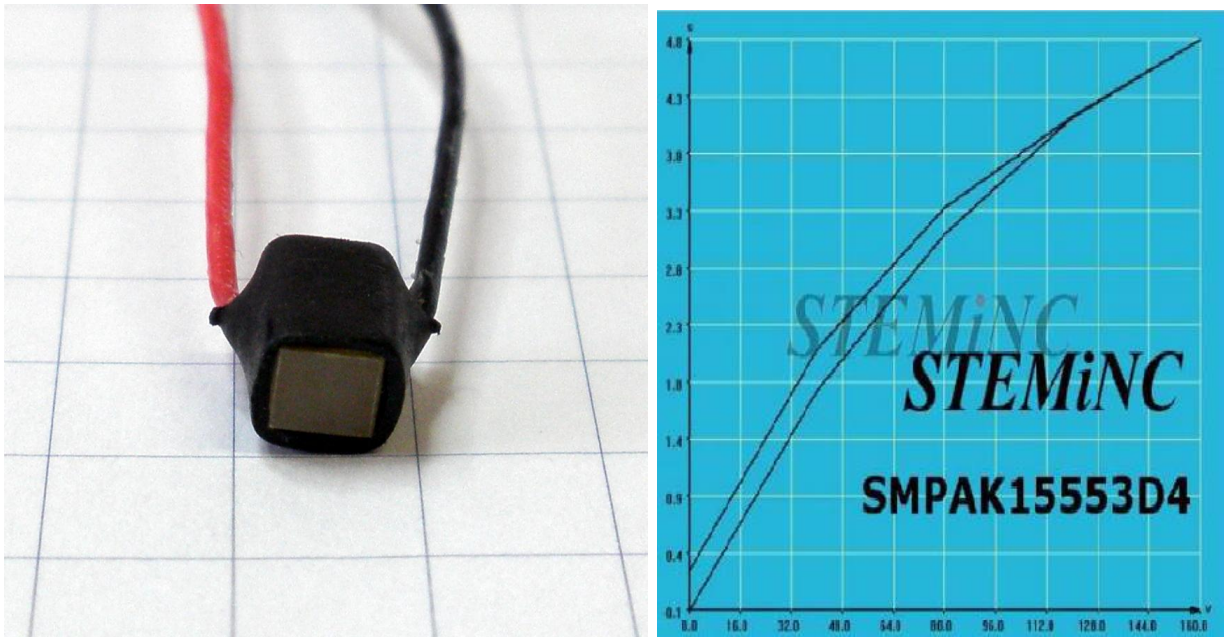

Figure 3.6: Left panel: STEMiNC SMPAK15553D4 PZT. Right panel: STEMiNC SMPAK15553D4 PZT hystereris curve.

Electronic scheme and wiring

The electronic scheme of the connections between the capacitive sensors is the same scheme that has been adopted for the ICOS FPI in order to test the ADS100 electronic controller on the same configuration of the ICOS FPI. The scheme is reported in Fig. 3.7 (GREST project ref. 653982, 2018b), where CX1 and CX2 are coupled in an capacitance bridge in order to monitor the tilt of the x axis, CY1 and CY2 coupled for the y axis, and CZ is coupled with CREF, an external capacitive sensor (see Fig. 3.8). The external capacitive sensor is used as a reference for the capacitive drift due to air properties variations, such as temperature, pressure and humidity. The mechanical scheme of CREF is reported in Fig. 5.10 in the Appendix. The CREF is mounted externally from the two main parts of the GREST FPI 50 and it is anchored in the upper part of the external housing of the FPI.
The mirrors of the capacitive sensors are mounted on a self-lubrificationg PTFE cylindrical pistons (moved by the DM10 micrometers) and screwed with insulated red PVC support caps, which are also used to maintain the electric connections between the beveled surface of the gold mirrors and the electric wires. The electric wires are connected in three different points on the gold mirror (in a trefoil configuration) to ensure the electric connection and to reduce the edge effects. The wire used is a coaxial cable RG178PE Belden with an external diameter of 1.8 mm and a capacity of 104.9 pF/m. All connections have been done in the Laboratory of ADS International and using the same cable length of 40.0±0.2 cm, in order to maintain the same parasitic capacitance on all the capacitive bridges (see Fig. 3.9).
The electronic interface between the GREST FPI 50 and the ADS100 has been done using the following connectors (see Fig. 5.11 in the Appendix) produced by LEMO (https://www.lemo.com/it):

- ERA.1S.305.CLL, quantity 1, 5 pins, 4 used: used for the capacitive bridge signals (3 pins) and for common signal;
- ERA.00.250.CTL, quantity 3, 1 pin: used for the three signals of the X, Y and Z capacitive

bridges;

- EGJ.2B.306.CLA, quantity 1, 6 pins: used for the PZTs driving high voltage.

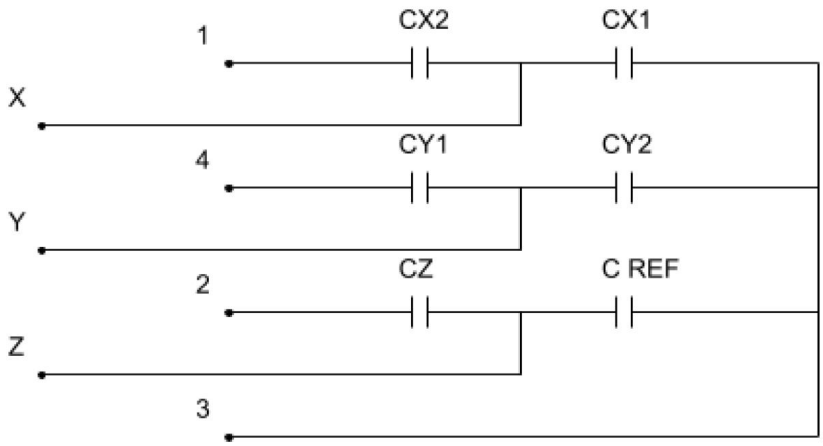

Figure 3.7: Electronic scheme of the capacitive sensors with the pinout function.

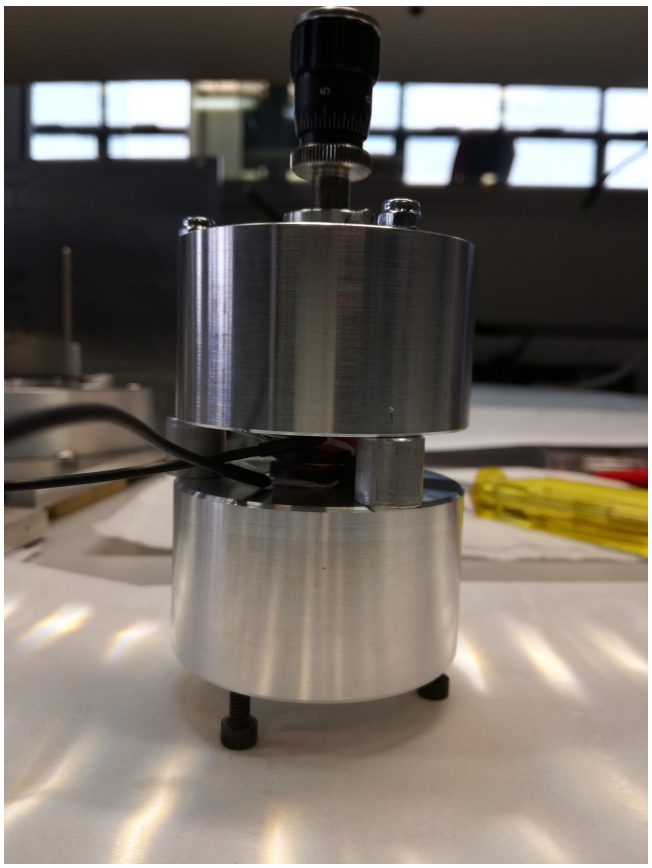

Figure 3.8: External reference capacitive sensor.

ADS100 controller and software layout

The ADS100 controller (see Fig. 3.10) has been developed by the company ADS International in order to control the GREST FPI 50 prototype, used as test bench for future test with

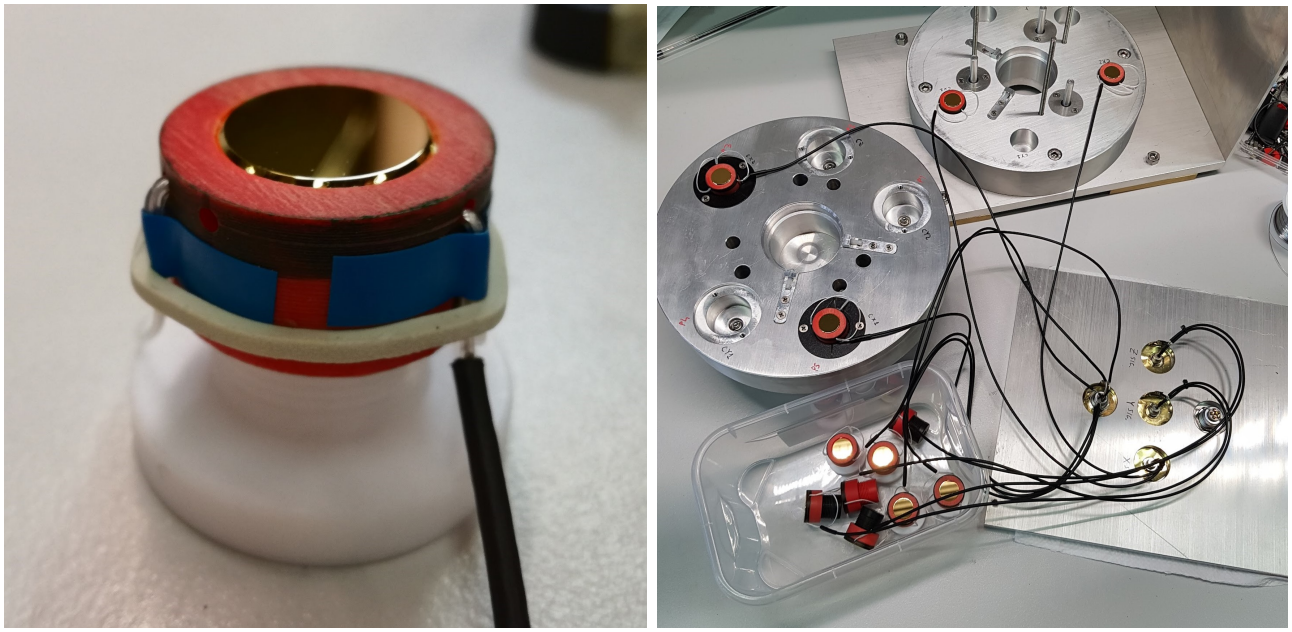

Figure 3.9: Left panel: gold mirror of a capacitive sensor mounted with the PTFE piston and the PVC support cap with the electric connection. Right panel: all the mirrors mounted during the integration phase with the prototype.

ICOS FPI (GREST project ref. 653982, 2018a). The ADS100 is the first digital controller for FPI which will replace the analogical ones developed by ICOS. The ADS100 represents a milestone on the control of the closed loop in the stability of FPIs with the ability of a digital filtering of the signal and switch operation mode as used in the various phases of the spectral line scan. The ADS100 has been developed in four steps: design of the Digital-Analog Converter (DAC) for the PZTs, design of the high voltage amplifier, design of the capacitive sensors interfaces and the selection of PIC32 micro processor. The electronics of the capacitive sensors is the most delicate part, because of the difficulties in minimizing the noise due to the various components on the board. The ADS100 is controlled by a Raspberry PI unit, in which the codes run.
The block diagram of the ADS100 software is shown in Fig. 3.11:

- the blue block on the top-left describes the capacitive sensors analog electronics;
- the gray block on the top-right describes the code running on the PIC32 micro processor: it reads the signals of the three capacitive bridges at 8 kHz, it buffers them (100 samples) and it computes the statistics of these signals (max, min, average and standard deviation values);
- the gray block on the bottom is the code running on the Raspberry PI controller. The Capsens ADC code manages the data computed by PIC32 to the screen and gives the possibility to save the data in a selected file. The Piezo DAC code controls the high voltage signals of the strokes of the PZTs given from the keyboard.

The last two codes has been merged in order to close the loop of the electronics control: the parallelism of the GREST FPI 50 is monitored by the capacitive sensors and it is maintained by the feedback response of the PZTs to the capacitive sensors signals. Moreover, the closed loop between the capacitive sensors and the PZTs is also kept during the space scan of the

GREST FPI 50. In collaboration with ADS International, we developed three program in C and Python 2.7, used for the calibration, closed loop and space scan:

- The calibration program reads for three seconds the capacitive bridges before and after a stroke corresponding to 10k digital units (the total stroke is 40k digital units) and computes the control matrix that will be used by the other two programs;
- The closed loop program uses the control matrix to maintain the parallelism of the GREST FPI 50 in a target position of the strokes of the PZTs with a frequency up to 40 Hz. In this way, the GREST FPI 50 operates as a CSE;
- The scan program is used to perform the spacing scan of the optical cavity maintaining the parallelism with the closed loop.

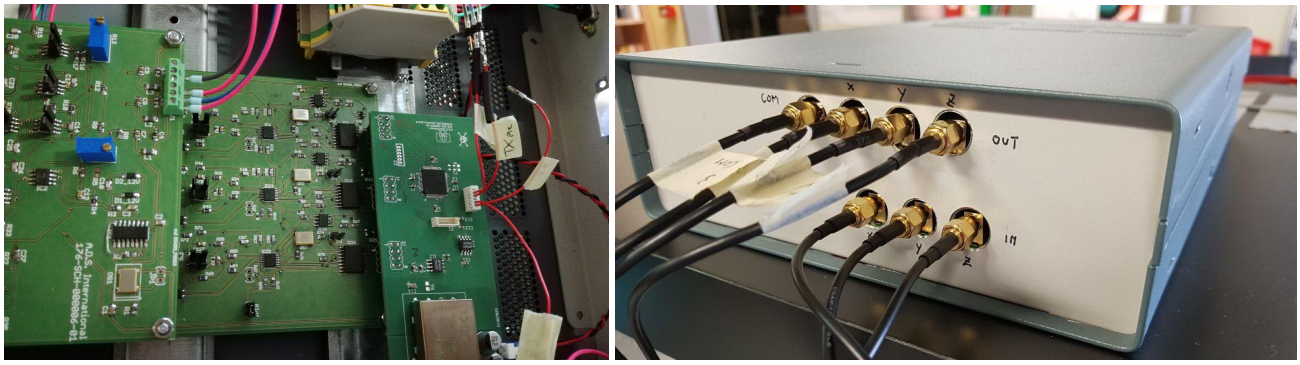

Figure 3.10: Left panel: Internal view of the ADS100 in a prototyping phase. Right panel: connections on the ADS100.

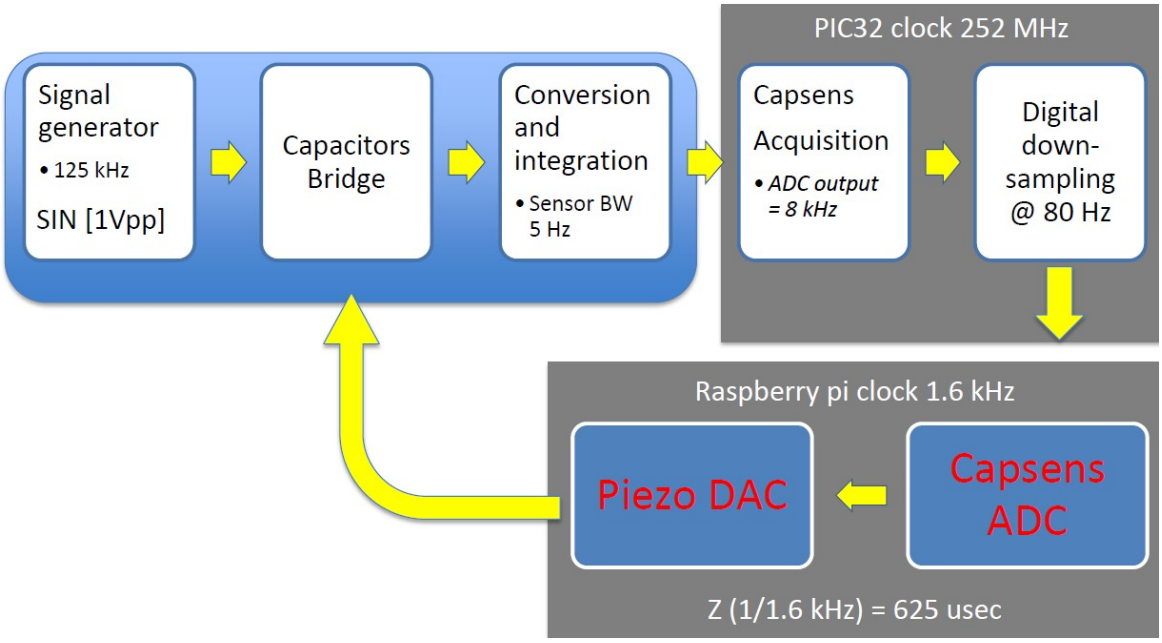

Figure 3.11: Block diagram of the ADS100 software.

Assembly

The two parts of the GREST FPI 50 have been manifactured by the mechanical workshop of the University of Rome Tor Vergata starting from two aluminium blocks. In addition, a parallelepiped housing for the prototype has been realized from aluminium slabs. The assembly and integration process has been done in the Laboratory of ADS International from the 5th to the 7th of February 2018. After wiring the gold mirrors, the electric wires have been cabled with the LEMO connectors and located in the fron part of the parallepiped housing, as shown in Fig. 3.12. Afterwards we have mounted the gold mirrors in the PTFE cylinder piston in such a way that the electric connection with the coaxial cable are maintained by the pressure of the red PVC cap, we have mounted the fixed couterpart of the capacitive sensors and placed them on the two parts of the GREST FPI 50, as shown in Fig. 3.13. Finally we have mounted the DM10 micrometers and fixed the positions of all the cables. The GREST FPI 50 totally assembled is visibl in Fig. 3.14. The GREST FPI 50 connected with the ADS100 electronic controller is shown in Fig. 3.15.

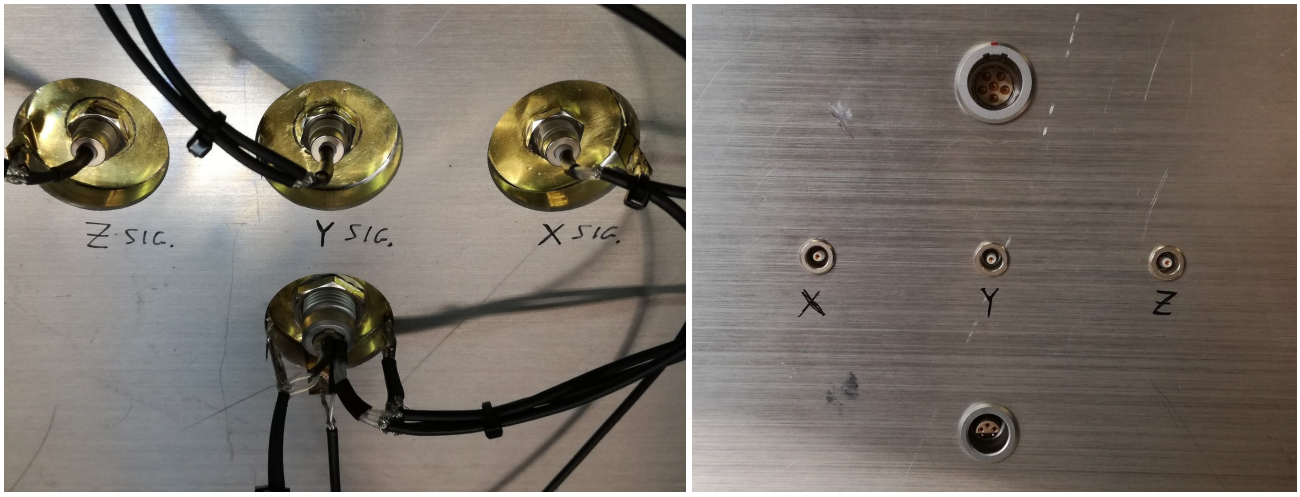

Figure 3.12: Left panel: LEMO connector wired (internal side of the prototype). Right panel: LEMO connectors (external side of the prototype).

3.3.2 Electronic Tests in ADS International

From the 2nd to the 4th of May 2018, we performed the electronic tests in the Laboratory of ADS International. Here we describe all the experimental procedure and the data analysis that we adopted to study the stability of the electronics and to determine the electronic noise (GREST project ref. 653982, 2018c).

Climatic chamber tests

We performed the electronic stability test using the climatic chamber WK3-1000/70-22613918 produced by Weiss Technik (see Fig. 3.16). In its internal volume of 1 m^3, it is possible to control the temperature from -60 °C to +200 °C with a precision of 0.1 °C and the humidity with an accuracy of 1%. We positioned the GREST FPI 50 and the ADS100 inside the climatic chamber in order to perform several test in a controlled environment (crucial for thermal

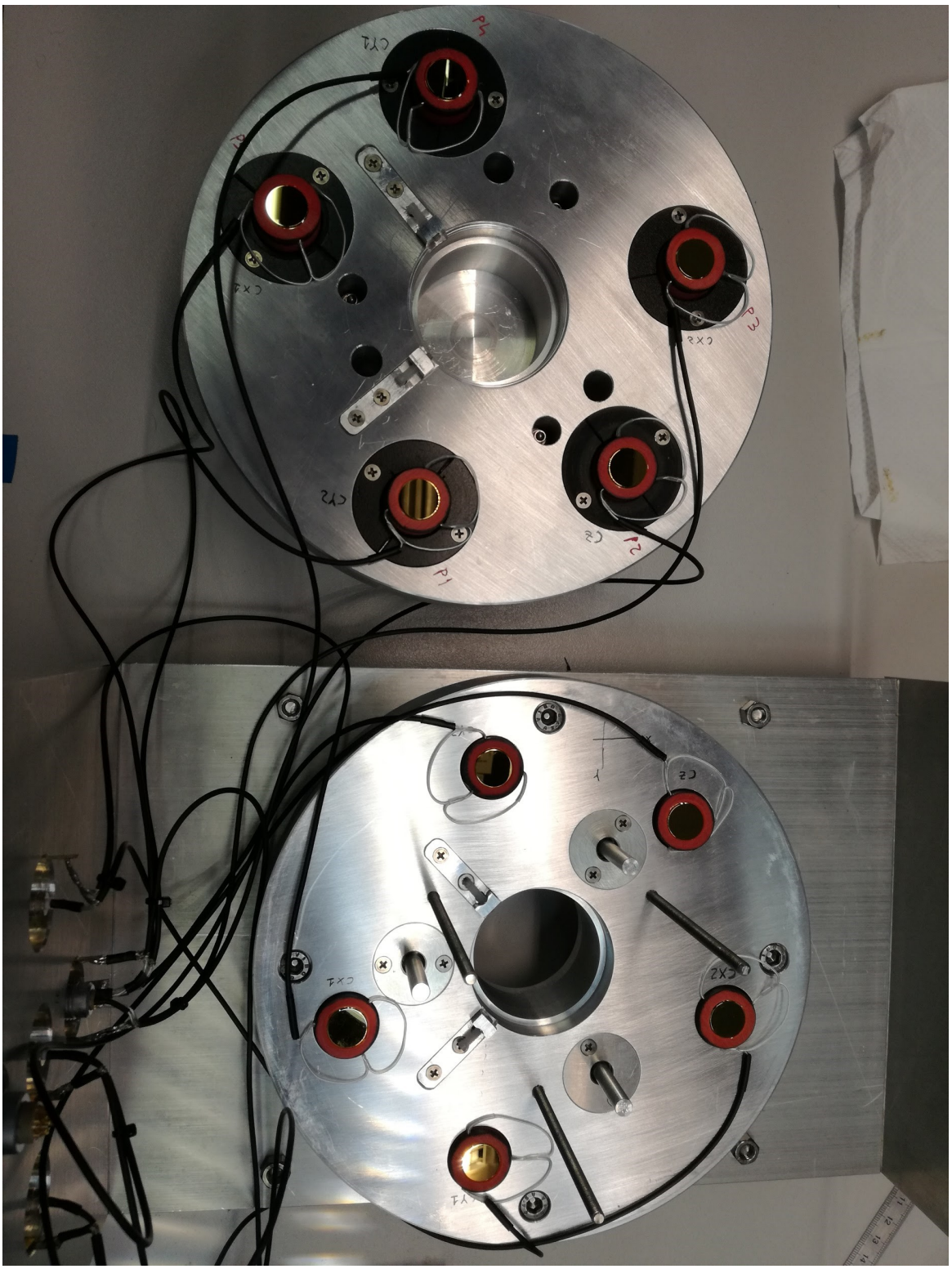

Figure 3.13: Wiring of the capacitive sensors of GREST FPI 50.

dilatation of the prototype), living the power suppliers outside the chamber (see Fig. 3.17). During the test the temperature was set to 20 °C and the humidity to 65%.

Figure 3.14: Lateral view of the GREST FPI 50 integrated with DM10 micrometers and placed in the housing. All cables are fixed in position during the assembly phase.

ADS100 digital electronic controller test

We performed several tests on the ADS100 electronic controller in order to characterize its noise through the standard deviation (STD) of the signal.
We realized a capacitive bridge using NP0 capacitance (characterized by high tolerance and stability in temperature) following the same scheme of Fig. 3.7. For the NP0 capacitive bridge we report the STD for the signal and also the STD of the digital filtering of the same signal with a low pass filter at 20 Hz. The STD of the unfiltered signals depends on the channel (one for each capacitive bridge) due to electronic design issues, and it spans from 0.38 mV to 0.15 mV. In the new version of the ADS100 this issues has been overcame using one single board for each channel, instead of a unique board. In fact, the noise level in the three channels in the new version of the ADS100 is approximately the same and it has an STD of 0.15 mV; using the digital filtering the STD is 0.08 mV. The tests performed inside (STD 0.16 mV) and outside (STD 0.15 mV) the climatic chamber showed that the noise level does not vary appreciably, so the ADS100 electronics seems to be not affected by variation in temperature of the order of $\pm$ 20 °C with respect to the operational ambient temperature of 20$\div$25 °C.
We repeated the same test using the capacitive sensors if the GREST FPI 50 prototype and we obtain an STD of the signal spanning from 0.20 mV to 0.40 mV. This slightly values depends on the mechanical defects of the prototype, such as the not perfect parallelism and/or misalignments of the two gold mirrors in each capacitive sensor, edge effects and eddy currents on the prototype (despite it has been connected to the ground).

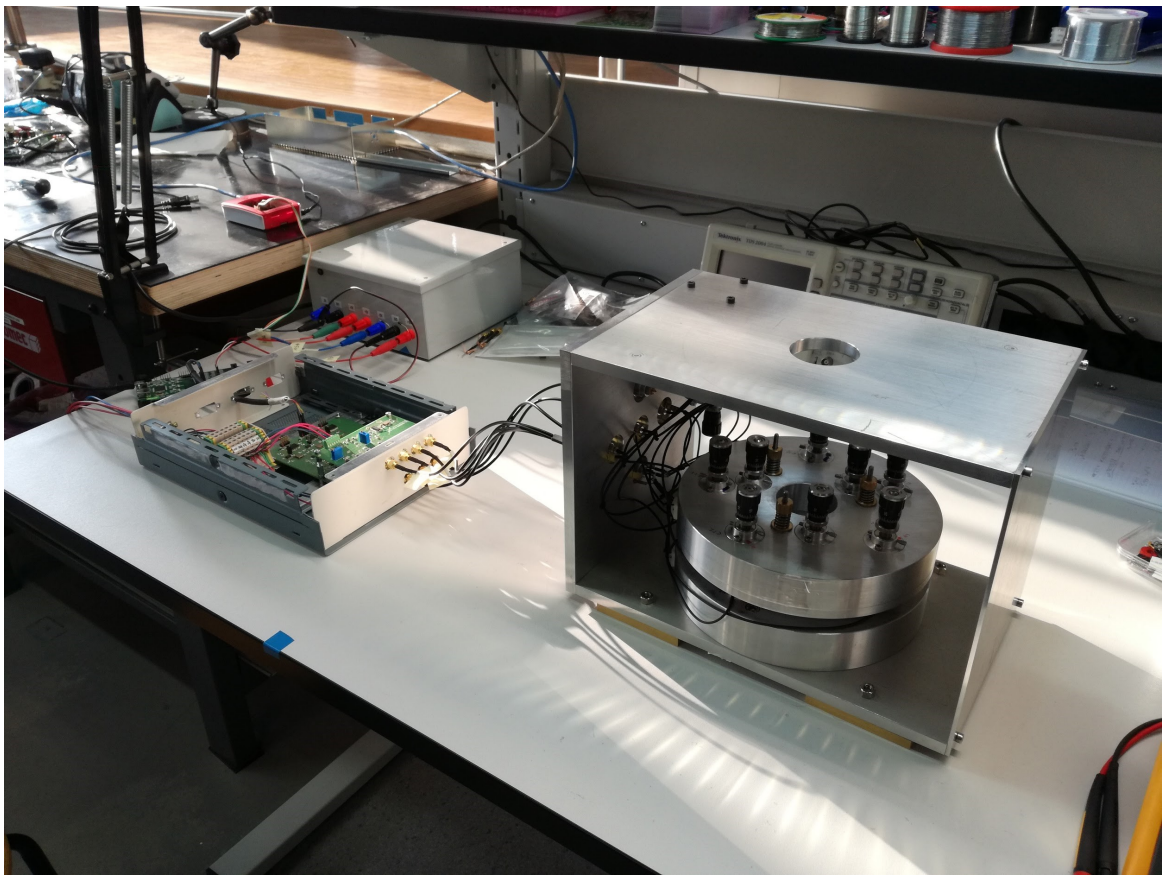

Figure 3.15: The GREST FPI 50 connected with the ADS100 controller.

3.3.3 Optical and Spectral tests in the UTOV Solar Physics Laboratory

From the 16th to the 18th of May 2018, we performed the optical stability tests and the spectral tests in the Solar Physics Laboratory of the University of Rome Tor Vergata. Here we describe the experimental setup, the procedure and the data analysis that we use to chacacterize the spectral behaviour of the GREST FPI 50 prototype (GREST project ref. 653982, 2018d).

Optical tests configuration

For the optical test, we used a Newport Smart Table ST Series pneumatic isolated optical table in order to perform the tests without mechanical vibrations coming from the environment. We realized two optical channels useful for the test (see Fig. 3.18 and Fig. 3.19):

- On the left, the box contains a Sodium lamp. A plastic plano-parabolic condenser is used to concentrate the light on a pinhole, which is a point-like source, and a plano-convex lens (30 mm diameter, +85 mm focal length) create a collimated beam of 25 mm of diameter. The Sodium collimated beam goes from left to right;

- On the right, a green laser CPS532 produced by Thorlabs emits a collimated beam at 532 nm of wavelength. A plano-parabolic condenser (30 mm diameter, +40 mm focal length) and a bi-convex lens (40 mm diameter, +200 mm focal length) are used in a keplerian configuration in order to create a beam expander, which increases the diameter of the

Figure 3.16: Climatic chamber by Weiss Technik with the GREST FPI 50 and the ADS100 inside. The power suppliers are placed outside.

collimated laser light beam from 2 mm to 25 mm. The laser collimated beam goes from right to left.

At the center, between this two light sources, the GREST FPI 50 is positioned over four perches. Below it a 45-degrees inclined flat mirror with an elliptical profile is placed. The mirror can be rotated by 180 degrees in order to send inside the GREST FPI 50 mirrors (of the optical cavity) the collimated light beam coming from the Sodium lamp of from the green laser.

Alignment procedure

To set the GREST FPI 50 correct operation, and so to parallelize the two mirrors of the optical cavity, we adopted the following allignment procedure:

- We set the gap of the optical cavity using the three DM10 micrometers insisting on the three PZTs and using a calibrated thickness of 1.00±0.01 mm;
- The coarse regulation of the parallelism (see Fig. 3.20) is performed using the same three DM10 of the previous step and, observing the interference fringes in afocal configuration (collimated beam), regulating the DM10 in order to obtain 5-6 fringes parallel to each other (so the tilt of the two mirrors should be of the order of 1 μm);
- The calibration of the capacitive sensors is performed using a calibrated thickness of 40 μm. Using the DM10, we regulate the distance between the two gold mirrors using the calibrated thickness and, after removing it, we use the fine adjustment of the DM10 to

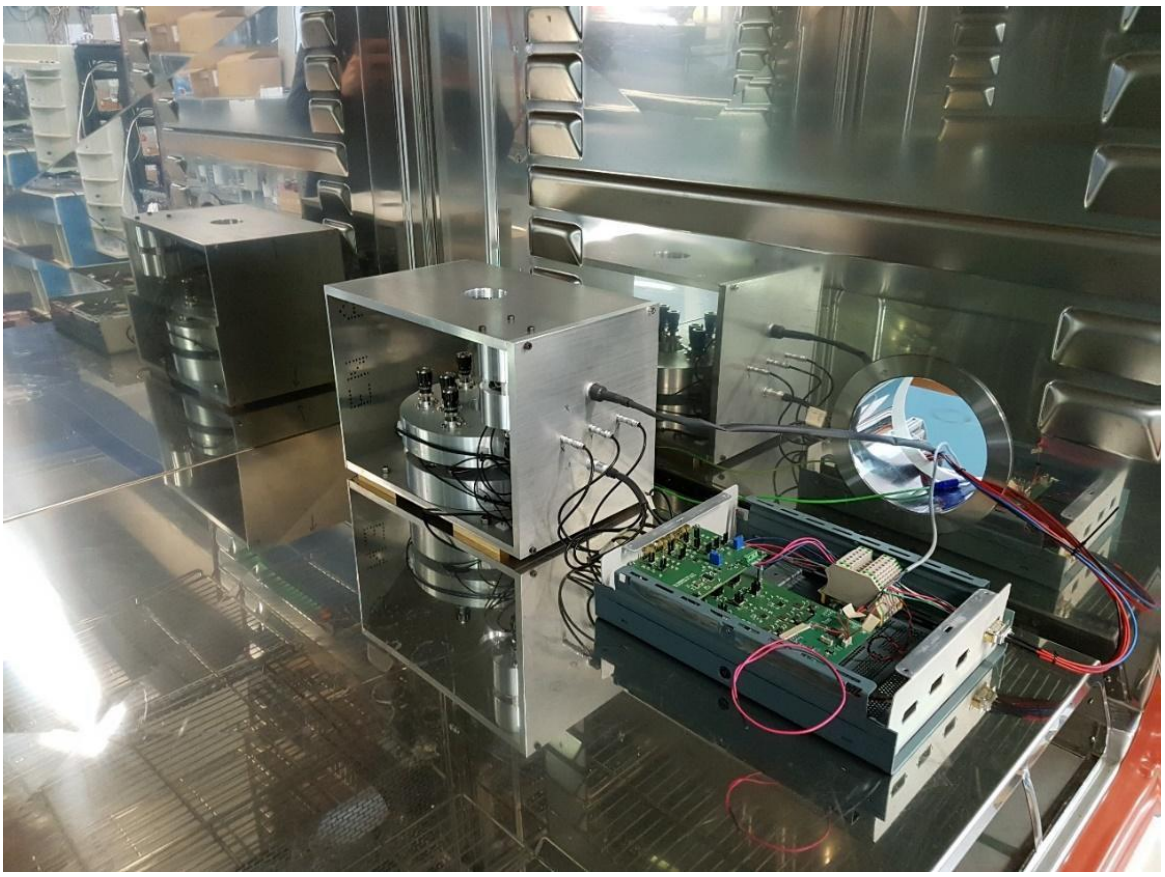

Figure 3.17: The GREST FPI 50 connected with the ADS100 controller.

increase their distance of other 10 μm, so obtaining the correct working distance of 50 μm;

- The fine parallelism calibration (see Fig. 3.21) is performed using the three PZTs driven by the control program, until only two fringes are visible in the afocal configuration (so the tilt of the two mirrors should be of the order of 200 nm);
- The calibration of the ADS100 in performed measuring the actuation matrix and, by inverting it, to obtain the control matrix used in the programs.

Parallelism control

It is known that the parallelism control in an FPI is of fundamental importance. During this test we use the collimated beam of the green laser. From the FPI theory, we know that the parameter which characterize the spectral behaviour of an FPI is the reflective finesse F_R. Supposing that we are operating with an high collimated beam, with very little polishing defects of the optical cavity, the only term which degradates the reflective finesse F_R to the effective finesse F_E is the parallelism (F_{PD}) between the two optical mirrors of the optical cavity:

$$F_E = \left(\frac{1}{F_R^2} + \frac{1}{F_{PD}^2} \right)^{-\frac{1}{2}} \tag{3.24}$$

In our case we evaluate $F_R \sim 30$ and $F_E \sim 2$. This indicate that the GREST FPI 50 prototype is not an FPI suitable for high resolution spectral observation, but it is enough for our spectral

Figure 3.18: Newport Smart Table ST series optical table with the optics for the test. On the left: Sodium lamp with optics for collimated beam. At the center: GREST FPI 50 prototype on four perches with the 45° inclined mirror. On the right: green laser with optics for the collimated beam.

stability tests.

Spectral test and noise

In this section we describe the calibration of the PZTs strokes monitoring them through the capacitive sensors. As a reference, we tested one of the three PTZ and we measured the variation of the signal in the more sensitive capacitance bridge to this PZT (due to the geometry of the prototype). The same can be done with the other PZTs and capacitive bridges, obtaining analogous values. We used the collimated green laser beam to illuminate the GREST FPI 50 and we measured the fringe position. We set the optical system to have three fringes on a PointGrey 2.8 MP CCD (model GS3-U3-28S4M-C).
We used the ADS100 to move the PTZ giving a signal of 15 k digital unit; therefore measuring again the fringe positions, in particular their shift, as shown in Fig. 3.22. Given the laser wavelength, the fringe shift correspond to an increase of the distance between the edges of the two mirrors of 92.4 nm. Considering the geometry of the prototype, the PZT insist on a lever of 67.5 nm with respect to the pivot point. Therefore, the displacement of 92.4 nm of the edges of the mirrors corresponds to a displacement of the PZT equal to 1177 nm. With this measurement, we evaluate that 13 digital units of PZT signal correspond to 1 nm of PZT elongation. Measuring the difference of the signals of the capacitive bridge before and after the displacement, we evaluate that 1 nm on the PZT corresponds to $3.3 \cdot 10^{-3}$ V.
Now we consider an overall movement of all the three PZTs maintaining the parallelism: in this case all the PZTs move of the same quantity, varying the optical cavity and performing the spacing scan. This test has been done using the Sodium collimated beam. In this case we can interpret the variations of the signal of the capacitive bridges to assess the noise level of

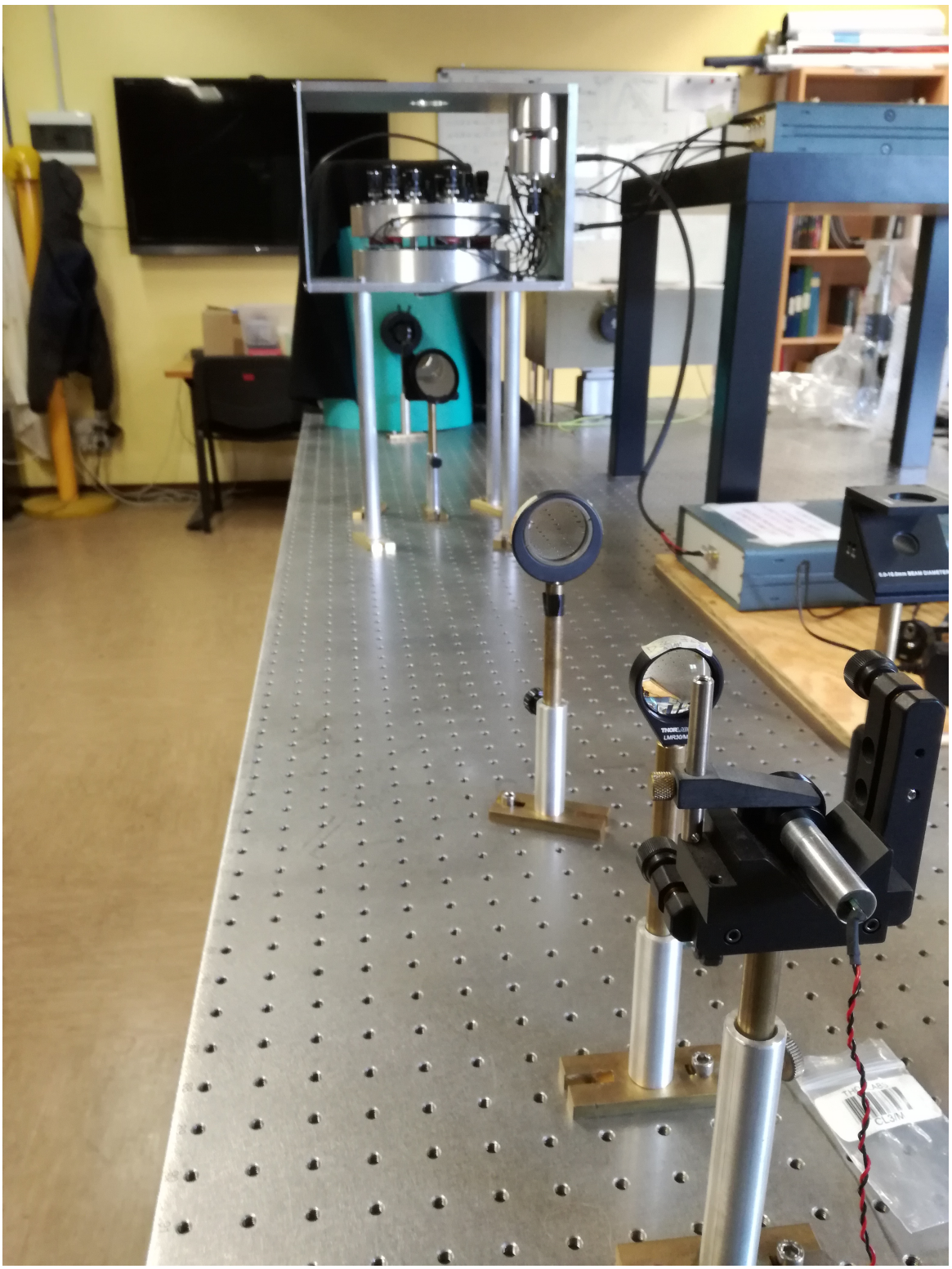

Figure 3.19: Optical setup seen from the laser and the beam expander.

the electronics in terms of the optical cavity errors. We obtain an STD equal to $2.5 \cdot 10^{-4}$ V. This value correspond to a gap distance noise (distance error between the two mirrors of the optical cavity) of 7.6 nm and to a spectral noise (wavelength position noise) of 5.0 pm.
Referring to the scientific requirements, we can convert the requirement for the single wavelength step in PZT strokes:

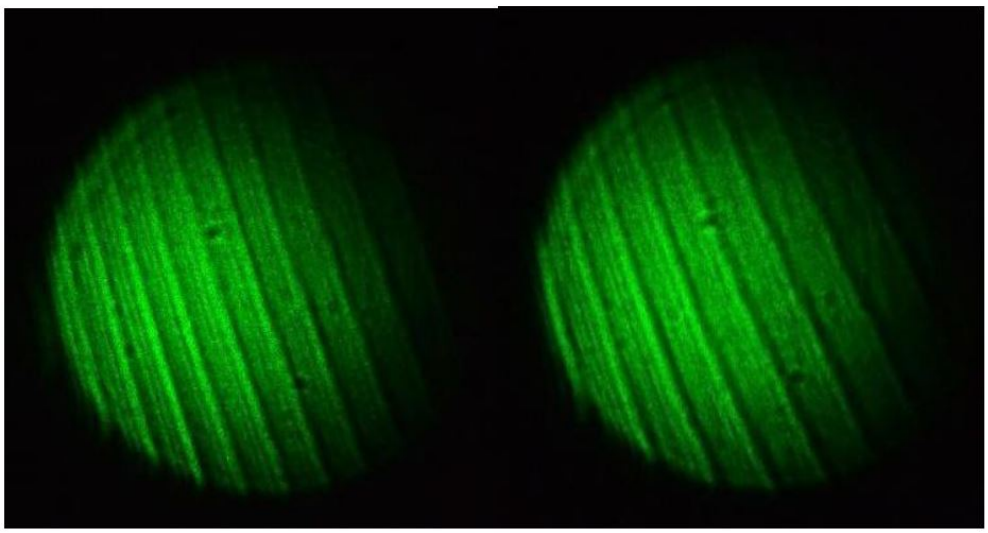

Figure 3.20: Interference fringes pattern during the coarse parallelism calibration using the DM10 micrometers.

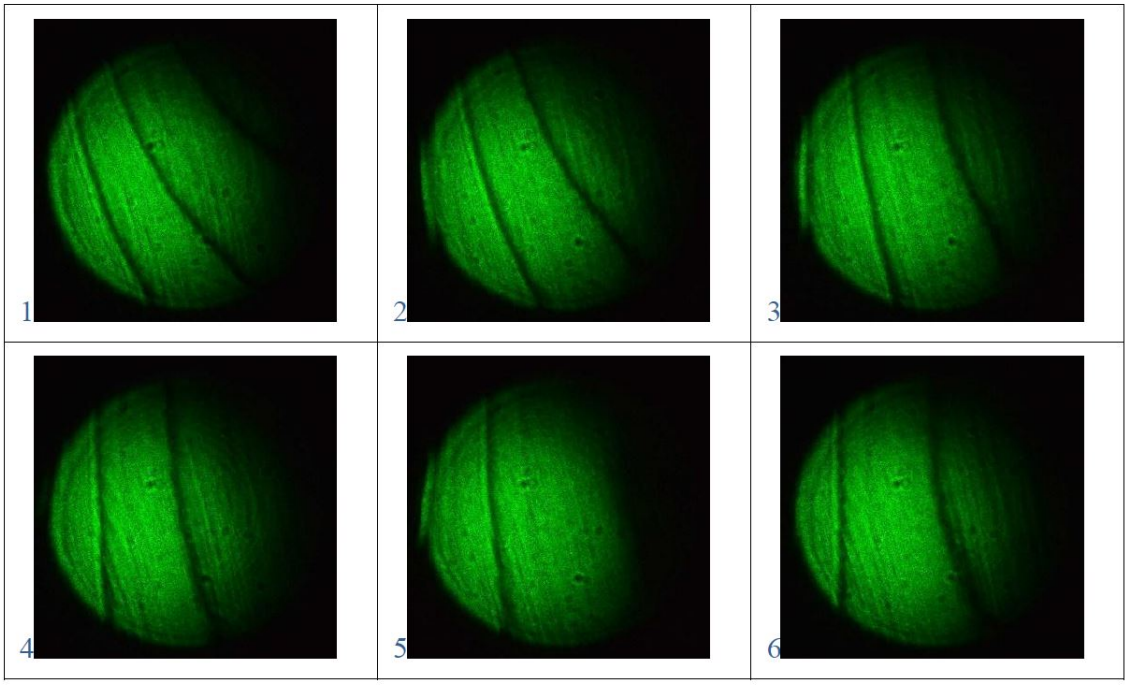

Figure 3.21: Interference fringes pattern during the fine parallelism calibration using the PZTs.

- In the fine spectral scan scenario, 2.3 pm step at 617.3 nm requires a stroke of 8.6 nm, which correspond to 110 digital units of PZT stroke;
- In the medium resolution spectral scan scenario, 8.8 pm step at 854.2 nm requires a stroke of 24 nm, which correspond to 306 digital units of PZT stroke;
- In the low resolution spectral scan scenario, 70 pm step at 854.2 nm requires a stroke of 190 nm, ehich correspond to 2421 digital units of PZT stroke.

The FSR of our prototype with the cavity of 1 mm gap is 160 pm in the Sodium line at

589.2 nm. We measured the wavelength variation of the ring system in the image plane of the CCD (using a Cosmicar 50 mm f/1.8 imaging lens), obtaining:

$$\Delta\lambda = FSR\frac{\Delta r}{D} = 7.2pm \tag{3.25}$$

where Δr is the variation of the third maxima ring and D is the ring diameter. In Fig. 3.23 we report some images of the spectral scan of the Sodium spectral line: the intensity decrease in clearly visible going from the continuum to the line core, and the Fabry-Perot fringes enlarge themselves.

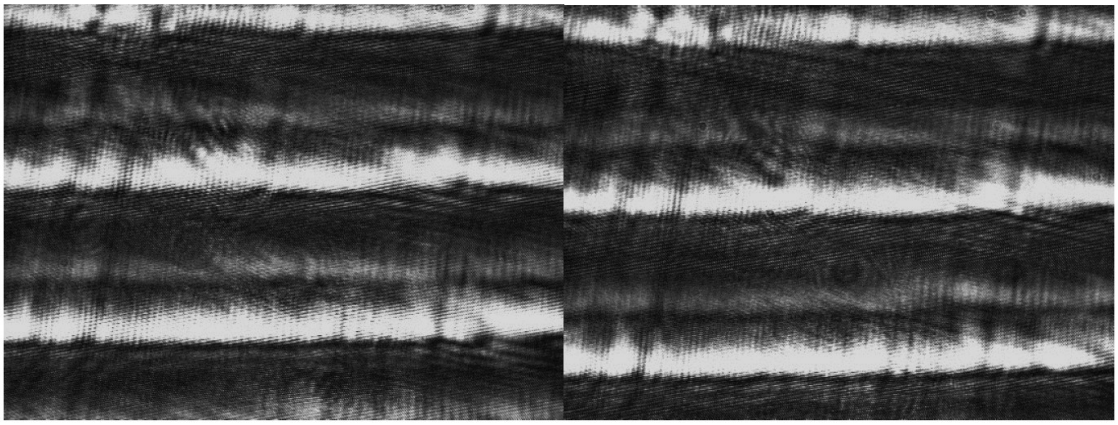

Figure 3.22: Interference fringes pattern shift for a 15 k digital unit signal in one PZT.

3.3.4 Final report and future developments

The results obtained during our tests are promising and satisfying. Using the NP0 capacitors we obtain a very low value of the electronic noise, which confirm the goodness of the ADS100 electronics. The noise measured with the GREST FPI 50 is quite good, considering the mechanical limitation of the prototype, such as the non-parallelism and the misalignments of the capacitive sensors. We are able to realize a digital controller for FPIs controlled by a Raspberry PI at 40 Hz in closed loop configuration. With the actual electronics, we have a gap distance noise of 2.4 nm, which correspond to 1.7 pm of spectral noise. Summarily, we report in the following table the obtained results:

	FPI	NP0	NP0 filtered
Bridge Noise (STD)	$2.5{\cdot}10^{-4}$V	$1.5{\cdot}10^{-4}$V	$0.8{\cdot}10^{-4}$V
Gap Distance Noise	7.6 nm	4.5 nm	2.4 nm
Spectral Noise	5.0 pm	3.2 pm	1.7 pm

The Solar Physics Group of the University of Rome Tor Vergata and the company ADS International are now working on improving the configuration of the GREST FPI 50 in conbination with a new version of the ADS100, which can be mounted on universal rack. In the near future, we are planning to test the ADS100 with an ICOS FPI.

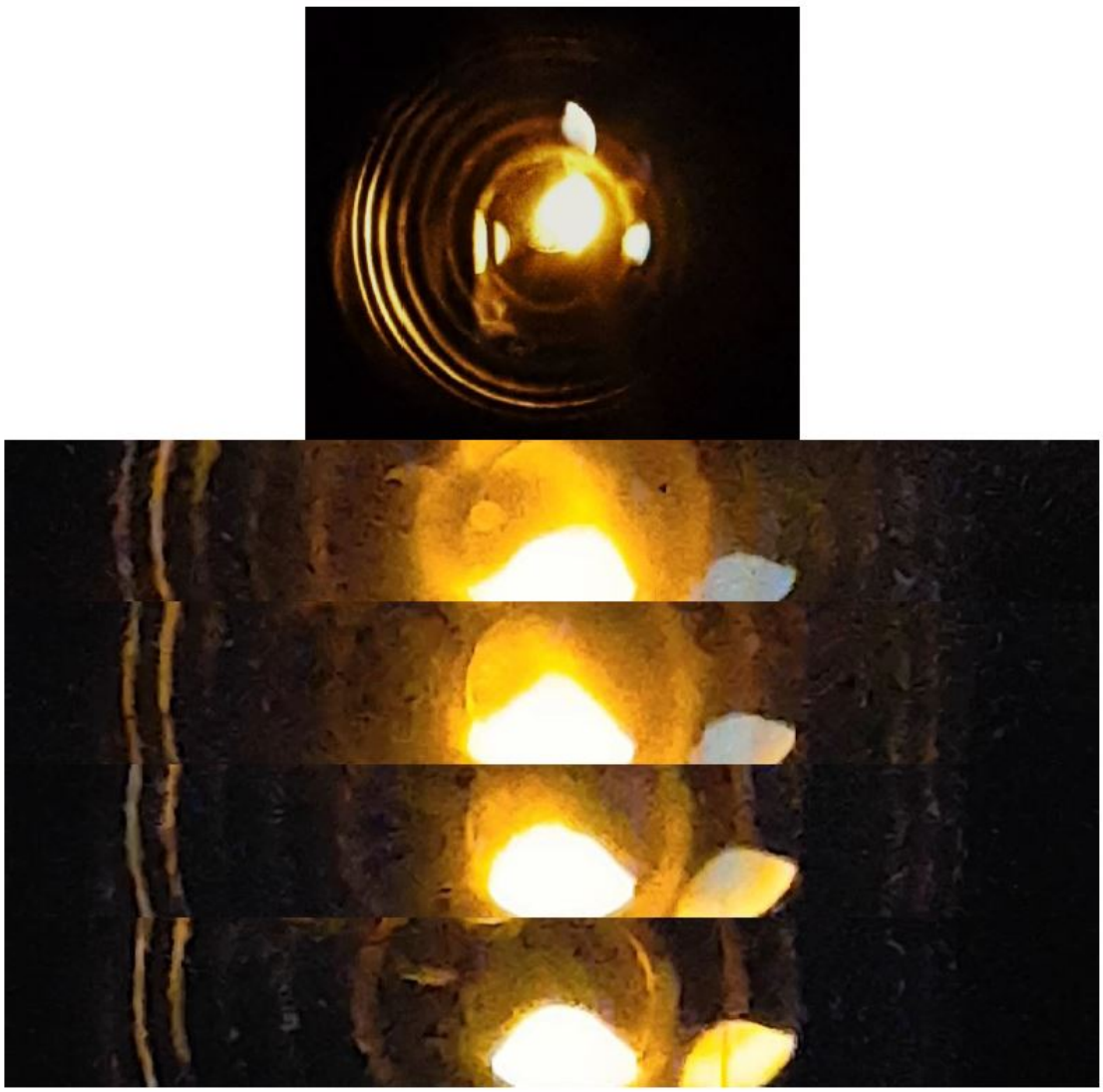

Figure 3.23: Fabry-Perot fringes during the spectral scan of the Sodium line.

3.4 Feasibility Study of a Narrow Band Imager based on FPIs with off-axis parabolic mirrors

The design of the optical scheme of a Narrow Band Imager based on two large diameter ($\simeq$ 20 centimeters) FPIs for new generation large aperture (4 meters) solar telescopes like EST or DKIST presents some constraints. The high spectral resolution ($\geq$ 300.000) and the large field of view ($\geq$ 90 arcsec) requires the use of large optical elements and this implies large optical paths. The use of large optical elements and especially of large FPIs is dictaded by the étendue of the optical system (i.e. the product between the area of the source and the solid angle subtend by the entrance pupil): using large diameter 4-meter class primary mirror and observing a FoV of 60÷80 arcsec, the diameter of the FPIs must be of the order of 200÷250 mm, in order to avoid too many blue-shift from the center to the edge of the FoV (in classical mount). In this section we present a feasibility study of an already proposed optical scheme by Greco and Cavallini (Greco and Cavallini, 2013) in order to reduce the dimension of the instrument maintaining the good optical and spectral performances and analyzing the alignment tolerances.

3.4.1 The conceptual idea of Greco and Cavallini

Greco and Cavallini (Greco and Cavallini, 2013) proposed a new optical design for the post-focus imaging spectro-polarimeter for DKIST (previously called Advanced Technology Solar Telescope, ATST) with high spatial ($\sim$ 30 km on the solar surface) and spectral resolution ($\geq$ 300.000) based on two FPI with a diameter of 200 mm and interference pre-filters of 70 mm of diameter. This instrument is devoted to the study of the smallest structures in the solar atmosphere which release magnetic energy through magneto-hydrodynamic processes. This instrument has been designed taking into account various constraints:

- high spectral resolving power ($\geq$ 300.000);
- large field-of-view ($\geq$ 90 arcsec);
- high spatial resolution ($\sim$ 30 km on the solar surface);
- small exposure time to freeze the seeing ($\leq$ 10 ms);
- large wavelength range from 850 nm to 1650 nm;
- low instrumental polarization ($\leq$ 0.5%).

All this requirements has been satisfied in the optical design of Greco and Cavallini. FPIs has been chosen as the best spectrometric elements due to the high transmission with respect to gratings and due to modern high transmission coating. FPIs must be used in classical mount (collimated light beam) in order to have higher spectral transmittance with respect to the telecentric mount. Large diameter FPIs of 200 mm are mandatory for the étendue of the optical system and to avoid too many blue-shift from the center to the edge of the field-of-view due to high incidence angles of the marginal rays (maximum tolerated shift of three FWHM with an angle of 0.31 degrees). The interference pre-filter are not larger than 70 mm of diameter due to modern optical coating challanges. The off-axis parabolic mirrors are chosen to avoid the chromatic aberration of achromatic doublets in the infrared region.
The *Principal Optical Path* is showed in Fig. 3.24. The confocal off-axis parabolic mirrors M1, M2, M3, M4, M5, M6 and M6 are in Gregorian configuration, and the last convex parabolic mirror M8 is in a Galileian configuration. I1 is the common focal plane for M1 and M2, and the same is I2 for M3 and M4 and I3 for M5 and M6. P1 is the pupil image (200 mm diameter) of the primary mirror (4 m diameter) of the ATST telescope and it is not obscured thanks to the off-axis gregorian optical scheme of ATST. In the pupil image P2 the first Fabry-Perot FP1 is placed. Then a pupil adapter made with the two smaller off-axis parabolic mirrors M4 and M5 is realized to create another pupil image P3 of the interference pre-filter IF1. In the pupil image P4 the second Fabry-Perot FP2 is placed. After M8, an air-spaced doublet is used to reduce the Petzval field curvature introduced by the off-axis parabolic mirrors and to create the image ($\sim$ 50 mm diameter) on CCD1. According to the simulation performed with Code V by Greco and Cavallini (Greco and Cavallini, 2013), all the other aberrations of the CCD1 image plane are null and the sistem is diffraction limited.
The *Secondary Optical Path* are used for the instrument calibration. The *Reference Path* is used to obtain broad-band images of the same field-of-view of the spectro-polarimeter in a nearby spectral region using the transmitted light through M1. This images are useful for the post-facto image rconstruction. The *Orthogonality Path* is used for the collimation of the two FPIs with respect to the solar beam using removable pellicle beam splitter and additional CCD cameras. The *Parallelism Path* is used to verify the parallelism of the FPIs' optical plates

using He-Ne Laser and optical fibers inserted in I2 and I3. The *Tuning Path* for the spectral calibration is realized with an halogen lamp and an optical fiber placed in I1. For further details see (Greco and Cavallini, 2013).

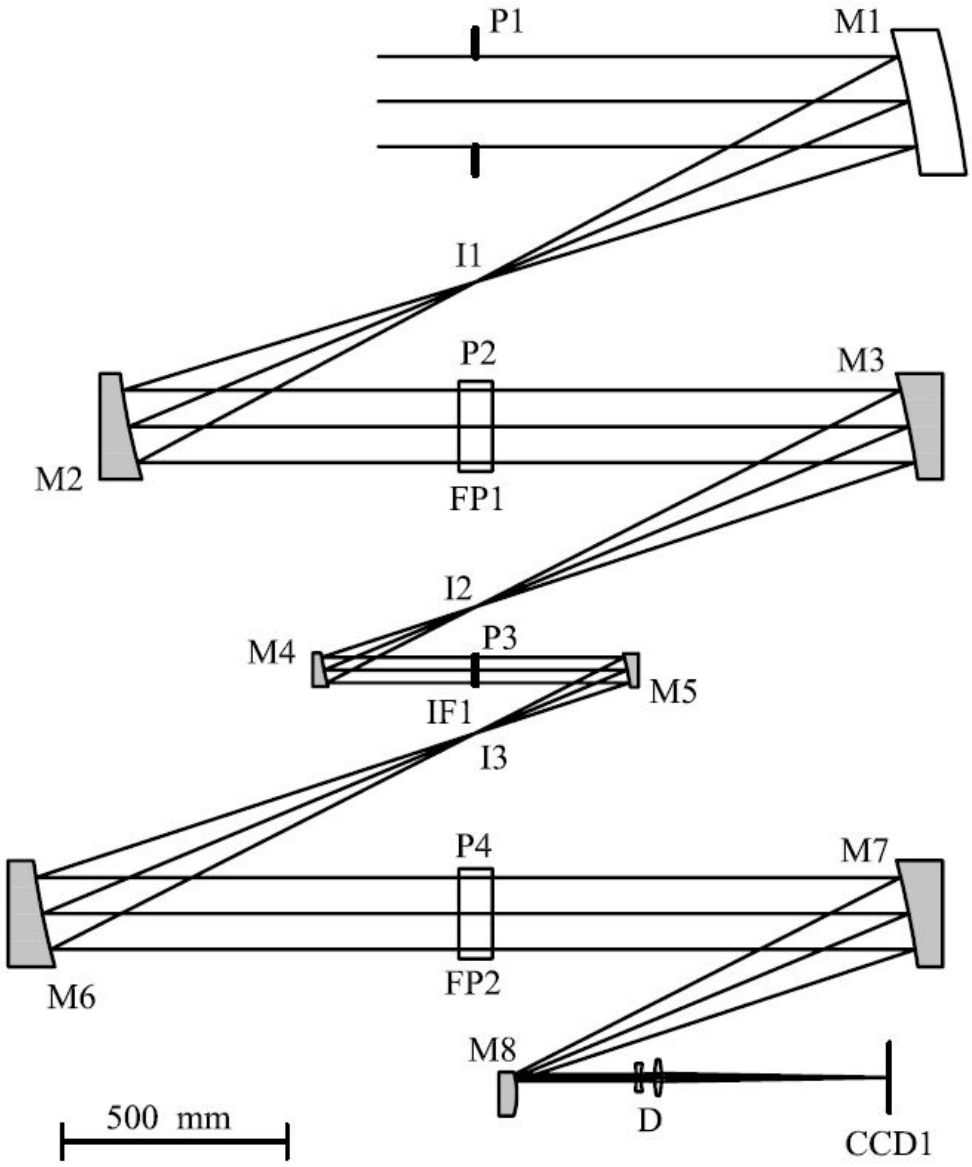

Figure 3.24: Optical scheme proposed by Greco and Cavallini (Greco and Cavallini, 2013) for the imaging spectro-polarimeter for ATST based on two large diameter FPIs. M1 is a partially reflecting off-axis parabolic mirror. M2, M3, M4, M5, M6 and M7 are off-axis parabolic mirrors. M8 is a convex parabolic mirror. D is an imaging air-spaced doublet. P1, P2, P3 and P4 are pupil image. I1, I2 and I3 are focal plane. FP1 and FP2 are the Fabry-Perot interfeometers and IF1 is the filter wheel with the interference pre-filters.

3.4.2 Optimization and implementation for an optical 3D configuration

The optical scheme of Greco and Cavallini is excellent because it is diffraction limited and it satisfies all the requirements. Its trouble is the encumbrance, approximately 2.5×4×0.7 meters, due to the large optical elements and the long optical paths, needed for the proper operation of the instrument. For this reason, I decided to explore a new possible alternative version of this optical scheme for an imaging spectro-polarimeter based on two large diameter FPIs. The aim of this new optical version of the instruments is to reduce its encumbrance by exploiting a 3D optical design instead of a 2D-plano optical design.
First of all, I reproduce the optical scheme of Greco and Cavallini with Zemax. Thus I explore various 3D optical configuration. Here I present the version that I retain the most functional. I decided to rise up to different planes the mirror M1, the couple M4-M5 (with the interference pre-filter) and the mirror M8 with the following doublet D and the CCD camera by illuminating different sectors of the generating parabola of the off-axis parabolic mirrors. During the implementation of this choice, I also simulated the dimensions of the thermostated boxes for the FPIs in order to avoid the ray cutting. In Fig. 3.25, Fig. 3.26 and Fig. 3.27 are reported respectively the upper, the inclined and the lateral view of the new proposed optical scheme version. In Fig. 3.28 I report the spot diagrams at the center and at the edge of the 90 arcsec FoV of the instrument: all the rays are inside the Airy disk, so the new proposed version continue to remain diffraction limited. In addition, this new optical configuration is also polarimetric compensated because the off-axis parabolic mirrors are coupled to each other (M2-M3, M4-5 and M6-M7) and the generating parabolas of the off-axis coupled mirrors are illuminated in opposite sectors. This new version reduce radically the encumbrances to 2.3×2.5×0.8 meters, so that this optical scheme could be mounted on standard optical tables. The three-dimensional angle between the couples M1-M2 and M3-M4, M3-M4 and M5-M6, M5-M6 and M7-M8 (clearly visible in Fig. 3.27) is set to 90 degrees and it can not be decreased anymore (reducing even more the dimension of the instrument), otherwise the instrument would not be polarization-free.

3.4.3 The tolerance problem

During the analysis both of the original and the new version of the optical scheme of Greco and Cavallini, I have noticed some critical issues. The optical quality of the instrument is very sensitive to tolerance and collimation problems. It is well known that off-axis parabolic mirrors are very difficult to align and collimate, especially a little tilt or decentering of this kind of mirror leads to the onset of severe astigmatism and other aberrations. Performing the Tolerance Analysis with Zemax, I have noticed that tilts, decentering and focussing discrepancies of the order of 0.1 mm can affect dramatically the performance of the instrument. This discrepancies on the radius of curvature of the off-axis parabolic mirrors due to manufacturing errors (polishing or Laser ablation) or mounting errors (tilt, decentering, collimation, thermal dilatation, etc.) are reasonable in an instrument with this long optical paths. The tolerance analysis showed that the radius of curvature of all the mirrors, their decentering and all their distance (except for the distance M2-M3) are quite critical. The worse contributors to the image degradation are the tilts of M1, M2, M3, M4, M6 and M7.
To show the instrument sensitivity to the tolerance issues, I report here two examples of spot diagrams obtained with Zemax. In Fig. 3.29 I report the spot diagrams at the center and at the edge of the 90 arcsec FoV obtained increasing only the dinstance between M3 and M4 of 0.1 mm: the spot in the image plane increases its dimension to 75 μm and to 84 μm at the

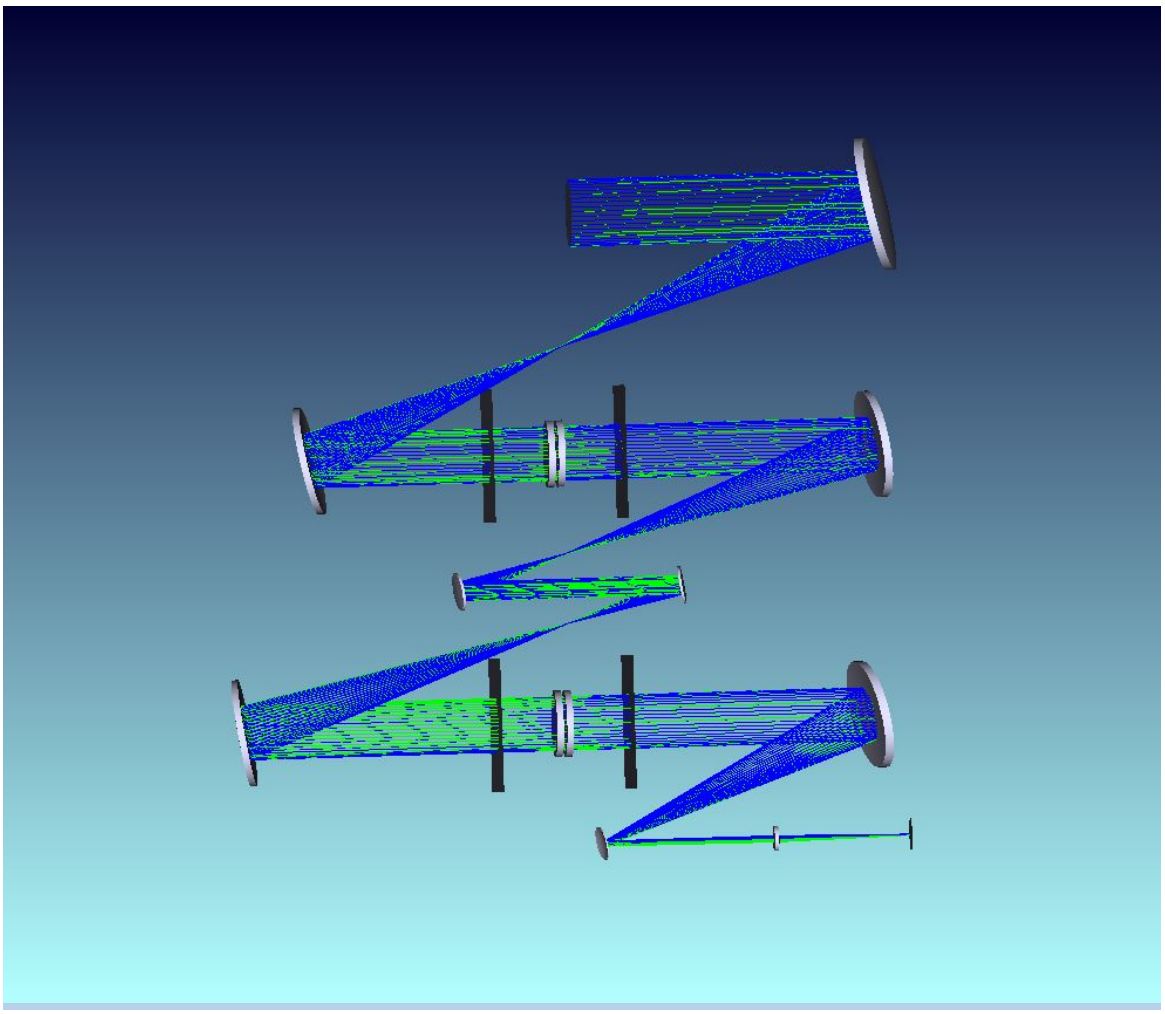

Figure 3.25: Upper view of the new proposed version of the optical scheme for the imaging spectro-polarimeter based on two large diameter FPIs and off-axis parabolic mirrors.

center and at the edge of the FoV, respectively. In Fig. 3.30 I report the spot diagrams at the center and at the edge of the 90 arcsec FoV obtained increasing the radius of curvature of M1 of 0.1mm: the spot in the image plane increases its dimension to 42 μm and to 50 μm at the center and at the edge of the FoV, respectively. In both cases the instruments is no longer diffraction limited because the rays goes outside the Airy disk (38 μm of diameter). If this were just a focus problem, the use of a focus recovery system could be considered.

3.4.4 Ways to solve the tolerance problem and future developments

There could be different ways to solve the tolerance problem explained before. One possible solution could be to use off-axis parabolic mirrors with less off-axis distance, in order to reduce the astigmatism; this solution should be carefully studied from an opto-mechanical point of view because the light beams will be closer to each other. Another possible solution could be the usage of off-axis parabolic mirrors with longer focal length, easier and less critical to manufacture, but this solution will not resolve the encumbrances problem of the original idea of Greco and Cavallini due to the longer optical paths dictated by the longer focal lengths. Another yet solution could be to use off-axis Maksutov cameras (made by spherical mirrors

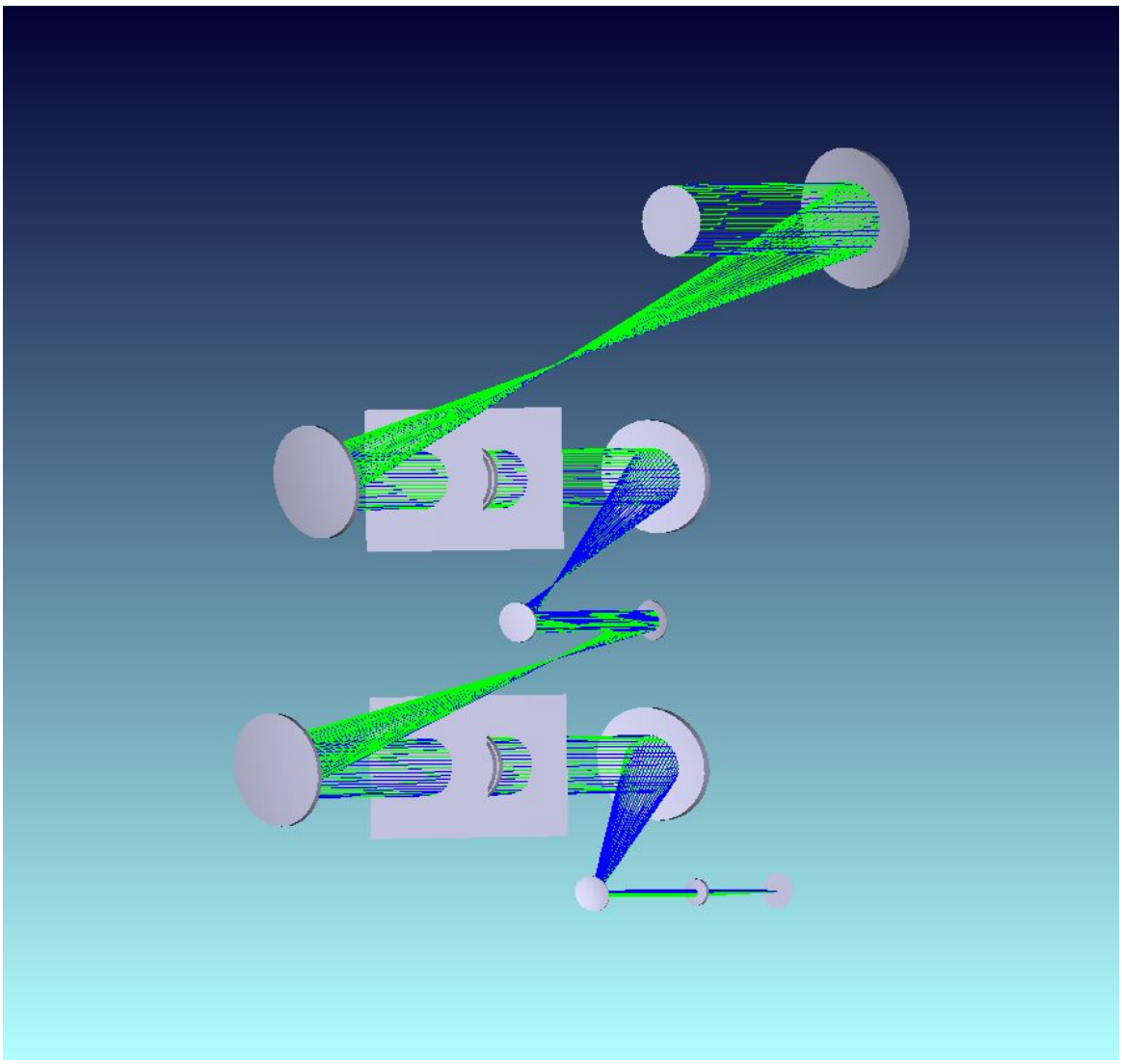

Figure 3.26: Inclined view of the new proposed version of the optical scheme for the imaging spectro-polarimeter based on two large diameter FPIs and off-axis parabolic mirrors. The dummy square optical surfaces stands for the thermostated box for the FPIs.

and meniscus corrective lens) because they are less sensitive to collimation problem and they are free from astigmatism and present few chromatic aberration. If one wanted to follow this last path, then it would be more appropriate to return back to the current optical design of instruments based on two FPIs with four large diameter achromatic doublets instead of off-axis parabolic mirrors due to noticeable realization troubles.
Regarding the future, EST will host four post-focus instruments based on FPIs and such optical studies are becoming increasingly important. This work is framed in the preliminary studies carried on by the Solar Physics Group of the University of Rome Tor Vergata as leader of the working package for the science cases, optical scheme and feasibility study of one of the post-focus instruments for EST. The target of this kind of instrument is to achieve the technical requirements set by Greco and Cavallini: high spatial, spectral and temporal resolution, large field-of-view, large wavelength range and low instrumental polarization, which are mandatory to study the dynamics and the thermodynamics of the solar turbulent convection and the physical processes involved in the magnetic coupling of the solar atmosphere.

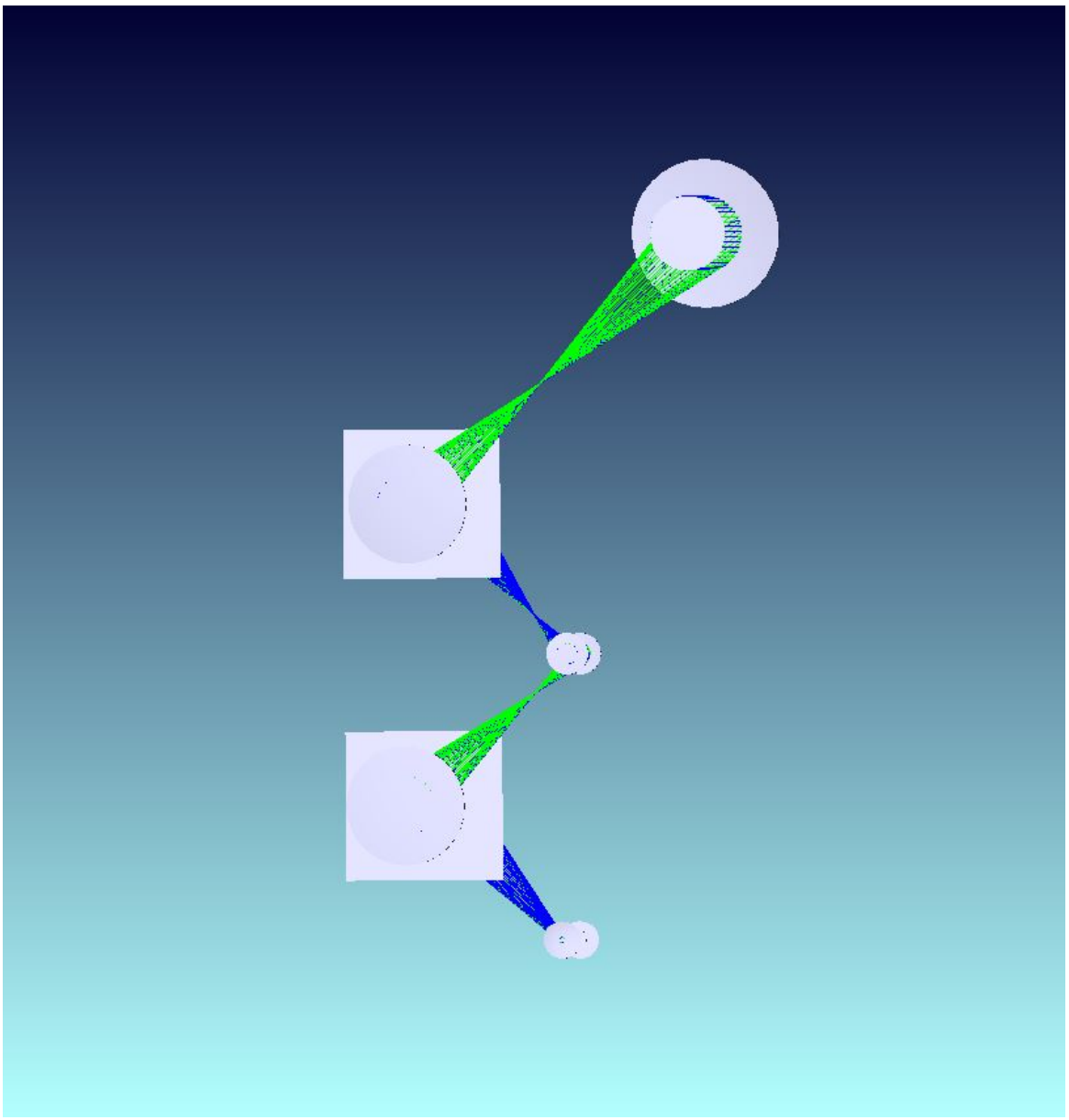

Figure 3.27: Lateral view of the new proposed version of the optical scheme for the imaging spectro-polarimeter based on two large diameter FPIs and off-axis parabolic mirrors. The dummy square optical surfaces stands for the thermostated box for the FPIs.

3.5 Optical design and realization of a MOF telescope

The study of the physical processes occurring on the larger scale of the solar convection, the mesogranulation and the supergranulation, needs solar telescopes with large FoV, i.e. full-disk ($\geq$ 32 arcmin) or large portion of the solar disk ($\geq$ 10 arcmin). The FPIs can not use properly with high spectral resolution for solar full disk imaging due to the large angle subtend by the solar disk, which causes a worsening of the effective finesse. For this reason, telescope based on Magneto-Optical Filters (MOFs) are preferred for high spectral resolution solar full disk imaging. The optical design of such telescope is quite critical due to the large FoV and the aberration control on the image plane. In addition, full disk telescopes are planned to be used for complementary observations with EST or DKIST, which will provide high resolution observations with small FoV. In this section, we show the theory of the MOF and we present the

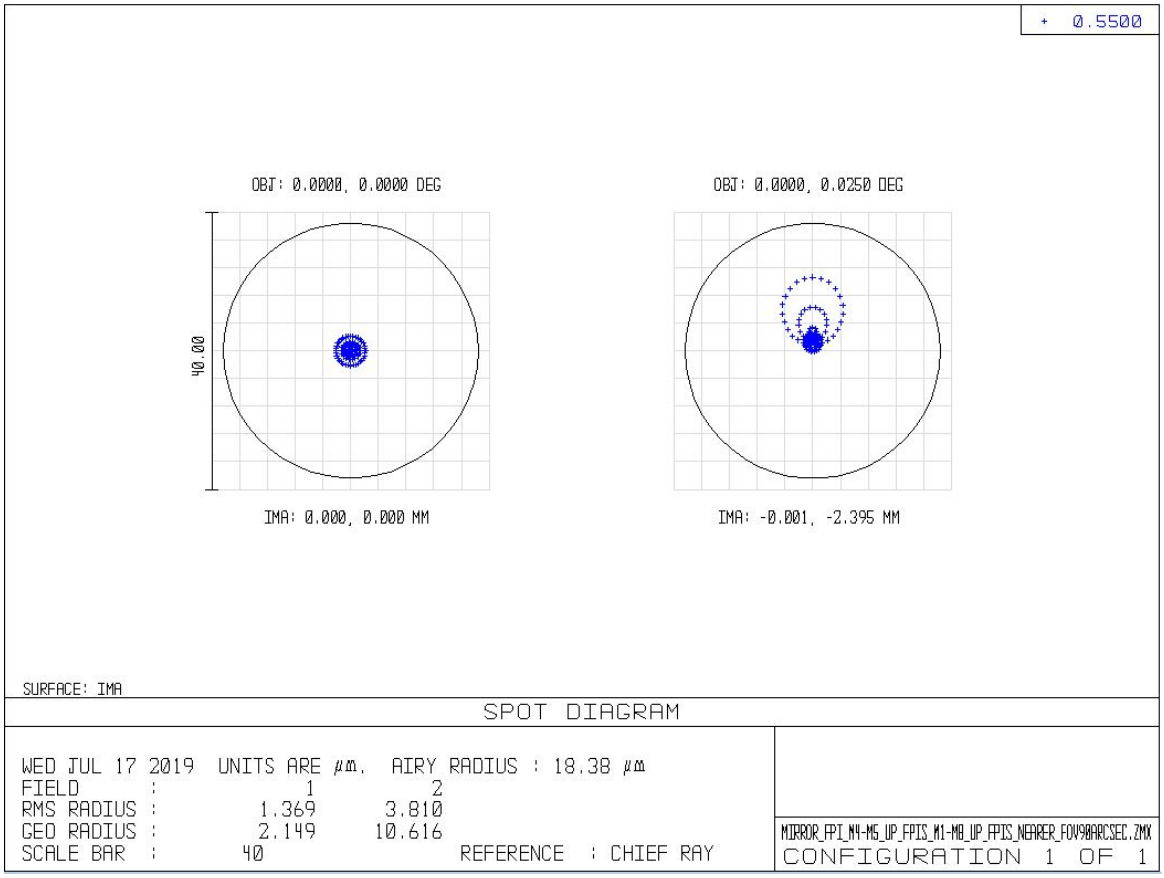

Figure 3.28: Spot diagrams at the center and at the edge of a 90 arcsec FoV of the new proposed version of the optical scheme for the imaging spectro-polarimeter based on two large diameter FPIs and off-axis parabolic mirrors. Black circles stand for the Airy disk.

optical scheme of the *Tor vergata Solar Synoptic Telescope* (TSST) that we realize using Zemax.

3.5.1 The Tor vergata Solar Synoptic Telescope (TSST): Halpha and MOF

The *Tor vergata Solar Synoptic Telescope* (TSST) is being realized in the Solar Physics Laboratory of the University of Rome Tor Vergata and it has been funded by the *Progetti di Rilevante Interesse Nazionale* (PRIN) of the *Ministero dell'Istruzione, dell'Università e della Ricerca* (MIUR) of Italy.
The TSST is principally devoted to Space Weather studies (flare, flare forecasting, and so on) using Hα images, magnetograms and dopplergrams. Thanks to its wide FoV, it can be used fruitfully to study the solar convection on large spatial scale and the acoustic and gravity waves of the solar surface (helioseismology).
The TSST is composed by two telescopes operating with two different narrow-band filters mounted on an EQ8 PRO Synscan equatorial mount http://skywatcher.com/product/eq8-synscan/ by Sky-Watcher (load capacity 50 kg). The two optical tube telescopes are mounted on the EQ8 mount using a Losmandy bar.
The Hα telescope is the DayStar SR-127 (Fig. 3.31) http://www.daystarfilters.com/SR127/SR127.shtml produced by Daystar Filters. The Daystar SR-127 telescope uses a FPI to select the Hα spectral line (produced by the transition between the second and the third

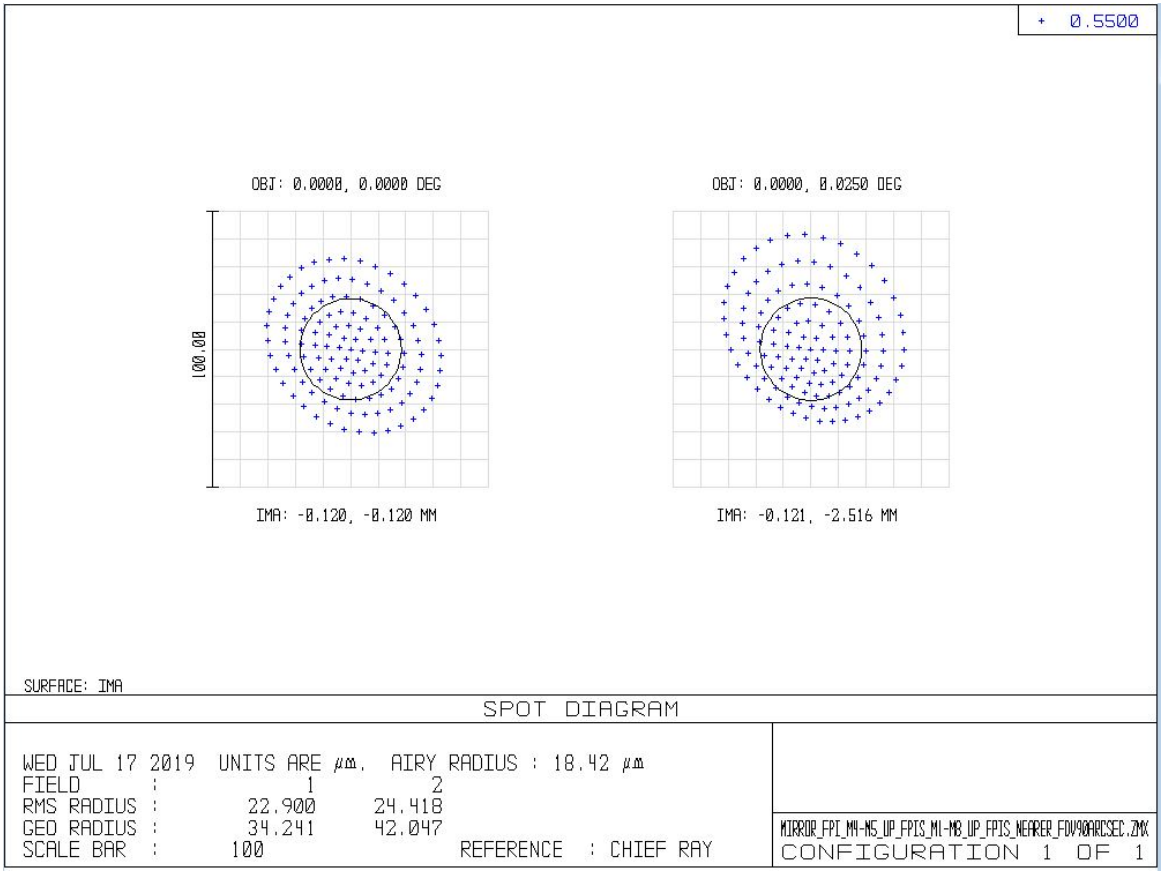

Figure 3.29: Spot diagrams at the center and at the edge of the 90 arcsec FoV in the new proposed version of the optical scheme increasing the distance between M3 and M4 of 0.1 mm. The instrument is no longer diffraction limited because the rays goes outside the Airy disk.

quantic level of the hydrogen atoms) from the solar spectrum. The objective of the SR-127 telescope is an achromatic doublet with a diameter of 127 mm and a focal lengh of 1000 mm approximately. An internal optical system based on a 4X telecentric Barlow lens is used to reach the effective focal lenght of 4064 mm, producing an image of the solar disk of 38.5 mm. In the collimated part of the light beam, the temperature-stabilized FPI is placed, so that it works in classical mount. The bandpass of the Hα telescope is 0.04 nm. We have chosen this telescope amoung others, i.e. Coronado or Lunt, because its FPI works in a collimated beam and not in a converging beam, ensuring better spectral cleaning and behaviour. We want to use the Daystar SR-127 with the Daystar 0.33X focal reducer http://www.icstars.com/Store/daystar/imaging-focal-reducer.html in order to have an image of the solar disk of 12.7 mm. This focal reducer is made by two identical crown-facing achromatic doublets used to reduce the focal length of a factor 0.5X. Inserting a spacing of 20 mm between the focal reducer and the camera, the reducing factor becomes 0.33X (1341 mm of effective focal length). The aberration control of the focal reducer is guaranteed by the use of two identical achromatic doublets; in fact one doublet erases the aberrations introduced by the other.

The MOF telescope is based on Magneto-Optical Filters (MOFs) (Agnelli et al., 1975; Cimino et al., 1968) and it is designed to obtain dopplergrams and magnetograms of the entire solar disk (Cacciani and Fofi, 1978; Cacciani et al., 1990; Cacciani and Moretti, 1994; Cacciani et al., 1997, 1994). We design the entire optical scheme of the the MOF telescope using Zemax. The objective of the MOF telescope is a *Spindler & Hoyer* achromatic lens with a diameter of 80

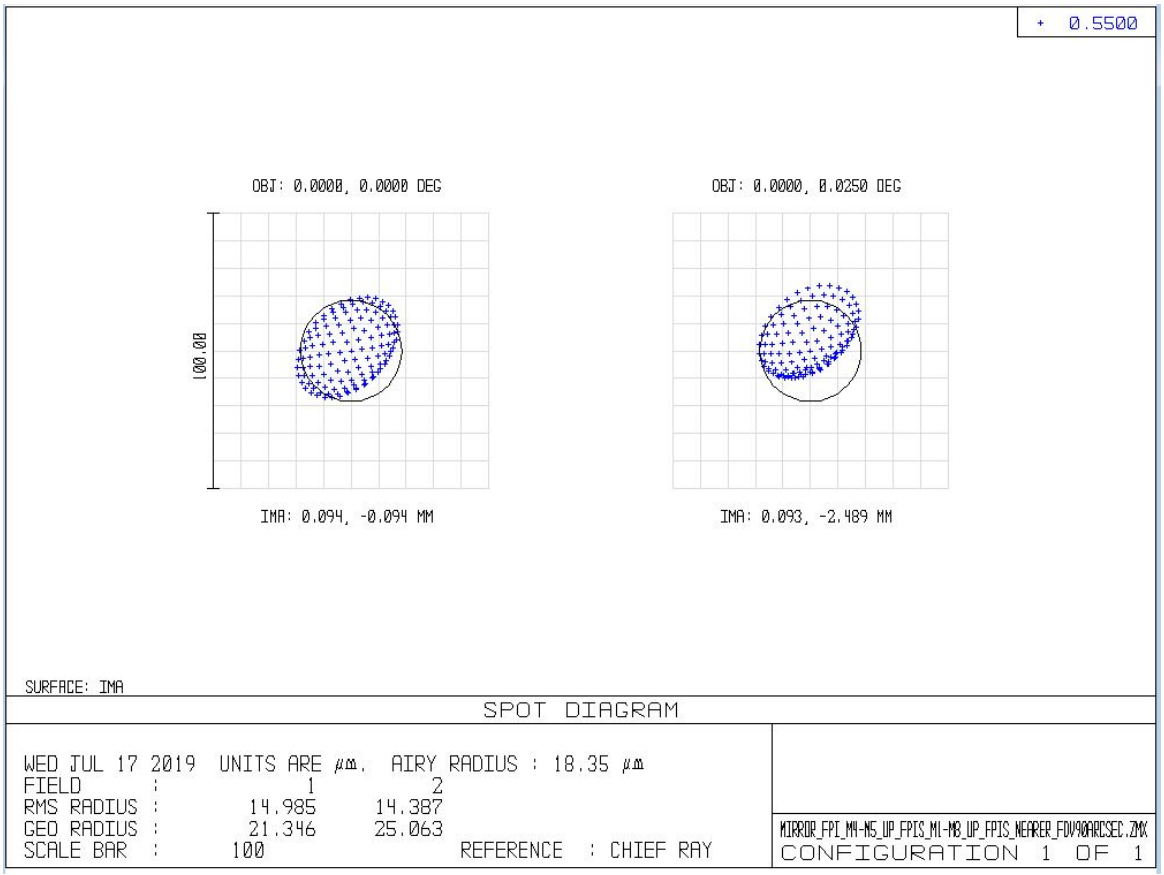

Figure 3.30: Spot diagrams at the center and at the edge of the 90 arcsec FoV in the new proposed version of the optical scheme increasing the radius of curvature of M1 of 0.1 mm. The instrument is no longer diffraction limited because the rays goes outside the Airy disk.

mm and a focal length of 1185 mm. The effective focal length of the MOF telescope is 963 mm, in order to have images with approximately the same diameter of ones obtained from the Hα telescope. The MOF telescope used a combination of the Zeeman effect and the Macaluso-Corbino effect (Macaluso and Corbino, 1898; Macaluso et al., 1899b,a) to select two pics on the wing of the Potassium K D1 spectral line at 769.9 nm, which is formed approximately at $300 \div 400$ km above the base of the solar photosphere.
The two CMOS cameras that we plan to use in the first preliminary phase are the Dalsa Pantera 1M60 https://www.stemmer-imaging.com/media/uploads/websites/documents/products/cameras/DALSA/en-Teledyne-DALSA-Pantera-1M60-KTEDA52-201210.pdf. The sensor has 1024×1024 pixels of 12 μm of dimensions, therefore the sensor dimensions are 12.29×12.29 mm. The Quantum Efficiency is around 50% for both Hα spetral line at 656.3 nm and Potassium K D1 spectral line at 769.9 nm. The pixel scale for the Hα telescope is 1.8 arcsec/pixel and for the MOF telescope is 2.6 arcsec/pixel.

3.5.2 The MOF theory

A MOF is a filter based on resonant scattering and it consists in a glass cylindrical cell filled with a vapour of an alkaline metal placed inside an high longitudinal magnetic field and placed between two crossed linear polarizer (P1 and P2) (Cacciani et al., 1994).
The cell is made with a cylindrical glass tube and in the extremities two plano-parallel and flat

Figure 3.31: Hα solar telescope Daystar SR-127.

optical window ($\lambda/4$ optical quality) are settled. On the lateral surface of the cylindrical cell, two wells are filled with Potassium, which are heated by two Ni-Cr wires, thus generating a Potassium vapor inside the cell. The entire volume of the cell is filled with Argon gas in order to avoid the Potassium condensation on the two optical windows.
The magnetic field B, generated by rare earth magnets, causes the Zeeman splitting of the Potassium D1 spectral line at 769.9 nm. From the cell will emerge only the two σ_+ and σ_- components with right and left circular polarization, because the longitudinal magnetic field is oriented along the optical axis and the linear π components oscillates along the optical axis. Increasing and decreasing the magnetic field the distance of the two components can be varied. Inside the cell, another quantum effect happens: the Macaluso-Corbino effect (Macaluso and Corbino, 1898; Macaluso et al., 1899b,a), which causes the emergence of circular polarization on the wings of the two σ_+ and σ_- components, similar to the Faraday rotation effect, but it happens only in the spectral line wings. The Potassium vapour inside the cell and permeated by the magnetic field is practically a left circular polarizer in the σ_+ component and a right circular polarizer in the σ_- component. After the two crossed polarized P1 and P2 there should be no

light (except for the leakage of the polarizers), but, thanks to the Macaluso-Corbino effect, on the P2 polarizer will arrive circular polarized light in correspondence of σ_+ and σ_-, and so two peaks of transmission on the external wings of the Zeeman splitted lines will appear. Then, in our case, the transmission profile of the MOF is made by two peaks placed on the wings of the Potassium K D1 spectral line at 769.9 nm, as shown in Fig. 3.32. Varying the density of the Potassium vapour inside the cell, and so the temperature of the heating in the two wells, the amplitude of the two Macaluso-Corbino peaks can be varied.
A MOF-based telescope can be used in Solar Physics to obtain dopplergrams (D) and magnetograms (M) by measuring both polarization states (+ and −) in the red (R) and blue (B) wings of a solar absorption spectral line, using the following relations:

$$D = \frac{R^+ - B^+}{R^+ + B^+} + \frac{R^- - B^-}{R^- + B^-} \tag{3.26}$$

$$M = \frac{R^+ - B^+}{R^+ + B^+} - \frac{R^- - B^-}{R^- + B^-} \tag{3.27}$$

The two peaks of the Macaluso-Corbino effect must be separated to measure the signals alternatively in the two wings of the Potassium spectral line. To perform this spectral separation, two cells filled with Potassium vapour are needed: the first cell is the MOF and the second cell is called Wing Selector (WS). The WS has the task of selecting one of the two transmission peaks using a quarter wave plate with the axis at 45° with respect to the axis of P2, so that the WS cell can absorb the radiation at only one of the Zeeman lines, letting the radiation pass at the other Zeeman line. The magnetic field of the WS cell must be higher than the MOF cell because its Zeeman lines must be superimposed to the transmission peaks of the Macaluso-Corbino effect of the MOF cell. Tuning the magnetic field and the heating temperature of the wells of the WS cell, and rotating alternatively the axis of the quarter wave plate at ±45° with respect to the P2 axis, it is possible to select one of the two peaks of the Macaluso-Corbino effect, obtaining a spectral sampling on the red and blue wings of the Potassium spectral line.

3.5.3 Optical design of MOF telescope

The polarimetric scheme of the TSST MOF telescope is similar to the one of the Velocity And Magnetic Observations of the Sun (VAMOS) telescope (Oliviero et al., 1998b,a,c; Severino et al., 2001; Vogt et al., 1999; Oliviero et al., 2002), located at the Observatory of Capodimonte in Naples.
I describe the polarimetric scheme of TSST MOF telescope, referring to Fig. 3.33. The axis of the first quarter wave plate is at 45° with respect to the axis of the first half wave plate, which is parallel to the axis of the P1 linear polarizer. Rotating the axis of the first half wave plate of 45°, so that it is at 0° and 45° with respect to P1, it is possible to select alternatively the two components of the left and right circolar polarization of the solar light. In fact the quarter wave plate separates these two components polarizing them linearly along two symmetrical direction with respect to the quarter wave plate and forming between them an angle of 90°. The half wave plate directs the polarization axes of these two components parallel and perpendicular to the axis of P1, so that the two components pass alternatively through P1 and go inside the MOF cell. The axis of the linear polarizer P2 is perpendicular to the one of P1, the axis of the second half wave plate is parallel to the axis of P2 and the axis of the second quarter wave plate is at 45° with respect to the axis of the second half wave plate. Rotating the axis of the

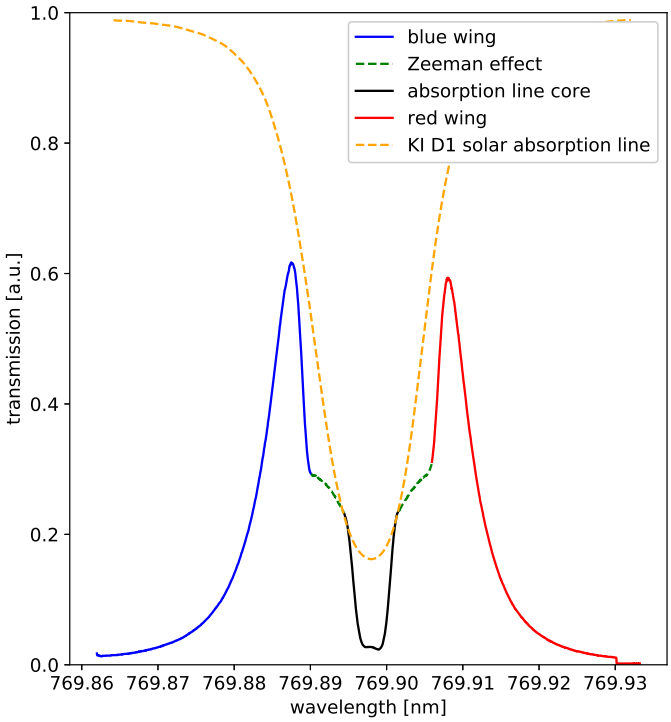

Figure 3.32: Spectral transmission of the MOF cell around the Potassium KI D1 spectral line at 769.9 nm. The blue and red wings are plotted respectively in blue and red. The Zeeman effect near the line core is plotted with green dashed lines. The line core is plotted in black. The reference Potassium KI D1 spectral line from atlas is plotted with yellow dashed line. Figure from (Calchetti et al., 2020).

second half wave plate similarly to the axis of the first half wave plate, the radiation coming from the MOF cell acquires alternatively left and right circular polarization, and thus the WS cell selects alternatively the two transmission peaks of the MOF cell.

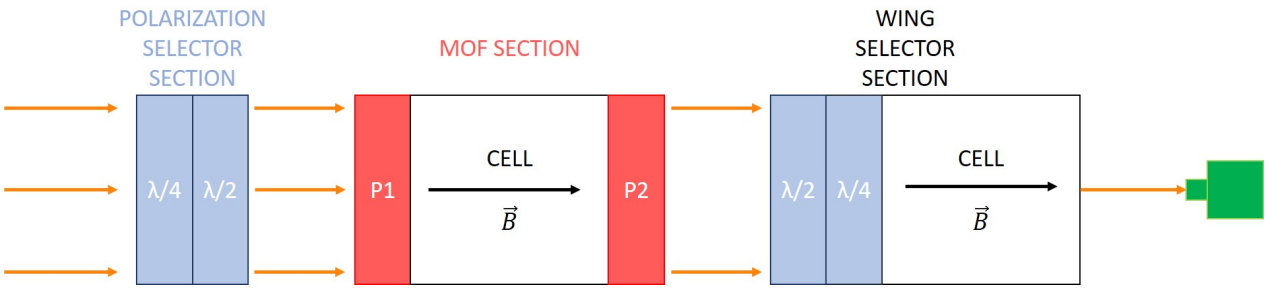

Figure 3.33: Polarimetric scheme of the TSST MOF telescope. Figure from (Calchetti et al., 2020).

I designed the entire optical scheme of the MOF telescope using Zemax software. The optical scheme has been implemented in order to satisfy the following requirements:

- Entrance pupil diameter of 80 mm, in order to have an angular resolution on the solar photosphere of 2 arcsec approximately;
- Large FoV (half-diameter 0.27 degrees) in order to perform full disk imaging;

- Collimated beam inside the MOF and the WS cells, in order to avoid the internal vapour seeing;
- Collimated beam in the polarimetric optics (half wave plates, quarter wave plates and polarizers), in order to have better spectral response;
- Corrective lenses near the final focal plane, to ensure an aberration free image;
- Compact scheme to reduce dimensions and weights for the EQ8 SynScan equatorial mount.

The overall view of the optical scheme is shown in Fig. 3.34. The objective lens L1 is a a *Spindler & Hoyer* with a diameter of 80mm and a focal length of 1185mm. In the converging beam after L1, three pre-filters are placed: an IR cut filter (> 825 nm), a UV cut filter (< 700 nm), and a wide Potassium filter (41 nm bandwidth centered at 769 nm). This three prefilter are used to reject the unwanted and useless solar radiation and to avoid the Intensity Effect in MOF cell (Oliviero et al., 2011). The latter effect leads to the saturation of the Potassium atoms of the vapour inside the MOF cell, modifying the spectral behaviour of the vapour due to the decrease of the optical depth. L2, L3, L4 and L5 are achromatic doublets (diameter 50.8 mm, focal length 200 mm, anti-reflection coating from 650 nm to 1050 nm), equal to each other and oriented to realize a double-keplerian telescope with an imaging lens. M1 and M2 are two equal flat mirrors (diameter 50.8 mm, optimized for near-infrared). L2 is placed after the image produced by L1 and it is used to collimate the solar beam for the first polarimetric block and the MOF cell. M1 is used to turn the optical path, reducting the linear dimension of the telescope. After M1, an interference filter (IF) centered in the Potassium line is placed (2 nm bandwidth) to reduce the ghosts and the spurious images produced by the optical system. Still in the collimated part, the quarter wave plate (QWP), the half wave plate (HWP), the linear polarizer P1, the MOF cell and the linear polarizer P2 (equal to P1) are placed. M2 is used to turn again the optical beam towards L3, which creates a second focal plane. Simmetrically to this second focal plane with respect to L3, L4 is placed to collimate again the optical beam for the second polarimetric block of the optical system. P3 is used to cancel the spurious polarization signal that could be induced by M2. Then the HWP, the QWP and the WS cell are placed. The last doublet L5 is used as imaging lens. In order to correct the focal plane aberrations, especially field curvature and distortion due to the high focal ratio of the achromatic doublets, two corrective lens (CL) are placed: a bi-convex N-BK7 lens with a focal length of 75 mm and a plano-concave N-BK7 lens with a focal length of -75 mm. The distance betwen the two corrective lens, their distance from L5 and their distance from the final focal plane has been optimized with Zemax in order to obtain the best possible image.
The spot diagrams in the image focal plane of the MOF TSST telescope at the center and at the edge (0.27 degrees) of the FoV are shown in Fig. 3.35. The Airy disk is plotted as a black circle. The image is far diffraction limited at the center of the FoV and near diffraction limited at the edge of the FoV. The rays going slightly outside the Airy disk at the edge of the FoV will not causes appreciably image degradation because the will smear by the typical diurnal seeing (1-2 arcsec) and they are below the image pixel scale with the Dalsa Pantera 1M60 CMOS camera.
The Ray fan plot (rays position in the image plane with respect to the ones in the pupil plane) in the image focal plane of the MOF TSST telescope at the center and at the edge (0.27 degrees) of the FoV are shown in Fig. 3.36. There is a residual spherical aberration and even less distortion at the center of the FoV, but the spot is entirely inside the Airy disk, then this two aberration are not visible in the image focal plane. There is a residual of distorion and

even less spherical aberration and field curvature at the edge of the FoV, but they will not be appreciable in the image focal plane due to the diurnal seeing and the image pixel scale as told before.
We can therefore assert that with good approximation the MOF TSST telescope is diffraction limited and that it works in optimal conditions for solar diurnal obasevations.
The tolerance analysis performed with Zemax has allowed us to extimate that misalignments and tilts of 0.2 mm and 1 degrees, respectively, will not affect the performance of the instrument, which will remain diffraction limited.

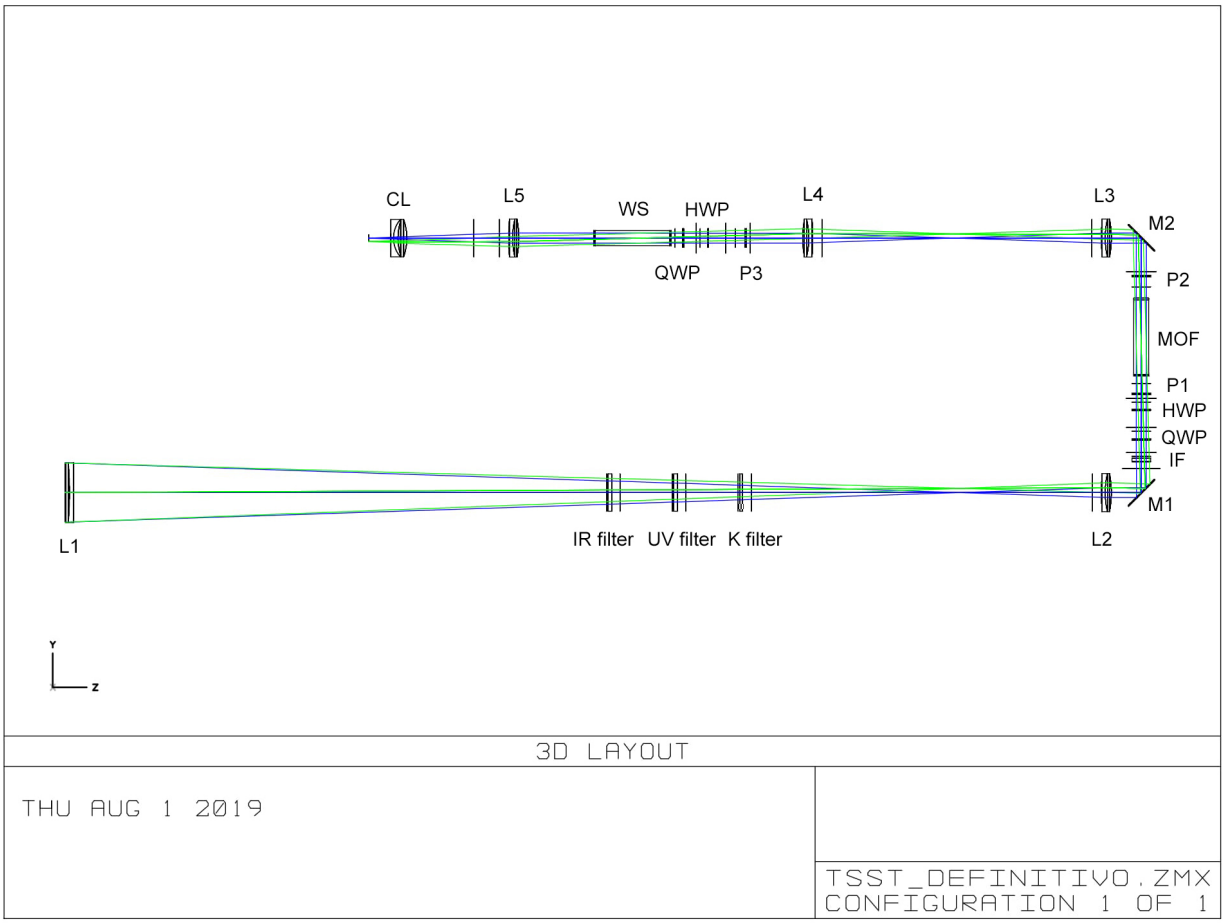

Figure 3.34: Optical scheme of the MOF TSST telescope. L1, L2, L3, L4 and L5 are achromatic doublet lens. M1 and M2 are flat mirrors. QWP and HWP are respectively quarter wave plates and half wave plates. P1, P2 and P3 are linear polarizer. CL is a group of corrective lens.

3.5.4 Mechanical Scheme and Assembly

I realized the mechanical scheme and the assembly of the holder for the MOF cell and for the WS cell, reported in the Appendix in Fig. 5.12 and in Fig. 5.13. They have been designed in order to keep the cells inside the longitudinal magnetic field generated by the magnets and

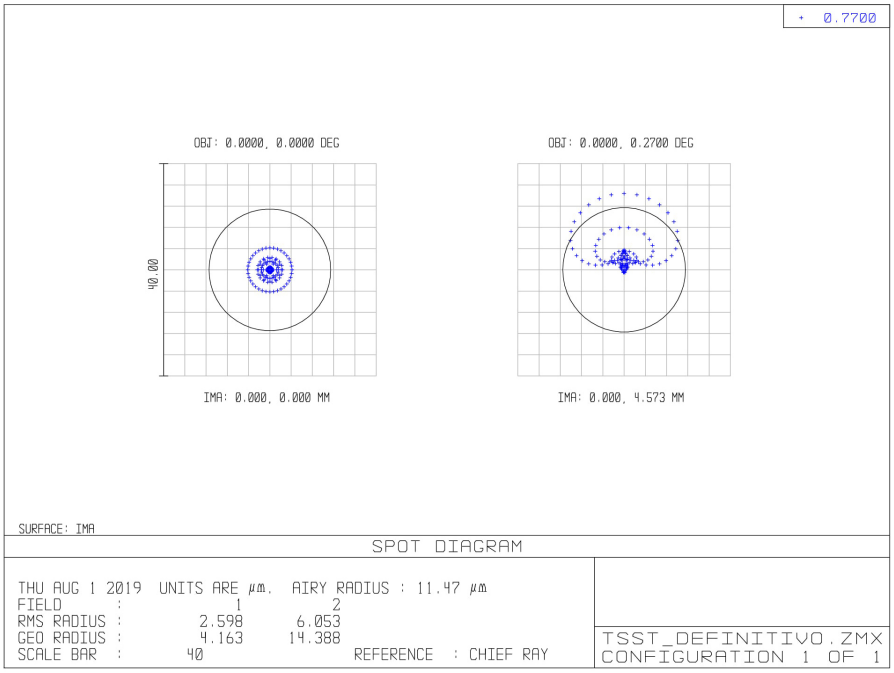

Figure 3.35: Spot diagrams in the image focal plane of the MOF TSST telescope at the center and at the edge (0.27 degrees) of the FoV. The airy disk is show with a black circle.

canalized by soft Iron cores. The two parts of the holder can be staved off and brought closer with aluminum shims in order to vary the longitudinal component of the magnetic field which insists on the cells. In Fig. 3.37 the MOF cell and its holder are shown.
In the Appendix, in Fig. 5.14 the L1 objective lens, in Fig. 5.15 one of the achromatic doublets (L2, L3, L4 and L5) mounted with the post-holder clamp platform, in Fig. 5.16 the plano-concave and the bi-convex lenses which made the corrective optics, in Fig.5.17 the quarter wave plate, the half wave plate and the linear polarizer, in Fig. 5.18 the rotating mount with the controller for the half wave plate, in Fig. 5.19 the mount of the quarter wave plate with micrometer and mount of the linear polarizer, are shown.
At the present time, the telescope is being assembled, aligned and collimated.

3.5.5 Calibration and tests

The first spectral calibration of the MOF and WS cells has been performed in the Solar Physics Laboratory of the Observatory of Capodimonte in Naples with M. Oliviero in order to characterize the bandpass of the instrument (Calchetti et al., 2020).
Previously, we have shown that the two effect involved in the physical processes inside the cell, the Zeeman effect and the Macaluso-Corbino effect, are strongly dependent on the magnetic field intensity and on the density on the vapour (so the heating temperature of the wells of the cells), respectively. The aim of this spectral calibration is to find the temperatures and the magnetic fields of the MOF and WS cells in order to ensure a proper operation of the filter for Solar Physics studies, as states in (Severino et al., 2007; Oliviero et al., 2010): the two peaks of the Macaluso-Corbino effect of the MOF cell must have a distance of approximately 0.02 nm

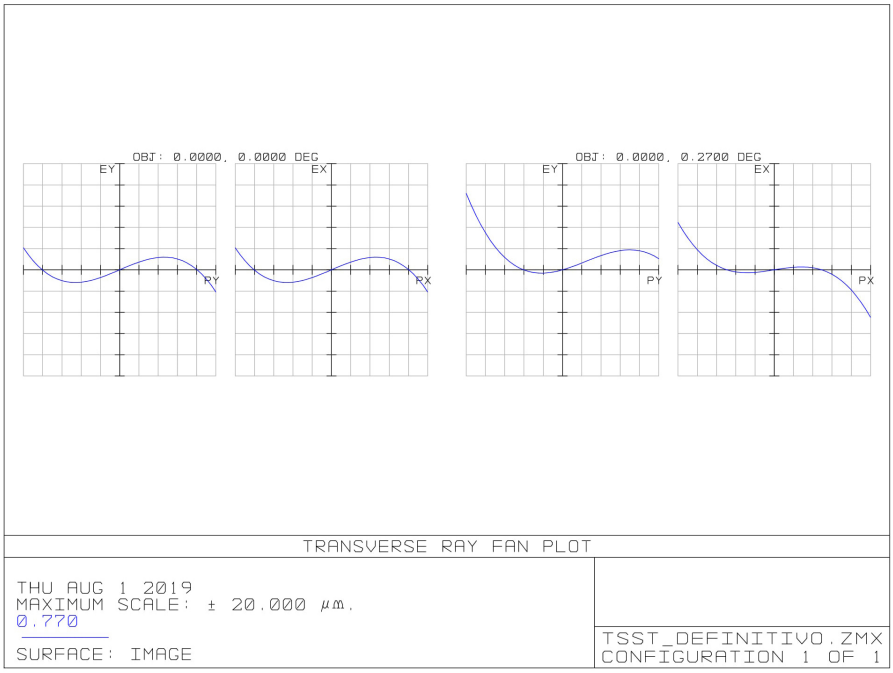

Figure 3.36: Ray fan plot in the image focal plane of the MOF TSST telescope at the center and at the edge (0.27 degrees) of the FoV.

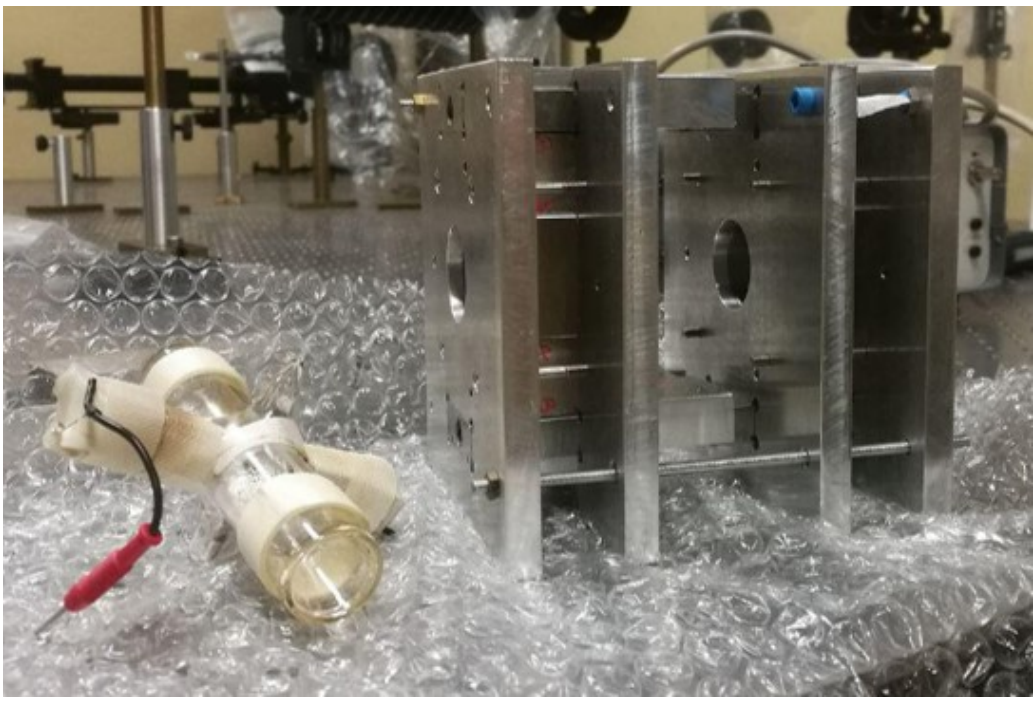

Figure 3.37: MOF cell with its holder.

and the WS passband must match the MOF one in order to select alternatively one of the two peaks in the red and blue wings.
Since the two peaks are nearly symmetrical, during this preliminar calibration phase, we have

focused our attention on the red wing passband using a tunable laser system (see Fig. 3.38) with a spectral step of 0.0396 pm in the spectral region containing the Potassium KI D1 spectral line.
For the spectral calibration of the MOF cell, we have used the following optical configuration: the laser beam is separated by a beam splitter, which sends the light to a reference photodiode and to the optical calibration path; the latter is constituted by two crossed linear polarizer and between then the MOF cell is interposed; then the light goes in the second photodiode.
For the spectral calibration of the WS cell, we have used the following optical path: the laser beam is separated by a beam splitter, which sends the light to a reference photodiode and to the optical calibration path; the latter is constituted by a linear polarizer, a quarter wave plate and the WS cell; then the light goes in the second photodiode.
We measured the longitudinal magnetic field inside the holder of the MOF and of the WS using a gaussmeter based on Hall effect. The magnetic field of the MOF cell has been set at 1230 Gauss and the magnetic field of the WS cell has been set at 2260 Gauss. In Fig. 3.39 (left panel) we show the spectral transmission of the MOF cell at different heating temperatures of the wells; the proper operation temperature is T = 225 °C in order to have a spectral distance between the two Macaluso-Corbino peaks equal to 0.02 nm and to have the absorption at the core of the spectral line due to the π polarization component of the Zeeman splitting. In Fig. 3.39 (right panel) we show the spectral transmission of the WS cell at different heating temperatures of the wells; the proper operation temperature is T = 181 °C in order to have complete absorption in the Macaluso-Corbino peak in the red wing of the MOF transmission profile. In Fig. 3.40 the spectral transmissione of both MOF and WS cells used together for different heating temperatures of the wells is shown. To reduce the spectral contamination in the sidelobes, the operation temperatures has been set at T = 241 °C and T = 183 °C for the MOF and the WS cells, respectively. We evaluated also a spurious signal in the sidelobes of about the 2.5%: this values will be of fundamental importance to compute the amount of cross-talk between the dopplergrams and the magnetograms.

3.5.6 Future perspectives

In this Chapter, I have presented the optical scheme of the MOF TSST telescope and the preliminary spectral calibration of the MOF and WS cells. This telescope will acquire maps of the velocity and the magnetic field in the solar photosphere, which are substantial for understanding the physical processes involved in the Space Weather events, in solar large scale convection, i.e. mesogranulation and supergranulation, and to study the large spatial scale behaviour of the velocity and the magnetic field on the solar photosphere.
At the present time the TSST is in assembly phase of the optical and polarimetrical components, as shown in Fig. 3.41. The future steps will be the optical alignment and collimation using laser, shear interferometer and reference optical thickness. Afterwards the spectral calibration phase should be repeated to characterize the MOF and WS cells transmission with the new and more stable thermal controller with the whole optical line mounted.
The first light of the TSST is planned in the second half of 2020 on the roof above the Solar Physics Laboratory of the University of Rome Tor Vergata. The joint observations of the TSST with VAMOS telescope in Naples will be used to create an archive of dopplergrams and magnetograms of the solar photosphere, which will be usefull for Space Weather applications. Future plans foresee the installation of the TSST in a remote dome in some Observatory of the Canary Islands, probably at the Roque de los Muchachos in La Palma.

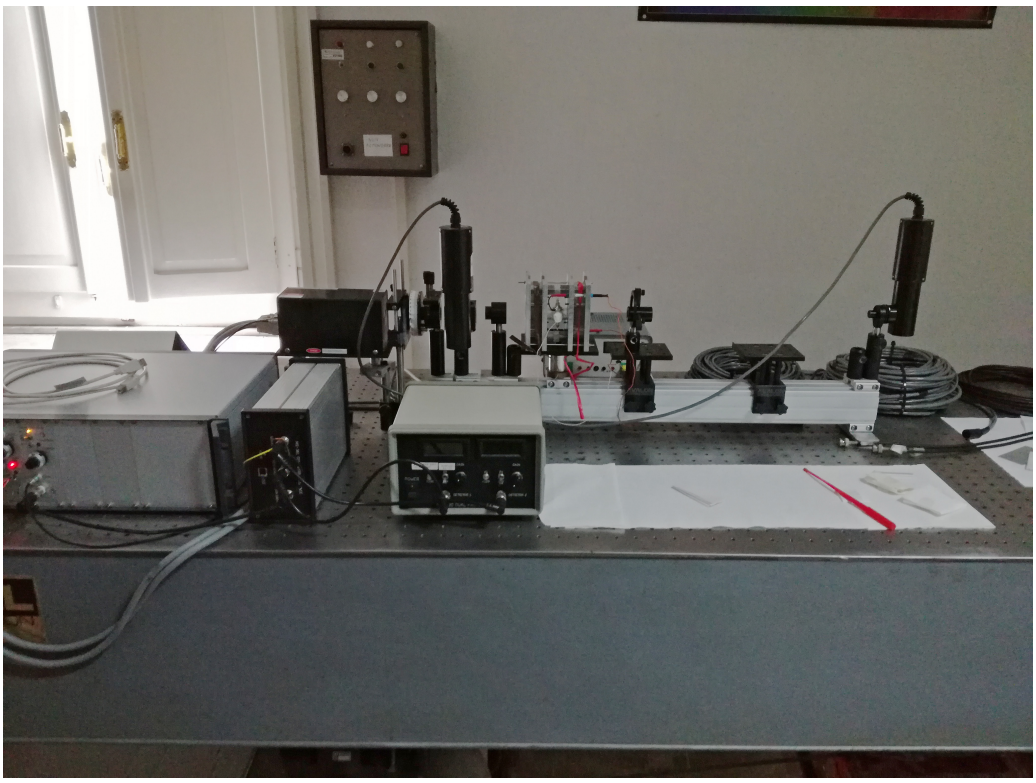

Figure 3.38: Tunable laser system of the Observatory of Capodimonte in Naples used for the preliminary spectral calibration of the MOF and the WS cells.

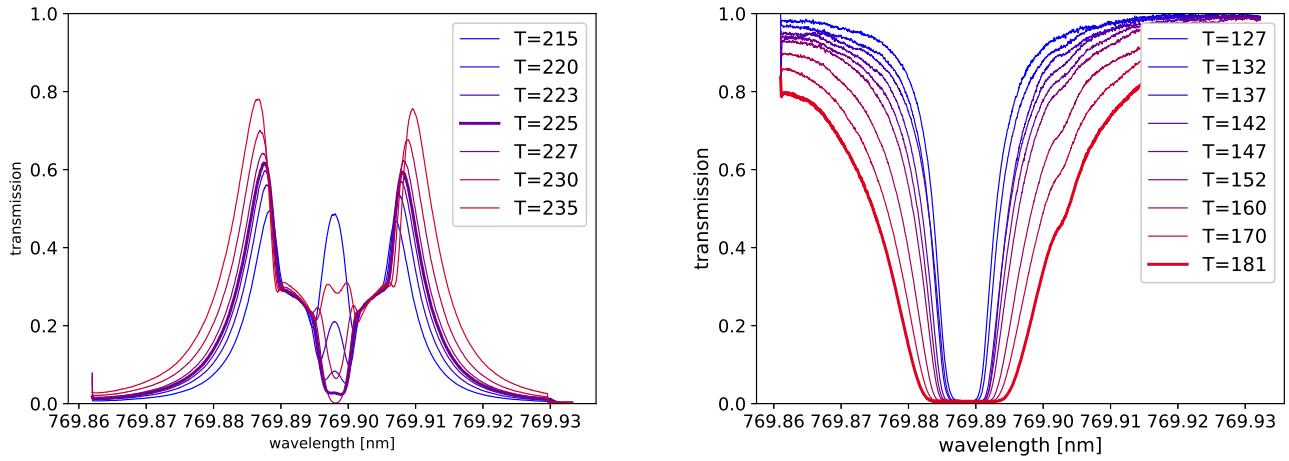

Figure 3.39: Left pane: spectral transmission of the MOF cell at different heating temperatures of the wells and with a magnetic field of 1230 Gauss. The proper operation temperature is T = 225 °C. Right panel: spectral transmission of the WS cell at different temperatures of the wells and with a magnetic field of 2260 Gauss. The proper operation temperature is T = 181 °C.

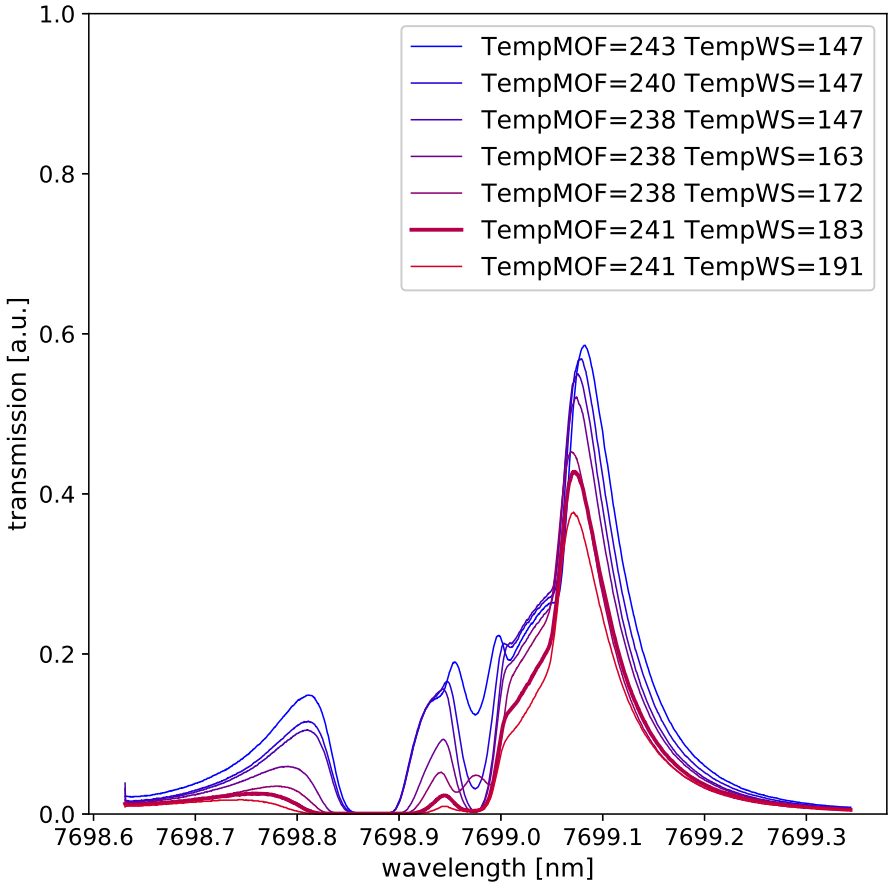

Figure 3.40: Transmission of the MOF and WS cells used together and different heating temperatures of the wells of both cells. To reduce the spectral contamination in the sidelobes, the operation temperatures has been set at T = 241 °C and T = 183 °C for the MOF and the WS cells, respectively. Figure from (Calchetti et al., 2020).

Figure 3.41: TSST MOF telescope in assembly phase. The holders and post-holders are placed on the optical rail. The next step is the insertion of the optical and polarimetrical components.

Chapter 4

Conclusions and future perspectives

In this last Chapter of this thesis, I summarize the obtained results, their scientific impact and I suggest possible future developments of my work.
During this three years of my PhD, I focused my attention on the physical processes related to the solar turbulent magneto-convection and on the instrumental solutions that are used to observe it. Despite the good agreement between spectro-polarimetric observations and radiative MHD simulation, the knowledge of the turbulent solar magneto-convection presents some aspects that are not completely clear and several scientific questions are unresolved, both for a lack of knowledge of the physical processes and for instrumental limitations in solar high resolution observations, especially the spatial resolution and the polarimetric accuracy. Contrary to what one might think, there are no enough photons for high resolution solar spectro-polarimetry and the instruments are photon starved.
In the first part of the thesis, I compared two of the most used methods to analyze spectro-polarimetric dataset: the Center of Gravity Method and the Inversion Techniques. To perform this analysis, I made use of an high resolution spectro-polarimetric dataset acquired with the IBIS instrument at the Dunn Solar Telescope. The results, published in (Viavattene et al., 2018), shows that spectro-polarimetric inversions tend to overestimate weak magnetic fields in Quiet Sun regions, confirming actual results in literature (del Toro Iniesta and Ruiz Cobo, 2016).
Afterwards, I used the same dataset to perform a validity analysis of the Gallavotti-Cohen Fluctuation Relation on the solar turbulent convection. The GCFR describes the asymmetry properties of a generic flux indicator, such as the entropy production rate or the vertical heat flux, which can be used as a driver to study the solar convection. My analysis showed a strong evidence that the solar convection is a system in non-equilibrium steady-state, which satisfies the symmetry conjecture predicted by the GCFR. I published this results in (Viavattene et al., 2019a,b) and we are now submitting a paper. At the end of this analysis, I used the obtained results to give a first experimental raw extrapolation of the Rayleigh number of the solar photospheric plasma. Future work can be done on the verification of the GCFR in solar photospheric regions with strong magnetic fields (pores or sunspots) in order to see if the theorem is still valid or if there is a change of behaviour. In this case it would be appropriate to analyze the data with the inversion techniques instead of the Center of Gravity Method. Other future work can infer on the magnetic field value below which we can define the Quiet Sun.
Regarding the instrumental part of my thesis, I worked on three different projects on Fabry-Perot Interferometers and Magneto-Optical Filters.
Firstly, I participated in the design, assembly and test phases of a FPI prototype controlled with one of the first digital controller, developed in collaboration with ADS International Company

of Lecco. Our test were centered on the characterization of the electronical noise and stability of the digital controller and we obtained very promising results. This kind of digital controllers will be very useful and important for next generation instrumentation for Solar Physics based on large diameter FPIs for very high resolution spectro-polarimetry. Nowadays, together with ADS International, we are finalizing a commercial version of the digital controller for FPIs with improved performances.
Following the trail of next generation narrow band instruments based on FPIs, secondly, I realized a feasibility study of a new optical scheme, based on the conceptual idea of Greco and Cavallini (Greco and Cavallini, 2013). The optical scheme is based on off-axis parabolic mirrors, instead of classical achromatic doublets, and large diameter FPIs. I implemented a new 3D optical configuration in order to reduce the encumbrances, maintaining the diffraction limit properties. I analyzed the tolerance and collimation issues and I proposed several alternatives to reduce the tolerance sensitivity of the instrument. This kind of new generation optical schemes are the suitable candidate for the first-light post-focus instrument for the European Solar Telescope. At the present time, we are collaborating with OptoService company of Rome to propose a complete opto-mechanical feasibility study for a narrow band imager for EST based on large diameter FPIs.
Thirdly, I entirely realized a new optical scheme for a full-disk solar telescope based on MOF technology, which will be coupled with and Halpha telescope to form the Tor vergata Solar Synoptic Telescope. The TSST will acquire magnetograms and dopplergrams of the entire solar disk (Calchetti et al., 2020). This data will be used mainly for Space Weather applications and for flare forecasting, but they can be also used as complementary data to study the large scale patterns of the solar convection. The TSST telescope will be operational in the second half of 2020. It is currently in assembly and alignment phase of the optical components. We plan to do a second spectral characterization session at the Observatory of Capodimonte in Naples before the first light.

Chapter 5

Appendices

5.1 Detailed Mechanical and Technical Schemes

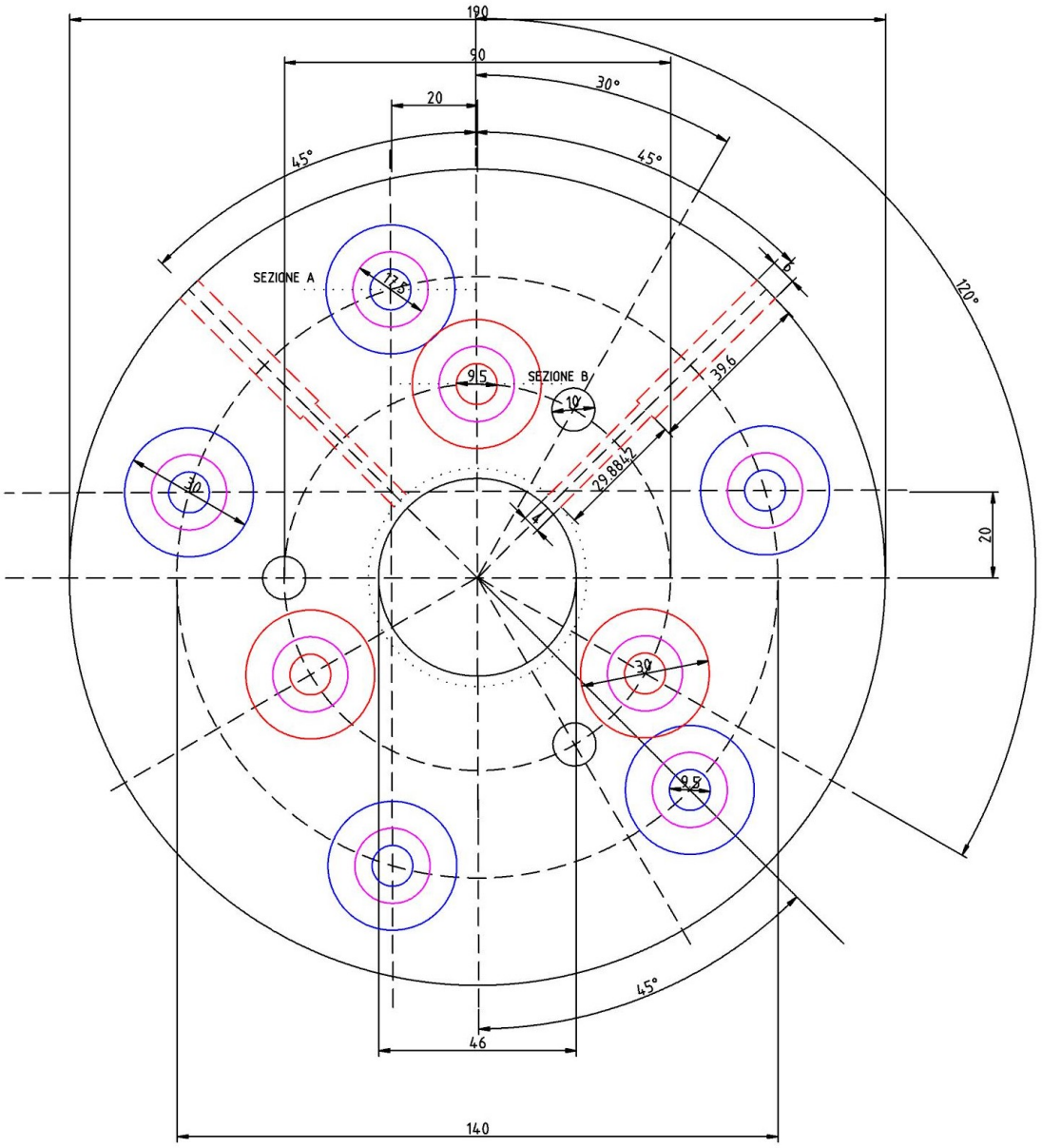

Figure 5.1: Upper mechanical part seen from the top of the GREST FPI 50.

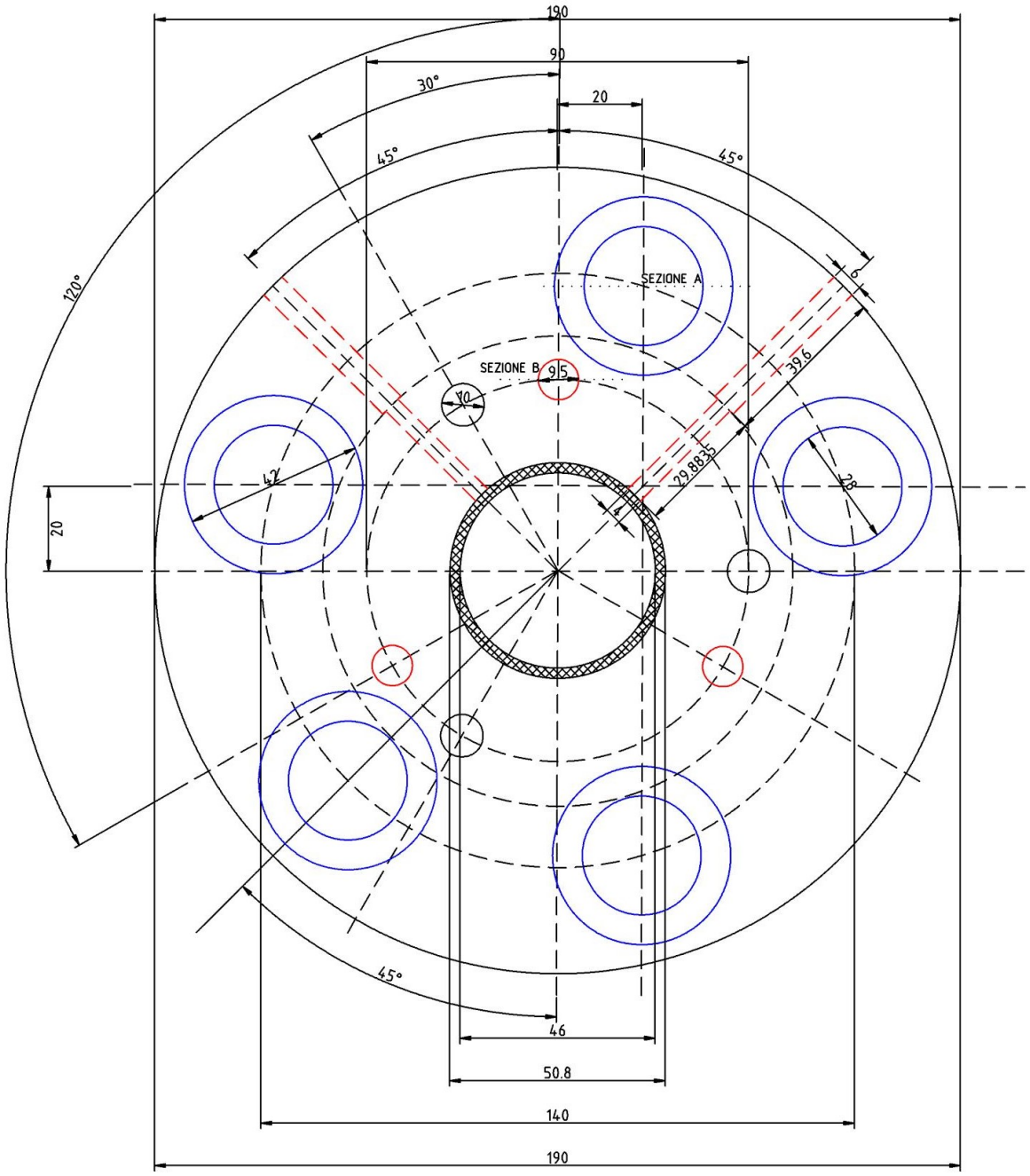

Figure 5.2: Upper mechanical part seen from the bottom of the GREST FPI 50.

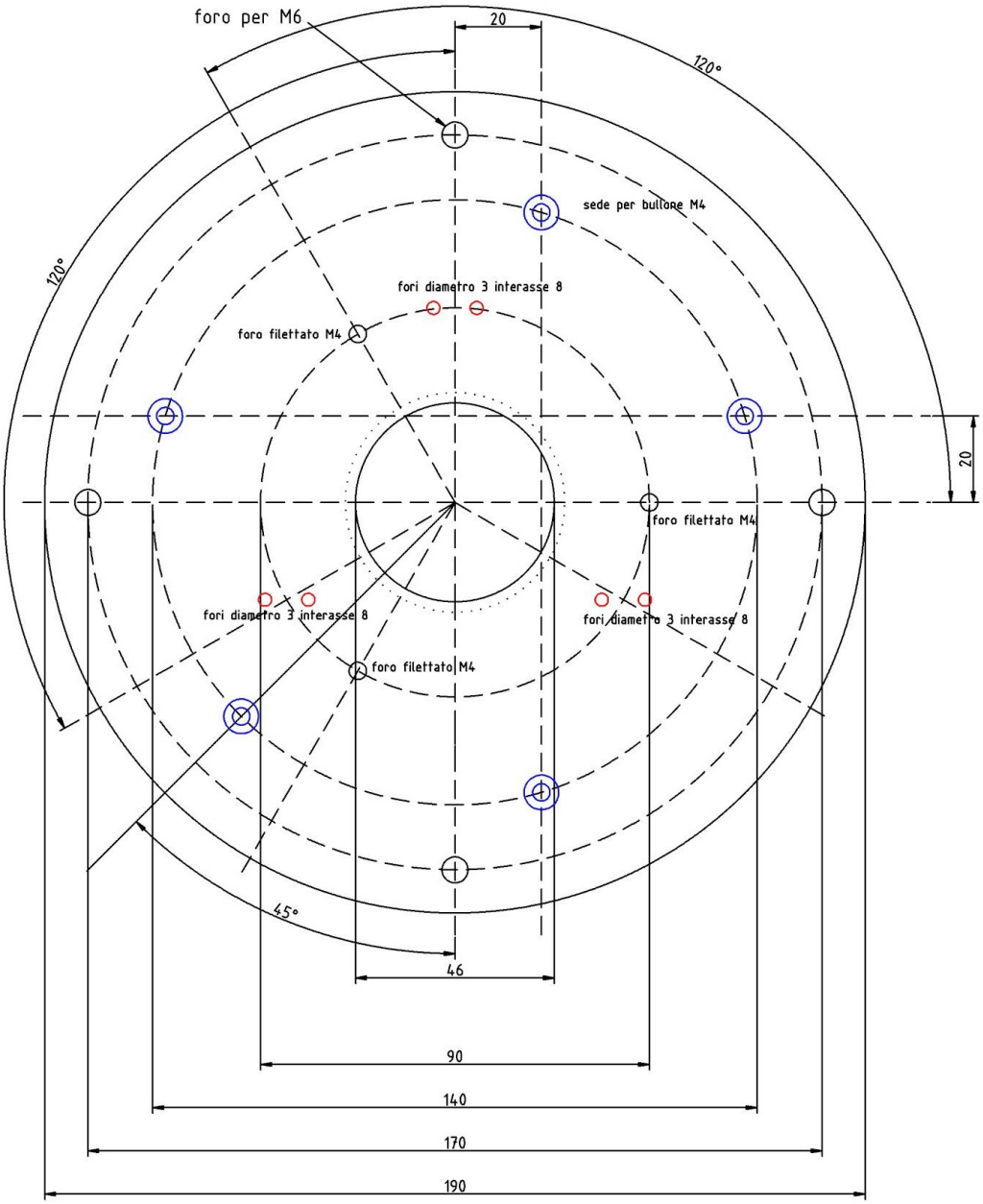

Figure 5.3: Lower mechanical part seen from the top of the GREST FPI 50.

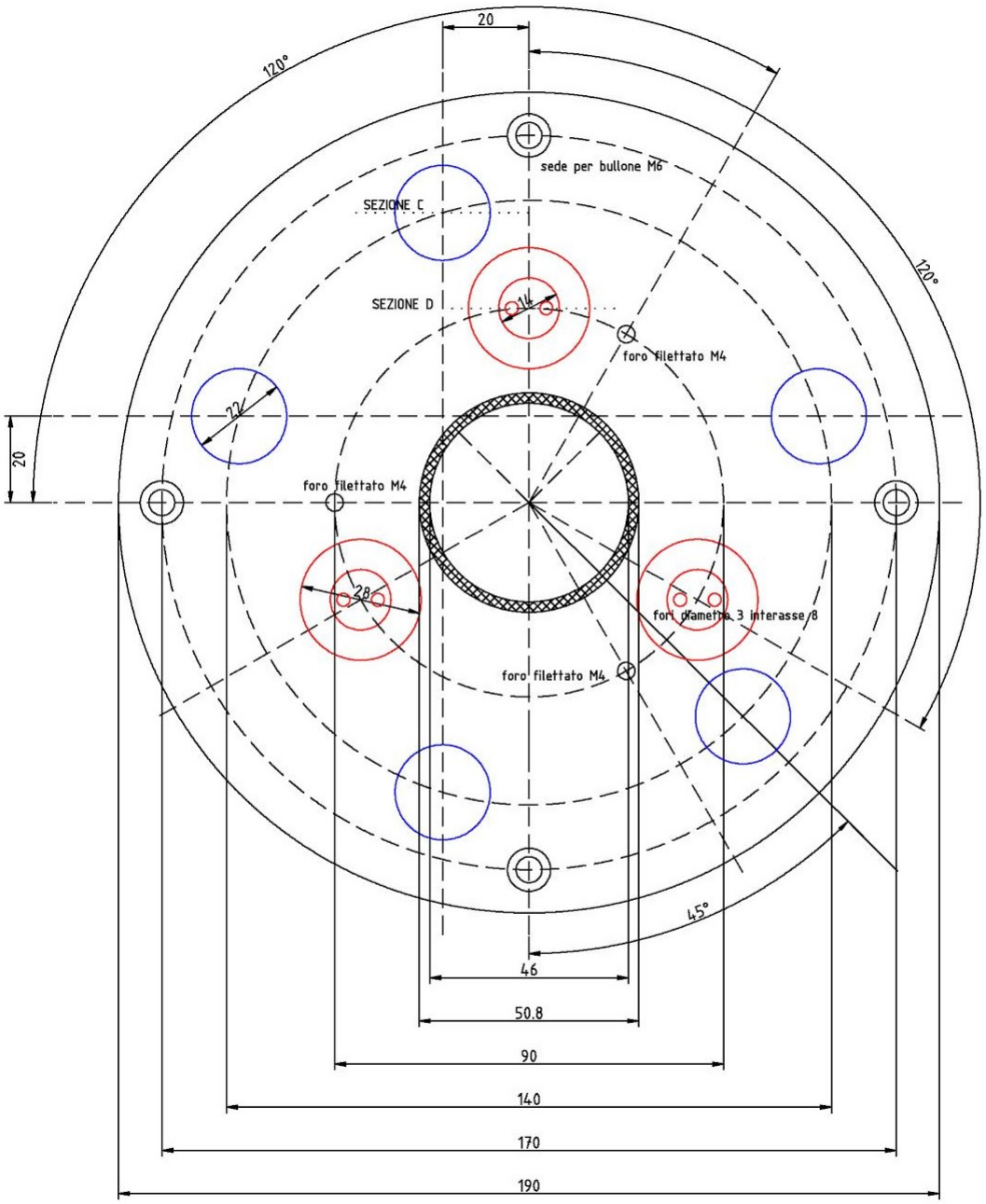

Figure 5.4: Lower mechanical part seen from the bottom of the GREST FPI 50.

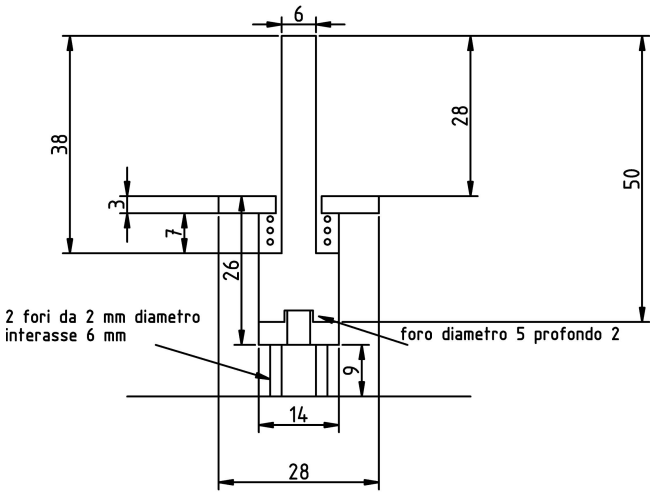

Figure 5.5: Lateral detailed view of the PZT assembly of the GREST FPI 50.

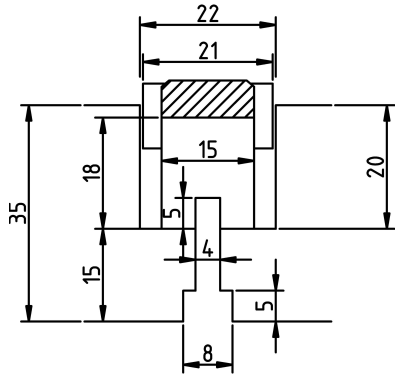

Figure 5.6: Lateral detailed view of the fixed gold mirror of the capacitor sensors of the GREST FPI 50.

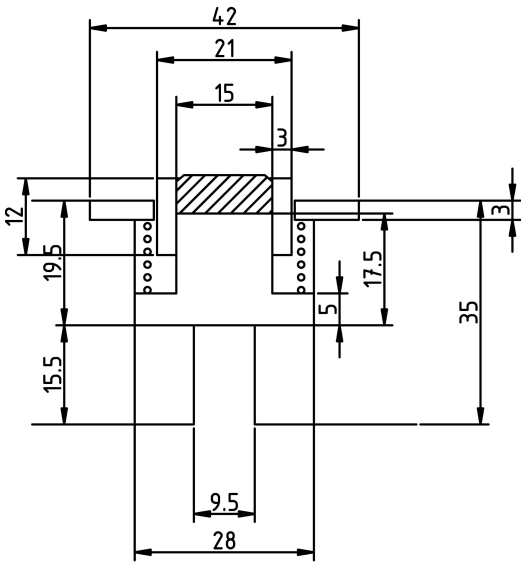

Figure 5.7: Lateral detailed view of the moving gold mirror of the capacitor sensors of the GREST FPI 50.

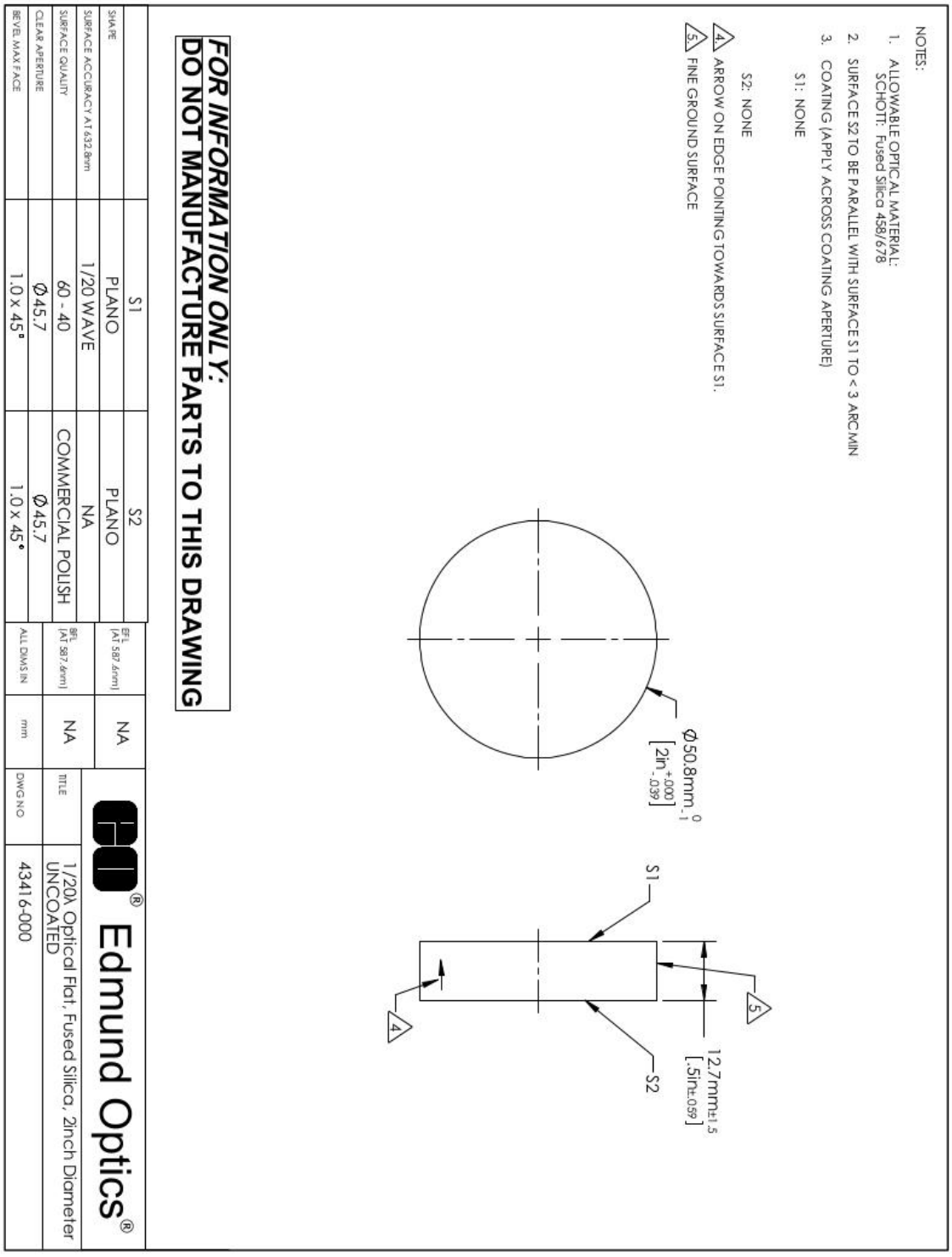

Figure 5.8: Technical drawing of the 50.8 mm optical flat by Edmund Optics used in the GREST FPI 50.

Figure 5.9: Technical drawing of the gold mirrors by Gestione SILO used as capacitive sensors in the GREST FPI 50.

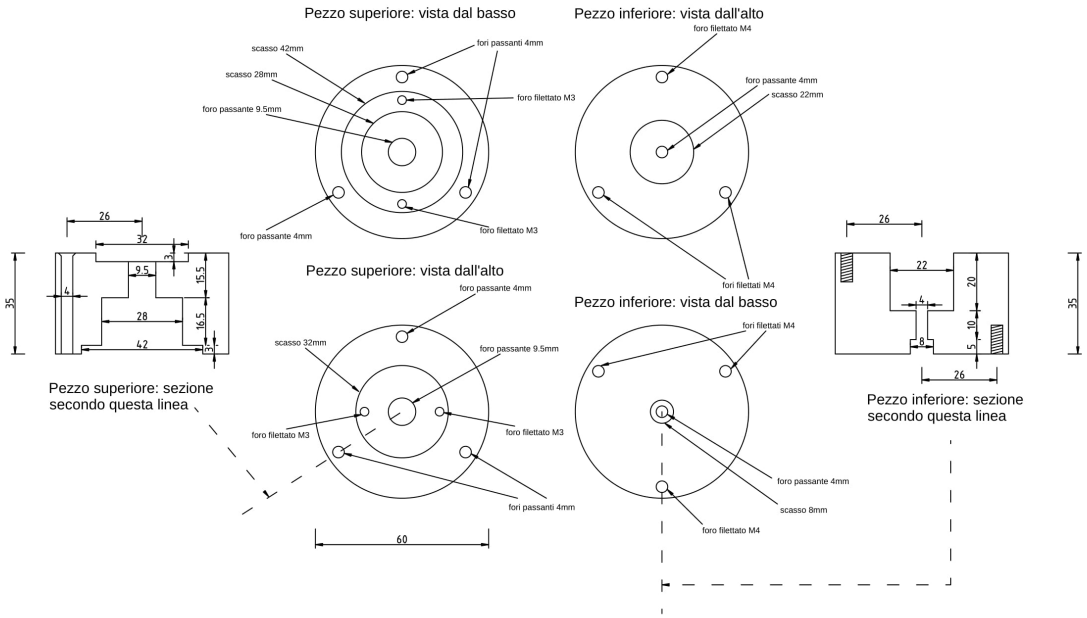

Figure 5.10: Scheme of the external reference capacitive sensor of the GREST FPI 50.

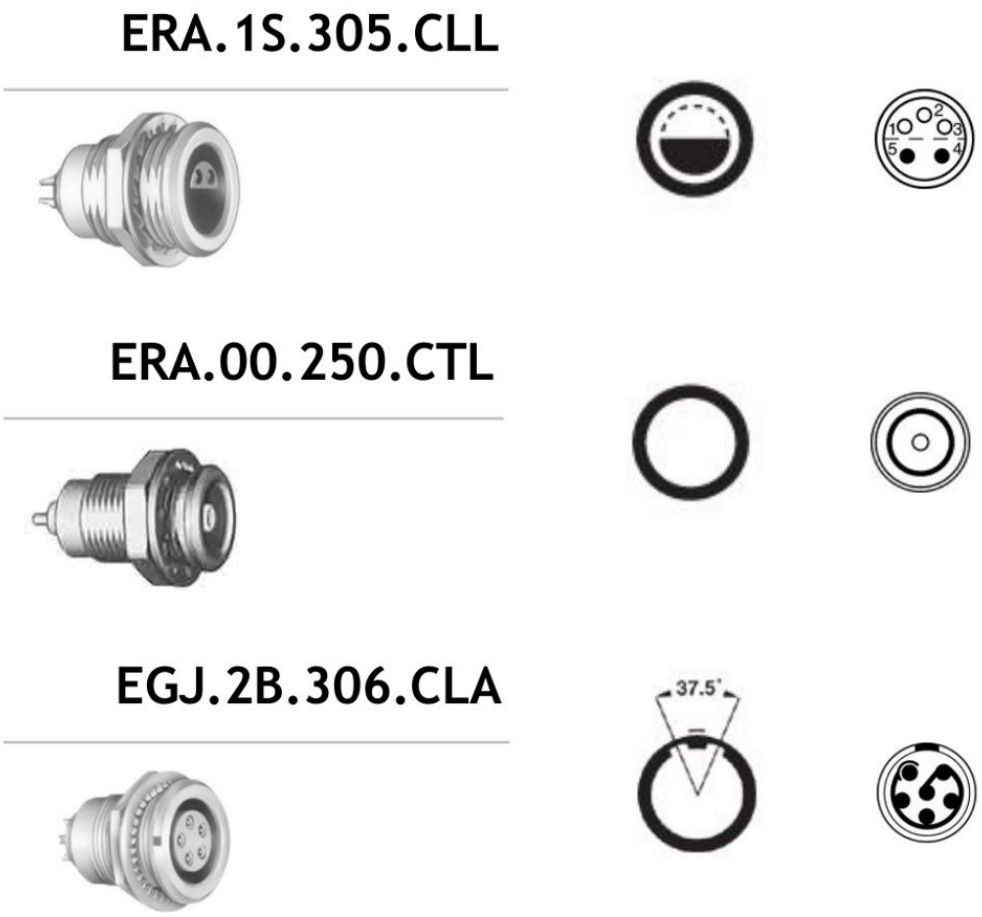

Figure 5.11: Technical drawing of the LEMO connectors of the GREST FPI 50.

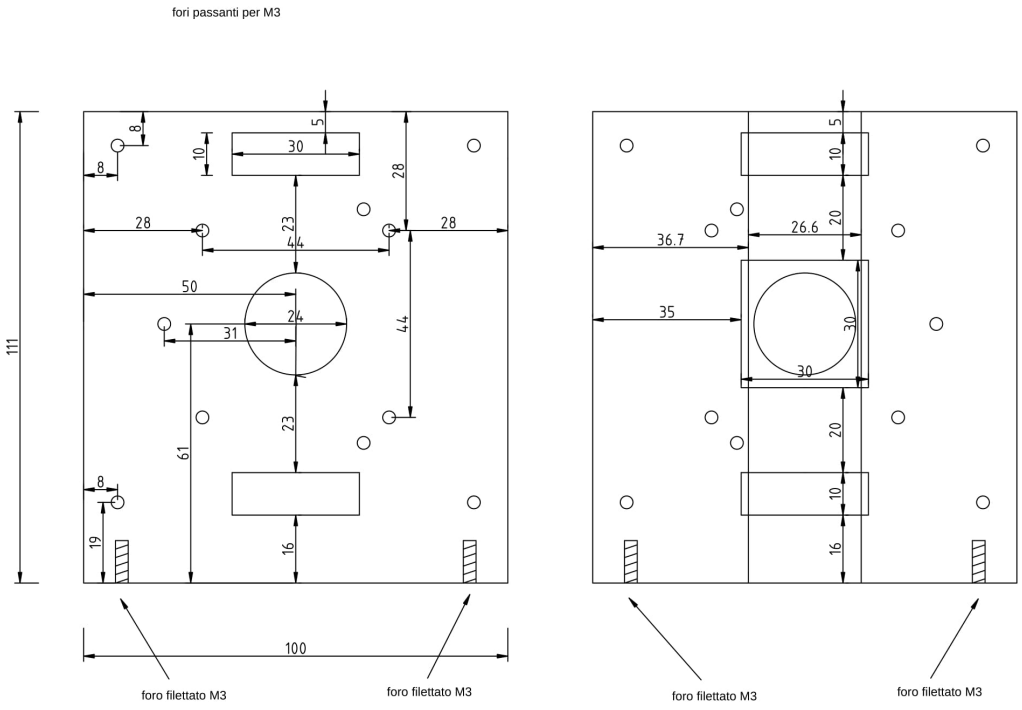

Figure 5.12: Drawing of the holder for the MOF cell for the TSST telescope.

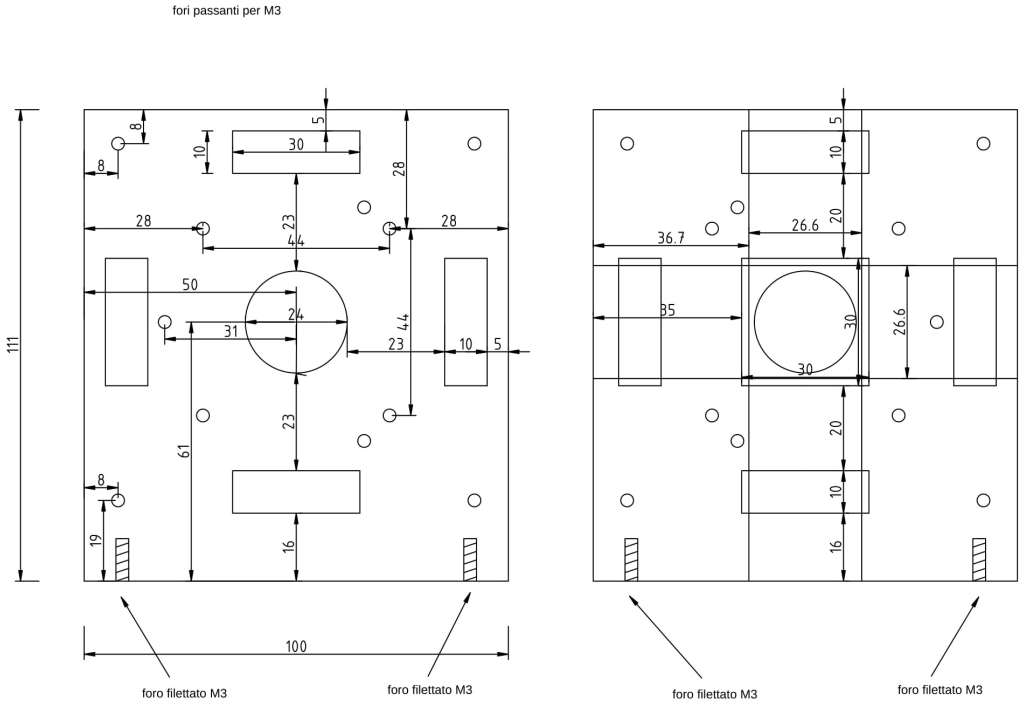

Figure 5.13: Drawing of the holder of the WS cell for the TSST telescope.

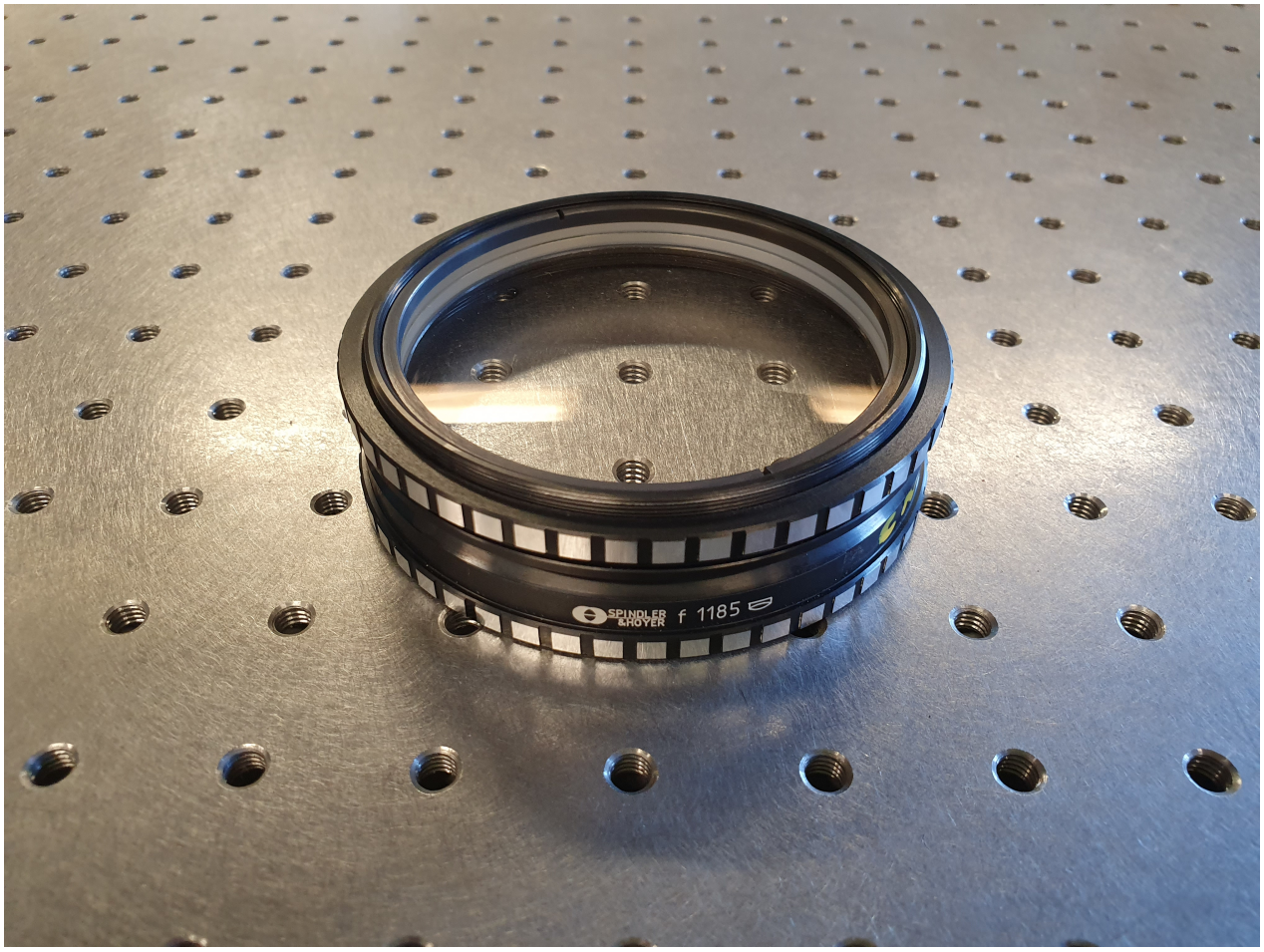

Figure 5.14: L1 objective lens of MOF TSST telescope.

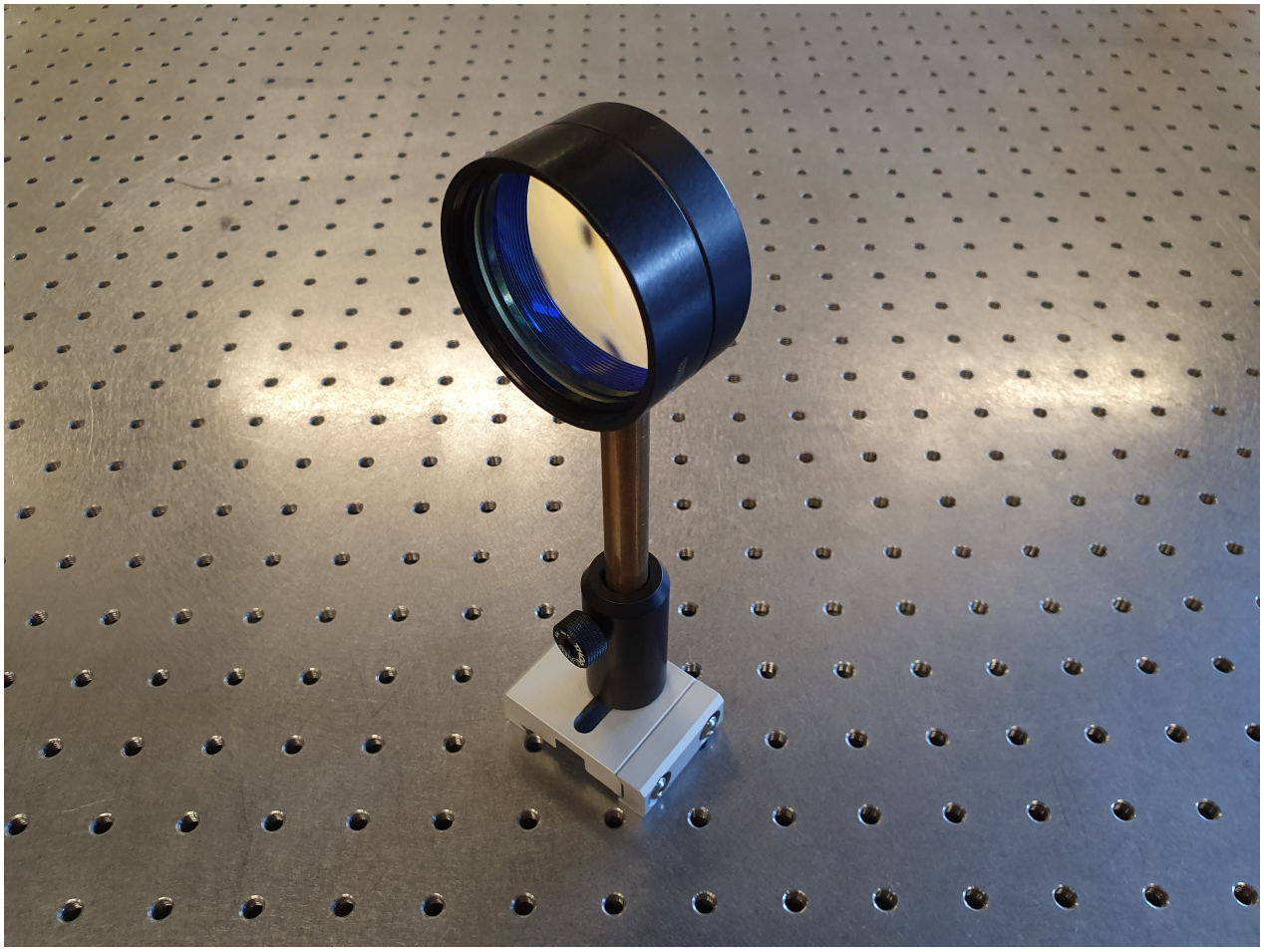

Figure 5.15: One of the achromatic doublets (L2, L3, L4 and L5) mounted with the post-holder clamp platform of the MOF TSST telescope.

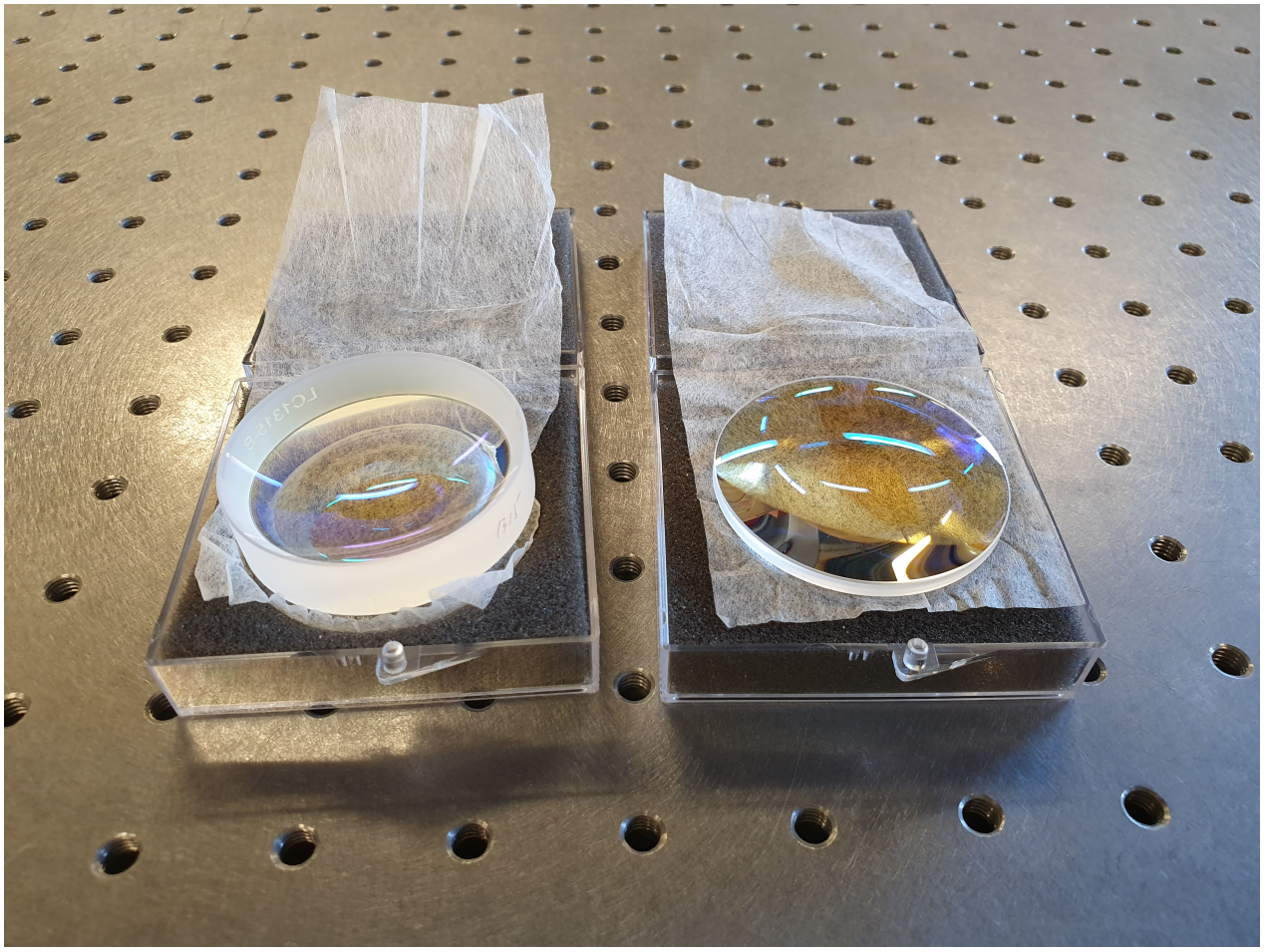

Figure 5.16: The plano-concave and the bi-convex lenses which made the corrective optics for the MOF TSST telescope.

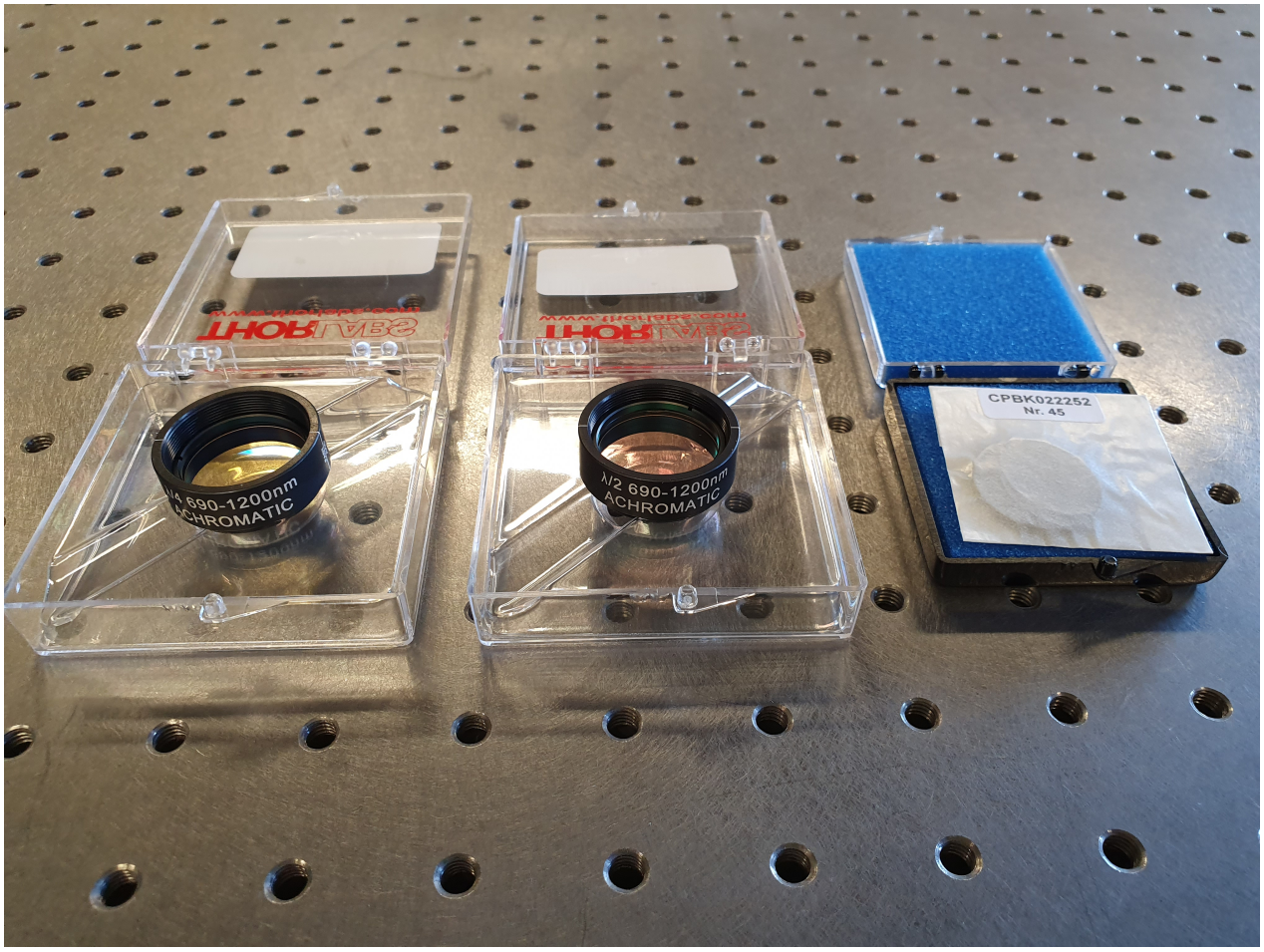

Figure 5.17: Quarter wave plate, halh wave plate and linear polarizer of the MOF TSST telescope.

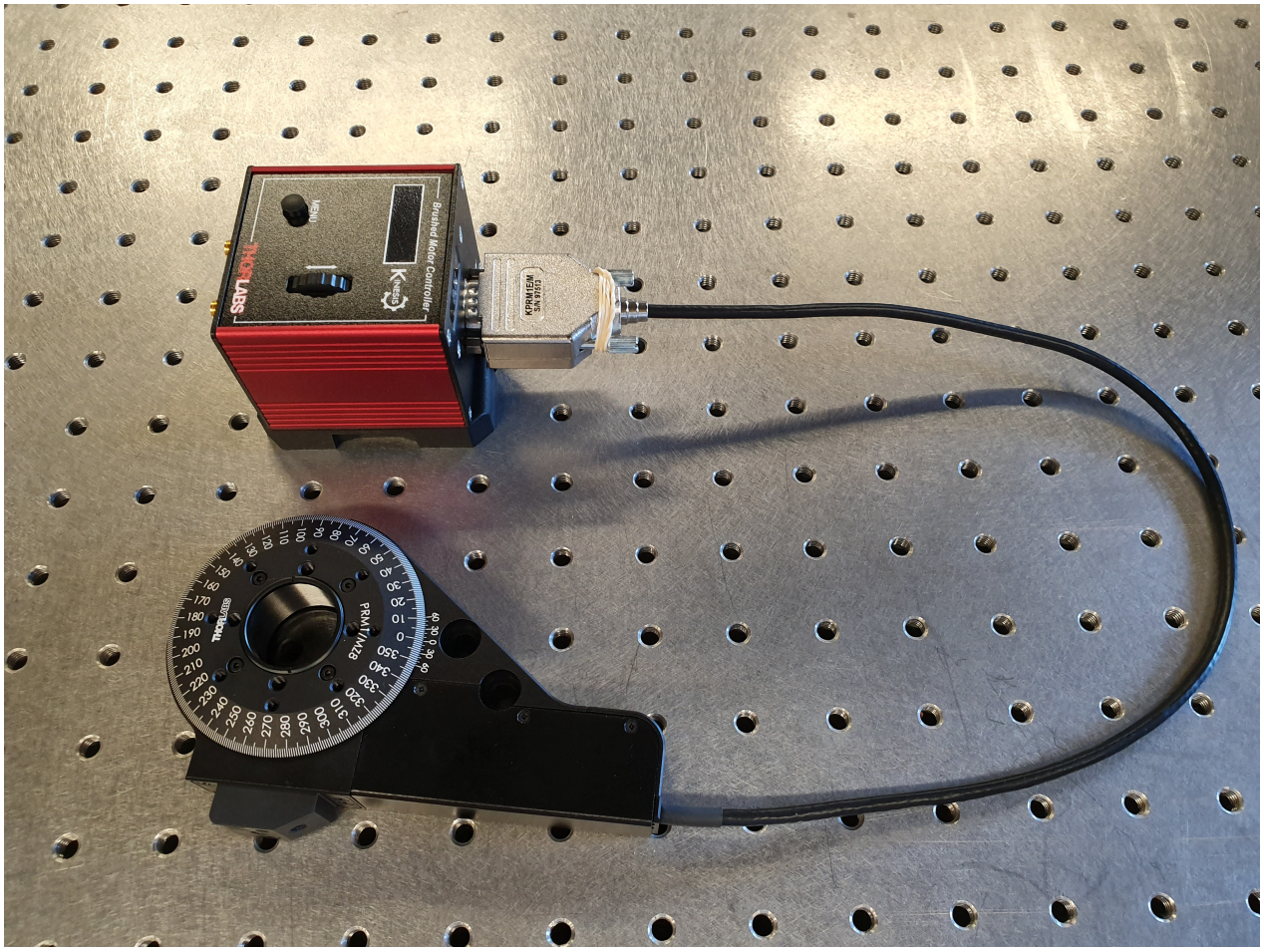

Figure 5.18: Rotating mount with the controller for the half wave plate for the MOF TSST telescope.

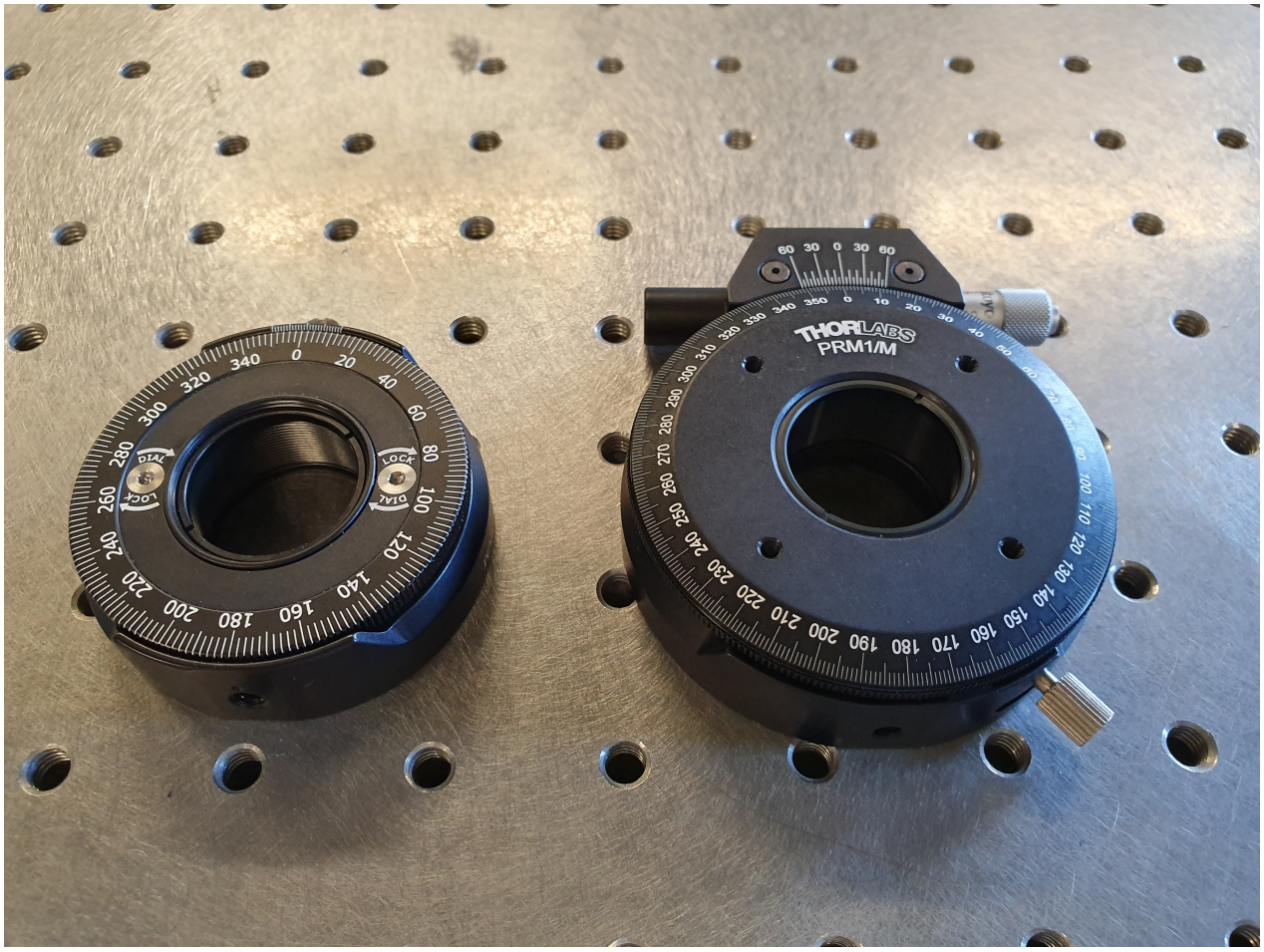

Figure 5.19: Mount of the quarter wave plate with micrometer and mount of the linear polarizer for the MOF TSST telescope.

Chapter 6

Acknowledgments

I would like to thank my tutor Dr. Dario Del Moro and my cotutors Dr. Giuseppe Consolini and Dr. Luca Giovannelli for guiding me during this three years of my PhD and for all the reseach and scientific opportunities that they gave me. I thank the head of our group Prof. Francesco Berrilli for the scientific guidance of the group, Dr. Fabio Giannattasio, Dr. Valentina Penza e Dr. Daniele Calchetti for their collaboration during the analysis of the validity of the Gallavotti-Cohen Fluctuation Theorem on the solar convection.
I thank Dr. Daniele Gallieni (head), Dr. Gaetano Martiniello and Dr. Pierluigi Fumi of ADS International Company of Lecco for their collaboration for the development, integration and test phases of the H2020 GREST Fabry-Perot Interferometer prototype with the ADS100 digital controller.
I thank Dr. Maurizio Oliviero of the INAF Observatory of Capodimonte of Naples for his collaboration and for the spectral characterization of the Tor vergata Solar Synoptic Telescope MOF and WS cells.
I would like also to thank my Master Thesis tutor Prof. Francesca Zuccarello and my cotutors Prof. Manolo Collados and Prof. Basilio Ruiz Cobo for their collaboration and their usefull mentoring guidance during my PhD.
I really thank Prof. Giovanni Gallavotti of the University of Rome La Sapienza for his priceless comments, collaboration and hints of ideas for the work of testing the validity of the Gallavotti-Cohen Fluctuation Theorem on the solar convection.
I thank Dr. Ilaria Ermolli for giving me the opportunity to partecipate to the dismounting campaign of the Interferometric BIdimensional Spectropolarimeter at the Dunn Solar Telescope (NM, USA) and its shipping to Italy.
I thank Dr. Roberta Forte, Dr. Alice Cristaldi, Dr. Daniele Galuzzo, Dr. Mija Lovric, Dr. Arnaldo Florio, Dr. Mariarita Murabito and Prof. Giancarlo de Gasperis for valuables discussions.
I thank Dr. Maurizio Oliviero and Dr. Fabio Lepreti for the referral process of this PhD thesis: their comments and suggestions contributed considerably to the readability and completeness of the thesis. Finally, I really thank the PhD Coordinator Prof. Paolo de Bernardis, the PhD Deputy Coordinator Prof. Nicola Vittorio and the previous Coordinators and Deputy Coordinators Prof. Pasquale Mazzotta and Prof. Roberto Capuzzo-Dolcetta for all the research and financial opportunity given during the whole period of the PhD.

Bibliography

Abramenko, V., Yurchyshyn, V., Goode, P., and Kilcik, A. (2010). Statistical Distribution of Size and Lifetime of Bright Points Observed with the New Solar Telescope. *ApJ*, 725(1):L101–L105.

Abramenko, V. I., Carbone, V., Yurchyshyn, V., Goode, P. R., Stein, R. F., Lepreti, F., Capparelli, V., and Vecchio, A. (2011). Turbulent Diffusion in the Photosphere as Derived from Photospheric Bright Point Motion. *ApJ*, 743(2):133.

Agnelli, G., Cacciani, A., and Fofi, M. (1975). The Magneto-Optical Filter. I: Premilinary Observations in Na D Lines. *Sol. Phys.*, 44(2):509–518.

Arnaud, J., Briand, C., and Rayrole, J. (1996). THEMIS: Télescope Héliographique pour l'Étude du Magnétisme et des Instabilités Solaires. *Journal des Astronomes Francais*, 53:5–9.

Arnaud, J., Mein, P., and Rayrole, J. (1998). The Solar Telescope THEMIS. In *Crossroads for European Solar and Heliospheric Physics. Recent Achievements and Future Mission Possibilities*, volume 417 of *ESA Special Publication*, page 213.

Artus, H. (1976). Concept of a solar research centre with vacuum tower telescope made by VEB Carl Zeiss JENA. *Jena Review*, 21:138–142.

Asplund, M., Nordlund, Å., Trampedach, R., Allende Prieto, C., and Stein, R. F. (2000). Line formation in solar granulation. I. Fe line shapes, shifts and asymmetries. *Astronomy and Astrophysics*, 359:729–742.

Beckers, J. M. (1969a). The Profiles of Fraunhofer Lines in the Presence of Zeeman Splitting. I: The Zeeman Triplet. *Sol. Phys.*, 9:372–386.

Beckers, J. M. (1969b). The Profiles of Fraunhofer Lines in the Presence of Zeeman Splitting. II: Zeeman Multiplets for Dipole and Quadrupole Radiation. *Sol. Phys.*, 10:262–267.

Bellot Rubio, L. and Orozco Suárez, D. (2019). Quiet Sun magnetic fields: an observational view. *Living Reviews in Solar Physics*, 16(1):1.

Bellot Rubio, L. R., Ruiz Cobo, B., and Collados, M. (1998). An Hermitian Method for the Solution of Polarized Radiative Transfer Problems. *ApJ*, 506:805–817.

Berrilli, F. (2003). Spatio-temporal patterns in solar surface convection. *Mem. Soc. Astron. Italiana*, 74:576.

Berrilli, F., Consolini, G., Florio, A., and Pietropaolo, E. (2001). Solar granulation: properties of velocity fields from THEMIS-IPM observations. *Memorie della Societa Astronomica Italiana*, 72:669–672.

Berrilli, F., Consolini, G., Pietropaolo, E., Caccin, B., Penza, V., and Lepreti, F. (2002). 2-D multiline spectroscopy of the solar photosphere. *A&A*, 381:253–264.

Berrilli, F., Ermolli, I., Florio, A., and Pietropaolo, E. (1999). Average properties and temporal variations of the geometry of solar network cells. *A&A*, 344:965–972.

Böhm-Vitense, E. (1958). Über die Wasserstoffkonvektionszone in Sternen verschiedener Effektivtemperaturen und Leuchtkräfte. Mit 5 Textabbildungen. *Z. Astrophys.*, 46:108.

Born, M. and Wolf, E. (1959). Principles of Optics.

Buehler, D., Lagg, A., Solanki, S. K., and van Noort, M. (2015). Properties of solar plage from a spatially coupled inversion of Hinode SP data. *A&A*, 576:A27.

Cacciani, A. and Fofi, M. (1978). The Magneto-Optical Filter. II. Velocity Field Measurements. *Sol. Phys.*, 59(1):179–189.

Cacciani, A. and Moretti, P.-F. (1994). Magneto-optical filter: concept and applications in astronomy. In Crawford, D. L. and Craine, E. R., editors, *Proc. SPIE*, volume 2198 of *Society of Photo-Optical Instrumentation Engineers (SPIE) Conference Series*, pages 219–228.

Cacciani, A., Moretti, P. F., and Rodgers, W. E. (1997). Measuring Doppler and Magnetic Fields Simultaneously. *Sol. Phys.*, 174:115–128.

Cacciani, A., Ricci, D., Rosati, P., Rhodes, E. J., Smith, E., Tomczyk, S., and Ulrich, R. K. (1990). Solar magnetic fields measurements with a magneto-optical filter. *Nuovo Cimento C Geophysics Space Physics C*, 13:125–130.

Cacciani, A., Rosati, P., Ricci, D., Egidi, A., Apporchaux, T., Marquedant, R. J., and Smith, E. J. (1994). Theoretical and experimental study of the magneto optical filter.

Caccin, B., Gomez, M. T., Marmolino, C., and Severino, G. (1977). Response functions and contribution functions of photospheric lines. *A&A*, 54(1):227–231.

Caccin, B. and Penza, V. (2000). Line-Depth and T_{eff} Variations with the Solar Cycle due to Possible Size-Changes of Photospheric Granulation. In Wilson, A., editor, *The Solar Cycle and Terrestrial Climate, Solar and Space weather*, volume 463 of *ESA Special Publication*, page 293.

Calchetti, D., Viavattene, G., Berrilli, F., Del Moro, D., Giovannelli, L., and Oliviero, M. (2020). Tor vergata synoptic solar telescope: Preliminary optical design and spectral characterization.

Calcines, A., López, R. L., and Collados, M. (2013). a High Resolution Integral Field Spectrograph for the European Solar Telescope. *Journal of Astronomical Instrumentation*, 2(1):1350007.

Calvo, F., Steiner, O., and Freytag, B. (2016). Non-magnetic photospheric bright points in 3D simulations of the solar atmosphere. *A&A*, 596:A43.

Canuto, V. M. and Mazzitelli, I. (1991). Stellar Turbulent Convection: A New Model and Applications. *ApJ*, 370:295.

Canuto, V. M. and Mazzitelli, I. (1992). Further Improvements of a New Model for Turbulent Convection in Stars. *ApJ*, 389:724.

Cao, W., Gorceix, N., Coulter, R., Coulter, A., and Goode, P. R. (2010). First light of the 1.6 meter off-axis New Solar Telescope at Big Bear Solar Observatory. In *Ground-based and Airborne Telescopes III*, volume 7733 of *Proc. SPIE*, page 773330.

Carlsson, M. and Hansteen, V. (2005). Chromospheric Waves. In Innes, D. E., Lagg, A., and Solanki, S. A., editors, *Chromospheric and Coronal Magnetic Fields*, volume 596 of *ESA Special Publication*, page 39.1.

Carlsson, M., Stein, R. F., Nordlund, Å., and Scharmer, G. B. (2004). Observational Manifestations of Solar Magnetoconvection: Center-to-Limb Variation. *ApJ*, 610(2):L137–L140.

Cattaneo, F., Emonet, T., and Weiss, N. (2003). On the Interaction between Convection and Magnetic Fields. *ApJ*, 588(2):1183–1198.

Cavallini, F. (1998). The Italian Panoramic Monochromator. *A&AS*, 128:589–598.

Cavallini, F. (2006). IBIS: A New Post-Focus Instrument for Solar Imaging Spectroscopy. *Sol. Phys.*, 236:415–439.

Cavallini, F., Berrilli, F., Cantarano, S., and Egidi, A. (2001). IBIS: a new instrument for solar bidimensional spectroscopy. *Mem. Soc. Astron. Italiana*, 72:554–557.

Centeno, R., Socas-Navarro, H., Lites, B., Kubo, M., Frank, Z., Shine, R., Tarbell, T., Title, A., Ichimoto, K., Tsuneta, S., Katsukawa, Y., Suematsu, Y., Shimizu, T., and Nagata, S. (2007). Emergence of Small-Scale Magnetic Loops in the Quiet-Sun Internetwork. *ApJ*, 666(2):L137–L140.

Ching, E. S. C. (2014). Statistic and scaling in turbulent rayleigh-bénard convection.

Ciliberto, S., Garnier, N., Hernandez, S., Lacpatia, C., Pinton, J.-F., and Ruiz Chavarria, G. (2004). Experimental test of the Gallavotti-Cohen fluctuation theorem in turbulent flows. *Physica A Statistical Mechanics and its Applications*, 340:240–250.

Cimino, M., Cacciani, A., and Sopranzi, N. (1968). An Instrument to measure Solar Magnetic Fields by an Atomic-Beam Method. *Sol. Phys.*, 3(4):618–622.

Collados, M. (2008). European Solar Telescope (EST): project status. In *Ground-based and Airborne Telescopes II*, volume 7012 of *Proc. SPIE*, page 70120J.

Collados, M., Bettonvil, F., Cavaller, L., Ermolli, I., Gelly, B., Grivel-Gelly, C., Pérez, A., Socas-Navarro, H., Soltau, D., and Volkmer, R. (2010a). European Solar Telescope: project status. In *Ground-based and Airborne Telescopes III*, volume 7733 of *Proc. SPIE*, page 77330H.

Collados, M., Bettonvil, F., Cavaller, L., Ermolli, I., Gelly, B., Pérez, A., Socas-Navarro, H., Soltau, D., Volkmer, R., and EST Team (2010b). European Solar Telescope: Progress status. *Astronomische Nachrichten*, 331:615.

Collados, M., Bettonvil, F., Cavaller, L., Ermolli, I., Gelly, B., Pérez, A., Socas-Navarro, H., Soltau, D., Volkmer, R., and EST Team (2013). The European Solar Telescope. *Mem. Soc. Astron. Italiana*, 84:379.

Criscuoli, S., Del Moro, D., Giorgi, F., Romano, P., Berrilli, F., Ermolli, I., Viticchié, B., and Zuccarello, F. (2012). Properties of G-band Bright Points derived from IBIS observations. *Memorie della Societa Astronomica Italiana Supplementi*, 19:93.

Cristaldi, A. and Ermolli, I. (2017). 1D Atmosphere Models from Inversion of Fe I 630 nm Observations with an Application to Solar Irradiance Studies. *ApJ*, 841(2):115.

Dawes, W. R. (1864). Results of some recent Observations of the Solar Surface, with Remarks. *Monthly Notices of the Royal Astronomical Society*, 24:161.

De Groot, S. R. and Mazur, P. (2013). *Non-equilibrium thermodynamics*. Courier Corporation.

de la Cruz Rodríguez, J. and Piskunov, N. (2013). DELO-Bezier Formal Solutions of the Polarized Radiative Transfer Equation. *ApJ*, 764:33.

Del Moro, D. (2004). Solar granulation properties derived from three different time series. *Astronomy and Astrophysics*, 428:1007–1015.

Del Moro, D., Giannattasio, F., Berrilli, F., Consolini, G., Lepreti, F., and Gošić, M. (2015). Super-diffusion versus competitive advection: a simulation. *A&A*, 576:A47.

Del Moro, D., Giovannelli, L., Pietropaolo, E., and Berrilli, F. (2017). JP3D compression of solar data-cubes: Photospheric imaging and spectropolarimetry. *Experimental Astronomy*, 43:23–37.

del Toro Iniesta, J. C. and Ruiz Cobo, B. (2016). Inversion of the radiative transfer equation for polarized light. *Living Reviews in Solar Physics*, 13:4.

Denker, C., Cao, W., Chae, J., Coulter, R., Kuhn, J. R., Marquette, W. H., Moon, Y., Park, Y., Ren, D., Tritschler, A., Varsik, J. R., Wang, H., Yang, G., Shoumko, S., and Goode, P. R. (2005). The New Solar Telescope at Big Bear Solar Observatory - A Progress Report. *AGU Spring Meeting Abstracts*, pages SP43A–07.

Denker, C., Goode, P. R., Ren, D., Saadeghvaziri, M. A., Verdoni, A. P., Wang, H., Yang, G., Abramenko, V., Cao, W., Coulter, R., Fear, R., Nenow, J., Shoumko, S., Spirock, T. J., Varsik, J. R., Chae, J., Kuhn, J. R., Moon, Y., Park, Y. D., and Tritschler, A. (2006). Progress on the 1.6-meter New Solar Telescope at Big Bear Solar Observatory. In *Society of Photo-Optical Instrumentation Engineers (SPIE) Conference Series*, volume 6267 of *Proc. SPIE*, page 62670A.

Denker, C., Marquette, W. H., Varsik, J., Wang, H., Goode, P. R., Moretto, G., Kuhn, J., and Coulter, R. (2004). The New Solar Telescope at Big Bear Solar Observatory. In *American Astronomical Society Meeting Abstracts #204*, volume 36 of *Bulletin of the American Astronomical Society*, page 795.

Domínguez Cerdeña, I., Sánchez Almeida, J., and Kneer, F. (2003). Inter-network magnetic fields observed with sub-arcsec resolution. *A&A*, 407:741–757.

Dunn, R. B. (1964a). An evacuated tower telescope. *Appl. Opt.*, 3:1353.

Dunn, R. B. (1964b). Solar Telescope Planned for Sacramento Peak. *AJ*, 69:540.

Evans, D. J. and Searles, D. J. (2002). The Fluctuation Theorem. *Advances in Physics*, 51:1529–1585.

Fowles, G. R. (1989). Introduction to Modern Optics.

Gallavotti, G. (1999). A local fluctuation theorem. *Physica A Statistical Mechanics and its Applications*, 263:39–50.

Gallavotti, G. and Cohen, E. G. D. (1995). Dynamical ensembles in stationary states. *Journal of Statistical Physics*, 80:931–970.

Gelly, B., Langlois, M., Moretto, G., Douet, R., Lopez Ariste, A., Tallon, M., Thiébaut, E., Geyskens, N., Lorgeoux, G., Léger, J., and Le Men, C. (2016). New life for the THEMIS solar telescope. In *Ground-based and Airborne Telescopes VI*, volume 9906 of *Proc. SPIE*, page 99065A.

Getling, A. V. (2001). Rayleigh-bénard convection: structures and dynamics.

Giannattasio, F., Berrilli, F., Biferale, L., Del Moro, D., Sbragaglia, M., Bellot Rubio, L., Gošić, M., and Orozco Suárez, D. (2014a). Pair separation of magnetic elements in the quiet Sun. *A&A*, 569:A121.

Giannattasio, F., Berrilli, F., Consolini, G., Del Moro, D., Gošić, M., and Bellot Rubio, L. (2018). Occurrence and persistence of magnetic elements in the quiet Sun. *A&A*, 611:A56.

Giannattasio, F., Consolini, G., Berrilli, F., and Del Moro, D. (2019). The Complex Nature of Magnetic Element Transport in the Quiet Sun: The Lévy-walk Character. *ApJ*, 878(1):33.

Giannattasio, F., Del Moro, D., Berrilli, F., Bellot Rubio, L., Gošić, M., and Orozco Suárez, D. (2013). Diffusion of Solar Magnetic Elements up to Supergranular Spatial and Temporal Scales. *ApJ*, 770(2):L36.

Giannattasio, F., Stangalini, M., Berrilli, F., Del Moro, D., and Bellot Rubio, L. (2014b). Diffusion of Magnetic Elements in a Supergranular Cell. *ApJ*, 788(2):137.

Gingerich, O., Noyes, R. W., Kalkofen, W., and Cuny, Y. (1971). The Harvard-Smithsonian reference atmosphere. *Sol. Phys.*, 18:347–365.

Goode, P. R., BBSO/NJIT Team, and Mees Solar Obs./U. Hawaii Team (2003). 1.6 m Off-Axis Solar Telescope at Big Bear Solar Observatory. In *AAS/Solar Physics Division Meeting #34*, volume 35 of *Bulletin of the American Astronomical Society*, page 848.

Greco, V. and Cavallini, F. (2013). Optical design of a near-infrared imaging spectropolarimeter for the Advanced Technology Solar Telescope. *Optical Engineering*, 52:063001.

GREST project ref. 653982 (2017). Wp3 “capacitance-stabilized fabry-perot development” - d3.3 “manifacturing of the mechanical parts of the fpi prototype”.

GREST project ref. 653982 (2018a). Wp3 “capacitance-stabilized fabry-perot development” - d3.5 “software coding”.

GREST project ref. 653982 (2018b). Wp3 “capacitance-stabilized fabry-perot development” - d3.6 “fpi and cse integration”.

GREST project ref. 653982 (2018c). Wp3 “capacitance-stabilized fabry-perot development” - d3.7 “cavity, parallelism and stability”.

GREST project ref. 653982 (2018d). Wp3 “capacitance-stabilized fabry-perot development” - d3.8 “spectral test”.

Gudiksen, B. V., Carlsson, M., Hansteen, V. H., Hayek, W., Leenaarts, J., and Martínez-Sykora, J. (2011). The stellar atmosphere simulation codebifrost. *Astronomy Astrophysics*, 531:A154.

Guglielmino, S. L., Martínez Pillet, V., Bonet, J. A., del Toro Iniesta, J. C., Bellot Rubio, L. R., Solanki, S. K., Schmidt, W., Gandorfer, A., Barthol, P., and Knölker, M. (2012). The Frontier between Small-scale Bipoles and Ephemeral Regions in the Solar Photosphere: Emergence and Decay of an Intermediate-scale Bipole Observed with SUNRISE/IMaX. *ApJ*, 745(2):160.

Hale, G. E. (1908a). On the Probable Existence of a Magnetic Field in Sun-Spots. *ApJ*, 28:315.

Hale, G. E. (1908b). SOLAR VORTICES (Contributions from the Mt. Wilson Solar Observatory, No. 26). *ApJ*, 28:100.

Hale, G. E. (1908c). The Zeeman Effect in the Sun. *PASP*, 20:287.

Hernandez, G. (1988). Fabry Perot Interferometers.

Herschel, W. (1801). Observations Tending to Investigate the Nature of the Sun, in Order to Find the Causes or Symptoms of Its Variable Emission of Light and Heat; With Remarks on the Use That May Possibly Be Drawn from Solar Observations. *Philosophical Transactions of the Royal Society of London Series I*, 91:265–318.

Hirzberger, J. (2002). On the brightness and velocity structure of solar granulation. *Astronomy and Astrophysics*, 392:1105–1118.

Hirzberger, J., Bonet, J. A., Vázquez, M., and Hanslmeier, A. (1999). Time Series of Solar Granulation Images. III. Dynamics of Exploding Granules and Related Phenomena. *ApJ*, 527(1):405–414.

Hurtado, P. I., Pérez-Espigares, C., del Pozo, J. J., and Garrido, P. L. (2011). Symmetries in fluctuations far from equilibrium. *Proceedings of the National Academy of Science*, 108(19):7704–7709.

Judge, P. G., Kleint, L., Uitenbroek, H., Rempel, M., Suematsu, Y., and Tsuneta, S. (2015). Photon Mean Free Paths, Scattering, and Ever-Increasing Telescope Resolution. *Sol. Phys.*, 290(3):979–996.

Judge, P. G., Tritschler, A., Uitenbroek, H., Reardon, K., Cauzzi, G., and de Wijn, A. (2010). Fabry-Pérot Versus Slit Spectropolarimetry of Pores and Active Network: Analysis of IBIS and Hinode Data. *ApJ*, 710:1486–1497.

Kaiser, A. and Schreiber, T. (2002). Information transfer in continuous processes. *Physica D Nonlinear Phenomena*, 166(1-2):43–62.

Keil, S. L., Rimmele, T. R., and Wagner, J. (2009). Advanced Technology Solar Telescope. *Earth Moon and Planets*, 104:77–82.

Kentischer, T. J., Schmidt, W., Sigwarth, M., and Uexkuell, M. V. (1998). TESOS, a double Fabry-Perot instrument for solar spectroscopy. *A&A*, 340:569–578.

Kraichnan, R. H. (1962). Turbulent thermal convection at arbitrary prandtl number. *The Physics of Fluids*, 5(11):1374–1389.

Krieg, J., Kneer, F., Koschinsky, M., and Ritter, C. (2000). Granular velocities of the Sun from speckle interferometry. *Astronomy and Astrophysics*, 360:1157–1162.

Lagg, A., Woch, J., Solanki, S. K., and Gandorfer, A. (2006). Supersonic Downflows in the Vicinity of a Solar Pore. In Casini, R. and Lites, B. W., editors, *Solar Polarization 4*, volume 358 of *Astronomical Society of the Pacific Conference Series*, page 437.

Landi Degl'Innocenti, E. (1982). On the effective Landé factor of magnetic lines. *Sol. Phys.*, 77:285–289.

Landi Degl'Innocenti, E. (1983a). Polarization in spectral lines. *Sol. Phys.*, 85:33–40.

Landi Degl'Innocenti, E. (1983b). Polarization in spectral lines. I - A unifying theoretical approach. *Sol. Phys.*, 85:3–31.

Landi Degl'Innocenti, E. (2004). Fisica solare.

Landi Degl'Innocenti, E. and Landi Degl'Innocenti, M. (1985). On the solution of the radiative transfer equations for polarized radiation. *Sol. Phys.*, 97:239–250.

Landi Degl'Innocenti, E. and Landolfi, M. (2004a). Polarization in spectral lines.

Landi Degl'Innocenti, E. and Landolfi, M., editors (2004b). *Polarization in Spectral Lines*, volume 307 of *Astrophysics and Space Science Library*.

Lebowitz, J. L. and Spohn, H. (1999). A Gallavotti-Cohen-Type Symmetry in the Large Deviation Functional for Stochastic Dynamics. *Journal of Statistical Physics*, 95:333–365.

Levenberg, K. (1944). Quart. appl. math. 2, 164-168.

Löhner-Böttcher, J., Schmidt, W., Stief, F., Steinmetz, T., and Holzwarth, R. (2018). Convective blueshifts in the solar atmosphere. I. Absolute measurements with LARS of the spectral lines at 6302 Å. *A&A*, 611:A4.

Macaluso, D. and Corbino, O. M. (1898). Sopra una nuova azione che la luce subisce attraversando alcuni vapori metallici in un campo magnetico. *Il Nuovo Cimento*, 8(1):257–258.

Macaluso, D., Corbino, O. M., and Magri, L. (1899a). Sulla relazione tra il fenomeno di Zeemann e la rotazione magnetica anomala del piano di polarizzazione della luce. *Il Nuovo Cimento*, 9(1):384–389.

Macaluso, D., Corbino, O. M., and Magri, L. (1899b). Sulle modificazioni che la luce subisce attraversando alcuni vapori metallici in un campo magnetico. *Il Nuovo Cimento*, 9(1):381–384.

Marquardt, D. (1963). J. soc. indust. appl. math. 11, 431-441.

Martínez González, M. J. and Bellot Rubio, L. R. (2009). Emergence of Small-scale Magnetic Loops Through the Quiet Solar Atmosphere. *ApJ*, 700(2):1391–1403.

Martínez González, M. J., Bellot Rubio, L. R., Solanki, S. K., Martínez Pillet, V., Del Toro Iniesta, J. C., Barthol, P., and Schmidt, W. (2012). Resolving the Internal Magnetic Structure of the Solar Network. *ApJ*, 758(2):L40.

Mein, P. and Rayrole, J. (1985). Themis solar telescope. *Vistas in Astronomy*, 28:567–569.

Mihalas, D. (1977). Stellar atmospheres, 2nd edition.

Muller, R., Roudier, T., Vigneau, J., and Auffret, H. (1994). The proper motion of network bright points and the heating of the solar corona. *A&A*, 283:232–240.

Niemela, J. J., Skrbek, L., Sreenivasan, K. R., and Donnelly, R. J. (2000). Turbulent convection at very high Rayleigh numbers. *Nature*, 404(6780):837–840.

Nordlund, Å. and Stein, R. F. (1991). *Granulation: Non-adiabatic Patterns and Shocks*, volume 388, page 141.

Nordlund, Å., Stein, R. F., and Asplund, M. (2009). Solar Surface Convection. *Living Reviews in Solar Physics*, 6(1):2.

Oliviero, M., Dolci, M., Severino, G., Straus, T., Cacciani, A., and Moretti, P. F. (1998a). VAMOS: Velocity and Magnetic Observations of the Sun. In Deubner, F.-L., Christensen-Dalsgaard, J., and Kurtz, D., editors, *New Eyes to See Inside the Sun and Stars*, volume 185 of *IAU Symposium*, page 53.

Oliviero, M., Moretti, P. F., Severino, G., Straus, T., Magrì, M., and Tripicchio, A. (2002). Preliminary Results on the Solar Photospheric Dynamics Observed with Vamos. *Sol. Phys.*, 209(1):21–35.

Oliviero, M., Severino, G., Berrilli, F., Moretti, P. F., and Jefferies, S. M. (2011). The intensity effect in magneto-optical filters. In *Proc. SPIE*, volume 8148 of *Society of Photo-Optical Instrumentation Engineers (SPIE) Conference Series*, page 81480V.

Oliviero, M., Severino, G., and Esposito, G. (2010). Planning magneto-optical filters for the study of magnetic oscillations of the Sun. *Ap&SS*, 328(1-2):325–329.

Oliviero, M., Severino, G., and Straus, T. (1998b). The VAMOS Data Analysis Pipeline. In Korzennik, S., editor, *Structure and Dynamics of the Interior of the Sun and Sun-like Stars*, volume 418 of *ESA Special Publication*, page 275.

Oliviero, M., Severino, G., and Straus, T. (1998c). VAMOS: velocity and intensity data analysis and first results on I-V phase difference at low l. *Mem. Soc. Astron. Italiana*, 69:623.

Orozco Suárez, D., Bellot Rubio, L. R., del Toro Iniesta, J. C., and Tsuneta, S. (2008). Magnetic field emergence in quiet Sun granules. *A&A*, 481(1):L33–L36.

Penza, V., Caccin, B., and Del Moro, D. (2004a). The sensitivity of the C I 538.0 nm Fe I 537.9 nm and Ti II 538.1 nm lines to solar active regions. *A&A*, 427:345–351.

Penza, V., Caccin, B., Ermolli, I., and Centrone, M. (2004b). Comparison of model calculations and photometric observations of bright "magnetic" regions. *A&A*, 413:1115–1123.

Press, W. H., T. S. A. V. W. T. and Flannery, B. P. (1992). Numerical recipes - the art of scientific computing. cambridge: Cambridge university press.

Puschmann, K. G., Ruiz Cobo, B., Vázquez, M., Bonet, J. A., and Hanslmeier, A. (2005). Time series of high resolution photospheric spectra in a quiet region of the Sun. II. Analysis of the variation of physical quantities of granular structures. *Astronomy and Astrophysics*, 441(3):1157–1169.

Rachkovsky, D. N. (1963). The theory of the absorption lines formation in a magnetic field. The case of a complete redistribution of quanta over the line frequencies. *Izvestiya Ordena Trudovogo Krasnogo Znameni Krymskoj Astrofizicheskoj Observatorii*, 30:267–272.

Rachkovsky, D. N. (1967). The reduction for anomalous dispersion in the theory of absorption line formation in a magnetic field. *Izvestiya Ordena Trudovogo Krasnogo Znameni Krymskoj Astrofizicheskoj Observatorii*, 37:56–61.

Rast, M. (2015). Daniel K. Inouye Solar Telescope (DKIST) Critical Science Plan. *IAU General Assembly*, 22:2257167.

Rast, M. P. (1995). On the Nature of "Exploding" Granules and Granule Fragmentation. *ApJ*, 443:863.

Reardon, K. P. and Cavallini, F. (2008). Characterization of Fabry-Perot interferometers and multi-etalon transmission profiles. The IBIS instrumental profile. *A&A*, 481:897–912.

Rees, D. E., Murphy, G. A., and Durrant, C. J. (1989). Stokes profile analysis and vector magnetic fields. II - Formal numerical solutions of the Stokes transfer equations. *ApJ*, 339:1093–1106.

Rees, D. E. and Semel, M. D. (1979). Line formation in an unresolved magnetic element - A test of the centre of gravity method. *A&A*, 74:1–5.

Rempel, M. (2014). Numerical Simulations of Quiet Sun Magnetism: On the Contribution from a Small-scale Dynamo. *ApJ*, 789(2):132.

Rezaei, R., Steiner, O., Wedemeyer-Böhm, S., Schlichenmaier, R., Schmidt, W., and Lites, B. W. (2007). Hinode observations reveal boundary layers of magnetic elements in the solar photosphere. *A&A*, 476(3):L33–L36.

Righini, A., Cavallini, F., and Reardon, K. P. (2010). Imaging performance of multi-etalon bidimensional spectrometers. *A&A*, 515:A85.

Rimmele, T. R. (2004). Recent advances in solar adaptive optics. In Bonaccini Calia, D., Ellerbroek, B. L., and Ragazzoni, R., editors, *Advancements in Adaptive Optics*, volume 5490 of *Proc. SPIE*, pages 34–46.

Rodriguez Hidalgo, I., Collados, M., and Vazquez, M. (1992). Centre-to-limb variation of solar granulation along the equator and the central meridian. *A&A*, 264(2):661–672.

Romano, P., Berrilli, F., Criscuoli, S., Del Moro, D., Ermolli, I., Giorgi, F., Viticchié, B., and Zuccarello, F. (2012). A Comparative Analysis of Photospheric Bright Points in an Active Region and in the Quiet Sun. *Sol. Phys.*, 280(2):407–416.

Roudier, T., Eibe, M. T., Malherbe, J. M., Rieutord, M., Mein, P., Mein, N., and Faurobert, M. (2001). Temporal height properties of the exploding granules. *A&A*, 368:652–661.

Roudier, T., Malherbe, J. M., Mein, P., Muller, R., Coutard, C., Lafon, M., and Grimaud, F. (2003). High spatial resolution capabilities of Doppler measurements with the Pic du Midi MSDP spectrograph. *Astronomy and Astrophysics*, 409:793–797.

Ruiz Cobo, B. (1992). Inversiòn de la ecuaciòn de transporte radiativo, phd thesis.

Ruiz Cobo, B. and del Toro Iniesta, J. C. (1992). Inversion of Stokes profiles. *ApJ*, 398:375–385.

Ruiz Cobo, B. and del Toro Iniesta, J. C. (1994). On the sensitivity of Stokes profiles to physical quantities. *A&A*, 283:129–143.

Sánchez Almeida, J., Bonet, J. A., Viticchié, B., and Del Moro, D. (2010). Magnetic Bright Points in the Quiet Sun. *ApJ*, 715(1):L26–L29.

Sánchez Almeida, J. and Trujillo Bueno, J. (1999). Radiative Transfer in Weakly Polarizing Media. *ApJ*, 526:1013–1025.

Scharmer, G., Owner-Petersen, M., Korhonen, T., and Title, A. (1999). The New Swedish Solar Telescope. In Rimmele, T. R., Balasubramaniam, K. S., and Radick, R. R., editors, *High Resolution Solar Physics: Theory, Observations, and Techniques*, volume 183 of *Astronomical Society of the Pacific Conference Series*, page 157.

Scharmer, G. B. (2006). Comments on the optimization of high resolution Fabry-Pérot filtergraphs. *A&A*, 447(3):1111–1120.

Scharmer, G. B., Bjelksjo, K., Korhonen, T. K., Lindberg, B., and Petterson, B. (2003). The 1-meter Swedish solar telescope. In Keil, S. L. and Avakyan, S. V., editors, *Innovative Telescopes and Instrumentation for Solar Astrophysics*, volume 4853 of *Proc. SPIE*, pages 341–350.

Schmidt, W. and Soltau, D. (1987). Construction of the German Solar Telescopes in the Observatorio del Teide, Tenerife: The Vacuum Tower Telescope. *Mitteilungen der Astronomischen Gesellschaft Hamburg*, 68:184.

Schmidt, W., von der Lühe, O., Volkmer, R., Denker, C., Solanki, S. K., Balthasar, H., Bello Gonzalez, N., Berkefeld, T., Collados, M., Fischer, A., Halbgewachs, C., Heidecke, F., Hofmann, A., Kneer, F., Lagg, A., Nicklas, H., Popow, E., Puschmann, K. G., Schmidt, D., Sigwarth, M., Sobotka, M., Soltau, D., Staude, J., Strassmeier, K. G., and Waldmann , T. A. (2012a). The 1.5 meter solar telescope GREGOR. *Astronomische Nachrichten*, 333:796.

Schmidt, W., von der Lühe, O., Volkmer, R., Denker, C., Solanki, S. K., Balthasar, H., Bello González, N., Berkefeld, T., Collados Vera, M., Hofmann, A., Kneer, F., Lagg, A., Puschmann, K. G., Schmidt, D., Sobotka, M., Soltau, D., and Strassmeier, K. G. (2012b). The GREGOR Solar Telescope on Tenerife. In Rimmele, T. R., Tritschler, A., Wöger, F., Collados Vera, M., Socas-Navarro, H., Schlichenmaier, R., Carlsson, M., Berger, T., Cadavid, A., Gilbert, P. R., Goode, P. R., and Knölker, M., editors, *Second ATST-EAST Meeting: Magnetic Fields from the Photosphere to the Corona.*, volume 463 of *Astronomical Society of the Pacific Conference Series*, page 365.

Semel, M. (1967). Contribution à létude des champs magnétiques dans les régions actives solaires. *Annales d'Astrophysique*, 30:513–513.

Severino, G., Moretti, P. F., Oliviero, M., and Vamos Team (2001). The Velocity And Magnetic Observations of the Sun (VAMOS) project: status and future prospects. In Wilson, A. and Pallé, P. L., editors, *SOHO 10/GONG 2000 Workshop: Helio- and Asteroseismology at the Dawn of the Millennium*, volume 464 of *ESA Special Publication*, pages 337–340.

Severino, G., Oliviero, M., and Landi Degl'Innocenti, E. (2007). Simulation of Magneto-Optical Filter Transmission Profiles. In Heinzel, P., Dorotovič, I., and Rutten, R. J., editors, *The Physics of Chromospheric Plasmas*, volume 368 of *Astronomical Society of the Pacific Conference Series*, page 617.

Shang, X.-D., Tong, P., and Xia, K.-Q. (2005). Test of steady-state fluctuation theorem in turbulent Rayleigh-Bénard convection. *Phys. Rev. E*, 72(1):015301.

Simon, G. W., Title, A. M., and Weiss, N. O. (1991). Simulating exploding granules and mesogranular flows. *Advances in Space Research*, 11(5):259–262.

Socas-Navarro, H. (2015). NICOLE: NLTE Stokes Synthesis/Inversion Code. Astrophysics Source Code Library.

Socas-Navarro, H., de la Cruz Rodríguez, J., Asensio Ramos, A., Trujillo Bueno, J., and Ruiz Cobo, B. (2015). An open-source, massively parallel code for non-LTE synthesis and inversion of spectral lines and Zeeman-induced Stokes profiles. *A&A*, 577:A7.

Socas-Navarro, H., Ruiz Cobo, B., and Trujillo Bueno, J. (1998). Non-LTE Inversion of Line Profiles. *ApJ*, 507:470–481.

Socas-Navarro, H., Trujillo Bueno, J., and Ruiz Cobo, B. (2000). Non-LTE Inversion of Stokes Profiles Induced by the Zeeman Effect. *ApJ*, 530:977–993.

Soltau, D. (1985). The German 60-cm Vacuum Tower Telescope and Its Post-Focus Facilities. In de Jager, C. and Chen, B., editors, *Solar Physics and Interplanetary Travelling Phenomena*, page 1191.

Soltau, D. (1987). Present and Future Observational Facilities of the German Vacuum Tower Telescope. In Schröter, E.-H., Vázquez, M., and Wyller, A. A., editors, *The Role of Fine-Scale Magnetic Fields on the Structure of the Solar Atmosphere*, page 362.

Soltau, D., Volkmer, R., von der Lühe, O., and Berkefeld, T. (2012). Optical design of the new solar telescope GREGOR. *Astronomische Nachrichten*, 333:847–853.

Srivastava, A. K., Shetye, J., Murawski, K., Doyle, J. G., Stangalini, M., Scullion, E., Ray, T., Wójcik, D. P., and Dwivedi, B. N. (2017). High-frequency torsional Alfvén waves as an energy source for coronal heating. *Scientific Reports*, 7:43147.

Stangalini, M., Giannattasio, F., Erdélyi, R., Jafarzadeh, S., Consolini, G., Criscuoli, S., Ermolli, I., Guglielmino, S. L., and Zuccarello, F. (2017). Polarized Kink Waves in Magnetic Elements: Evidence for Chromospheric Helical Waves. *ApJ*, 840(1):19.

Stangalini, M., Viticchiè, B., Del Moro, D., Piazzesi, R., and Berrilli, F. (2009). Spectropolarimetry with IBIS at NSO/DST: Evolution of Bright Points in the Quiet Sun. In *AGU Fall Meeting Abstracts*, page SH51A.

Stein, R. F. (2012). Solar Surface Magneto-Convection. *Living Reviews in Solar Physics*, 9(1):4.

Stein, R. F. and Nordlund, Å. (2006). Solar Small-Scale Magnetoconvection. *ApJ*, 642(2):1246–1255.

Steiner, O. (2003). Distribution of magnetic flux density at the solar surface. Formulation and results from simulations. *A&A*, 406:1083–1088.

Steiner, O., Grossmann-Doerth, U., Knölker, M., and Schüssler, M. (1998). Dynamical Interaction of Solar Magnetic Elements and Granular Convection: Results of a Numerical Simulation. *ApJ*, 495(1):468–484.

Stix, M. (2004). The Sun, an introduction.

Title, A. M., Tarbell, T. D., Topka, K. P., Ferguson, S. H., Shine, R. A., and SOUP Team (1989). Statistical Properties of Solar Granulation Derived from the SOUP Instrument on Spacelab 2. *ApJ*, 336:475.

Tritschler, A., Rimmele, T. R., Berukoff, S., Casini, R., Craig, S. C., Elmore, D. F., Hubbard, R. P., Kuhn, J. R., Lin, H., McMullin, J. P., Reardon, K. P., Schmidt, W., Warner, M., and Woger, F. (2015). DKIST: Observing the Sun at High Resolution. In van Belle, G. T. and Harris, H. C., editors, *18th Cambridge Workshop on Cool Stars, Stellar Systems, and the Sun*, volume 18 of *Cambridge Workshop on Cool Stars, Stellar Systems, and the Sun*, pages 933–944.

Trujillo Bueno, J. (2003). The Generation and Transfer of Polarized Radiation in Stellar Atmospheres. In Hubeny, I., Mihalas, D., and Werner, K., editors, *Stellar Atmosphere Modeling*, volume 288 of *Astronomical Society of the Pacific Conference Series*, page 551.

Unno, W. (1956). Line Formation of a Normal Zeeman Triplet. *PASJ*, 8:108.

Urban, P., Hanzelka, P., Musilová, V., Králík, T., La Mantia, M., Srnka, A., and Skrbek, L. (2014). Heat transfer in cryogenic helium gas by turbulent Rayleigh-Bénard convection in a cylindrical cell of aspect ratio 1. *New Journal of Physics*, 16(5):053042.

Utz, D., Hanslmeier, A., Muller, R., Veronig, A., Rybák, J., and Muthsam, H. (2010). Dynamics of isolated magnetic bright points derived from Hinode/SOT G-band observations. *A&A*, 511:A39.

Van Kooten, S. J. and Cranmer, S. R. (2017). Characterizing the Motion of Solar Magnetic Bright Points at High Resolution. *ApJ*, 850(1):64.

Vaughan, J. M. (1989). The Fabry-Perot Interferometer.

Viavattene, G. (2016). Master thesis: Spectro-polarimetric analysis of a short lived solar active region.

Viavattene, G., Berrilli, F., Collados Vera, M., Del Moro, D., Giovannelli, L., Ruiz Cobo, B., and Zuccarello, F. (2018). Remote sensing of the solar photosphere: a tale of two methods. In *Journal of Physics Conference Series*, volume 956 of *Journal of Physics Conference Series*, page 012006.

Viavattene, G., Berrilli, F., Consolini, G., Del Moro, D., Giannattasio, F., Giovannelli, L., and Penza, V. (2019a). Evaluating a proxy of the local entropy production rate on the solar photosphere. In *Journal of Physics Conference Series*, Journal of Physics Conference Series, in press.

Viavattene, G., Berrilli, F., Consolini, G., Del Moro, D., Giannattasio, F., Giovannelli, L., and Penza, V. (2019b). Statistical behaviour of a proxy of the entropy production rate of the solar photosphere. *Nuovo Cimento C Geophysics Space Physics C*, 42(1):8.

Viavattene, G., Zuccarello, F., Collados Vera, M., and Ruiz Cobo, B. (2019c). Spectropolarimetric analysis of a short lived solar active region. *Nuovo Cimento C Geophysics Space Physics C*, 42(1):10.

Viticchié, B. (2012). On the Polarimetric Signature of Emerging Magnetic Loops in the Quiet Sun. *ApJ*, 747(2):L36.

Viticchié, B., Del Moro, D., Berrilli, F., Bellot Rubio, L., and Tritschler, A. (2009). Imaging Spectropolarimetry with IBIS: Evolution of Bright Points in the Quiet Sun. *ApJ*, 700:L145–L148.

Viticchiè, B., Del Moro, D., Berrilli, F., Rubio, L. B., and Tritschler, A. (2011). IBIS 2D Spectropolarimetry: Analysis of G-band Bright Points. In Kuhn, J. R., Harrington, D. M., Lin, H., Berdyugina, S. V., Trujillo-Bueno, J., Keil, S. L., and Rimmele, T., editors, *Solar Polarization 6*, volume 437 of *Astronomical Society of the Pacific Conference Series*, page 75.

Viticchié, B., Del Moro, D., Criscuoli, S., and Berrilli, F. (2010). Imaging Spectropolarimetry with IBIS. II. On the Fine Structure of G-band Bright Features. *ApJ*, 723:787–796.

Vögler, A., Shelyag, S., Schüssler, M., Cattaneo, F., Emonet, T., and Linde, T. (2005). Simulations of magneto-convection in the solar photosphere. Equations, methods, and results of the MURaM code. *A&A*, 429:335–351.

Vogt, E., Oliviero, M., Severino, G., and Straus, T. (1999). Calibration of VAMOS Magnetic Data. In Wilson, A. and et al., editors, *Magnetic Fields and Solar Processes*, volume 9 of *ESA Special Publication*, page 405.

Wilken, V., de Boer, C. R., Denker, C., and Kneer, F. (1997). Speckle measurements of the centre-to-limb variation of the solar granulation. *Astronomy and Astrophysics*, 325:819–824.

Wittmann, A. (1974). Computation and Observation of Zeeman Multiplet Polarization in Fraunhofer Lines. II: Computation of Stokes Parameter Profiles. *Sol. Phys.*, 35:11–29.

Woeger, F. (2016). The DKIST Instrumentation Suite. In *AAS/Solar Physics Division Abstracts #47*, volume 47 of *AAS/Solar Physics Division Meeting*, page 201.02.

Zuccarello, F. and EST Team (2012). The European Solar Telescope: project status . *Memorie della Societa Astronomica Italiana Supplementi*, 19:67.

Zwaan, C. (1987). Elements and patterns in the solar magnetic field. *ARA&A*, 25:83–111.